GOETHE UNIVERSITÄT
FRANKFURT AM MAIN

Global analysis of halogenated trace gases in the UTLS: From long-lived to short-lived substances

Dissertation
zur Erlangung des Doktorgrades
der Naturwissenschaften

vorgelegt beim
Fachbereich 11 Geowissenschaften/Geographie
Institut für Atmosphäre und Umwelt
in Frankfurt am Main

von
Markus Jesswein
aus Burlington, Ontario

Frankfurt am Main (2023)
(D 30)

Vom Fachbereich 11 Geowissenschaften/Geographie der
Johann Wolfgang Goethe - Universität als Dissertation angenommen.

Dekan:
Prof. Dr. Jürgen Runge

Gutachter:
Apl. Prof. Dr. Andreas Engel (Goethe-Universität Frankfurt am Main)
Prof. Dr. Peter Hoor (Johannes Gutenberg-Universität Mainz)
Prof. Dr. Joachim Curtius (Goethe-Universität Frankfurt am Main)

Datum der Disputation: 01.12.2023

Abstract

In this dissertation, the distribution of chlorinated and brominated substances in the upper troposphere and lower stratosphere is investigated. These substances contribute significantly to the catalytic decomposition of ozone and are involved in the recurrent formation of the polar ozone hole in the Antarctic winter and spring. The Montreal Protocol, a multilateral environmental treaty to protect the ozone layer, has successfully reduced emissions of long-lived chlorine- and bromine-containing substances. Short-lived chlorinated and brominated substances, some of which are natural and anthropogenic in origin, are not regulated by the Montreal Protocol and it can be assumed that their relative contribution to the stratospheric halogen budget will increase, while the contribution of long-lived compounds will steadily decrease. The distribution of long- and short-lived halogenated substances are part of current research. For the upper troposphere and lower stratosphere, the very short-lived substances are particularly important. The lower stratosphere needs special investigation in this respect, since its composition is influenced by different transport processes. The influences on ozone trends in the lower stratosphere are subject to great uncertainties. Especially in the Southern Hemisphere, the number of observations is very limited.

In this work, the GhOST (Gas chromatograph for Observational Studies using Tracers) instrument was used during the SouthTRAC measurement campaign on the German HALO (High Altitude and LOng range) research aircraft, providing observations of halogenated hydrocarbons in Antarctic late winter to early spring 2019, a generally poorly sampled region. The polar vortex was, compared to previous years, significantly weaker and shifted towards the eastern South Pacific and South America. From the airborne measurements of chlorinated source gases, inorganic chlorine (the sum of active chlorine and reservoir gases; Cl_y) could be inferred with the result that Cl_y within the vortex increased up to 1687 ± 19 ppt at 385 K potential temperature, accounting for about 50 % of the total chlorine within the vortex and only 15 % of the total chlorine in the southern mid-latitudes. A comparison with the Northern Hemisphere could be made using the PGS measurement campaign in the Arctic winter 2015/2016. Under comparable conditions (season and distance from the tropopause), only 40 % of the total chlorine was in the inorganic form within the Arctic polar vortex and about 20 % was found in the mid-latitudes of the Northern Hemisphere. In addition, about 540 ppt more Cl_y was present in the Antarctic vortex than in the Arctic vortex, exceeding the annual variations previously reported for Antarctica.

The mean age of air plays an essential role in the derivation of Cl_y via the organic source gases, as was done in this work. A new method for determining the mean age of air from observational data has been introduced that accounts for extra-tropical input to the stratosphere in addition to tropical input. This new method was compared with the previously used method, which considered only the tropical input. The new method shows more realistic values especially near the tropopause. On average, the air of the lower stratosphere in the Northern Hemisphere was older than in the Southern Hemisphere by about 0.5 ± 0.3 years. About 65 K above the tropopause, the pattern changed with older air in the mid-latitudes of the Northern Hemisphere, but older air in high latitudes of the Southern Hemisphere, which implies differences in the strength and isolation of the respective polar vortex as well as the wave forcing in the shallow branch of the Brewer-Dobson circulation of the respective hemisphere. This is in good agreement with the distribution of Cl_y. The difference in the lower stratosphere was not clearly evident with the old method and it can be assumed that investigations of the differences in Cl_y of Northern and Southern Hemisphere will benefit from the new method.

Finally, the global and seasonal distribution of the two most important representatives of the short-lived brominated substances, CH_2Br_2 and $CHBr_3$, was investigated. For this

purpose, two additional HALO measurement campaigns have been used, the 2012 TACTS measurement campaign and the 2017 WISE measurement campaign, as well as the HIAPER Pole-to-Pole Observations (HIPPO) and Atmospheric Tomography (ATom) measurement campaigns. Observations of CH_2Br_2 show a pronounced seasonality in the free and upper troposphere of both hemispheres with slightly larger values in the Northern Hemisphere. $CHBr_3$, on the other hand, shows a generally higher variability and lower seasonality with larger mixing ratios at mid and high latitudes in the northern hemispheric winter and autumn. A comparison of the lower stratosphere is limited to autumn and spring of both hemispheres due to the limited data basis of the observations. The distributions in each spring are similar (less than 0.1 ppt differences for e.g., CH_2Br_2). In hemispheric autumn, larger differences are evident with substantially smaller mixing ratios in the southern hemispheric lower stratosphere. This suggests that the transport processes of the two hemispheres may be different and implies that the input of tropospheric air (flushing) to the Northern Hemisphere lowest stratosphere is more efficient than in the Southern Hemisphere. Vertical profiles of CH_2Br_2 and $CHBr_3$ in the mid-latitudes of both hemispheres and resulting vertical gradients support this conjecture. However, the Southern Hemisphere data set is insufficient to quantify this difference and further measurements are needed.

Observational data were compared with model results from the TOMCAT (Toulouse Offline Model of Chemistry And Transport) and CAM-Chem (Community Atmosphere Model with Chemistry, version 4) model, both using the Ordóñez et al. (2012) emission scenario. Seasonality in CH_2Br_2 in the Southern Hemisphere was not reproduced by the models. In contrast, the models show a pronounced seasonality of $CHBr_3$ in both hemispheres, which could not be confirmed by observations. Both models show a good agreement with the distribution of both substances in the lower stratosphere. Only the southern hemispheric autumn, with substantially smaller mixing ratios in the observations, was not reflected by the models. In contrast to the observations, the models show a comparable flushing of the lower stratosphere in both hemispheres.

Kurzzusammenfassung

In dieser Dissertation wird die Verteilung von Chlor- und Bromverbindungen in der oberen Troposphäre und unteren Stratosphäre untersucht. Diese Verbindungen haben einen wesentlichen Anteil am katalytischen Abbau von Ozon und sind maßgeblich beteiligt an der wiederkehrenden Enstehung des polaren Ozonlochs im antarktischem Winter und Frühjahr. Durch das Montreal Protokoll, einem multilateralen Umweltabkommen zum Schutze der Ozonschicht, sind erfolgreich die Emissionen langlebiger chlor- und bromhaltigen Verbindung reduziert worden. Kurzlebige Chlor- und Bromverbindungen, die teils natürlichen, teils anthropogenen Ursprungs sind, werden nicht durch das Montreal Protokoll reguliert, und es kann angenommen werden, dass ihr relativer Anteil am stratosphärischen Halogen-Budget zunehmen wird, bei stetig sinkendem Beitrag der langlebigen Verbindungen. Die Verteilungen der lang- und kurzlebigen halogenierten Substanzen sind Bestandteil aktueller Forschung. Für die obere Troposphäre und untere Stratosphäre sind die kurzlebigen halogenierten Substanzen besonders wichtig. In der unteren Stratosphäre bedarf es diesbezüglich besonderer Untersuchung, da ihre Zusammensetzung durch unterschiedliche Transportprozesse beeinflusst wird. Die Einflüsse auf Ozontrends in der unteren Stratosphäre sind mit großen Unsicherheiten behaftet. Gerade in der südlichen Hemisphäre ist die Anzahl an Beobachtungen stark limitiert.

Im Rahmen dieser Arbeit wurde das GhOST (Gas chromatograph for Observational Studies using Tracers) Instrument während der SouthTRAC-Messkampagne auf dem deutschen Forschungsflugzeug HALO (High Altitude and LOng range research aircraft) verwendet und bietet damit Beobachtungen von halogenierten Kohlenwasserstoffen im antarktischen späten Winter und Frühjahres 2019, einem bisher wenig beprobten Gebiet. Der Polarwirbel war, im Vergleich zu vorherigen Jahren, deutlich schwächer und in Richtung des östlichen Südpazifiks und Südamerika verlagert. Aus den flugzeuggetragenen Messungen der chlorierten Quellgase konnte anorganisches Chlor (die Summe aus aktivem Chlor und Reservoir-Gasen; Cl_y) hergeleitet werden mit dem Ergebnis, dass Cl_y innerhalb des Wirbels auf bis zu 1687 ± 19 ppt bei 385 K potentieller Temperatur ansteigt und damit etwa 50 % des Gesamtchlors innerhalb des Wirbels ausmacht und lediglich 15 % des gesamten Chlors in den südlichen mittleren Breiten. Ein Vergleich mit der Nordhemisphäre konnte mithilfe der PGS-Messkampagne im arktischen Winter 2015/2016 durchgeführt werden. Bei vergleichbaren Bedingungen (Saison und Abstand zur Tropopause) war lediglich 40 % des Gesamtchlors in der anorganischen Form innerhalb des arktischen Polarwirbels und etwa 20 % in den mittleren Breiten der Nordhemisphäre zu finden. Zusätzlich war etwa 540 ppt mehr Cl_y im antarktischen Wirbel als im arktischen Wirbel vorhanden, was die jährlichen Schwankungen, die bisher für die Antarktis berichtet wurden, übersteigt.

Das mittlere Alter der Luft (mean age of air) spielt für die Herleitung von Cl_y über die organischen Quellgase, wie es in dieser Arbeit durchgeführt wurde, eine wesentliche Rolle. Eine neue Methode zur Bestimmung des mittleren Alters der Luft aus Beobachtungsdaten wurde eingeführt, die zusätzlich zum tropischen Eintrag auch den extratropischen Eintrag in die Stratosphäre berücksichtigt. Diese neue Methode wurde mit der zuvor genutzten Methode, die lediglich den tropischen Eintrag berücksichtigt, verglichen. Die neue Methode zeigt vor allem nahe der Tropopause realistischere Werte. Im Durchschnitt war die Luft der unteren Stratosphäre der Nordhemisphäre um etwa 0.5 ± 0.3 Jahre älter als in der Südhemisphäre. Etwa 65 K oberhalb der Tropopause änderte sich das Muster mit älterer Luft in den mittleren Breiten der Nordhemisphäre, jedoch ältere Luft in hohen Breiten der Südhemisphäre, was Unterschiede in der Stärke und Isolation des jeweiligen Polarwirbels sowie den Wellenantrieb im flachen Ast der Brewer-Dobson-Zirkulaition der jeweiligen Hemisphäre impliziert. Dies steht in guter Übereinstimmung mit der Verteilung von Cl_y. Die

Differenz in der unteren Stratosphäre war mit der alten Methode nicht klar ersichtlich und es kann angenommen werden, dass Untersuchungen der Differenzen in Cl_y von Nord- und Südhemisphäre von der neuen Methode profitieren werden.

Zum Schluss wurde die globale und saisonale Verteilung der beiden wichtigsten Vertreter der kurzlebigen bromierten Substanzen, CH_2Br_2 und $CHBr_3$, betrachtet. Dazu sind zusätzlich zwei weitere HALO-Messkampagnen verwendet worden, die TACTS-Messkampagne 2012 und die WISE-Messkampagne 2017 sowie die HIAPER Pole-to-Pole Observations (HIPPO) und die Atmospheric Tomography (ATom) Messkampagne. Beobachtungen von CH_2Br_2 zeigen eine ausgeprägte Saisonalität in der freien und oberen Tropophäre beider Hemisphären mit leicht höheren Werten auf der Nordhemisphäre. $CHBr_3$ hingegen weist eine generell höhere Variabilität und geringere Saisonalität auf mit höheren Mischungsverhältnisse in mittleren und hohen Breiten im nordhemisphärischen Winter und Herbst. Ein Vergleich der unteren Stratosphäre ist nur begrenzt möglich, aufgrund der begrenzten Datengundlage der Beobachtungen auf Herbst und Frühjahr beider Hemisphären. Die Verteilungen im jeweiligen Frühjahr sind ähnlich (weniger als 0.1 ppt Differenzen für CH_2Br_2). Im hemisphärischen Herbst sind größere Unterschiede zu erkennen mit deutlich geringeren Mischungsverhältnissen in der südhemisphärischen unteren Stratosphäre. Dies deutet darauf hin, dass die Transportprozesse beider Hemisphären unterschiedlich sind und impliziert, dass der Eintrag troposphärischer Luft (Spülung bzw. Flushing) in die unterste Stratosphäre der Nordhemisphäre effizienter ist als in der Südhemisphäre. Vertikalprofile von CH_2Br_2 und $CHBr_3$ in den mittleren Breiten beider Hemisphären und resultierende Vertikalgradienten unterstützen diese Vermutung. Die Datengrundlage der Südhemisphäre ist jedoch nicht ausreichend, um diesen Unterschied zu quantifizieren und weitere Messungen sind notwendig.

Verglichen wurden die Beobachtungsdaten mit Modellergebnissen des TOMCAT (Toulouse Off-line Model of Chemistry And Transport) und CAM-Chem (Community Atmosphere Model with Chemistry, version 4) Model, beide mit der Nutzung des Ordóñez u. a. (2012) Emissionszenarios. Die Saisonalität in CH_2Br_2 in der Südhemisphäre wurde von den Modellen nicht wiedergegeben. Beide Modelle zeigen eine ausgeprägte Saisonalität von $CHBr_3$ in beiden Hemisphären, was durch Beobachtungen nicht bestätigt werden konnte. Beide Modelle zeigen eine gute Übereinstimmung mit der Verteilung beider Substanzen in der unteren Stratosphäre. Lediglich der südhemisphärische Herbst, mit deutlich geringeren Mischungsverhältnissen in den Beobachtungen, wurden von den Modellen nicht widergespiegelt, sondern eine vergleichbare Spülung der unteren Stratosphäre auf beiden Hemisphären.

List of Author's Publications

This cumulative dissertation summarizes the main methods, data, and results that are published in detail in the following three peer-reviewed articles, which are listed at the end of this work as well:

Jesswein, M., Bozem, H., Lachnitt, H.-C., Hoor, P., Wagenhäuser, T., Keber, T., Schuck, T., and Engel, A.: *Comparison of inorganic chlorine in the Antarctic and Arctic lowermost stratosphere by separate late winter aircraft measurements*, Atmos. Chem. Phys., 21, 17225–17241, 2021, DOI: https://doi.org/10.5194/acp-21-17225-2021

Jesswein, M., Fernandez, R. P., Berná, L., Saiz-Lopez, A., Grooß, J.-U., Hossaini, R., Apel, E. C., Hornbrook, R. S., Atlas, E. L., Blake, D. R., Montzka, S., Keber, T., Schuck, T., Wagenhäuser, T., and Engel, A.: *Global seasonal distribution of CH_2Br_2 and $CHBr_3$ in the upper troposphere and lower stratosphere*, Atmos. Chem. Phys., Atmos. Chem. Phys., 22, 15049–15070, 2022, DOI: https://doi.org/10.5194/acp-22-15049-2022

Wagenhäuser, T., **Jesswein, M.**, Keber, T., Schuck, T., and Engel, A.: *Mean age from observations in the lowermost stratosphere: an improved method and interhemispheric differences*, EGUsphere, 1–26, 2022, DOI: https://doi.org/10.5194/egusphere-2022-1197

Contents

List of Figures

List of Tables

List of Abbreviations

AoA	**a**ge **o**f **a**ir
ATom	**A**tmospheric **Tom**ograph
BDC	**B**rewer-**D**obson **C**irculation
CFC	**c**hloro**f**luoro**c**arbon
ECD	**e**lectron **c**apture **d**etector
EI	**e**lectron impact **i**onization
ExTL	**e**xtratropical-**T**ransition **L**ayer
EX-UTLS	**e**xtratropical-**u**pper **t**ropopshere and **l**ower **s**tratosphere
FCKW	**F**luor**c**hlor**k**ohlen**w**asserstoff
FSW	**f**inal **s**tratospheric **w**arming
GC	**g**as **c**hromatograph
GhOST	**G**as c**h**romatograph for **O**bservational **S**tudies using **T**racers
GWP	**g**lobal **w**arming **p**otential
HALO	**H**igh **A**ltitude and **LO**ng **R**ange research Aircraft
HCFC	**h**ydro**c**hloro**f**luoro**c**arbon
HFC	**h**ydro**f**luoro**c**arbon
HIPPO	**HI**APER **P**ole-to-**PO**le
LMS	**l**ower**m**ost **s**tratosphere
MAPD	**m**ean **a**bsolute **p**ercentage **d**ifference
MS	**m**ass **s**pectrometer
NCI	**n**egative **c**hemical **i**onization
NH	**N**orth **H**emisphere
ODP	**o**zone **d**epletion **p**otential
ODS	**o**zone **d**epletion **s**ubstance
PSC	**p**olar **s**tratospheric **c**loud
PFC	**p**erfluoro**c**arbon
PGI	**p**roduct **g**as **i**njection
PV	**p**otential **v**orticity
PVU	**p**otential **v**orticity **u**nit
QBO	**q**uasi-**b**iennial **o**scillation
rom	**r**atio **o**f **m**oments
SGI	**s**ource **g**as **i**njection
SH	**S**outh **H**emisphere
SSW	**s**udden **s**tratospheric **w**arming
TSE	**t**roposphere-**s**ratosphere **e**xchange
TST	**t**roposphere-**s**ratosphere-**t**ransport
TTL	**t**ropical **t**ropopause **l**ayer
UTLS	**u**pper **t**roposphere and **l**ower **s**tratosphere
VSLS	**v**ery **s**hort-**l**ived **s**ubstances

Deutsche Zusammenfassung

Die Ozonschicht in der Stratosphäre, der zweituntersten Schicht der Erdatmosphäre, ist ein wichtiger Bestandteil der Atmosphäre, die das gesamte Leben auf der Erde schützt. In den 1980er haben Farman, Gardiner und Shanklin (1985) einen außergewöhnlich starken Rückgang des polaren Ozons feststellen können. Die Ursache dieses wiederkehrenden Ereignisses, auch bekannt als antarktisches Ozonloch, sind synthetisch hergestellte Fluorchlorkohlenwasserstoffen (FCKWs). Auch wenn die Substanzen in der Atmosphäre nur in sehr geringen Mengen vorkommen, so können die Chlor und Brom, die beim Abbau dieser Substanzen freigesetzt werden, effektiv Ozon zerstören. Um die Ozonschicht zu schützen, wurde das Montreal Protokoll Ende der 1980er verabschiedet. Dieses multilaterale Umweltabkommen reglementiert die Reduzierung und Abschaffung der ozonzerstörenden Subtanzen, was zu einer langsamen Erholung der Ozonschicht führt. Zusätzlich zu den Substanzen, welche durch das Montreal Protokoll kontrolliert werden, gibt es kurzlebige halogenierte Substanzen mit atmosphärischen Lebenszeiten von weniger als 6 Monaten, die sowohl anthropogenen als auch natürlichen Ursprungs sind und deren Beitrag zur stratosphärischen Halogenbelastung zunimmt (Hossaini u. a., 2017; Laube und Tegtmeier, 2022). Eine fortlaufende Überwachung und Untersuchung der FCKWs, deren synthetische Ersatzsubstanzen sowie der kurzlebigen halogenierten Substanzen ist Bestandteil aktueller Forschung zur Überwachung des stratosphärischen Zustands hinsichtlich Ozon.

In der Stratosphäre sind In-situ-Beobachtungen bis zu einer Höhe von etwa 50 km begrenzt. Für die In-situ-Analyse von Spurengasen in der Stratosphäre stehen sowohl Flugzeugmessungen, die bis in die untere Stratosphäre reichen, als auch Ballonaufstiege zur Sammlung von Luftproben bis tief in die Stratosphäre zur Verfügung. Darüber hinaus liefern Fernerkundungsinstrumente Daten für Spurengase. Unterstützung für umfassende Analysen der Stratosphäre bieten modernste Chemie-Klima- und Chemie-Transport-Modelle. Diese Modelle erfordern einen realistischen Abschätzung von Emissionen, was eine enge Zusammenarbeit der experimentellen und theoretischen Forschung benötigt, um Mischungsverhältnisse in der Troposphäre und Stratosphäre zu simulieren. Aktuelle Emissionsszenarien, so zum Beispiel von kurzlebigen halogenierten Substanzen, weisen erhebliche Schwankungen auf und sind Thema aktueller Forschung (Hossaini u. a., 2013).

Das Hauptaugenmerk dieser Arbeit liegt auf der Region um die Tropopause, auch obere Troposphäre und untere Stratosphäre genannt (upper troposphere and lower stratosphere, UTLS). Sie wird daher sowohl von stratosphärischer als auch von der troposphärischer Luft durch Transportprozesse in der Stratosphäre sowie durch den Austausch zwischen Stratosphäre und Troposphäre über die Tropopause beeinflusst. Die extratropische obere Troposphäre und untere Stratosphäre ist grob gesagt die Region polwärts des subtropischen Jets zwischen etwa 8 und 20 km Höhe (z.B. Gettelman u. a., 2011). Der Transport in der Stratosphäre ist allgemein durch eine globale meridionale Zirkulation von den Tropen zu den Polen gekennzeichnet, auch Brewer-Dobson-Zirkulation genannt. Im Allgemeinen gibt es zwei Hauptwege für den Transport in die extratropische obere Troposphäre und untere Stratosphäre. Zum Einen die zur Brewer-Dobson-Zirkulation zugehörige Residualzirkulation mit ihren beiden Haupttransportpfaden und eine bidirektionale Mischung entlang isentropischer Flächen (z.B. Plumb, 2007; Birner und Bönisch, 2011). Die Haupttransportpfade der Residualzirkulation sind der flache Ast mit dem Transport knapp oberhalb der tropischen Tropopause und direkt in die mittleren Breiten beider Hemisphären und der tiefe Ast mit Transport von den Tropen tief in die Stratosphäre und sogar Mesosphäre beider Hemisphären und ein Absinken in den hohen Breiten, verstärkt jedoch auf der Winterhemisphäre. Zum Anderen gibt es bidirektionale Mischung über die Tropopause hinweg (stratospheric-tropospheric exchange, STE) (z.B. Holton u. a., 1995; Stohl u. a., 2003). In der Polarregion

reicht im hemisphärischen Winter der Polarwirbel bis in die untere Stratosphäre hinein. Der Polarwirbel zeichnet sich durch ein hochreichendes Tief aus, eingeschlossen von starken Westwinden (Polarjet). Der Wirbel kann als eine isolierte Region betrachtet werden, die durch den Polarjet als Transportbarriere zur Stratosphäre der mittleren Breiten getrennt ist. Es kommt zu einem starken Gradienten vieler Spurengase über die Transportbarriere des Wirbels zur Stratosphäre der mittleren Breiten mit dem Transport in den Polarwirbel über den tiefen Ast der Residualzirkulation sowie diabatisches Absinken kalter Luftmassen (z.B. Hartmann u. a., 1989; Schoeberl und Hartmann, 1991; Schoeberl u. a., 1992; Butchart, 2014).

Eine häufig angewendete Größe zur Quantifizierung des Transportes ist das sogenannte mittlere Alter der Luft (mean Age of Air, AoA). Diese Größe gibt die durchschnittliche Zeit an, die ein Luftpaket für den Transport von einem Bezugspunkt zu einem bestimmten Ort in der Stratosphäre benötigt hat. Der Bezugspunkt ist in der Regel der Erdboden oder die tropische Tropopause. Da jedoch Luftmassen, die in die Stratosphäre eingetragen werden, während des Transportes vermischt werden, besteht jedes Luftpaket in der Stratosphäre aus einer Anzahl von Luftpaketen mit unterschiedlichen Transitzeiten (z.B. Hall und Prather, 1993; Hall und Plumb, 1994). Das Altersspektrum stellt eine Wahrscheinlichkeitsdichtefunktion aller Transitzeiten eines Luftpakets dar, mit dem mittleren Alter als erstem Moment dieser Verteilung. Chemisch äußerst stabile Spurengase können genutzt werden, um das mittlere Alter der Luft zu bestimmen. Dazu gehören SF_6 und CO_2 (z.B. Volk u. a., 1997; Engel u. a., 2002; Bönisch u. a., 2009).

In dieser Dissertation wird die Verteilung von Chlor- und Bromverbindungen in der oberen Troposphäre und unteren Stratosphäre auf der Grundlage von flugzeuggestützen Beobachtungen untersucht. Diese Verbindungen sind maßgeblich am katalytischen Abbau von Ozon und damit an der wiederkehrenden Entstehung des polaren Ozonlochs beteiligt. Bezüglich der chlorierten Substanzen liegt der Fokus auf den wichtigsten Stellvertretern der FCKWs, der teilhalogenierten FCKWs und der Chlorkohlenwasserstoffe, im folgenden Quellgase genannt. Chlor wird hauptsächlich in Form von organischen Quellgasen (CCl_y) in die Stratosphäre transportiert, wo diese durch Photodissoziation und in Reaktion mit Radikalen langsam zersetzt werden. Das freigesetzte Chlor liegt anschließend in chemisch aktiven Vebindungen (Cl, Cl_2, ClO und Cl_2O_2, zusammengefasst zu ClO_x) vor oder wird in verhältnismäßig stabile Verbindungen überführt, auch Reservoirgase (HCl und $ClONO_2$) genannt. Aktive Verbindungen und Reservoirgase stellen anorganisches Chlor (Cl_y) dar. Von großer Bedeutung ist Cl_y in den Polarregionen. Sowohl die Menge an Cl_y innerhalb des Polarwirbels, als auch die stratosphärischen Temperaturen und Dynamik haben einen Einfluss auf die Größe des Ozonlochs (Newman, Kawa und Nash, 2004). So variiert die Größe des antarktischen Ozonlochs von Jahr zu Jahr.

Neben Chlor ist Brom eines der wichtigsten Halogene, die das stratosphärische Ozon beeinflussen. Trotz der geringeren Menge von Brom in der Stratosphäre ist die relative Effizienz in Bezug auf den Ozonabbau 60–65 mal höher als von Chlor (z.B. Sinnhuber u. a., 2009; World Meteorological Organization, Atmospheric Administration und Space Administration, 2018). Eine neuere Studie berichtet sogar von einer bis zu 74 mal höheren Effizienz von Brom im Vergleich zu Chlor (Klobas u. a., 2020). Die höhere Effizienz ist bedingt durch die weniger stabilen Reservoirgase für Brom und damit einem höheren Vorkommen von reaktiven Brom (z.B. Wofsy, McElroy und Yung, 1975; Spencer und Rowland, 1978). Der Fokus bei den Bromverbindungen liegt auf den kurzlebigen bromierten Verbindungen. Diese sind überwiegend natürlichen Ursprungs, etwa aus den Ozeanen, und nehmen einen wesentlichen Anteil von etwa 25 % aller Bromverbindungen ein. Ihre Verteilung in der Stratosphäre hängt in hohem Maße von lokalen Quellen, Transportwegen und chemischem Abbau während des Transportes ab. Aufgrund ihrer kurzen Lebensdauer können enthaltene Halogene schnell in der unteren Stratosphäre freigesetzt werden und mit Ozon reagieren. Die beiden wichtigsten Vertreter der kurzlebigen bromierten Substanzen, die in dieser Dissertation

untersucht werden, sind Dibrommethan (CH_2Br_2) und Bromoform ($CHBr_3$).

Der Hauptteil der Dissertation ist in drei Teile gegliedert. Nach einer kurzen Einführung in die letzte Flugzeugmesskampagne und der Vorstellung des Messgerätes, auf dem ein Großteil der präsentierten Ergebnisse beruht, geht der erste Teil auf die Bestimmung von Cl_y sowie auf die Methode zur Einteilung von Beobachtungen in die Bereiche Polarwirbel, Wirbel-Grenzregion und mittleren Breiten ein, den Aspekten von Jesswein u. a. (2021) folgend. Der zweite Teil beschäftigt sich mit dem Vergleich von Cl_y in der Nordhemisphäre und Südhemisphäre auf Grundlage zweier Messkampagnen mit dem HALO Forschungsflugzeug (High Altitude and LOng Range Research Aircraft), welche zu ähnlichen Zeiten auf der jeweiligen Hemisphäre stattfanden. Zusätzlich wird eine verbesserte Methode zur Bestimmung des mittleren Alters präsentiert, die die Bestimmung von Cl_y verbessert. Der interhemisphärische Vergleich und die verbesserte Methode zur Bestimmung des mittleren Alters sind in Jesswein u. a. (2021) und Wagenhäuser u. a. (2022) publiziert. Der dritte Teil beschäftigt sich mit der globalen und saisonalen Verteilung der beiden kurzlebigen bromierten Substanzen CH_2Br_2 und $CHBr_3$. Dazu werden Messdaten von insgesamt vier HALO Messkampagnen verwendet. Zusätzlich wird die Datengrundlage mit Hilfe zweier weiteren Messkampagnen, der HIPPO und ATom Mission, erweitert. Dies ist in Jesswein u. a. (2022) als dritte Publikation aufgeführt.

Ausgangspunkt der Dissertation ist die Begleitung der HALO Messkampagne SouthTRAC (Southern Hemisphere Transport, Dynamics, and Chemistry) (Rapp u. a., 2020) im späten Winter und frühen Frühling der Südhemisphäre im Jahr 2019. Ziel war die Untersuchung der Dynamik und chemischen Zusammensetzung der antarktischen oberen Troposphäre und unteren Stratosphäre, einem bisher wenig beprobten Gebiet. Mit dem GhOST (Gas chromatograph for Observational Studies using Tracers) Messinstrument, welches auf HALO eingesetzt wird, konnten In-Situ-Messungen von Spurengasen durchgeführt werden. GhOST ist ein zwei-kanaliger Gaschromatograph (GC). Der erste Kanal koppelt einen isotherm betriebenen GC mit einem Elektroneneinfangdetektor (electron capture detector, ECD) zur Messung von SF_6 und CFC-12 mit einer Zeitauflösung von etwa 1 Minute. Der zweite Kanal ist ein temperaturprogrammierter GC, welcher mit einem Quadrupol-Massenspektrometer (QP-MS) gekoppelt ist, mit dem ein breites Spektrum and halogenierten Kohlenwasserstoffe mit einer Zeitauflösung von 4 bis 6 Minuten gemessen wird.

Aus den flugzeuggetragenen Messungen der chlorierten Quellgase ist es möglich Cl_y zu bestimmen. Dazu bedarf es neben CCl_y aus den Quellgasen auch die Gesamtmenge an stratosphärischem Chlor (Cl_{total}). Die Differenz von Cl_{total} und CCl_y ergibt Cl_y. Für die Gesamtmenge an Chlor werden das mittlere Alter der Luft sowie troposphärische Zeitreihen der chlorierten Quellgase benötigt. Ersteres wird aus SF_6 Messungen hergeleitet und letzteres aus Bodenstationsdaten des AGAGE (Advanced Global Atmospheric Gases Experiment) Netzwerkes erhalten (Prinn u. a., 2018). Die Cl_y-Bestimmung auf diesem Weg wird im Folgenden semi-direkte Methode genannt. Für den Fall, dass nicht ausreichend Messungen von chlorierten Quellgasen vorliegen, kann CCl_y aus vergangenen Messungen herangezogen werden. Dazu werden Beobachtungen zweier Ballonaufstiege in den Jahren 2009 und 2011 herangezogen (Engel u. a., 2002). Zusätzlich benötigt man eine Referenzsubstanz, in dieser Dissertation CFC-12. Die Korrelationen der chlorierten Quellgase zur Referenzsubstanz aus den Ballonbeobachtungen werden auf den Zeitraum der Messkampagne skaliert und CCl_y als Funktion von CFC-12 dargestellt. Cl_y kann dann erneut aus der Differenz von Cl_{total} und CCl_y bestimmt werden. Im Folgenden wird dies die indirekte Methode genannt. Ein Vergleich der semi-direkten und indirekten Methode für die Bestimmung von Cl_y ist mit den Messungen während der SouthTRAC möglich. Cl_y beider Methoden unterscheidet sich geringfügig mit einer maximalen Differenz von 65 ppt bei etwa 5 Jahren mittleren Alters mit Cl_y oberhalb von etwa 1500 ppt.

Mit der Messkampagne im südhemisphärischen Winter und Frühjahr wurden während

einiger Flüge Luftmassen innerhalb und außerhalb des Polarwirbels beprobt. Es ist somit möglich die Luftmassen entsprechend ihrer Herkunft zu klassifizieren. Dazu wird die Methodik von Greenblatt u. a. (2002) zur Wirbelidentifikation erweitert. Diese auf Spurengasmessungen basierende Wirbelidentifikation nutzt die kompakte Korrelation von N_2O und potenzieller Temperatur innerhalb des Wirbels für die Bestimmung der Wirbelkante. Zusätzlich kann ein mittleres N_2O-Profil für die mittleren Breiten erstellt werden. Damit ist die Einteilung von Luftproben zum Polarwirbel, dem Wirbelgrenzbereich und den mittleren Breiten möglich. Mit einer iterativen Filterprozedur werden die N_2O-Beobachtungen der SouthTRAC Kampagne herausgefiltert, die für das Erstellen des Wirbelprofiles und des der mittleren Breiten benötigt werden. Für jeden Flug wird im Anschluss zu jeder N_2O-Beobachtung ein Wert laut Wirbelprofil (N_2O_{vor}) und ein Wert laut mittleren Breiten-Profil (N_2O_{mid}) erstellt und die relative Lage der N_2O-Beobachtung zu diesen beiden untersucht. Die parallel zu den N_2O durchgeführten Spurengasmessungen können dementsprechend ebenfalls zugeteilt werden. Mit Hilfe der Luftmassenklassifikation ist die Einteilung von Cl_y in die entsprechenden Regionen möglich. Cl_y steigt während SouthTRAC innerhalb des Wirbels auf bis zu 1687 ± 19 ppt bei 385 K potentieller Temperatur an und macht damit etwa 50 % des Gesamtchlors innerhalb des Wirbels aus. In den mittleren Breiten steigt Cl_y auf etwa 446 ± 124 ppt zwischen 380 and 400 K und macht lediglich 15 % des gesamten Chlors in den südlichen mittleren Breiten aus. Die Methodik und Ergebnisse sind in Jesswein u. a. (2021) publiziert.

Das GhOST-Instrument wurde bereits auf vorherigen Messkampagnen eingesetzt. Dazu gehört auch die PGS (POLSTRACC/GW-LCYCLE /SALSA) Kampagne im nordhemisphärischen Winter 2015 bis in das Frühjahr 2016 (Oelhaf u. a., 2019). Damit ist ein Vergleich von Cl_y im jeweiligen Winter und Frühjahr der Nord- und Südhemisphäre auf Grundlage der SouthTRAC und PGS Kampagne möglich. Da der Messmodus des MS-Kanals während der PGS Kampagne so gewählt wurde, dass der Fokus auf den bromierten Quellgasen lag, ist die Verwendung der indirekten Methode zur Bestimmung von Cl_y notwendig. Basierend auf diesen beiden Kampagnen ergibt sich eine geringfügig unterschiedliche Verteilung des Gesamtchlors in der jeweiligen Hemisphäre. Wurde im antarktischen Wirbel bis zu etwa 50 % des Chlors in der anorganischen Form gefunden, so lag der Anteil im arktischen Wirbel bei vergleichbarem Abstand zur Tropopause nur bei etwa 40 % des Gesamtchlors. In der Stratosphäre der mittleren Breiten sind die Cl_y-Mischungsverhältnisse in der Nordhemisphäre höher als in der Südhemisphäre.

Das mittlere Alter der Luft spielt für die Herleitung von Cl_y über die organischen Quellgase, wie sie in dieser Dissertation durchgeführt wurde, eine wesentliche Rolle. Die bisherige Methode zur Bestimmung des mittleren Alters der Luft aus Beobachtungsdaten berücksichtigt lediglich den tropischen Eintrag von Luft in die Stratosphäre. Eine neue Methode wird eingeführt, die zusätzlich zum tropischen Eintrag auch den extratropischen Eintrag in die Stratosphäre berücksichtigt. Beide Methoden werden zur Bestimmung des mittleren Alters während der PGS und SouthTRAC Kampagne genutzt und verglichen. Die größten Unterschiede der beiden Methoden liegen kurz oberhalb der Tropopause und bei Werten des mittleren Alters unterhalb von etwa 1.2 Jahren. Der maximale Unterschied liegt bei etwa 0.31 Jahren in der Nordhemisphäre und 0.42 Jahren in der Südhemisphäre. Die Methode mit lediglich tropischem Eintrag gibt nahe der Tropopause ein negatives Alter von bis zu -0.54 Jahren an. Die neue Methode mit extratropischem Eintrag verringert die Anzahl negativer Werte nahe der Tropopause und erscheint somit physikalisch plausibler. Wie bei der Analyse von Cl_y kann auch das mittlere Alter der Luft in der Nord- und Südhemisphäre verglichen werden. Die Luft der unteren Stratosphäre war im Durchschnitt um etwa 0.5 ± 0.3 Jahre älter in der Nordhemisphäre als in der Südhemisphäre. Etwa 65 K oberhalb

der Tropopause ändert sich das Muster mit älterer Luft in den mittleren Breiten der Nordhemisphäre, jedoch ältere Luft in hohen Breiten der Südhemisphäre. Das impliziert Unterschiede in der Stärke und Isolation des jeweiligen Polarwirbels sowie den Wellenantrieb im flachen Ast der Brewer-Dobson-Zirkulation der jeweiligen Hemisphäre. Diese Ergebnisse stehen allgemein in guter Übereinstimmung mit der Verteilung von Cl_y. Die Differenz in der unteren Stratosphäre war mit der alten Methode jedoch nicht klar ersichtlich und es kann angenommen werden, dass Untersuchungen der Differenzen in Cl_y von Nord- und Südhemisphäre von der neuen Methode profitieren werden. Diese Aspekte sind in ausführlicher Form in Jesswein u. a. (2021) und Wagenhäuser u. a. (2022) publiziert.

Der finale Teil der Dissertation beschäftigt sich mit der globalen und saisonalen Verteilung der zwei kurzlebigen bromierten Substanzen CH_2Br_2 und $CHBr_3$. Neben den bereits verwendeten zwei HALO Messkampagnen PGS und SouthTRAC wird die Datenbasis durch die TACTS (Transport and Composition in the Upper Troposphere/Lowermost Stratosphere) Kampagne 2012 und die WISE (Wave- driven ISentropic Exchange) Kampagne 2017 erweitert, ebenfalls mit dem GhOST Instrument auf dem HALO Forschungsflugzeug. Zusätzlich sind zwei global-skalige Missionen, die HIPPO (HIAPER-Pole-to-Pole) Mission von 2009 bis 2011 und die ATom (Atmospheric Tomography) Mission 2016 bis 2018 für die Analyse mit aufgenommen worden. Beobachtungen von CH_2Br_2 und $CHBr_3$ wurden hier mit verschiedenen Probensammlern sowie einem In-situ-Instrument getätigt. Somit stehen für die Südhemisphäre und Nordhemisphäre ausreichend Daten zur Verfügung, um das saisonale Verhalten der beiden Substanzen zu analysieren.

Die Beobachtungen von CH_2Br_2 zeigen eine ausgeprägte Saisonalität in der freien und oberen Troposphäre beider Hemisphären. In der Nordhemisphäre sind die Mischungsverhältnisse leicht höher als auf der Südhemisphäre, möglicherweise durch mehr Küstengebiete und damit mehr Quellregionen. $CHBr_3$ weist eine generell höhere Variabilität und geringere Saisonalität auf mit höheren Mischungsverhältnisse in mittleren und hohen Breiten im nordhemisphärischen Winter und Herbst.

Ein Vergleich der unteren Stratosphäre ist nur begrenzt möglich. Die Datengrundlage im Sommer und Winter ist, vor allem in der Südhemisphäre, deutlich geringer und nicht ausreichend für einen Vergleich. Die Analyse der unteren Stratosphäre ist somit auf Herbst und Frühjahr beider Hemisphären begrenzt. Die Verteilungen im jeweiligen Frühjahr sind ähnlich mit weniger als 0.1 ppt Differenzen für CH_2Br_2. Im hemisphärischen Herbst sind größere Unterschiede zu erkennen mit deutlich geringeren Mischungsverhältnissen in der südhemisphärischen unteren Stratosphäre. Dies deutet darauf hin, dass die Transportprozesse beider Hemisphären unterschiedlich sind und impliziert, dass der Eintrag troposphärischer Luft (Spülung bzw. Flushing) in die unterste Stratosphäre der Nordhemisphäre effizienter ist als in der Südhemisphäre. Vertikalprofile von CH_2Br_2 und $CHBr_3$ bis in die untere Stratosphäre der mittleren Breiten in Süd- und Nordhemisphäre unterstützen diese Vermutung. Sie zeigen gerade in der Südhemisphäre einen stärken negativen Gradienten der Mischungsverhältnisseder beiden kurzlebigen Substanzen. Die Datengrundlage der Südhemisphäre, gerade im südhemisphärischen Herbst, ist jedoch nicht ausreichend, um diesen Unterschied zu quantifizieren.

Für einen Vergleich mit den Beobachtungsdaten werden Ergebnisse des TOMCAT (Toulouse Off-line Model of Chemistry And Transport) und CAM-Chem (Community Atmosphere Model with Chemistry, version 4) Models, beide mit der Nutzung des Ordóñez u. a. (2012) Emissionszenarios, verwendet. Die Saisonalität von CH_2Br_2 in der Südhemisphäre wurde von den Modellen nicht wiedergegeben. Beide Modelle zeigen eine ausgeprägte Saisonalität von $CHBr_3$ in beiden Hemisphären, was durch Beobachtungen nicht bestätigt werden konnte. Die Verteilung beider Substanzen in der unteren Stratosphäre wird durch die Modelle gut erfasst. Lediglich der südhemisphärische Herbst, mit deutlich geringeren

Mischungsverhältnissen in den Beobachtungen, wurden von den Modellen nicht wiedergespiegelt, sondern eine vergleichbare Spülung der unteren Stratosphäre auf beiden Hemisphären. Alle genannten Aspekte sind in ausführlicher Form in Jesswein u. a. (2022) publiziert.

Aus Beobachtungen abgeleitete Schätzungen von Cl_y innerhalb des jeweiligen Wirbels, wie sie in dieser Dissertation vorgenommen wurden, sollten Bestandteil der Forschung bleiben, um die Auswirkungen und die Einhaltung des Montreal Protokolls zu überwachen. Dazu wird das mittlere Alter der Luft benötigt, wobei zukünftige Berechnungen von Cl_y von der verbesserten Methode zu Bestimmung des mittleren Alters mit Berücksichtigung des extratropischen Eintrags profitieren würden. Mit dem Rückgang der langlebigen Substanzen gewinnen unregulierte kurzlebige halogenierte Substanzen an Bedeutung für den Ozonabbau. Die Zahl der Beobachtungen, auf die sich diese Dissertation stützt, ist auf der Südhemisphäre noch wesentlich geringer als auf der Nordhemisphäre. Die Unterschiede, die sich in der unteren Stratosphäre im hemisphärischen Herbst gezeigt haben, bedürfen zur Bestätigung weiterer Untersuchungen. Zusätzlichen profitieren auch Chemie-Klima- und Chemie-Transport-Modelle von mehr Beobachtungsdaten. Sei es für einen Vergleich oder für die Erstellung verbesserter Emissionsszenarien.

Introduction

Atmospheric science is a relatively new applied discipline. The main concerns are meteorology and atmospheric dynamics, physics and chemistry of the atmosphere, as well as climate sciences, all based on theoretical principles, observational data and modelling data. An unexpected discovery was made in the 1980s by Farman, Gardiner, and Shanklin (1985) who observed a decline in polar ozone far larger than anticipated, known as the Antarctic "ozone hole". The ozone destruction was found to be caused by synthetically produced gases called chlorofluorocarbons (CFCs), used for refrigeration and industrial purpose. These substances make up only a small fraction of the chemical composition of the Earth's atmosphere and are therefore classified as trace gases. Nonetheless, although small in quantity, their effect is drastic. When decomposing, halogens from these substances are released, which effectively destroy ozone. A reduction in ozone has biological consequences due to the increased intensity of UV-B radiation (280–315 nm) that can reach the ground with harmful effects on human beings, plants, and animals (e.g. human skin cancer). Further, ozone effects the radiative balance of the atmosphere-Earth system through absorption of radiation (ultraviolet, visible and infrared spectral regions), depending on the altitude at which absorption takes place. The lower stratosphere, right above the tropopause, which separates the stratosphere from the troposphere, is a region of great importance for ozone changes. A loss of ozone in this region increases transmission of ultraviolet light towards the troposphere, leading to a warming effect of the climate. Furthermore, ozone absorbs and emits infrared radiation. Less ozone and thus cooling of the lower stratosphere results in reduced emission of infrared radiation from the stratosphere to the troposphere and to a cooling effect (Holloway and Wayne, 2010). The net effect of ozone depletion is believed to be cooling the climate. Ozone depletion has shown effect to climate change in the Southern Hemisphere. In the Northern Hemisphere, there may be similar but smaller effects of ozone depletion on climate. Unfortunately, there are no reports for the Northern Hemisphere yet regarding the effect of ozone depletion on climate (e.g. Barnes et al., 2019). To protect the stratospheric ozone layer, the Montreal Protocol regulates the phase out of ozone depleting substances (ODS) since its inception in 1987 in a step-wise manner, with different timetables for developed and developing countries. In contrast to controlled long-lived halogenated substances, chlorinated and brominated very short-lived substances (VSLS) appear to have an increasing relative contribution to stratospheric halogen loading (e.g. Hossaini et al., 2017; Hossaini et al., 2019; Engel and Rigby, 2018; Laube and Tegtmeier, 2022). Continued monitoring and investigation is important to provide reliable reports on the current state and future changes in the stratosphere with respect to the amount of CFCs, there substitutes, and uncontrolled substances.

Atmospheric in situ observations in the troposphere are generally well feasible with multiple ground stations distributed globally, equipped with modern technological instruments. In the stratosphere, in situ observations are limited, due to the remoteness and vertical extent up to about 50 km altitude. For in situ trace gas analysis of the stratosphere, these include aircraft measurements that can reach into the lower stratosphere, as well as balloon ascents to collect air samples deep into the stratosphere. Both, however, provide data for spatially and temporally limited domains. Particularly the Southern Hemisphere is considerably less covered by in situ observations. In addition, remote sensing instruments provide

data for trace gases, e.g. from satellites, whereas these data have to be properly calibrated pre-launch as well as re-calibrated with ground-based observations throughout the lifetime of the satellite sensors. In addition, for a comprehensive analysis, studies using state-of-the-art chemistry-climate and chemistry-transport models are a mandatory part of stratospheric research. These models require realistic treatments of emissions in order to simulate reasonable mixing ratios in the troposphere and stratosphere with current emission inventories, e.g. of short-lived brominated substances, showing significant variations (Hossaini et al., 2013).

The scientific objective of this cumulative dissertation is to investigate the global distribution of chlorinated and brominated substances based on in situ aircraft measurements to have an insight into possible differences in the lowermost stratospheric composition and transport pathways. The focus is on the upper troposphere and lower stratosphere (UTLS) of both hemispheres. The following research questions are addressed in this thesis:

- Are calculations of inorganic chlorine from a scaled correlation and one measured reference substance comparable to inorganic chlorine from in situ long-lived chlorinated substances?
- How does the distribution of inorganic chlorine differ inside and outside the polar vortex of the respective hemisphere, based on in situ aircraft observations in the Arctic winter of 2015/2016 and in the Antarctic winter of 2019?
- What is the observational based global seasonal distribution of the two major brominated VSLSs CH_2Br_2 and $CHBr_3$, and are there hemispheric differences?
- To what extent are the atmospheric models able to reproduce the seasonal distribution of the two Br-VSLSs?

This thesis starts with scientific background and relevant state of knowledge regarding the fields of atmospheric dynamics and chemistry, which are the focus of this work (Chapter1). Chapter 2 connects and summarizes the three publications to outline the guiding thread through the main findings of this thesis. After a brief introduction to the instrument I worked with and the most recent campaign in which I participated with the working group (section 2.1 and 2.2), the first publication is Jesswein et al. (2021) with the focus on inorganic chlorine (Cl_y) within the Arctic and Antarctic polar vortex. Methods for derivation of Cl_y and air mass classification based on in situ observations are presented to finally investigate the Cl_y distribution in southern hemispheric late winter and early spring 2019, summarized in section 2.3. Further results of Jesswein et al. (2021) and Wagenhäuser et al. (2022) are summarized in section 2.3. Observational data from the Northern Hemisphere and Southern Hemisphere are used to investigate inter-hemispheric differences in Cl_y. Furthermore, an improved method to derive mean age of age is presented, a parameter that is important for an accurate determination of Cl_y with the methods mentioned. The final publication is Jesswein et al. (2022) in which the focus moved on to the short-lived brominated substances (Br-VSLSs) and the global seasonal distribution of the two major Br-VSLSs CH_2Br_2 and $CHBr_3$. The substances, which are mainly of natural origin and not controlled under the Montreal Protocol, are expected to play an increasing role if long-lead substances continue to decline. Main findings are summarizes in section 2.5. Chapter 3 presents a general summary and an outlook. All three publication are attached to this thesis.

Chapter 1

Scientific background and state of knowledge

The following section gives a brief introduction to the scientific background of the atmospheric tracer research that was conducted in the course of this work. Besides a brief description of the upper troposphere and lower stratosphere, the region of major interest of this thesis in section 1.1, section 1.2 summarises main aspects of stratospheric dynamics and section 1.3 provides bundled information of atmospheric halogen chemistry and its relevance in stratospheric ozone loss.

1.1 The upper troposphere and lower stratosphere

The upper troposphere and lower stratosphere (UTLS) is a finite region around the tropopause, which is the boundary between the troposphere and the stratosphere. Thus, it is affected by both stratospheric and tropospheric air through transport processes in the stratosphere as well as stratosphere-troposphere exchange (STE) across the tropopause (more on this in section 1.2). As the tropopause lies within the UTLS, it is worth saying a few words about it. The tropopause or its position can be defined in different ways. The two most common ways are the thermal and dynamical tropopause definitions. The thermal tropopause is defined as the lowest level at which the temperature lapse rate decreases to 2 K/km and does not exceed in the 2 km above (WMO, 1957). The thermal tropopause is usually called WMO tropopause. The second tropopause definition is motivated by the large potential vorticity (PV) gradient across the tropopause. PV is proportional to the static stability (N^2) and as there is a jump in static stability at the tropopause, PV fits well for tropopause definition (Gettelman et al., 2011). A specific PV contour is selected to indicate the height of the tropopause with a commonly used value of 2 potential vorticity units (1 PVU = $1 \cdot 10^{-6}$ K $m^2 kg^{-1} s^{-1}$) outside the tropics, whereas inside the tropics, a potential temperature of Θ = 380 K or the cold point is used.

In this thesis, the focus is more on the extratropical UTLS (Ex-UTLS). It is, roughly speaking, the region poleward of the subtropical jet between around 8 to 20 km. In the polar region, the polar vortex can reach down into the Ex-UTLS (Gettelman et al. (2011) and Fig. 1.1, dark and light shaded region). Its upper boundary can also be defined by an isentropic surface, e.g. level of constant potential temperature of around 400 to 440 K, whereas the lower boundary can be defined around 5 km below the mean tropopause (Gettelman et al., 2011). The Ex-UTLS can be further subdivided, for instance with the use of the potential temperature for height allocation. Thus, the lowermost stratosphere (LMS) is generally defined from the tropopause up to a potential temperature level of Θ = 380 K (Holton et al., 1995), approximately the isentropic surface which does not intersect with the tropical tropopause. An extratropical transition layer (ExTL) exists in the lowermost stratosphere and has characteristics of both stratosphere and troposphere (Fig. 1.1, dark shaded region), first mentioned

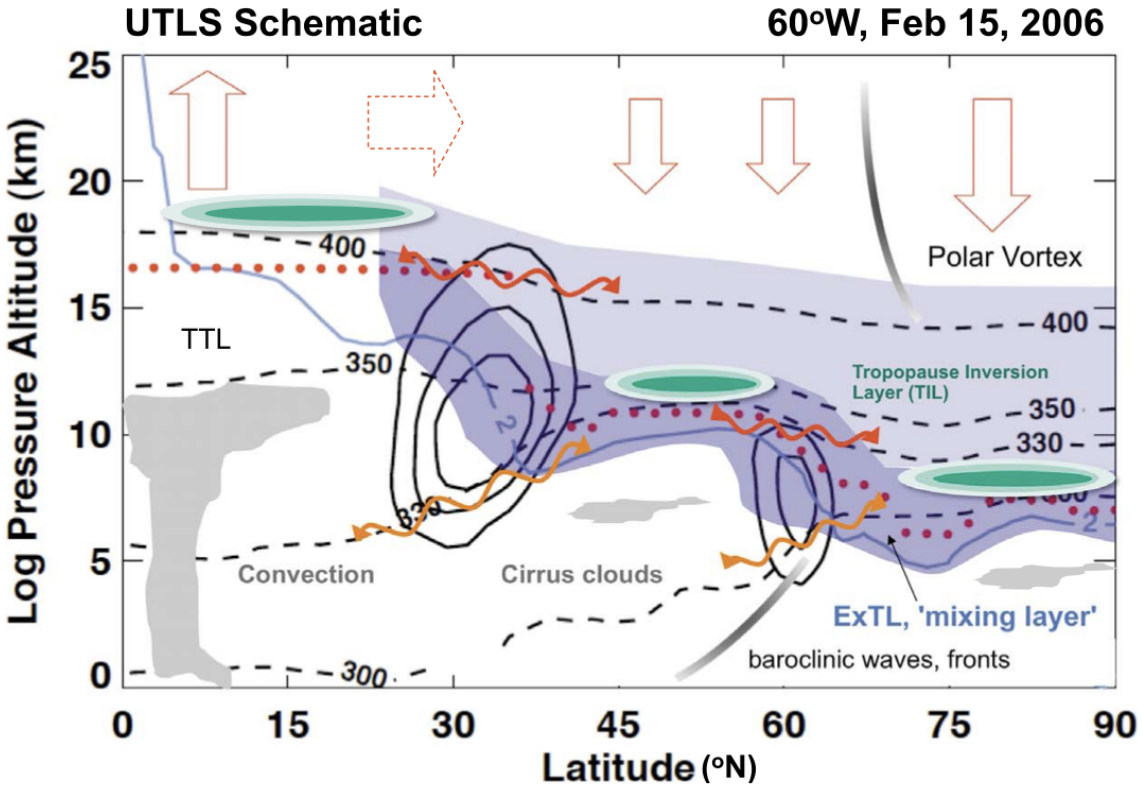

FIGURE 1.1: This figure from Gettelman et al. (2011) illustrates a schematic of transport and mixing processes in the northern hemispheric UTLS. Closed black contours show zonal wind (subtropical jet and polar jet), dashed black lines show potential temperature surfaces, red dots show thermal tropopause and the blue solid line shows the 2 PVU dynamical tropopause. In addition, the Ex-UTLS is illustrated in dark and light blue shading and the ExTL in dark blue shading, clouds and fronts are shown in gray shading, static stability contours on the TIL in green shading, quasi-isentropic exchange in red wavy arrows, cross-isentropic exchange orange wavy arrows, and the Brewer-Dobson Circulation in large red arrows with solid arrows for the deep branch and dotted arrows for the shallow branch.

in WMO (2003). It can be considered a transition region with strong gradients of tropospheric and stratospheric tracers respectively.

The UTLS is a region of high interest and plays an important role in terms of the radiative balance of the atmosphere. For instance, changes in the structure and chemical composition of the UTLS result in large changes in radiative forcings of the atmosphere, which affect the surface climate (Riese et al., 2012). Further, although the Montreal Protocol and its subsequent amendments successfully led to the reduction of long-lived ozone-depleting substances and already visible ozone recovery in the upper stratosphere, ozone in the lower stratosphere continued to show a decline between 1998 and 2016, more pronounced in the Northern Hemisphere (Ball et al., 2018; Ball et al., 2019; Ball et al., 2020). Suggestions for the explanation of these ozone trends are, on the one hand, a change in atmospheric transport and dynamical variations, although the causes are not determined yet (e.g. Chipperfield et al., 2018; Ball et al., 2020). On the other hand, anthropogenic and natural very short-lived substances (VSLSs) can contribute to lower stratospheric ozone changes (e.g. Hossaini et al., 2015; Ball et al., 2018). These substances are not controlled under the Montreal Protocol and preferentially release reactive halogens into the lower stratosphere (e.g. Ball et al., 2018).

1.2 Dynamics of the stratosphere

The study of (lower) stratospheric tracer distributions also requires consideration of stratospheric dynamics. This is characterized by the global-scale mean meridional circulation, primarily the transport of air from the tropics to the poles. The hypothesis of such a circulation originated from its namesakes Dobson and Brewer, based on ozone, water vapor, and helium measurements and thus is referred to as the Brewer-Dobson circulation (BDC) (Dobson, Harrison, and Lawrence, 1929; Brewer, 1949).

The underlying drivers for the residual mean circulation are tropospheric Rossby waves. These planetary and synoptic-scale waves propagate upward into the stratosphere and release their momentum into the middle and upper stratosphere of the mid-latitudes as they break and dissipate, a region also called "surf zone" (McIntyre and Palmer, 1983; McIntyre and Palmer, 1984). The zonal mean background flow in the middle and upper stratosphere can be described approximately by the geostrophic balance and the resulting geostrophic wind. There is a pressure gradient from the summer to the winter pole. With the Coriolis force rightward in the NH and a leftward in the SH, there is an eastward flow on the winter hemisphere and a westward flow on the summer hemisphere. Propagation of the waves is only possible with an eastward background flow (e.g. Charney and Drazin, 1961) and thus only on the winter hemisphere. The released momentum of these waves causes a westward force, opposite to the mean flow. This results in a weakening of the background flow and a poleward force leading to a mean poleward mass flux. This wave-induced force is also called an "extratropical pump" or "Rossby-wave pump" (Holton et al., 1995; Plumb, 2002).

The mean residual circulation can be further divided into two major branches with distinct characteristics. The deep branch is more associated with planetary wave breaking in the middle to the upper stratosphere with transport times of several years. Transport is more from the latitudes close to the equator up into the stratosphere and back down in the mid and high latitudes of the winter hemisphere (e.g. Birner and Bönisch, 2011). The shallow branch is more associated with synoptic and planetary-scale waves breaking in the subtropical lower stratosphere and the transport time is about one year or less into the extratropical lowermost stratosphere (Birner and Bönisch, 2011). Further, the shallow branch can be observed on both hemispheres throughout the year (e.g. Plumb, 2002; Butchart, 2014). Figure 1.1 displays the Brewer-Dobson circulation with solid red arrows for the deep branch and the dotted arrow for the shallow branch.

The mean stratospheric tracer transport can be described by the mean residual circulation, and a two-way mixing along isentropic surfaces (e.g. Plumb, 2007). Drivers for the two-way mixing are, as with the mean residual circulation, wave breaking and dissipation. Mixing by planetary waves occurs predominantly in winter and results in the mid-latitude "surf zone" (e.g. McIntyre and Palmer, 1983) bracketed by transport barriers at the edge of the winter polar vortex and the edge of the tropics with much weaker mixing than in the "surf zone (e.g. Plumb, 2007; Birner and Bönisch, 2011). Mixing by synoptic-scale waves occurs in the subtropical lower stratosphere throughout the year (e.g. Butchart, 2014). The two-way isentropic mixing or quasi-isentropic mixing in the lower stratosphere is illustrated in Fig 1.1 by red wavy arrows.

1.2.1 Transport in the Ex-UTLS

Since the results of this work essentially relate to the Ex-UTLS, it is worth taking a somewhat closer look at the transport processes of the lower stratosphere and the ExTL. In general, there are two major paths for air into the Ex-UTLS. One is the mean stratospheric mass transport mentioned above with the two branches of the mean residual circulation and the two-way isentropic mixing. The second one is a two-way exchange across the tropopause

(orange wavy arrows in Fig. 1.1), also called stratospheric-tropospheric exchange (STE) (e.g. Holton et al., 1995; Stohl et al., 2003).

The ExTL and its depth can be studied using tracer-tracer correlations (Gettelman et al., 2011). For instance, the vertical extent of the ExTL can be characterized by using substances with sharp gradients across the tropopause. These include O_3, CO, and H_2O. O_3 has a strong stratospheric source and tropospheric sink, and vice versa to those of CO and H_2O. Hoor et al. (2004) and Hoor, Fischer, and Lelieveld (2005) used CO measurements from aircraft campaigns in the Northern Hemisphere to identify a mixing layer around the local tropopause extending to around 20–25 K in potential temperature. To have a global view of the ExTL, Hegglin et al. (2009) derived the thickness of the ExTL for the NH and SH from measurements of O_3, CO, and H_2O from the Atmospheric Chemistry Experiment Fourier Transform Spectrometer (ACE-FTS) on Canadas's SCISAT-1 satellite. Major findings were a shallower mixing layer in the SH with weaker troposphere-stratosphere-transport (TST) compared to the NH and an overall weak seasonality.

The Ex-UTLS above the ExTL is less influenced by extratropical tropospheric air and more by tropical air, e.g. by isentropic mixing. A seasonal change in the fraction of tropospheric air in the Ex-UTLS was identified based on observations. Based on in situ CO measurements, Hoor, Fischer, and Lelieveld (2005) infer a tropospheric fraction of 35 % in the chemical composition in the winter and spring LMS over Europe, whereas this fraction increased to about 55 % in summer and autumn. Bönisch et al. (2009) confirm this seasonality based on in situ observations of SF_6 and CO_2, with somewhat more extreme fraction of below 20 % in April and greater than 80 % in October. These results suggest a "flushing" of the LMS from summer to mid-autumn by strong quasi-horizontal mixing across the weak subtropical jet. Observations from the ACE-FTS showed, that this "flushing" of the LMS is most evident in the NH and much weaker in the SH (Hegglin and Shepherd, 2007), which is also confirmed by CO results from Hegglin et al. (2009).

1.2.2 The isolated stratospheric polar vortex

In the polar regions, the stratospheric polar vortex can reach down into the Ex-UTLS (Gettelman et al., 2011, and references therein). The stratospheric polar vortex is an area of low geopotential height above the polar region, enclosed by strong westerly winds. It is formed in hemispheric autumn when, with the onset of the polar night, there is no more solar radiation in the polar region. Due to the temperature difference and consequently a pressure gradient between polar and mid-latitude, these strong westerly winds are established in the stratosphere (polar night jet) (e.g. Schoeberl and Hartmann, 1991). The vortex can be considered as an isolated region, separated by the jet as a transport barrier to the stratosphere of the mid-latitudes. This leads to strong gradients in potential vorticity and long-lived tracers such as N_2O over the jet, and furthermore to different concentrations of tracers within the vortex compared to those in the mid-latitude stratosphere (e.g. Hartmann et al., 1989; Schoeberl et al., 1992). Differences in tracer concentrations are further enhanced by diabatic descent inside the vortex as a result of diabatic cooling as well as downwelling of air within the vortex from the deep branch of the BDC (Schoeberl and Hartmann, 1991; Schoeberl et al., 1992; Butchart, 2014).

The polar vortices in the northern and southern hemispheres differ in some aspects. Significantly more surface structure of the NH, due to more land masses, generates more upward propagating waves than in the SH. This results in a weaker and more disturbed stratospheric vortex in the NH, which is smaller and less symmetrical in shape than the SH stratospheric vortex (e.g. Waugh and Randel, 1999). The greater disturbance of the NH polar vortex also leads to frequent events of sudden stratospheric warmings (SSW) where the stratospheric temperature suddenly increases and the vortex breaks down in mid-winter.

These SSWs can be further divided into major SSWs, where westerlies reverse to easterlies, and minor SSWs, where the polar temperature gradient reverses but not the circulation (Butler et al., 2017). Major SSWs occur roughly six times per decade in the NH (Charlton and Polvani, 2007). Occurrence in SH is much lower due to less wave forcing with only one observed major SSW in September 2002 (e.g. Krüger, Naujokat, and Labitzke, 2005) and one minor SSW from mid-August to early September 2019 (Safieddine et al., 2020; Wargan et al., 2020) since observations began in the 1940s.

At the end of the polar winter, the vortex weakens and the winter westerlies reverse to summer easterlies in the wake of final stratospheric warming (FSW). Compared to SSWs, the FSW events are driven by a combination of wave-induced and radiation processes (Salby and Callaghan, 2007). Consequently, the Arctic vortex collapses earlier than the Antarctic vortex with a lifespan around a month shorter (Waugh and Randel, 1999). With the return of the sunlight in SH spring, a rapid ozone depletion takes place in the vortex with further cooling and thus prolongs the stability of the vortex, which is linked to long-term trends in FSW events (Butler and Domeisen, 2021, and references therein). In the NH, the variability of the persistence of the polar vortex is tied to the variability of wave forcings rather than ozone depletion, since temperatures within the vortex go less deep than in the SH vortex, limiting the chemical depletion of ozone (Butler and Domeisen, 2021, and references therein).

1.2.3 Quantification of transport

A conceptual tool to analyze transport and mixing in the stratosphere is the mean age of air (AoA; Hall and Plumb, 1994). Simplified, the age of air is the average time it takes for a parcel of air to travel from a reference point to a specific point in the stratosphere. The reference is typically set to the Earth's surface or the tropical tropopause as the transport happens predominantly via the tropical tropopause. However, an air parcel in the stratosphere is not characterized by a simple transit time. Rather, air injected into the stratosphere is quickly dispersed and irreversibly mixed. Thus, every air parcel in the stratosphere consists of a subset of air parcels with different transit times to the location of interest(Hall and Prather, 1993; Hall and Plumb, 1994). Kida (1983) introduced the term age spectrum for the statistical distribution of the transit times of an air parcel, e.g. a probability density function (PDF) of the transit times from the reference point to the location of the air parcel, mathematically described by the Green's function. The first moment of the age spectrum is the mean age of air Γ (AoA) and the second moment is the width of the age spectrum Δ (see Hall and Plumb, 1994, and Appendix A.2). Mean AoA, however, cannot be observed directly in the atmosphere.

Passive tracers can be used to derive mean AoA (e.g. Hall and Plumb, 1994; Strunk et al., 2000; Engel et al., 2002). Mixing ratios of a suitable passive (age) tracer at a specific location ($\vec{x}$) and time (t) can be derived using the age spectrum by the following equation

$$\chi(\vec{x}, t) = \int_0^\infty \chi_0(t - t')G(\vec{x}, t, t')\mathrm{d}t', \tag{1.1}$$

with $\chi_0(t - t')$ the mixing ratio time series at the reference surface, $\chi(\vec{x}, t)$ the mixing ratio at a specific location and time, t' the transit time, and $G(\vec{x}, t, t')$ the age spectrum. Conversely, on this concept also the mean AoA can be determined from observed stratospheric tracer mixing ratios and time series at the reference point (Hall and Plumb, 1994; Volk et al., 1997; Engel et al., 2002). An ideal tracer to determine the mean AoA is conserved in the stratosphere with no sources and sinks and exhibits a linear tropospheric growth rate. Two substances, which come close to these conditions, are SF_6 and (deseasonalized) CO_2 (e.g. Volk et al., 1997; Engel et al., 2002; Bönisch et al., 2009). For instance, SF_6 shows only a very

small non-linearity by having a second-order growth rate. The temporal mixing ratio trend can thus be approximated by a second-order fit. The nonlinearity can be addressed by a correction term if the width of the age spectrum Δ is parameterized (Hall and Plumb, 1994; Volk et al., 1997). Hall and Plumb (1994) revealed that the width of Δ is related to Γ, so that the ratio of Δ^2/Γ (ratio of moments; rom) is nearly constant in the stratosphere. This approximation can be used to derive mean AoA. Another well-used approach to derive mean AoA is the use of the inverse Gaussian function for the shape of $G(\vec{x}, t, t')$. As for the second-order growing tracer, a parameterization of Δ is needed. A range of age spectra $G(\vec{x}, t, t')$ by a set of mean AoA (e.g. from 0 to 10 years) can be calculated. Fictitious mixing ratios from the age spectra are compared with the observed mixing ratios so that the best match then corresponds to the age of the air (e.g. Ray et al., 2017; Leedham Elvidge et al., 2018).

Mean AoA is an appropriate metric for inert tracers. For tracers that undergo chemical degradation during transport into and through the stratosphere, the mean AoA assumption no longer applies (Plumb, Vohralik, and Ryan, 1999). Chemical loss during transport would reduce the tail of an age spectrum, as molecules with long arrival times have, on average, spent more time exposed to chemical losses. Plumb, Vohralik, and Ryan (1999) introduced a modified age spectrum G^* accounting for that with the mean arrival time Γ^* as the first moment (see Fig 1.2). Further, Γ^* of relevant chlorinated and brominated substances can be parameterized in terms of their stratospheric lifetimes τ and mean AoA by the following

$$\Gamma^*(x) = a\Gamma(x)\exp(-b\Gamma(x)/\tau), \tag{1.2}$$

with respective coefficients a and b for the respective substance (which can be taken from Plumb, Vohralik, and Ryan, 1999). A useful application of Γ^* is the consideration of correlations of substance with different atmospheric lifetimes. The correlations of these substances, which undergo chemical degradation in the stratosphere, can change over time. In order to make a generalized conclusion about their relationship, the mean arrival time can be used to normalize this correlation or even to scale a correlation to a certain point in time.

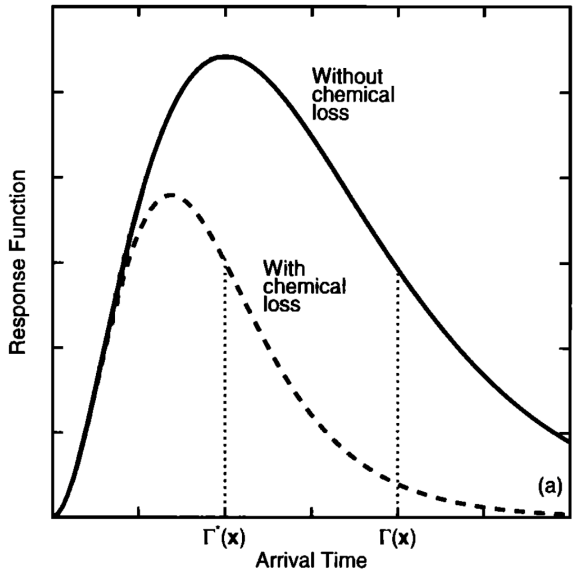

FIGURE 1.2: This figure from Plumb, Vohralik, and Ryan (1999) illustrates a schematic representation of model response to a delta pulse emission at the ground with and without chemical loss processes included. Γ^* indicates the mean arrival time and Γ the mean age.

1.3 Atmospheric halogen chemistry

The gases nitrogen (78.084 %), oxygen (20.942 %), and argon (0.934 %) are the main components of the atmosphere. Substances that make up much less than 1 % are called trace gases. The amount of these substances is usually given in parts per million (ppm) and even parts per trillion (ppt), which is the ratio of the molar amount of the substance in a given volume to the total molar amount of all constituents in that volume, referred as mixing ratio. Halogenated substances, which are the focus of this work, belong to the trace gases (Seinfeld and Pandis, 2016). A classification can be as follows (e.g. Seinfeld and Pandis, 2016):

- Chlorofluorocarbons (CFCs) – Fully halogenated with chlorine and fluorine
- Hydrochlorofluorocarbons (HCFCs) – Partly halogenated with chlorine and fluorine
- Hydrofluorocarbons (HFCs) – Party halogenated with fluorine
- Halons – Party or fully halogenated with bromine, chlorine and/or fluorine. They contain at least one atom of bromine
- Perfluorocarbons (PFCs) – Fully halogenated with fluorine
- Bromo-, Chloro- and Iodocarbons – Halogenated with a single type of halogen except for fluorine
- Natural, mixed halogenated hydrocarbons – Mostly natural in origin and a short atmospheric lifetime < 6 month. Also referred to as very short-lived substances (VSLS).

CFCs were first synthesized in the late 1920s to replace toxic gases like ammonia (NH_3), methyl chloride (CH_3Cl), or sulfur dioxide (SO_2) which were used as refrigerant agents up to this time. In addition, they have been used as propellants, blowing agents, and solvents (Seinfeld and Pandis, 2016). The chemical stability of CFCs allows them to easily disperse and propagate up to the stratosphere. Molina and Rowland (1974) and Rowland and Molina (1975) first proposed that the photo-dissociation of CFCs in the stratosphere produces a significant amount of chlorine atoms, which induce a catalytic cycle that leads to the destruction of stratospheric ozone. Besides leading to stratospheric ozone depletion, CFCs are strong greenhouse gases (Seinfeld and Pandis, 2016).

As replacements for the CFCs in e.g. refrigeration units, air conditioning, and foam-blowing applications, HCFCs and HFC were introduced. These substances contain carbon-hydrogen bonds and thus are prone to be decomposed by hydroxyl (OH) radicals in the lower atmosphere (Wallington et al., 1994). This means additionally that they have shorter lifetimes compared to CFCs (Carpenter et al., 2014). While HCFCs still contain chlorine atoms, HFCs are free of chlorine and do not directly contribute to the destruction of ozone. However, both HCFCs and HFCs are still strong greenhouse gases.

Halons have been introduced into the atmosphere mainly through their use as fire extinguishing agents. In contrast to the previously mentioned substances, they contain bromine and some contain both bromine and chlorine atoms. Like chlorine, bromine induces a catalytic cycle that leads to a rapid ozone depletion (Wofsy, McElroy, and Yung, 1975). In fact, bromine has an up to 74 times higher efficiency in destroying stratospheric ozone compared to chlorine (further information in section 1.3.2 and Klobas et al., 2020). Thus, although the mixing ratios of bromine-containing substances in the atmosphere are much smaller, they play an important role in stratospheric ozone depletion.

Like HFCs, PFCs do not contribute to ozone depletion. PFCs are extremely stable compounds and are efficient absorbers of infrared radiation and therefore are potent greenhouse gases.

The aforementioned substances are almost exclusively synthetic products of anthropogenic origin and have either a high ozone depletion potential (ODP) and/or a high global warming potential (GWP). Bromo-, chloro-, and iodocarbons are mostly of biogenic origin with methyl chloride (CH_3Cl) and methyl bromide (CH_3Br) as the major natural contributors. Furthermore, mostly natural very short-lived substances (VSLS) with lifetimes shorter than six months can contribute to ozone loss in the stratosphere. Due to their relatively short lifetimes, they can quickly release chlorine and bromine to climate-sensitive altitudes (e.g. the lower stratosphere) (Hossaini et al., 2015).

Following the discovery of catalytic ozone depletion by synthetically produced substances, 24 states and the European Union initially signed the Montreal Protocol and committed to reduction steps in the production and consumption of ozone-depleting substances (ODSs). It entered into force in 1989 and has been amended in the following years to further phase down and phase out CFCs, HCFCs, HFCs, carbon tetrachloride, methyl chloroform, methyl bromide, and halons (UNEP, 2023). The protocol is to date the only UN treaty ever that has been ratified by every country on Earth (UNEP, 2023).

1.3.1 Relevant trace gas species

The substances, which are the focus of this thesis are listed in table 1.1 together with their ODPs relative to CFC-11 as a reference and their GWP relative to CO_2 on a time scale of 100 years. All values are taken from table A-5 in Burkholder and Hodnebrog (2022).

TABLE 1.1: Trace gas species within the scope of this thesis. For each substance, the ODP relative to CFC-11 as well as the GWP relative to CO_2 is given.

Group	Chemical Formula	Name	ODP	GWP (100-yr)
CFCs	$CFCl_3$	CFC-11	1	6410
	CF_2Cl_2	CFC-12	0.75	10500
	$CFCl_2CF_2Cl$	CFC-113	0.82	6530
HCFCs	CHF_2Cl	HCFC-22	0.038	1910
	CH_3CF_2Cl	HCFC-142b	0.057	2190
	CH_3CFCl_2	HCFC-141b	0.102	808
Chlorocarbons	CCl_4	Tretrachloromethane	0.87	2150
	CH_3Cl	Methyl chloride	0.015	6
	CH_3CCl_3	Methyl chloroform	0.12	164
Br-VSLS	CH_2Br_2	Dibromomethane	3–4	1
	$CHBr_3$	Bromoform	1–5	<1
Others	SF_6	Sulfur hexafluoride	-	24700
	N_2O	Nitrous oxide	0.017	2273

With regard to chlorinated substances, the focus is on the major contributors to stratospheric chlorine loading. As a result of varying emissions and regulations, as well as different lifetimes, halogenated substances have distinct trends in the atmosphere. At present, there are two global measurement networks that monitor the mixing ratios of halogenated substances long term. The station network of the Global Monitoring Laboratory (GML) of the National Oceanic and Atmospheric Administration (NOAA) and the network of the Advanced Global Atmospheric Gases Experiment (AGAGE). Figure 1.3 displays the results of the GML NOAA network for the chlorinated substances of interest and N_2O. In addition, halons and CH_3Br are displayed but are not further discussed in this work.

CFCs have been produced since the late 1920s. Tetrachloromethane production began around two decades earlier (Walker, Weiss, and Salameh, 2000). The total lifetimes are very long with 52 years for CFC-11, 102 years for CFC-12, 93 years for CFC-113, and 32 years

for CCl_4 (see table A-5 in Burkholder and Hodnebrog (2022)). The heavy usage of these substances led to an initial exponential increase, followed by a near linear growth of their atmospheric mixing ratios (see Fig. 1.3 and Walker, Weiss, and Salameh (2000)). With the beginning of the regulations from the Montreal Protocol and the accompanying reduction of CFCs and CCl_4, the atmospheric mixing ratios of CFCs and CCl_4 leveled off and slightly began to decrease.

HCFCs were introduced as temporary alternatives to CFCs. They have shorter atmospheric lifetimes, e.g. 11.9 years for HCFC-22, 9.4 years for HCFC-141b, and 18 years for HCFC-142b (table A-1 in the appendix of World Meteorological Organization, Atmospheric Administration, and Space Administration (2018)) and deliver less reactive chlorine to the stratosphere. Compared to CFCs, the restriction on use is less drastic, so consumption in developed countries was not reduced by 100% until the beginning of 2020 and in developing countries until 2030 (UNEP, 2019). Thus, atmospheric mixing ratios have continued to increase and are slowly beginning to plateau.

CH_3CCl_3, formerly used as e.g. a solvent in the electronics industry, has a total lifetime of 5 years (see table A-5 in Burkholder and Hodnebrog (2022)). After its production and usage have been phased out due to the regulations of the Montreal Protocol, atmospheric mixing ratios dropped rapidly and its influence on climate and ozone depletion is now very small (Engel and Rigby, 2018).

CH_3Cl is the only chlorine substance mentioned here, which is not controlled under the Montreal Protocol. Major sources are tropical and subtropical plants, biomass burning, the ocean, salt marshes, and fungi (Engel and Rigby, 2018), whereas the major anthropogenic source is thought to be coal combustion (McCulloch et al., 1999). Some further studies have investigated emissions from a range of natural and anthropogenic sources, although the impacts of these on the overall budget are not yet clear (Engel and Rigby, 2018, and references therein).

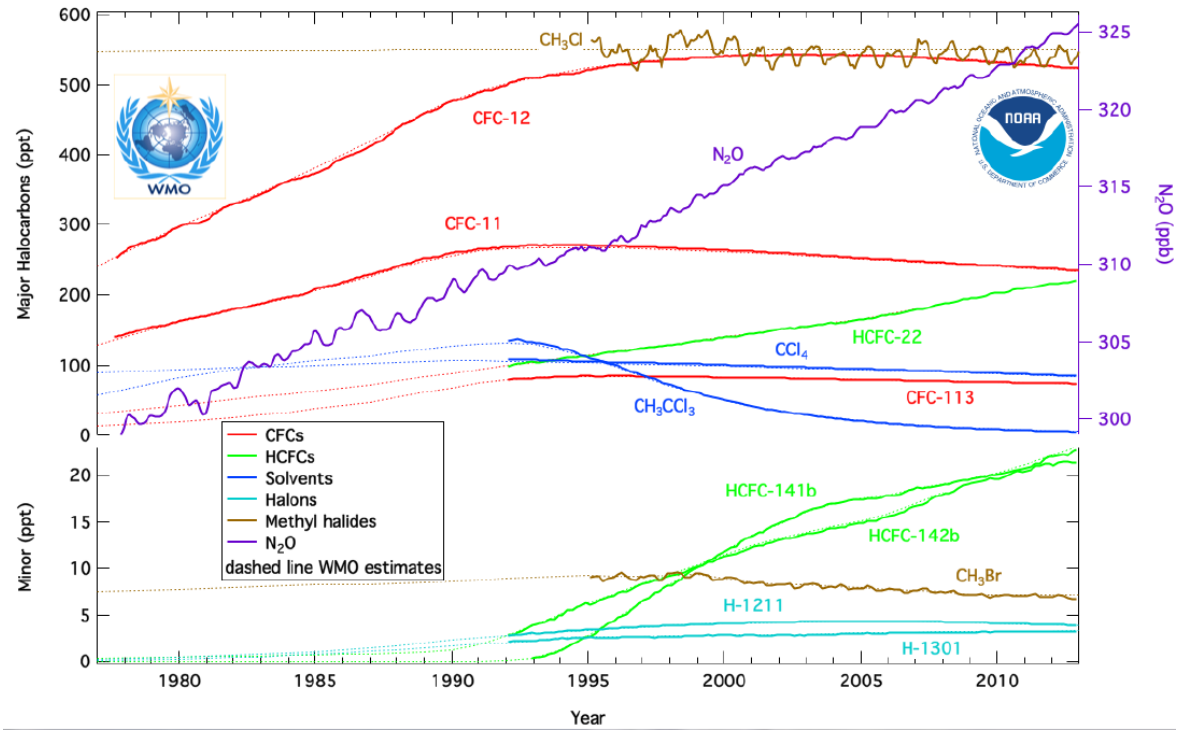

FIGURE 1.3: Atmospheric mixing ratios of important halocarbons at twelve samplings sited from either continuous instruments or discrete flask samples operated by the Global Monitoring Laboratory (NOAA, 2023)

Another part of the thesis is about short-lived brominated substances (Br-VSLS), which have lifetimes of less than six months. The two most abundant Br-VSLS are bromoform ($CHBr_3$) and dibromomethane (CH_2Br_2) with total lifetimes of 13 days (8–23 days) and 147 days (80–890 days) (table A-5 in Burkholder and Hodnebrog (2022)). Bromine from the Br-VSLS contributes to about a quarter to stratospheric bromine (e.g. Engel and Rigby, 2018; Laube and Tegtmeier, 2022) and their relative contribution will continue to increase due to the decrease in long-lived brominated substances such as the halons, which are regulated by the Montreal Protocol. The main sources of Br-VSLS are open ocean and coastal regions via the metabolism of marine organisms like phytoplankton and macro-algae (Carpenter and Liss, 2000; Quack et al., 2007; Leedham et al., 2013). A further source may be winter sea ice as suggested by Sturges et al. (1993) and Abrahamsson et al. (2018).

Two other substances, which are not the main focus of this work, but can be used for e.g. transport and air mass classification, are nitrous oxide (N_2O) and sulfur hexafluoride (SF_6).

N_2O is predominately emitted by biological sources in water and soil and to a lesser extent anthropogenically by agricultural activities, biomass burning, fossil fuel combustion, and from industrial sources (Seinfeld and Pandis, 2016). It is an important greenhouse gas and the atmospheric concentration continues to rise (see Fig. 1.3). N_2O is well mixed in the troposphere because it has a long lifetime (123 years). When it enters the stratosphere, it is mainly photochemically decomposed. The reaction with excited oxygen ($O(^1D)$) leads to the formation of NO and thus represents the main input of NO in the stratosphere. NO contributes to the catalytic ozone destruction cycle. Thus, N_2O may play an even more important role in future ozone destruction as concentrations of halogenated substance will further decrease (e.g. Portmann, Daniel, and Ravishankara, 2012).

SF_6 has no harm to stratospheric ozone but is a very efficient greenhouse gas (see table 1.1) and is thus regulated by the Kyoto Protocol in 1997. The dominant usage is in gas-insulated equipment for electrical transmission and distribution systems and in blanketing or degassing of molten reactive metals such as magnesium and aluminum (e.g. Maiss and Brenninkmeijer, 1998; Simmonds et al., 2020). A formerly stated lifetime of 3200 years (e.g. Ravishankara et al., 1993) was recently corrected by observations in the Arctic polar vortex, from which it has been estimated to have a global lifetime of about 850 (580-1400) years (Ray et al., 2017). SF_6 is well known as a tracer for transport processes in the atmosphere, e.g. for the determination of mean age of air (AoA). In contrast, studies show that a mesospheric sink of SF_6 leads to a significant bias towards higher mean AoA derived from SF_6 (Leedham Elvidge et al., 2018; Loeffel et al., 2022) and complicates the use of SF_6 as transport tracer in the future.

1.3.2 Stratospheric chlorine chemistry

Chlorine is primarily injected into the stratosphere in the form of long-lived organic source gases (listed above), predominantly via the tropical tropopause layer (TTL). A small fraction of around 3% is contributed by chlorinated VSLS with the larger portion of more than 80% in the form of source gas injection (SGI) and the remainder in product gas injection (PGI) (e.g. Hossaini et al., 2019). Major Cl-VSLS source gases are dichloromethane (CH_2Cl_2), chloroform ($CHCl_3$), tetrachloroethene (C_2Cl_4), trichloroethene (C_2HCl_3) and 1,2-dichloroethane (CH_2ClCH_2Cl) and product gases are phosgene ($COCl_2$) and hydrogen chloride (HCl) (e.g. Engel and Rigby, 2018). Cl-VSLS and their product gases, however, are not the focus of this thesis.

Chlorine catalytic cycles and reservoir species

The organic source gases including CFCs, HCFCs, and Cl-VSLS have an important sink in the stratosphere, which is photo-dissociation and the release of atomic chlorine. The atomic chlorine can participate in catalytic chain reactions which destroy ozone (e.g. Molina and Rowland, 1974; Seinfeld and Pandis, 2016). After the reaction of atomic chlorine with ozone

$$Cl + O_3 \longrightarrow ClO + O_2, \tag{1.3}$$

ClO can also react with either O or NO to re-release atomic chlorine:

$$ClO + O \longrightarrow Cl + O_2 \tag{1.4}$$

$$ClO + NO \longrightarrow Cl + NO_2. \tag{1.5}$$

These reactions are most efficient in the upper stratosphere (at around 40 km). At lower altitudes, where the O concentration is significantly lower, the reaction via HO_2 gains in importance to release atomic chlorine, again followed by reaction (1.3).

$$ClO + HO_2 \longrightarrow HOCl + O_2 \tag{1.6}$$

$$HOCl + h\nu \longrightarrow OH + Cl \tag{1.7}$$

In addition, the reaction of two ClO to form the ClO dimer (Cl_2O_2) becomes more important in the polar lower stratosphere at larger pressure, lower temperature, and in conditions with low NO_x (NO and NO_2) (Molina and Molina, 1987). Furthermore, during the polar night, there is essentially no photo-dissociation of O_2 and thus no production of atomic oxygen, which is needed for one of the catalytic cycles (Eq. 1.4).

$$ClO + ClO + M \longrightarrow Cl_2O_2 + M \tag{1.8}$$

$$Cl_2O_2 + h\nu \longrightarrow ClOO + Cl \tag{1.9}$$

$$ClOO + M \longrightarrow Cl + O_2 + M \tag{1.10}$$

M represents a collision partner (e.g. N_2 or O_2). In fact, the catalytic cycle including Cl_2O_2 is the primary process for the ozone removal in the ozone hole (75%) (e.g. Molina and Molina, 1987; Solomon, 1999).

Also worth mentioning is the reaction of ClO and BrO, which can participate in polar ozone destruction, presented by the following equation, disregarded intermediate steps:

$$ClO + BrO \longrightarrow Cl + Br + O_2. \tag{1.11}$$

Neither the reaction including Cl_2O_2 nor the reaction including ClO and BrO requires atomic oxygen but produces two reactive halogen atoms, able to destroy ozone (Seinfeld and Pandis, 2016). The chlorine substances Cl, Cl_2, ClO, and Cl_2O_2 can be summarized as ClO_x.

Without any disturbance, the catalytic cycles would repeat continuously, resulting in a severe loss of ozone. However, active chlorine can be quickly converted to relatively stable species, predominantly via methane (CH_4) and nitrogen dioxide (NO_2) (Eq. 1.12 and 1.13). These substances are called reservoir species with HCl and $ClONO_2$ being the dominant reservoir species. $ClONO_2$ is not only a reservoir for chlorine but also for nitrogen.

$$ClO + NO_2 + M \longrightarrow ClONO_2 + M \tag{1.12}$$

$$Cl + CH_4 \longrightarrow HCl + CH_3 \tag{1.13}$$

Re-activation of chlorine, for instance from $ClONO_2$, can happen via photodissociation or gas-phase reactions with e.g. O, OH, or Cl (e.g. Clarmann and Johansson, 2018). In the polar winter stratosphere, however, the most important re-activation of chlorine happens in the presence of heterogeneous reaction partners. These reaction partners in the polar lower stratosphere are polar stratospheric clouds (PSCs). PSCs play an important role in stratospheric ozone depletion. The most important heterogeneous reaction on PSC surfaces are:

$$ClONO_2 + HCl(s) \longrightarrow HNO_3(s) + Cl_2 \tag{1.14}$$

$$ClONO_2 + H_2O(s) \longrightarrow HNO_3(s) + HOCl \tag{1.15}$$

The label (s) shows the reactant in the solid phase as opposed to the gas phase. HOCl from reaction equation (1.13) can react further with HCl(s) to form Cl_2, especially when concentrations of $ClONO_2$ are low, or can be rapidly photolyzed into active chlorine when sunlight returns after the winter solstice. Produced Cl_2 is ready for photodissociation when sunlight returns to subsequently undergo catalytic reactions with ozone while H_2O and HNO_3 remain in the condensed phase and thus even prolong ozone depletion by delaying chlorine deactivation (Tritscher et al., 2021, and reference therein).

Partitioning of stratospheric chlorine

The chemically active species (ClO_x), together with the reservoir species HCl and $ClONO_2$, form total inorganic chlorine (Cl_y), also called available chlorine. The sum of all chlorine from the source gases, as thus not yet available chlorine, results in the organic chlorine (CCl_y). Finally, Cl_y and CCl_y together represent total chlorine (Cl_{total}).

The total amount of chlorine in the stratosphere is controlled by input from the troposphere and by transport and mixing processes. Thus, total chlorine at any altitude is a representation (e.g. by using mean AoA) of total tropospheric chlorine delayed by about 3 to 5 years (e.g. Montzka et al., 1996; Engel et al., 2002). Figure 1.4 shows the evolution of mid-latitude total stratospheric chlorine in the time period of 1975 to 2013, where the maximum was reached between 1996–1997 below around 20 km and started to decline around the year 2000, whereas the maximum was reached slightly later at higher altitudes. The rate of stratospheric chlorine decline is expected to be altitude-dependent.

The partitioning of Cl_{total} into Cl_y and CCl_y plays a major role since only chlorine in inorganic form can contribute to ozone destruction. Chlorine is transported into the stratosphere primarily in organic source gases (source gas injection, SGI) where they are slowly decomposed by photo-dissociation and reaction with radicals (e.g. OH), leading to the formation of Cl_y. With rising altitude, CCl_y decreases and Cl_y increases. The vertical distribution of Cl_y and CCl_y changes not only with altitude but also with latitude. The amount of organic chlorine in the lower and middle stratosphere is higher in the tropics compared to mid-latitudes and vice versa for inorganic chlorine due to transport of Cl_y from the tropics and in situ production (e.g. Daniel et al., 1996; Patra et al., 2000).

Of great importance is Cl_y in the polar regions. For instance, the size of the Antarctic ozone hole varies and is mainly controlled by the amount of Cl_y and stratospheric temperature and dynamics (Newman, Kawa, and Nash, 2004). Cl_y in the polar region shows high

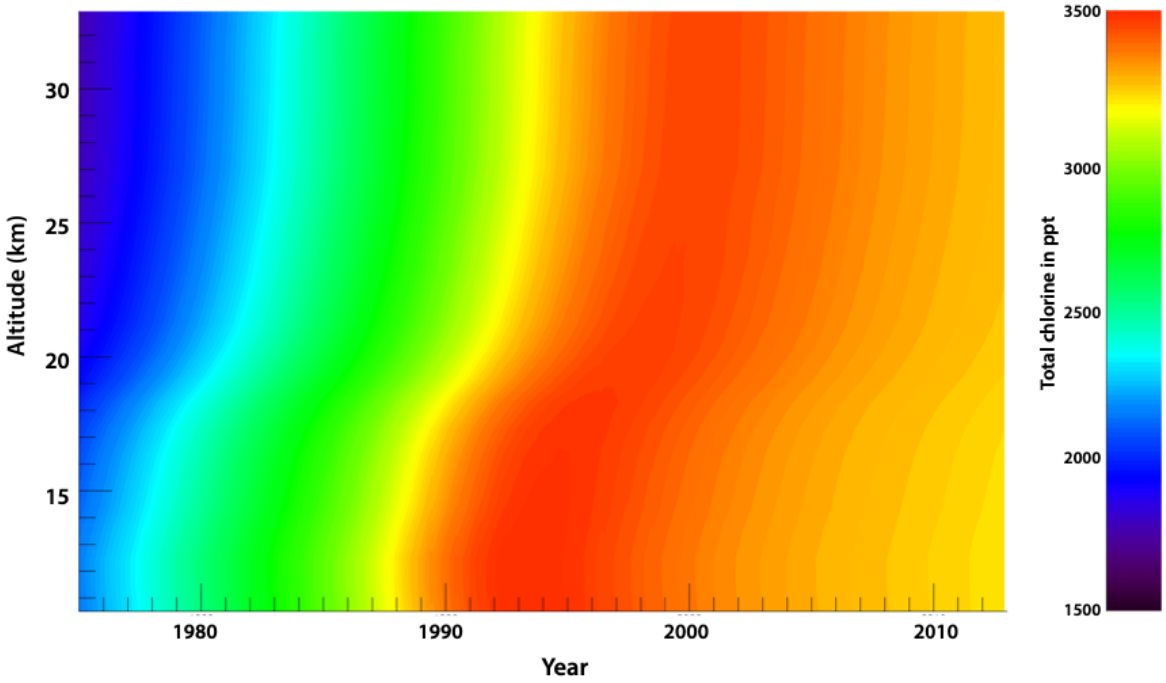

FIGURE 1.4: Evolution of total stratospheric chlorine (ppt) for mid-latitudes, calculated based on tropospheric data from NOAA. Typical profiles of the mean age of air in the stratosphere (derived from observations of SF_6 and CO_2) and a parameterization of the age spectrum are used for the calculation of the effects of mixing and transport in the stratosphere (updated from Engel et al., 2002) (Carpenter et al., 2014)

year-to-year variability. Strahan et al. (2014) inferred a $2\,\sigma$ variability of 196 ppt, which is ten times the annual decline rate of 20-22 ppt/year due to regulations of the Montreal Protocol, and implies the need for a roughly ten-year recording of Cl_y for determination of a significant trend in polar regions. The main source of this inter-annual variability is the quasi-biennial oscillation (QBO) with its pattern of alternating easterly and westerly zonal winds in the lower and middle stratosphere of the tropics, which affect the polar lower stratosphere with a delay of about one year (Strahan et al., 2015). A dependence of ozone hole area and Cl_y could only be found before 1992, a time period of rapidly increasing Cl_y (Strahan et al., 2014). From the time Cl_y slowly decreases, dynamically driven temperature variations dominate the ozone hole area variation (Newman, Kawa, and Nash, 2004; Strahan et al., 2014). A clear dependence of ozone hole area and Cl_y can only be found for outstanding cold temperature in the polar regions, e.g. temperatures $1\,\sigma$ below the 35-year mean in the near vortex edge region at levels between 30–100 hPa (Strahan et al., 2014; Strahan and Douglass, 2018).

1.3.3 Stratospheric bromine chemistry

Besides chlorine, bromine is one of the major halogenated components affecting stratospheric ozone (e.g. Engel and Rigby, 2018) with its importance first described by Wofsy, McElroy, and Yung (1975). Bromine has a much smaller abundance in the stratosphere compared to chlorine. Laube and Tegtmeier (2022) provide an estimate of Br loading of the stratosphere of 18.9 ppt in 2020. The major contributors to stratospheric bromine are the halons with around 39 % from purely anthropogenic sources, and methyl bromide (CH_3Br) with around 35 %, both with anthropogenic and natural sources. Compared to chlorine, the

contribution of very short-lived substance is much higher with around 26 % (see Fig. 1.5 and Laube and Tegtmeier, 2022).

Despite the smaller abundance of bromine, the relative efficiency of bromine in terms of ozone depletion is 60–65 times higher than that of chlorine (e.g. Sinnhuber et al., 2009; World Meteorological Organization, Atmospheric Administration, and Space Administration, 2018). A more recent study reports an even 74 times higher efficiency of bromine (Klobas et al., 2020). This is because bromine reservoir species are significantly less stable leading to an enhanced abundance of reactive bromine (Wofsy, McElroy, and Yung, 1975; Spencer and Rowland, 1978). It also affects the length of the catalytic cycles, e.g., the number of catalytic cycles performed before the radical is removed, which is much greater for bromine than for chlorine (Lary, 1997).

Bromine catalytic cycles and reservoir species

Wofsy, McElroy, and Yung (1975) and Yung et al. (1980) first described the comprehensive catalytic chain reaction for bromine which destroy ozone. Similar to chlorine, bromine reacts with ozone as followed

$$\mathrm{Br} + \mathrm{O_3} \longrightarrow \mathrm{BrO} + \mathrm{O_2}. \tag{1.16}$$

The reaction of BrO with O, NO, and HO_2 play the same roles as their chlorine analogs (see Yung et al., 1980, and reaction equations 1.4 to 1.6). In addition and as already described, BrO can interact with ClO. This is described by equation 1.11, leaving aside all intermediate steps. The substances Br, Br_2, and BrO can be summarized as BrO_x.

HOBr, as one of the possible products of the reaction of BrO and HO_2, is quickly photolysed to Br and OH and does not act as a significant reservoir (Yung et al., 1980). Br can be also converted to HBr by reaction with HO_2 (Wofsy, McElroy, and Yung, 1975; Spencer and Rowland, 1978; Yung et al., 1980):

$$\mathrm{Br} + \mathrm{HO_2} \longrightarrow \mathrm{HBr} + \mathrm{O_2}. \tag{1.17}$$

Br does not react with either CH_4 or H_2, which are the typical reactions of formation of e.g. HCl, because these reactions are endothermic (e.g., Wofsy, McElroy, and Yung, 1975; Spencer and Rowland, 1978). The importance of HBr, however, is very limited in the stratosphere. The amount of HO_2 in the stratosphere is very small and HBr has a great reactivity towards OH to re-release Br (e.g. Yung et al., 1980). For instance, Johnson et al. (1995) showed that the production of HBr with HO_2 has a yield of less than 5 %.

The most important reservoir species of Br is $BrONO_2$, which can make up 10–20 % of total inorganic bromine (e.g. Spencer and Rowland, 1978). It is formed by the reaction between BrO and NO_2 with a collision partner M

$$\mathrm{BrO} + \mathrm{NO_2} + \mathrm{M} \longrightarrow \mathrm{BrONO_2} + \mathrm{M}. \tag{1.18}$$

During the day, the relatively long photolysis wavelength allows very efficient photodissociation of $BrONO_2$ throughout the stratosphere (Burkholder et al., 2019).

$$\begin{aligned} \mathrm{BrONO_2} + h\nu &\longrightarrow \mathrm{BrO} + \mathrm{NO_2} \\ &\longrightarrow \mathrm{Br} + \mathrm{NO_3} \\ &\longrightarrow \mathrm{BrO} + \mathrm{NO} + \mathrm{O}(^3\mathrm{P}) \end{aligned} \tag{1.19}$$

$BrONO_2$ can further be destroyed by heterogeneous reaction via hydrolysis in sulfuric acid aerosols or in combination with halogens at surfaces (e.g. Burkholder et al., 2019; Tritscher et al., 2021).

$$BrONO_2 + H_2O(s) \longrightarrow HOBr + HNO_3(s) \tag{1.20}$$

$$BrONO_2 + HCl(s) \longrightarrow BrCl + HNO_3(s) \tag{1.21}$$

HOBr can further react with HCl(s) to from BrCl. BrO_x together with the reservoir species $BrONO_2$ and HBr form total inorganic bromine (Br_y). During sunlight, around half of Br_y is present in the form of BrO.

Brominated very short-lived substances

Part of this thesis is addressed to the brominated very short-lived substances (Br-VSLS). VSLSs contribute to stratospheric ozone depletion, but have very small radiative forcings due to their short lifetimes (e.g. Engel and Rigby, 2018). Further, VSLSs show a much higher variability compared to long-lived substances. Their distribution in the stratosphere is to a large extent dependent on localized sources, transport pathways, and chemical degradation during transport. Due to their short lifetime, contained halogens can be rapidly released into the lowest stratosphere and react with ozone. As mentioned in section 1.1, changes in chemical composition in the UTLS region have a relatively large impact on the surface climate.

In this work, the two major Br VSLS CH_2Br_2 and $CHBr_3$ are considered (details can be found in Sec. 1.3.1). These two Br-VSLSs contribute to a large extent (about 85 %) to ozone depletion in the lower stratosphere (Hossaini et al., 2015). They also account for about 80 % of the total VSLS organic bromine in the UTLS, whereas the remaining 20 % are contributed by the mixed bromochlorocarbons CH_2BrCl, $CHBrCl_2$, and $CHBr_2Cl$ (e.g. Keber et al., 2020).

The contribution of short-lived substances to stratospheric bromine is nearly constant (see Fig. 1.5). However, Tegtmeier et al. (2020) speculated a relatively weak positive trend in tropical mean Br from VSLSs of 0.017±0.012 ppt per decade for 1979–2013. As the anthropogenic substances will further decrease due to the regulations of the Montreal Protocol, the relative contribution of the Br-VSLS will increase. Total bromine from the Br-VSLS amounts to around 5 (3–7) ppt, partly injected in the organic form (source gas injection; SGI) with 2.1 (0.5–4.4) ppt Br and partly in inorganic form (product gas injection; PGI) with 2.8 (1.8–4.2) ppt Br (Laube and Tegtmeier, 2022). Observational-based distributions of the organic source gases are rather rare and predominantly focus on the tropics and the Northern Hemisphere. Best estimates can be found in Laube and Tegtmeier, 2022. For instance, CH_2Br_2 and $CHBr_3$ at the tropical tropopause ranging from 0.81 (0.49-1.08) ppt to 0.59 (0.17–0.89) ppt from the level of zero clear-sky radiative heating (LZRH) to the tropical tropopause (TTP) and 0.45 (0.05–1.60) ppt to 0.18 (0.01–0.54)ppt from LZRH to TTP, respectively (Wofsy, 2011; Brinckmann et al., 2012; Sala et al., 2014; Navarro et al., 2015; Pan et al., 2017). Keber et al. (2020) investigated the distribution of Br-VSLS in the UTLS of the NH. They found systematically higher mixing ratios of $CHBr_3$ at the extratropical tropopause than those at the TTP. A similar but less pronounced feature was found for CH_2Br_2.

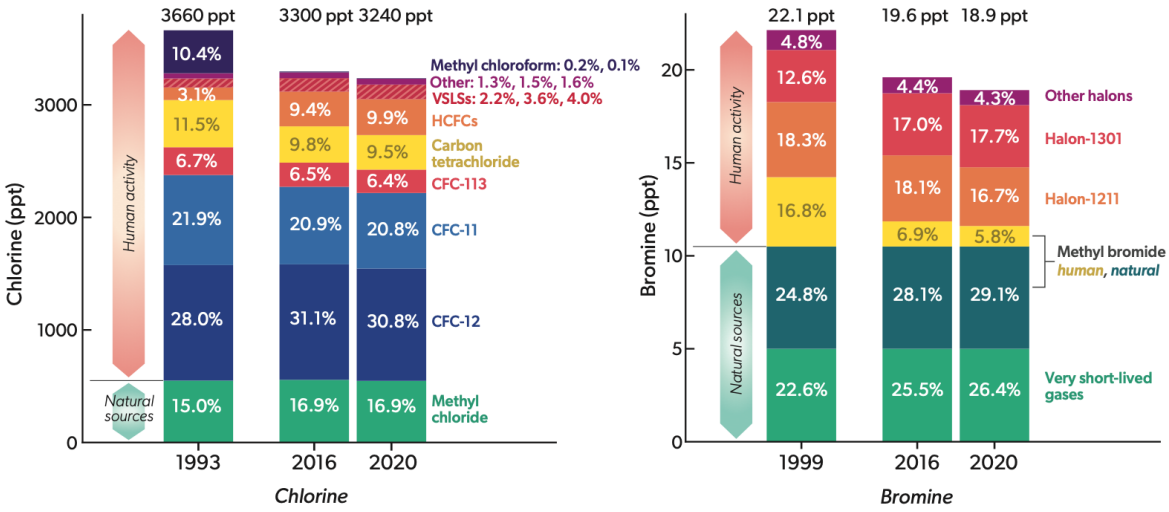

FIGURE 1.5: Chlorine and bromine input to the stratosphere for a reference year (1993 for chlorine and 1999 for bromine), 2016, and 2020 for the different species and classes of compounds. This figure is from Laube and Tegtmeier (2022).

Chapter 2

Global distribution of halogenated trace gases in the UTLS

The cumulative dissertation on hand focuses on the global distribution of halogenated substances on basis of observation within the UTLS. Airborne measurements were carried out in the Southern Hemisphere, which extends the already existing database, which is predominantly located in the tropics and the Northern Hemisphere. The idea is to be able to compare the distribution of both hemispheres on the basis of highly accurate in-situ observations and further get insights into the possible differences in the distribution for long-lived substances (focus on Cl_y) and short-lived substances (focus on Br-VSLS). After introducing the basic concepts of UTLS, transport, and halogenated substances in the previous section, in the following section, the measurements of the last years are discussed as well as concepts for the analysis and interpretation of the observations with key findings, which are collected in contributed publications. The thesis follows the content and logical structure of the publications and disregards their different chronological order.

As I personally participated at the SouthTRAC campaign in 2019, the results start with a brief overview of this campaign in Section 2.1. Further, the results are based to a large extent on measurements of the GhOST (Gas chromatograph for Observational Studies using Tracers) instrument, which has been involved in several campaigns by the German of the High Altitude and LOng Range Research Aircraft (HALO). For this reason, Section 2.2 presents a description of the instrument.

2.1 The SouthTRAC campaign

The Southern Hemisphere Transport, Dynamics, and Chemistry (SouthTRAC) campaign took place in the SH late winter and early spring 2019. On the one hand, dynamical and chemical composition aspects should be investigated in the Antarctic UTLS, for instance, the impact of the polar vortex on the UTLS (see objectives at DLR, 2022a). On the other hand, gravity wave (GW) activity should be investigated, where GW may propagate into the upper mesosphere (Rapp et al., 2020).

For this, flights were performed with the HALO aircraft, which is capable of reaching an altitude of around 14.5 km, corresponding to around 420 K potential temperature outside the tropics. The Basic HALO Measurements and Sensor System (BAHAMAS) is part of HALO. BAHAMAS is installed permanently and provides meteorological and aircraft parameters along the flight tracks (DLR, 2022b), besides the campaign-related instruments. In addition, local tropopause information along the flight tracks as well as equivalent latitude were derived using the Chemical Lagrangian Model of the Stratosphere (CLaMS) (Grooß et al., 2014). The underlying meteorological fields are from ERA-5 reanalysis of the ECMWF (Hersbach et al., 2020). The aircraft was based in Rio Grande, Argentina (RGA, 53° S, 67° W)

FIGURE 2.1: The HALO aircraft on the taxiway in Rio Grande (Argentina) during the SouthTRAC campaign 2019.

with the hot spot of gravity waves breaking (southern Atlantic and eastern Pacific) as well as Antarctica in a reachable distance for the aircraft.

The campaign consisted of two phases. The first phase took place from September 6 to October 9, 2019 and the second phase from November 2 to 15, 2019. In between, HALO returned to Germany. This results in 23 scientific flights with a total of 183 hours of measurement time, of which nine flights were transfer flights from Oberpfaffenhofen (EDMO), Germany, to Rio Grande (RGA), Argentina, and back via Sal (SID), Cabo Verde, and Buenos Aires (EZE), Argentina (see Fig. 2.2a) and one local flight operated from SID. The remaining 13 flights were local flights from RGA (see Fig. 2.2b) with 10 in the first phase and 3 in the second phase. Due to a technical problem with the aircraft, the second phase was terminated earlier than planned. With the local flights, a region between 36° to 70° S and 32 to 84° W could be sampled, up to a maximum potential temperature of around 410 K.

2.2 Instrument details

A substantial part of the results of this work is based on measurements performed with the GhOST (Gas chromatograph for Observational Studies using Tracers) instrument, which is deployed regularly on board the HALO aircraft.

GhOST is a two-channel gas chromatograph instrument. The first channel couples an isothermally operated gas chromatograph (GC) with an electron capture detector (ECD) and is thus referred to as GhOST-ECD. With a time resolution of around 1 min, measurements of SF_6 and CFC-12 are performed. A similar setup was used during the SPURT campaign (Bönisch et al., 2009; Engel et al., 2006). The second channel is temperature-programmed GC coupled with a quadrupole mass spectrometer (QP-MS) and is referred to as GhOST-MS. For the MS channel, air samples are dried before entering the analysis system using magnesium perchlorate ($Mg(ClO_4)_2$). Subsequently, because of the very small mole fraction of the halogenated species, a cryogenic pre-concentration system is installed prior to the GC.

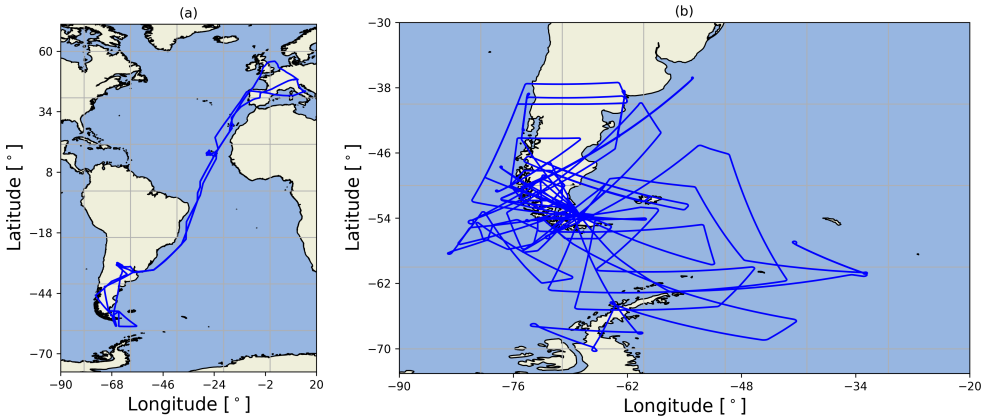

FIGURE 2.2: Flight tracks of HALO of (a) the transfers from and to Oberpfaffenhofen, Germany (48° N, 11° E) and (b) during the two phases with the base in Rio Grande, Argentina (53° S, 67° W). The figure is taken from (Jesswein et al., 2021).

A sample loop filled with HayeSepD adsorbent material is cooled to -80°C with a Stirling cooler to trap the compounds. For analysis, the sample loop is then heated to about 200°C and purged with helium towards the GC-MS (Obersteiner et al., 2016; Sala et al., 2014). This measurement setup allows air samples to be taken with a temporal resolution of four to six minutes, depending on the ionization mode.

The MS is operated either in electron impact ionization mode (EI) or in negative chemical ionization (NCI) mode. In EI, high-energy electrons are emitted from a cathode (called a filament). These electrons collide with the sample molecules, generating positively charged ions. Each substance fragments into a characteristic spectrum of ions with different mass-to-charge ratios, making it easy to identify each substance. To keep the chromatography time as short as possible, for each substance one fragment is selected for which the chromatographic peak is not disturbed by other substances. This results in a time resolution of around 6 min per measurement cycle. With NCI, an additional reactant gas is required. An argon-methane mixture (around 5 % methane) has proven to be suitable for the investigation of halogenated substances. In the reaction chamber, the reactant gas collides with the high-energy electrons emitted by the filament and secondary electrons (thermal electrons) with significantly lower energy are formed. The thermal electrons react with the sample molecules. In the case of the halocarbons studied here, a halogen anion is formed. These can be tracked on the masses of their main isotopes. For chlorinated substances, these are ^{35}Cl and ^{37}Cl, whereas, for brominated substances, these are ^{79}Br and ^{81}Br, since all bromine and chlorine species, respectively, yield the same fragments in the MS. NCI and thus the observation of the main isotopes requires that the substances are well separated by the GC and thus clean peaks of the substances can be detected, which works on the GhOST for the brominated substances quite well, but less for the chlorinated substances of which there are many more. A good separation of the brominated substance was achieved with a time resolution of around 4 min per measurement cycle. The substances for further analysis within the NCI mode are listed in table 2.1a, whereas the list of substances using the EI mode includes chlorinated and brominated substances as can be seen in table 2.1b. The extended spectrum of substances in EI mode is at the expense of reproducibility, limit of detection, and time resolution.

TABLE 2.1: Reproducibilities and detection limits of the GhOST-MS in (a) NCI mode and (b) EI mode. The values were taken before the most recent use of the corresponding mode during laboratory conditions, which was just before the WISE campaign for NCI and SouthTRAC campaign for EI.

(a) NCI mode

Substance	Reprod. [%]	Det. Lim [ppt]
Halon 1301	1.0	0.05
Halon 1211	0.5	0.006
Halon 1202	7.6	0.006
Halon 2402	1.5	0.007
CH_3Br	-	-
CH_2Br_2	0.7	0.01
CH_2BrCl	9.2	0.13
$CHBr_2Cl$	2.2	0.002
$CHBrCl_2$	3.4	0.002
$CHBr_3$	2.2	0.085

(b) EI mode

Substance	Reprod. [%]	Det. Lim [ppt]
COS	0.40	0.96
CFC-11	0.20	0.36
CFC-12	0.30	0.47
CFC-113	0.64	0.18
Halon 1301	3.83	0.93
Halon 1211	2.78	0.25
Halon 2402	5.79	0.09
HCFC-22	0.41	1.31
HCFC-141b	0.82	0.39
HCFC-142b	0.84	0.50
HFC-125	0.79	0.62
HFC-134a	0.49	3.51
HFC-143a	1.67	1.86
CH_3Cl	0.39	0.76
CH_2Cl_2	0.78	0.46
$CHCl_3$	0.95	0.66
CCl_4	0.44	0.22
C_2Cl_4	1.31	0.11
CH_3CCl_3	8.67	0.53
CH_3Br	1.69	0.31
CH_2Br_2	2.59	0.11
$CHBr_2Cl$	8.91	0.75
$CHBr_3$	2.82	0.24
CH_3I	6.75	0.08

2.3 Stratospheric chlorine - deriving Cl_y and air mass classification

The following sections summarize the concepts, methods, data, and key results that are published in detail in:
Jesswein, M., Bozem, H., Lachnitt, H.-C., Hoor, P., Wagenhäuser, T., Keber, T., Schuck, T., and Engel, A.: *Comparison of inorganic chlorine in the Antarctic and Arctic lowermost stratosphere by separate late winter aircraft measurements*, Atmos. Chem. Phys., 21, 17225–17241, 2021, DOI: https://doi.org/10.5194/acp-21-17225-2021

2.3.1 Inferring inorganic chlorine

Although the size of the ozone hole is strongly influenced by dynamic aspects, it is important to measure the amount of Cl_y in the stratosphere, for instance to understand possible changes in the relationship between Cl_y and ozone hole area as chlorine levels decrease. There are different methods to derive Cl_y whereby some methods required certain atmospheric conditions. In the best case, the inorganic chlorinated substances are measured directly. This was done, for instance, in Wetzel et al. (2015) using balloon measurements with

two instruments, the MIPAS-B (Michelson Interferometer for Passive Atmospheric Sounding) and TELIS (TErahertz and submillimeter LImb Sounder). Only for Cl_2O_2, which could only be partly measured, they used a ClO–Cl_2O_2 relation which relied on model data. In addition, Cl_y can be obtained solely from the reservoir species. In the upper stratosphere, HCl represents nearly all Cl_y (e.g. Anderson et al., 2000; Froidevaux et al., 2006; Wetzel et al., 2015). Under certain conditions in the lower polar stratosphere, Cl_y is present almost completely in the form of the reservoir gas HCl. The pre-requisite is a strong polar vortex, severe ozone depletion, and denitrification. The catalytic ozone depletion ceased and Cl reacted with CH_4 to form HCl. In addition, the ratio of NO/NO_2 increases and NO reacts with ClO to form Cl, followed by the production of HCl (Strahan and Douglass, 2018, and reference therein). Thus, for these conditions, measurements of the reservoir species are sufficient.

A different approach is the calculation of Cl_y as the difference between Cl_{total} and CCl_y, which was done in the course of this work. Cl_{total} can be derived from mean AoA and tropospheric time trends of the organic source gases. Age spectra are generated by using a width parameterization (rom of 1.25 years). These spectra together with tropospheric time trends of the chlorinated substances are used to calculate the stratosphere mixing ratios, considering no chemical degradation (Cl_{total}). If measurements of all relevant chlorinated substances are available, Cl_y is simply derived by subtracting CCl_y from Cl_{total} (hereafter referred to as semi-direct Cl_y). If there are no or only limited measurements of chlorinated substances, CCl_y can be calculated indirectly based on correlations from measurements taken at a different time and place, for instance, a previous measurement campaign. These correlations of the chlorinated substances to a reference substance, for instance, CFC-12 or N_2O (e.g. Wetzel et al., 2015; Marsing et al., 2019), have to be adapted to account for tropospheric trends which can be done with a modified method described in Plumb, Vohralik, and Ryan (1999) using Γ^* and G^* (see section 1.2.3). The correlations scaled in this way to the time period of interest can be used, to determine CCl_y from the reference substance alone. Cl_{total} is again derived from mean AoA and tropospheric time trends of the organic source gases. Cl_y is then determined via the difference of Cl_{total} and CCl_y from scaled correlations (hereafter referred to as indirect Cl_y).

During the SouthTRAC campaign, we were able to measure all major long-lived chlorinated substances with the GhOST-MS as well as SF_6 with the GhOST-ECD. Thus, it was possible to compare the semi-direct and indirect determination of Cl_y. This is an important aspect in the context of this work, because it allows us to compare Cl_y from different observations. Not all relevant long-lived chlorinated substances are always measured, but e.g. only one representative. Tropospheric time trends for the entry mixing ratios and mean AoA were taken from the AGAGE (Advanced Global Atmospheric Gases Experiment) Network (Prinn et al., 2018). For the indirect method, observations from two balloon flights inside the Arctic polar vortex in 2009 and 2011 from a cryogenic whole-air sampler (Engel et al., 2002) were used.

CFC-12 was chosen as the reference substance for the indirect method. The scaled correlations from the balloon observations and correlations from observations during SouthTRAC for the chlorinated substances against CFC-12 agree well. Figure 2.3 shows exemplary correlations of CFC-11, CH_3Cl, and HCFC-142b against CFC-12, with scaled balloon observations in red and observations during SouthTRAC in black. This method demonstrates the comparability of observations that are not only about 10 years apart, but also from the polar region of the NH and scaled to the polar region of the SH. Based on this good agreement, we were able to provide a correlation function for the determination of Cl_y using CFC-12 for the period of the SouthTRAC campaign.

$$\chi_{Cl_y} = c_0 + c_1\chi_{CFC-12} + c_2(\chi_{CFC-12})^2 \tag{2.1}$$

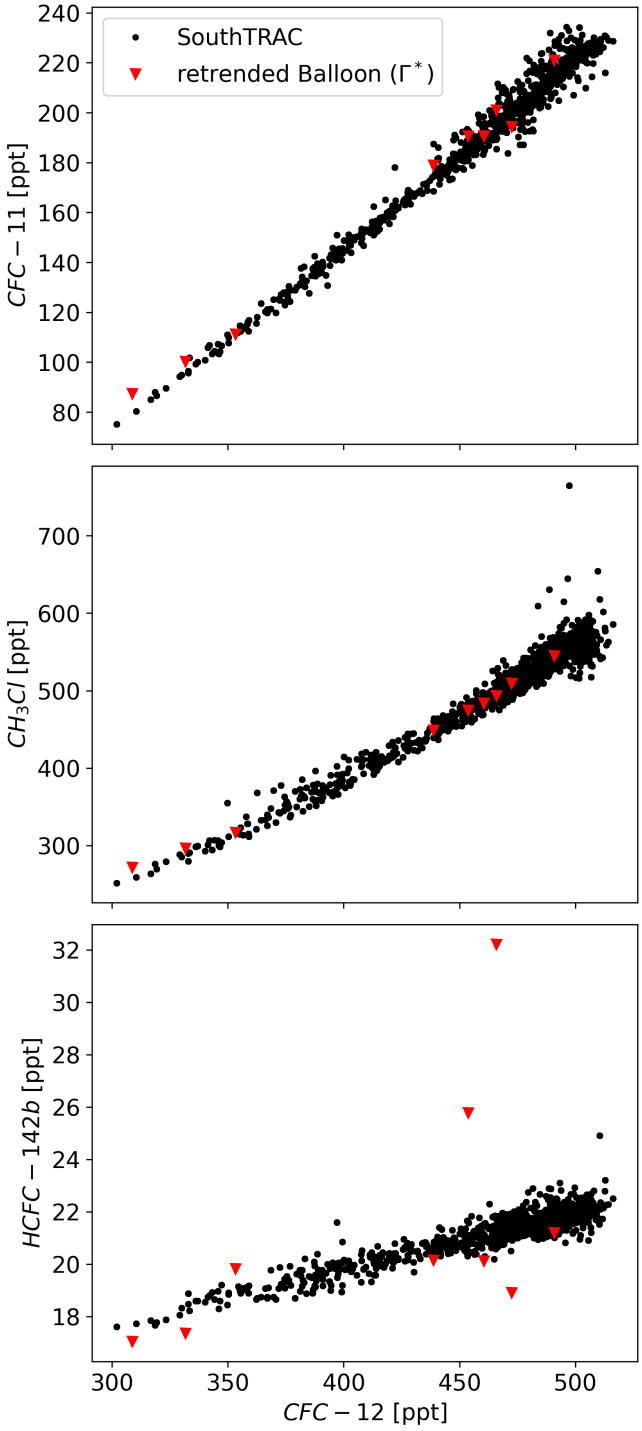

FIGURE 2.3: Correlation between CFC-12 and CFC-11, between CFC-12 and CH_3Cl, and between CFC-12 and HCFC-142b. GhOST-MS observations are shown in black, the balloon observations scaled to the time of the SouthTRAC campaign using Γ^* are shown in red. The figure is taken from Jesswein et al. (2021).

The correlation coefficients on the basis of the balloon observations are c_0 = 2965.27 ppt, c_1 = -2.807, and c_2 = -6.06944$\times 10^{-3}$ ppt^{-1}. Further correlation coefficients regarding N_2O as the reference substance as well as coefficients based on SouthTRAC observations can be found in (Jesswein et al., 2021). A comparison of semi-direct and indirect derived Cl_y for the SouthTRAC campaign is part of sect. 2.3.3.

2.3.2 Air mass classification

Observational studies in the winter polar region introduce the difficulty of separating air masses inside and outside the polar vortex with different compositions. High concentrations of the reactive halogenated substances can be maintained inside the polar vortex as there is less mixing with the surroundings due to the separation by the polar night jet. Aircraft-based observations can sample these different air masses along the flight paths, making it necessary to classify them in terms of their origin.

To find the vortex edge, the maximum gradient of PV restricted by the proximity of a relatively strong polar jet is widely used and known as the Nash criterion (Nash et al., 1996). This method relies on meteorological reanalysis which may not resolve small-scale features like vortex filaments. These filaments, however, may differ from the chemical composition of the surrounding atmosphere. A tracer-based vortex definition was introduced by Greenblatt et al. (2002), which uses the tight correlation of N_2O and potential temperature inside the vortex for the determination of the vortex edge. Some key points of the inner vortex N_2O profiles are a large vertical gradient with much lower values than at mid-latitudes at comparable isentropic levels due to diabatic descent and low variability on isentropic surfaces (about 6 ppb; Greenblatt et al., 2002) as the long isolation leads to well-mixed air masses. In comparison, the profile at mid-latitudes shows a weaker gradient and a much larger variability as it can be influenced by both tropical and polar air (e.g. Krause et al., 2018; Marsing et al., 2019). In between, there is a transition region (vortex boundary region), which is influenced by the vortex as well as by mid-latitudes.

In this work, we expanded the vortex identification by Greenblatt et al. (2002). Besides only distinguishing between vortex and non-vortex measurements, we would like to allocate measurements to the vortex, vortex boundary region, and mid-latitudes. For this, we use observations of several flights to create a reference profile for the vortex and mid-latitudes. This was done using two vertical coordinates, potential temperature (Θ) and potential temperature relative to the local tropopause ($\Delta\Theta$) and observations of N_2O. Here and in the following, the dynamic PV-based tropopause is used (see sect. 1.1). The vortex profile was generated by taking only the flights, which probably had contact with the vortex. Data were further pre-filtered by taking only observations pole-wards of 60° equivalent latitude and 20 K above the local tropopause (e.g. above the ExTL). For the mid-latitude profile, all flights were taken, focusing only on measurements between 40° and 60° equivalent latitude and 20 K above the local tropopause. An iterative filter procedure is then used to obtain the lower envelope for the vortex profile and the upper envelope for the mid-latitude profile. Exemplary the filter procedure for the SouthTRAC data is shown in Fig. 2.4 (the flowchart is displayed in the Appendix B in Fig. B.1). As an intermediate step, the remaining observations were binned in 5 K intervals. The means of these bins were used to generate a polynomial fit functions for the profiles.

For every flight, a reference N_2O data set for the vortex (N_2O_{vor}) and mid-latitudes (N_2O_{mid}) is calculated using the fit functions and the observed Θ and $\Delta\Theta$. Every N_2O measurement point is then compared to the respective N_2O_{vor} and N_2O_{mid} value. The following

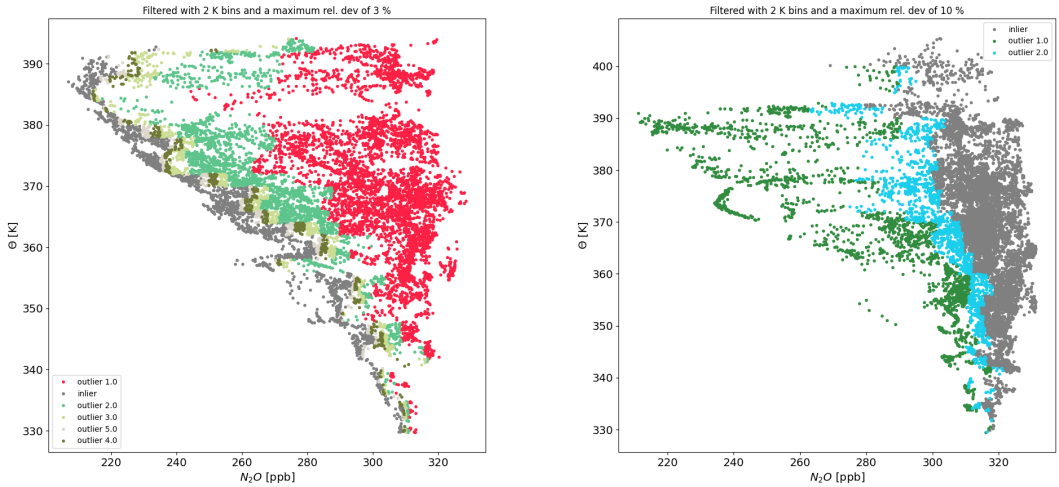

(A) (B)

FIGURE 2.4: Measurements included for generating the vortex profile (A) and mid-latitude profile (B) during the SouthTRAC campaign. Colors indicate the iteration over the measurement data to get remaining data for the final envelope. The figures are taken from Jesswein et al. (2022).

then applies for each N_2O measurement:

- $N_2O < N_2O_{vor}$ + vortex cutoff $\Rightarrow$ assigned to the vortex.
- $N_2O > N_2O_{mid}$ - mid-latitude variability $\Rightarrow$ assigned to the mid-latitudes.
- N_2O_{vor} + vortex cutoff $< N_2O < N_2O_{mid}$ - mid-latitude variability $\Rightarrow$ assigned to vortex boundary region
- N_2O_{vor} + vortex cutoff $> N_2O > N_2O_{mid}$ - mid-latitude variability $\Rightarrow$ overlap and not classified

The allocation of the measured chlorinated source gas observations is done by the respective N_2O data point allocation. For the prescribed cutoff, a value of 20 ppb was used, proposed by Greenblatt et al. (2002). The associated variability of the mid-latitude profile was set to 15 ppb, matching the variability in N_2O in the mid-latitudes of roughly 10 % (Strahan, Loewenstein, and Podolske, 1999).

2.3.3 Evaluation of Cl_y calculations and in-situ air mass classification

The spectrum of substances measured during the SoutTRAC campaign can be used to compare the semi-direct and indirect determination of Cl_y. Calculated Cl_y from both methods was mapped for the SouthTRAC campaign against mean AoA in Fig 2.5. Research in recent years indicates that the SF_6 lifetime is shorter than the previous assumptions due to the presence of important loss mechanisms in the mesosphere, leading to a biased mean AoA (e.g. Ray et al., 2017). For this, Fig. 2.5 includes a corrected mean AoA. The used correction function is based on the comparison of SF_6-derived mean AoA to a combined mean AoA based on five alternative tracers (Leedham Elvidge et al., 2018). Cl_y by the semi-direct and indirect method differ only slightly with a maximum difference of about 65 ppt at 5 years of mean

AoA. Between 1 and 4 years, the difference is well below about 30 ppt. The good comparability of these two methods offers the possibility to compare Cl_y from different measurement campaigns, although they may differ in terms of measured chlorinated substances.

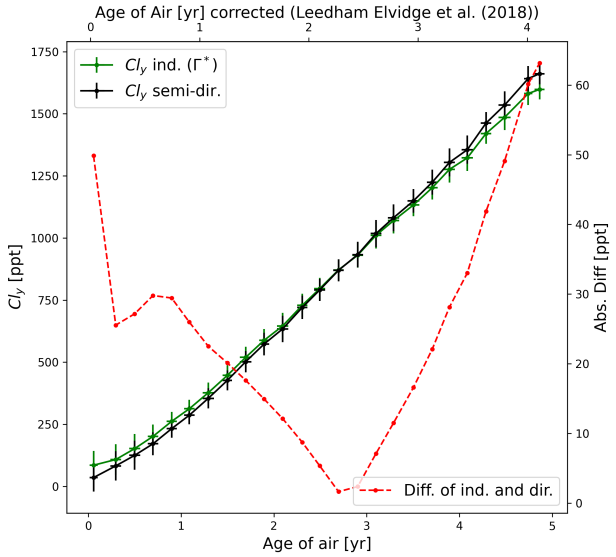

FIGURE 2.5: Indirectly (green) determined Cl_y based on balloon observations in 2009 and 2011 and semi-directly (black) determined Cl_y as a function of the age of air (bottom axis) and corrected age of air (top). The figure is taken from Jesswein et al. (2021).

For the air mass classification, N_2O measurements of the University of Mainz Airborne Quantum Cascade Laser-spectrometer (UMAQS) were used. The instrument is based on direct absorption spectroscopy using a continuous-wave quantum cascade laser with a sweep rate of 2 kHz (Müller et al., 2015). N_2O measurements showed an overall uncertainty of 0.6 ppb. Using the iterative process presented in sect. 2.3.2, a vortex and mid-latitude reference profile in Θ was created (See Fig. 2.6; reference profiles in $\Delta\Theta$ are shown in Jesswein et al. (2021)).

In general, it can not be assumed to have a single N_2O vortex profile throughout the winter. Subsidence of vortex air due to radiative cooling leads to changes in the N_2O profile during winter. However, N_2O data from the SouthTRAC campaign did not reveal a strong diabatic descent within the time period of measurements. Thus, only one vortex profile was generated and used for all observations.

The air mass classification during the flights can be exemplarily demonstrated by flight ST14 on September 26, 2019 in Fig. 2.7. Displayed are original and up-sampled measurements of CFC-11 (see Appendix B or Jesswein et al. (2021) for more information about up-sampling measurements). The background colors show the regions the samples can be assigned to. The measurements follow well the air mass classification with smaller values within the vortex and vortex boundary region. For instance, vortex filaments are typically assigned to the vortex boundary region, as these filaments are decaying and are mixed with the background air. The up-sampled measurements show even better agreement with the classification with sharp gradients at the transitions, e.g. at 4:10 and 5:50 UTC.

Taking the up-sampled observations with the air mass classification, chlorine partitioning into inorganic and organic chlorine in the Antarctic lower stratosphere during SouthTRAC was investigated. Only measurements polewards of 40° equivalent latitude were

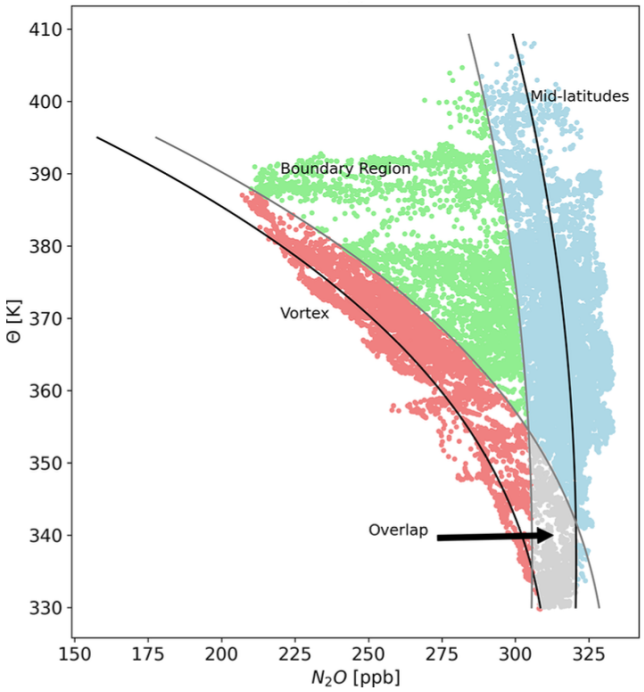

FIGURE 2.6: Mid latitude and vortex profile of N_2O versus potential temperature (Θ). The vortex cutoff criterion of 20 ppb and mid-latitude variability of 15 ppb are illustrated as grey lines right of the vortex and left of the mid-latitude profile. The overlap region is declared for the area where the vortex cutoff and mid-latitude variability cross. The figure is taken from Jesswein et al. (2021).

taken into account. Measurements have been binned in 5 K potential temperature bins between 270 (e.g. 20 K above the mean tropopause) and 420 K. Bins including less than five data points are not included (see Fig. 2.8). The uncertainty in each bin is represented by the $1\,\sigma$ standard deviations of the mean. Below the potential temperature level, for which air mass classification was possible, Cl_y is given for all measurements. Above, Cl_y is estimated separately for each region. Measurements, which are within the overlap are included in both, vortex and mid-latitudes.

Tropospheric Cl_y is close to zero. In the troposphere, chlorine is almost exclusively in organic form, and observations of total chlorine during SouthTRAC are in good agreement with the total chlorine, derived from ground-based AGAGE measurements. From the height at which the division into regions is possible, the vortex, vortex boundary region, and mid-latitude profiles of Cl_y show different gradients. The mid-latitude profile shows only a weak gradient with mixing ratios reaching 446 ± 124 ppt between 380 and 400 K. In the vortex boundary region, mean mixing ratios reach a maximum of 1090 ± 377 ppt at the Θ level of 395 K. The profile variability increases with height, due to the air mass classification. At the highest levels in the vortex boundary region, Cl_y decreases, probably influenced by the lower number of observations at this altitude range which are more towards mid-latitudes. Between 330 and 385 K, observations of Cl_y could be derived for the polar vortex. A significant increase up to a value of 1687 ± 19 ppt could be observed. Thus, up to half of the total chlorine could be found in inorganic form below a value of 400 K. As mentioned in sect. 1.3.2, the relation of ozone hole area and Cl_y is masked by dynamically driven temperature variations. The ozone hole area in 2019 was about 10×10^6 km^2 in size and thus only 20 % of that of mid-September in 2018 (Wargan et al., 2020) as a result of a minor SSW event with an early chlorine deactivation.

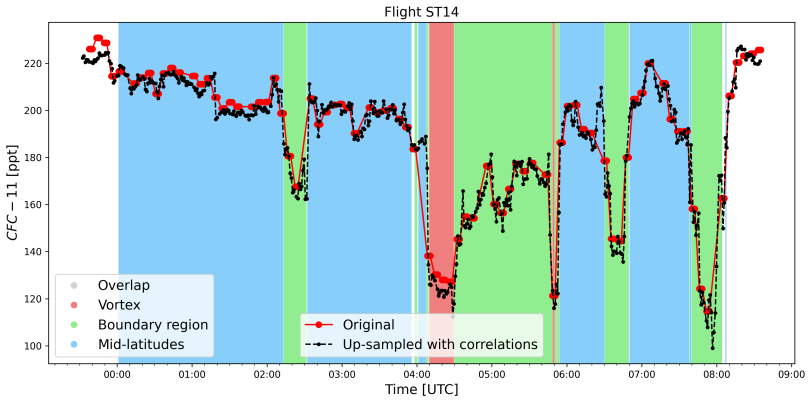

FIGURE 2.7: CFC-11 measured with the GhOST-MS during the flight ST14 on 26 September 2019. Original data are shown in red, and up-sampled data are in black. Color-coded background indicates the region where samples were taken, derived by air mass classification in Θ coordinates. The figure is taken from Jesswein et al. (2021).

2.4 Stratospheric chlorine - inter-hemispheric difference of lowermost stratospheric Cl_y

The following sections summarize the concepts, methods, data, and key results that are published in detail in:
Jesswein, M., Bozem, H., Lachnitt, H.-C., Hoor, P., Wagenhäuser, T., Keber, T., Schuck, T., and Engel, A.: *Comparison of inorganic chlorine in the Antarctic and Arctic lowermost stratosphere by separate late winter aircraft measurements*, Atmos. Chem. Phys., 21, 17225–17241, 2021, DOI: https://doi.org/10.5194/acp-21-17225-2021

and

Wagenhäuser, T., Jesswein, M., Keber, T., Schuck, T., and Engel, A.: *Mean age from observations in the lowermost stratosphere: an improved method and inter-hemispheric differences*, EGUsphere, 1–26, 2022, DOI: https://doi.org/10.5194/egusphere-2022-1197

2.4.1 Seasonally overlapping data from NH and SH

The GhOST instrument was installed on several HALO campaigns before, mostly focusing on the NH. One of the campaigns, which took place at a similar season as the SouthTRAC campaign but on the NH, is the PGS campaign. The PGS campaign, which consisted of three partial missions POLSTRACC (Polar Stratosphere in a Changing Climate), GW-LCYCLE (Investigation of the Life cycle of gravity waves), and SALSA (Seasonality of Air mass transport and origin in the Lowermost Stratosphere) conducted flights in the Arctic winter from December 17, 2015 to March 18, 2016 (Oelhaf et al., 2019). The campaign was split into two phases. The second phase from February 26 to March 18, 2016 took place during a comparable period to the SouthTRAC campaign (late winter/early spring). Flights of the second phase are displayed in Fig. 2.9. These observations were taken for a comparison of the distribution of Cl_y in the lowermost stratosphere in respective late winter. As during the SouthTRAC campaign, meteorological data have been recorded by the on-board instrument BAHAMAS and $\Delta\Theta$ as well as equivalent latitude have been derived via the CLaMS model using ERA-5 reanalyses.

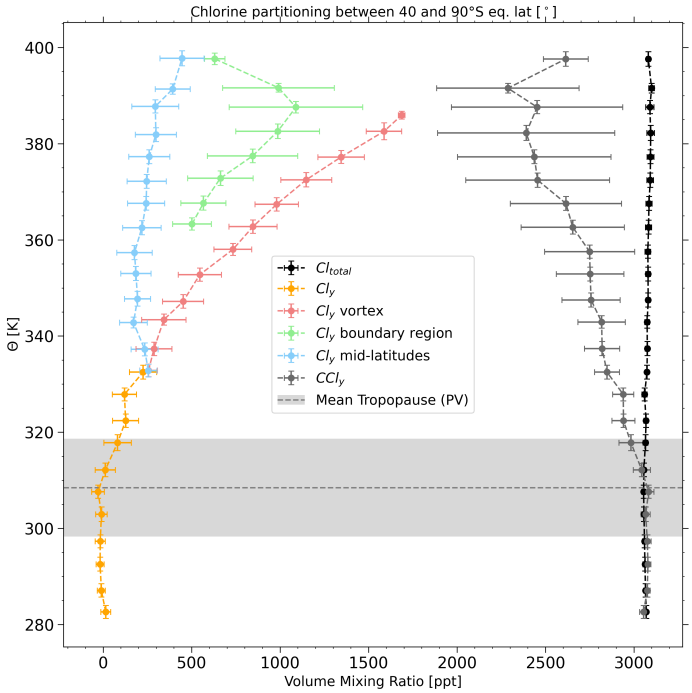

FIGURE 2.8: Vertical profiles of Cl_y, Cl_y by region from 20 K above the local tropopause, CCl_y , and Cl_{total} averaged over 40–90° S equivalent latitude for all flights during SouthTRAC. The figure is taken from Jesswein et al. (2021).

Unlike during the SouthTRAC campaign, the GhOST-MS was operated in NCI mode with a focus on the brominated substances (see table 2.1a). Nonetheless, CFC-12 was measured with the GhOST-ECD channel. Cl_y for the PGS campaign was thus determined via the indirect method, which has been shown to deliver comparable results to the semi-direct method. As for SouthTRAC, the scaled correlations from observations of the cryogenic whole-air sampling from two balloon flights inside the Arctic polar vortex in 2009 and 2011 were used, resulting in a correlation function for Cl_y (eq. 2.1) with the coefficients c_0 = 3011.05 ppt, c_1 = -2.774, and c_2 = -5.88360×10^{-3} ppt^{-1} when using CFC-12 as the reference substance.

Observations of Cl_y were separated into the vortex, vortex boundary region, and mid-latitudes with the method previously introduced in sect. 2.3.2. N_2O was measured aboard HALO during PGS by the TRIHOP instrument (Krause et al., 2018). The TRIHOP instrument is an infrared absorption quantum cascade laser-spectrometer operated by the University of Mainz, similar to the UMAQS instrument during SouthTRAC.

2.4.2 Hemispheric comparison of lower stratospheric inorganic chlorine

On the basis of the SouthTRAC and PGS campaigns, we compared the amount of Cl_y inside the respective vortex. Vertical profiles Cl_{total} and Cl_y inside the Antarctic and Arctic vortex were analyzed using Θ and $\Delta\Theta$ as the vertical coordinate. The Cl_y observations assigned to the vortex were binned into 5 K intervals of Θ and $\Delta\Theta$. Likewise, this binning was done for Cl_{total}. The profiles as well as the mean PV-based tropopause are displayed in Fig. 2.10.

Mean tropopause heights were comparable for the two campaigns (at 306 K during PGS and at 308 K during SouthTRAC). Regarding Cl_{total}, there is a difference of about 60 ± 9.6 ppt between PGS (2015/2016) and SouthTRAC (2019). The trend of the controlled chlorinated substances was stated to be around -12 ± 0.9 ppt/yr (Engel and Rigby, 2018), which, based on the period between these two campaigns, would account for about 45 ppt of the difference.

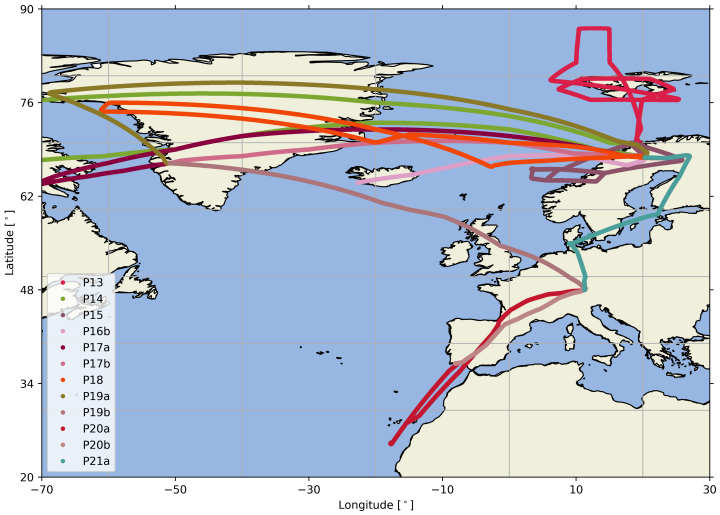

FIGURE 2.9: Flight tracks of HALO during the second phase of the PGS campaign with the base in Kiruna, Sweden.

The remaining difference of about 15 ppt may be due to larger chlorine input from the NH. The overall picture of the vortex profiles in Θ and $\Delta\Theta$ is similar. SouthTRAC polar vortex Cl_y values are larger than the PGS polar vortex values at comparable distance to the local tropopause. In Θ coordinates (Fig. 2.10a), differences reach a maximum of around 444 ppt at around 385 K. The maximum difference is even larger in $\Delta\Theta$ coordinates with 540 ppt at 65 K, although the difference becomes smaller at higher $\Delta\Theta$ levels (Fig. 2.10b). Based on these two campaigns, a slightly different partitioning of the total chlorine within the respective hemispheric vortex is obtained. Within the Antarctic vortex, up to around 50 % was found in the inorganic form. In the Arctic vortex, only around 40 % of total chlorine was found in the inorganic form at a comparable distance to the tropopause.

For the inter-hemispheric difference of Cl_y (Fig. 2.11), observations of the two campaigns were represented in an altitude-latitude cross-section. As the horizontal coordinate, we have chosen geographical latitude for tropospheric values and equivalent latitude for stratospheric values hereafter referred to as equivalent latitude*. For the vertical coordinate, $\Delta\Theta$ was used, as tropopause height is slightly different for the campaigns, and a tropopause relative coordinate accounts for tropopause variability and allows for a better comparison of Cl_y. Observations have been binned into 5° latitude and 5 K of $\Delta\Theta$, with bins containing at least five data points taken into account for the analysis. The difference was then calculated by subtracting each southern hemispheric altitude-latitude bin from the corresponding northern hemispheric bin if present.

There is hardly any overlapping data in the troposphere with only two bins showing only little difference between the two hemispheres. Furthermore, in the lowermost stratosphere up to around 20 K above the local tropopause, differences are still small with some exceptions between 0 and 5 K of $\Delta\Theta$ and 30 to 35° equivalent latitude and between 10 and 15 K of $\Delta\Theta$ and 45 to 50° equivalent latitude. Both bins have around 200 ppt more Cl_y during PGS than during SouthTRAC.

In the lower stratosphere, a separation into two areas can be seen. The higher latitudes show overall higher mixing ratios during SouthTRAC. Two bins show outstandingly high differences of about 900 ppt more Cl_y in the SH. These differences are much larger than the

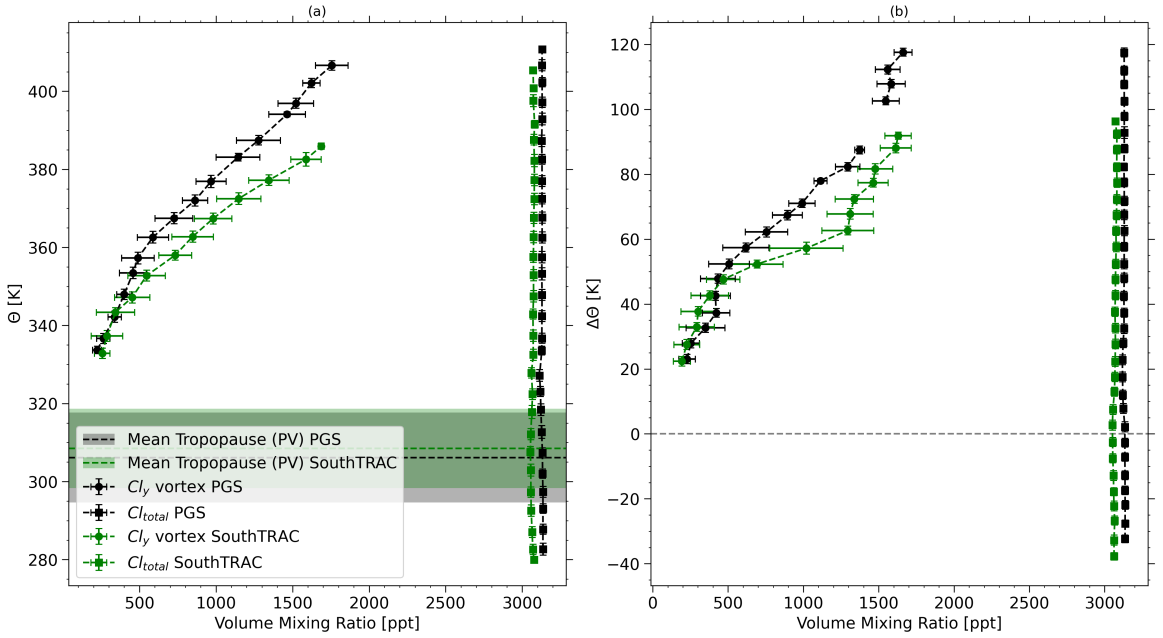

FIGURE 2.10: (a) Comparison of the vertical profiles of Cl_y inside the respective vortex where classification was possible and total chlorine from PGS (black) and SouthTRAC (green). Data are averaged over 40 to 90° equivalent latitude of the respective hemisphere and are displayed as a function of Θ. Vertical and horizontal error bars denote $1\,\sigma$ variability. PV tropopause for PGS (black) and SouthTRAC (green) are displayed as dashed horizontal lines with the $1\,\sigma$ variability as shaded areas. Panel (b) is the same data as (a) but as a function of ΔΘ relative to the local tropopause (PV) displayed with a dashed grey line. The figure is taken from Jesswein et al. (2021).

differences from the vertical profiles inside the respective vortex in Fig. 2.10. Due to differences in Arctic and Antarctic vortex size, strength, and stability, it is very likely that observations of different regions, e.g., from the vortex core and vortex boundary region, have been compared, since the coordinates used are not relative to the vortex edge. A possible reason for the differences at high-latitudes is a difference in transport in both hemispheres. For instance, Konopka et al., 2015 used model simulations with meteorological reanalysis data to show that mean AoA is always younger polewards of 60° in the NH compared to the corresponding season in the SH. Older air, e.g. with longer transit times is associated with larger amounts of Cl_y as more Cl_{total} is already converted to inorganic form. The mid-latitude stratosphere shows consistently higher Cl_y mixing ratios during PGS with differences reaching up to 315 ppt. The amount of Cl_{total} declined between the time of the PGS campaign and the SouthTRAC campaign and arguably would mask the inter-hemispheric difference in Cl_y. But the maximum difference of Cl_{total} between 2015/2016 and 2019 of 60 ± 9.6 ppt would not change the overall picture, as it would only account if it was completely converted to the inorganic form. Further, the observed differences are clearly larger than the temporal difference on Cl_{total}. Explanations of the differences in the mid-latitude stratosphere are somewhat limited. Results compiled in Engel and Rigby, 2018 show updates to mid-latitude stratospheric Cl_y trends, based on chlorine reservoir species. Southern hemispheric trends are overall negative, whereas northern hemispheric trends are non-significantly negative or even slightly positive (Mahieu et al., 2014; Froidevaux et al., 2015; Froidevaux et al., 2019). But although these trends differ hemispherically, they do not explain the differences of around 200 ppt and more, based on observations from the PGS and SouthTRAC campaign. Observational-based results show, however, that mean AoA in the

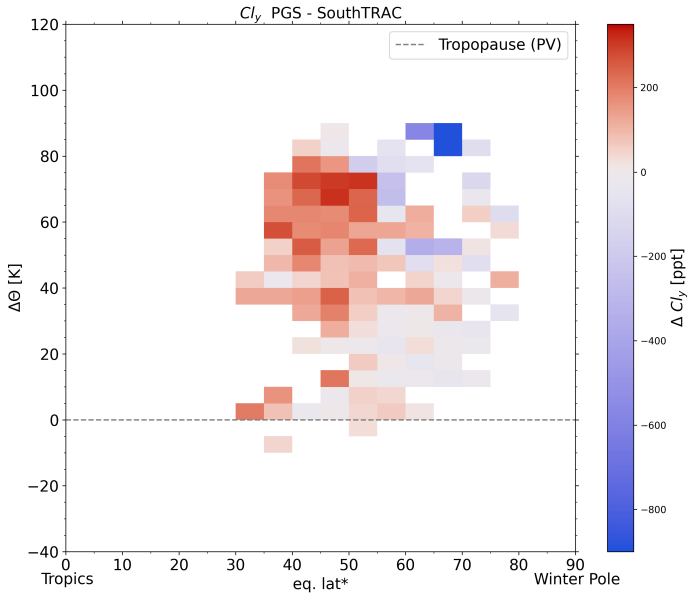

FIGURE 2.11: Difference of the latitude–altitude cross section of Cl_y from PGS and SouthTRAC. Data are binned using equivalent latitude* and ΔΘ. The figure is taken from Jesswein et al. (2021).

NH lowermost stratosphere undergoes a seasonal cycle where mean AoA increases from October to April, and the distribution is driven by the strength of the downward transport and isolation from the troposphere (Bönisch et al., 2009). However, such an observational-based analysis is lacking for the SH.

2.4.3 Improved method for deriving mean age - towards more accurate inorganic chlorine

Mean AoA, used for the estimation of Cl_{total} in the previous section, was derived with the common assumption, that all air passes through the tropical tropopause into the stratosphere. This assumption works well for the stratosphere above about 380 K of Θ. In the lowermost stratosphere, however, transport mechanisms across the extratropical tropopause gain importance and can influence the composition of the lowermost stratosphere. This also has implications on deriving age spectra and mean AoA from mixing ratios of trace gases (Hauck et al., 2019; Hauck et al., 2020). The method to derive mean AoA must be expanded to account for the input from the extratropical tropopause.

An extended approach accounts for input into the stratosphere from i individual source regions with individual time series $\chi_i(t')$. The origin fractions $f_i(\vec{x}, t)$ introduced by Hauck et al. (2020) can then be used to describe the percentage of air at a point in the stratosphere that has tropospheric section i as origin, thus the weight of each $\chi_i(\vec{x}, t)$ of the total mixing ratio. Equation 1.1, e.g. the mixing ratio of a suitable age tracer at a specific location in the stratosphere can be extended as followed

$$\chi(\vec{x}, t) = \sum_{i=0}^{n-1} (f_i(\vec{x}, t) * \int_0^{\infty} \chi_{0,i}(t - t') G(\vec{x}, t, t') \mathrm{d}t') \tag{2.2}$$

This is only valid, if the sum of all origin fractions is 1 ($\sum_{i=0}^{n-1} f_i(\vec{x},t) := 1$). Following Hauck et al., 2020, entry regions are defined as a northern (90–30° N), tropical (30° S–30° S), and southern (90–30° S) section. As there are no long-term time series at the tropopause for mean AoA calculation available, in the course of the work in Wagenhäuser et al. (2022), the tropical ground time series was used, shifted by an individual constant (t_{xi}) for every entry region (derived time shifts for NH extratropical, tropical, and SH extratropical entry region are listed in Wagenhäuser et al., 2022). By extending the equations by Volk et al. (1997) for a quadratically increasing tracer, mean AoA with multiple entry regions can be expressed as followed

$$\Gamma(\vec{x},t)_{1,2} = t - \lambda + t_m(\vec{x},t) + \frac{b}{2c} \pm \sqrt{(t - \lambda + t_m(\vec{x},t) + \frac{b}{2c})^2 - \frac{a + bt + ct^2 + t_m(\vec{x},t) * (b + 2ct) - \chi(\vec{x},t)}{c} - \sum_{i=0}^{n-1} [f_i(\vec{x},t) * t_{xi}^2]} \tag{2.3}$$

with the weighted mean time shift $t_m(\vec{x},t) = \sum_{i=0}^{n-1}(f_i(\vec{x},t) * t_{xi})$ and λ represents the ratio of moments. This method is hereafter referred to as the exTR-TR-method (extra-tropical and tropical method) whereas the method using only tropical input hereafter is referred to as TR-only method.

The methods are compared using observational data of SF_6 from different measurement campaigns. Further, results were corrected for mesospheric loss with a correction function given in Leedham Elvidge et al. (2018). Maximum absolute differences between the mean AoA derived from the exTR-TR and TR-only methods were about 0.31 years in the NH and 0.42 years in the SH with the largest difference at mid- to high-latitudes close to the tropopause. The TR-only method derived negative mean AoA value near the tropopause down to about -0.54 years. The exTR-TR method has reduced the amount of negative mean AoA values near the tropopause. Mean AoA derived using our new exTR-TR method thus appears physically reasonable even close to the tropopause.

As with the Cl_y comparison, we can also compare the mean AoA in the NH and SH based on both campaigns PGS and SouthTRAC. For this purpose, observations from the first phase of SouthTRAC and the second phase of PGS were used, which have a high seasonal overlap. Mean AoA results of both hemispheres were binned into $\Delta\Theta$ – equivalent latitude bins (5 K – 5°), considering only bins with at least five data points. Figure 2.12 and 2.13 show the distribution of mean AoA using the exTR-TR method and the old TR-only method for both campaigns and the difference between them, respectively. With the new exTR-TR method (Fig. 2.12), the NH mid-latitude lowermost stratosphere reveals overall higher mean AoA values than in the SH up to around 60 to 65 K of $\Delta\Theta$ with, on average 0.5 ± 0.3 years older air in the NH than in the SH. $\Delta\Theta$ levels above show a different pattern with older air in NH mid-latitudes up to 55° (around 0.7 ± 0.4 years difference), but older air in the SH polewards of 55° (reaching values of 2.1 years difference). These findings indicate a more confined air mass which descends inside the SH vortex with a strong gradient towards the mid-latitudes. In the NH, however, descending old air is mixed with younger air from the lowermost stratosphere of the mid-latitudes. Using the old TR-only method (Fig. 2.13), the pattern in the lower stratosphere above around 60 to 65 K is quite similar. However, a less clear picture is obtained below these levels with bins slightly positive or negative in mean AoA. The TR-only method disregards the inter-hemispheric gradient in SF_6 mixing ratios. As a result, mean AoA values are young biased in the NH and old biased in the SH. These biases mask inter-hemispheric differences in mean AoA in the lowermost stratosphere detected by the new exTR-TR method.

Comparing inter-hemispheric differences of mean AoA using the exTR-TR method (Fig.

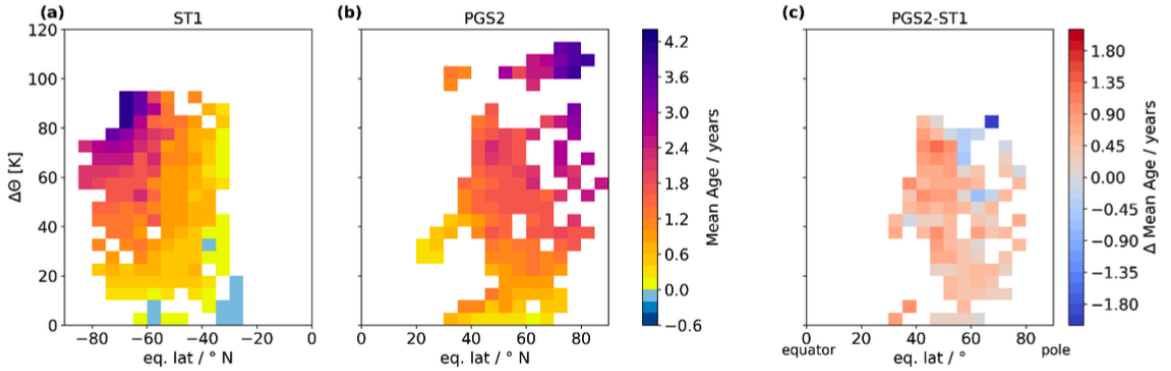

FIGURE 2.12: Comparison of exTR-TR method derived mean AoA latitude-altitude distributions during SouthTRAC phase 1 (a) and PGS phase 2 (b). The hemispheric difference based on these two campaign phases is shown in panel (c). Altitude is given in ΔΘ. Horizontally, data are sorted by eq. lat. The figure is taken from Wagenhäuser et al. (2022)

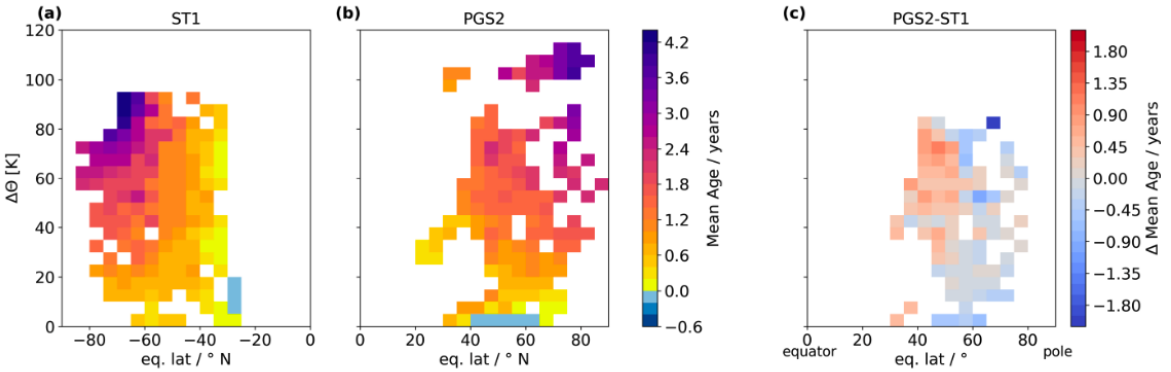

FIGURE 2.13: Same as Fig. 2.12 but using the TR-only method. The figure is taken from Wagenhäuser et al. (2022).

2.12 (c)) and the TR-only method 2.13 (c)) with the inter-hemispheric difference of Cl_y (Fig. 2.11), a greater similarity between the TR-only method based inter-hemispheric difference and the inter-hemispheric difference in Cl_y can be found. Similar to the differences in mean AoA below around 60 to 65 K of ΔΘ, differences in Cl_y are only marginal with slightly positive and negative values of Cl_y. The connection is in the determination of Cl_{total}, which is needed for the calculation of Cl_y via the methods used here (see section 2.3.1 for the semi-direct and indirect determination of Cl_y). The determination of Cl_{total} in the stratosphere depends on tropospheric time trends of the chlorinated substances and on calculated mean AoA to estimate the stratospheric mixing ratios without any chemical degradation. Thus, Cl_y from the difference of Cl_{total} and CCl_y benefits indirectly from more accurate mean AoA values. Mean AoA derived from the ExTR-TR method show a clear pattern below about 60 K of ΔΘ with older air in the NH. It can be assumed that the inter-hemispheric difference is more pronounced below about 60 K of ΔΘ than is assumed in Jesswein et al. (2021), where Cl_y (section 2.3.3 and 2.4.2) was derived using mean AoA with the TR-only method. In future analyses of the distribution of Cl_y, the new method with consideration of the tropical as well as the extra-tropical transport should be considered.

2.5 Stratospheric bromine - global seasonal distribution of Br-VSLS

The following sections summarize the concepts, methods, data, and key results that are published in detail in:
Jesswein, M., Fernandez, R. P., Berná, L., Saiz-Lopez, A., Grooß, J.-U., Hossaini, R., Apel, E. C., Hornbrook, R. S., Atlas, E. L., Blake, D. R., Montzka, S., Keber, T., Schuck, T., Wagenhäuser, T., and Engel, A.: *Global seasonal distribution of CH_2Br_2 and $CHBr_3$ in the upper troposphere and lower stratosphere*, Atmos. Chem. Phys., Atmos. Chem. Phys., 22, 15049–15070, 2022, DOI: https://doi.org/10.5194/acp-22-15049-2022

2.5.1 Expansion of the data

The idea to investigate the global distribution of the two largest representatives of the short-lived brominated substances CH_2Br_2 and $CHBr_3$ was initiated by a previous publication from our working group. In the work of Keber et al. (2020), aircraft measurements of Br-VSLSs with the GhOST-MS at the tropopause and lowermost stratosphere in NH mid-latitudes to high-latitudes during winter and late summer to early autumn were analyzed. Mixing ratios of $CHBr_3$ were systematically higher at the extratropical tropopause than those at the tropical tropopause. CH_2Br_2 exhibited a similar but less pronounced seasonality. In addition, the increase was more pronounced in winter with increased lifetimes at higher latitudes. The question of how the distributions are in the other seasons and on the SH remained open. The SouthTRAC campaign further expands the data basis of the GhOST-MS measurements towards the SH, but still leaves some large gaps in seasonality. These seasonal gaps were filled with additional measurements from other aircraft campaigns. All missions and their flight tracks are displayed in Figure 2.14, with the already mentioned mission PGS (purple flight tracks) and SouthTRAC (orange flight tracks). In the following, we go into the additional measurements.

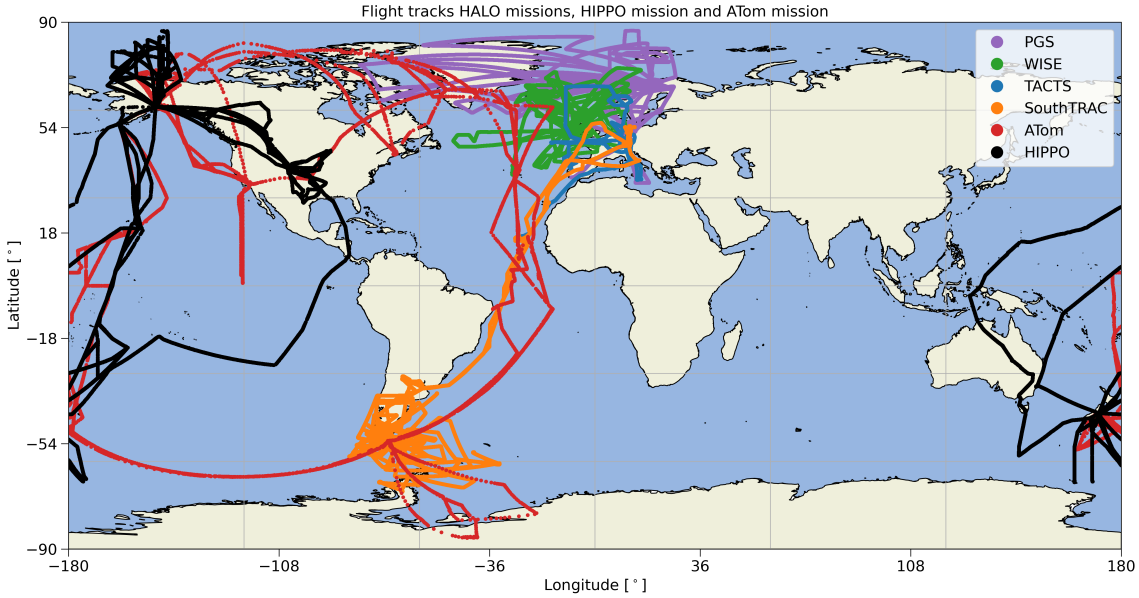

FIGURE 2.14: Flight tracks of the HALO missions TACTS (blue), WISE (green), PGS (purple), and SouthTRAC (orange) as well as flight tracks of the HIPPO mission (black) and ATom mission (red). The figure is taken from Jesswein et al. (2022).

Further HALO missions, which are included here, are the TACTS (Transport and Composition in the Upper Troposphere/Lowermost Stratosphere) mission and the WISE (Wave-driven ISentropic Exchange) mission. TACTS was conducted in August and September 2012 with flights covering an area from Cabo Verde islands to the Norwegian archipelago (Fig 2.14, blue flight tracks). The base of the mission was Oberpfaffenhofen (Germany). Flights of the WISE campaign were between September and October 2017, mainly conducted from Shannon (Ireland). Observations from WISE are from the Atlantic Ocean and western Europe (Fig. 2.14 green flight tracks). The GhOST-MS was operated in NCI mode during both campaigns similar as it was done during the PGS campaign. Local tropopause information for both campaigns was derived using the CLaMS model with underlying meteorological fields from ERA-Interim reanalysis of ECMWF (Dee et al., 2011).

In addition to the HALO missions, another two missions were added. The HIPPO (HIAPER Pole-to-Pole) mission and the ATom (Atmospheric Tomography) mission, both with flights in a broad latitudinal range in the NH and SH. The HIPPO mission was split into seasonal segments, which took place in January 2009 (HIPPO–1), October to November 2009 (HIPPO–2), March to April 2010 (HIPPO–3), June to July 2011 (HIPPO–4), and August to September 2011 (HIPPO–5), with a repeated flight pattern of altitude cross sections over the Pacific Basin and North American mainland (Wofsy, 2011) (Fig. 2.14 black flight tracks). As given in the name of the mission, the NSF/NCAR High-performance Instrumented Airborne Platform for Environmental Research (HIAPER) Gulfstream V (GV) aircraft was used for the measurements. For the analysis of CH_2Br_2 and $CHBr_3$, data from two whole air samplers (WASs) were used. The University of Miami operates the Advance Whole Air Sampler (AWAS). Air samples were collected in stainless steel canisters (Atlas, 2016). In addition, the NOAA Whole Air Sampler (NWAS) was installed in HIAPER, which stores air samples in glass flasks. Subsequently, the air samples were analysed in ground-based laboratories with GC-MS systems. Results from both laboratories were provided on scales consistent with NOAA/ESRL ground-based station results (Hossaini et al., 2013; Hossaini et al., 2016).

The ATom mission consists of four sub-missions, conducted in July to August 2016 (ATom–1), January to February 2017 (ATom–2), September to October 2017 (ATom–3), and April to May 2018 (ATom–4). Each sub-mission started and ended in Palmdale (California, USA) with the route to the western Arctic, south to the South Pacific, east to the Atlantic, and north to Greenland, returning across central North America using the NASA DC-8 aircraft, which can reach an altitude of around 12 km (Wofsy et al., 2021; Thompson et al., 2022) (Fig. 2.14 red flight tracks). Measurements of two WAS and one in-situ instrument were used. The University of California – Irvine (UC-Irvine) research group operated a whole air sampler (hereafter referred to as WAS), storing air in stainless steel canisters. Air samples were analysed afterwards using GC with flame ionization detection (FID), ECD, and MS (Barletta et al., 2019). In addition, the NOAA/GML's Programmable Flask Package Whole Air Sampler (PFP) was operated using glass flasks with subsequent analysis of the samples at the NOAA's Global Monitoring Division laboratory for trace gases by GC-MS. During the ATom mission, the NCAR Trace Organic Gas Analyzer (TOGA) was operated in addition, which is an in-situ instrument with a GC-MS system (Apel et al., 2015), similar to the GhOST-MS. The two WAS and the TOGA instrument generally show a good correlation and consistency in mole fractions for CH_2Br_2 and $CHBr_3$, based on the data that was taken at about the same time (Asher et al., 2019). For both, HIPPO and ATom, local tropopause information and equivalent latitude were derived using CLaMS with underlying ERA-5 reanalyses, like for PGS and SouthTRAC.

2.5.2 TOMCAT and CAM-Chem model simulations

The observational distribution was compared to model simulations of two models. In collaboration with Ryan Hossaini (Lancaster University, Lancaster, UK), the distribution of the two Br-VSLS was simulated using the TOMCAT (Toulouse Off-line Model of Chemistry And Transport) model for the period of the measurement campaigns (2009 to 2019). TOMCAT is a Eulerian offline three-dimensional chemistry transport model (CTM) (Chipperfield, 2006; Monks et al., 2017). A hybrid vertical sigma – pressure ($\sigma - p$) coordinate with 60 levels up to around 60 km is used by the model and the horizontal resolution of the model was set to $2.8° \times 2.8°$ (latitude $\times$ longitude). The necessary meteorological input fields for the simulation with the TOMCAT model are taken from the ECMWF ERA-5 reanalysis (Hersbach et al., 2020). The internal time step of the model was 30 min. Based on that, monthly means were generated for this study. Further, the model configuration reads an offline monthly varying climatological OH concentration field, developed for the TransCom-CH_4 project (Patra et al., 2011).

The second model used in this study is the CAM-Chem (Community Atmosphere Model with Chemistry, version 4) model, the atmospheric component of the NCAR Community Earth System Model (CESM) (Lamarque et al., 2012), in collaboration with Rafael P. Fernandez (FCEN-UNCuyo, Mendoza, Argentina). CAM-Chem is a three-dimensional chemistry climate model (CCM). The WACCM (Whole Atmosphere Community Climate Model) physics module for the stratosphere is included, and it uses the chemical mechanism of MOZART (Model for OZone and Related chemical Tracers) with different possibilities of complexity for tropospheric and stratospheric chemistry. Further, a detailed treatment of tropospheric Br-VSLS sources and chemistry is included (described in Fernandez et al., 2014; Fernandez et al., 2017). The model has 56 hybrid vertical levels up to around 40 km and the horizontal resolution was set to $0.96° \times 1.25°$ (latitude $\times$ longitude). NASA Goddard Global Modeling and Assimilation Office (GMAO) GEOS5-generated meteorology fields are used for CAM-Chem. The model simulated output in 5 min steps, however, monthly means of the tracers are used for this study. Like for TOMCAT, model results are available from 2009 to 2019.

One of the main difficulties in modeling halogen chemistry in the atmosphere is describing the sources of organic source gases, whose global emission levels and distributions are difficult to determine because of their large geographic and temporal variability. There are several emission scenarios for Br-VSLS, either being "bottom-up" scenarios, where conclusions about emissions are drawn from surface atmospheric and oceanic measurements, or "top-down" scenarios, where emission inventory are based on parameters observed in the atmosphere, e.g. from aircraft measurements. Keber et al. (2020) compared different emission scnearios, including the one of Warwick et al. (2006) (top-down), Liang et al. (2010) (top-down), Ordóñez et al. (2012) (tow-down), and Ziska et al., 2013 (bottom-up). They concluded that no scenario was able to capture the tropical and extratropical values from their observations, but with the Ordóñez et al. (2012) scenario showing an overall good agreement, especially for CH_2Br_2. Thus, in this analyses, both models are using the Ordóñez et al. (2012) scenario.

Briefly described, the Ordóñez et al. (2012) scenario used observations of different aircraft missions. These campaigns are the same as in the Liang et al. (2010) scenario, which are the PEM-Tropics (A and B), TRACE-P, INTEX (A and B), TC4, ARCTAS, STRAT, Pre-AVE and AVE missions (Liang et al., 2010), but in addition, the NASA POLARIS and SOLVE mission are included (Ordóñez et al., 2012). In the tropics (20° S–20° N), the VSLS emissions are weighted towards the concentration of chlorophyll-*a* (chl-*a*). Several studies found a correlation of chl-*a* and water bromoform in open ocean water. Chl-*a* thus has been used as a proxy for oceanic bio-productivity (Ordóñez et al., 2012; Hossaini et al., 2013). A monthly-varying

satellite chl-*a* climatology was used which allows some seasonality in the magnitude of the $CHBr_3$ and CH_2Br_2 emission fields (Hossaini et al., 2013). Outside the tropics, separated into 20°–50° and above 50°, a constant ocean sea flux was assumed with a factor of 2.5 larger in the coastal emission to the open ocean emission (Ordóñez et al., 2012). As an example, Fig. 2.15 illustrates the resulting global emission field of CH_2Br_2 in September (global emission field of $CHBr_3$ for September displayed in Fig. B.2 in the Appendix).

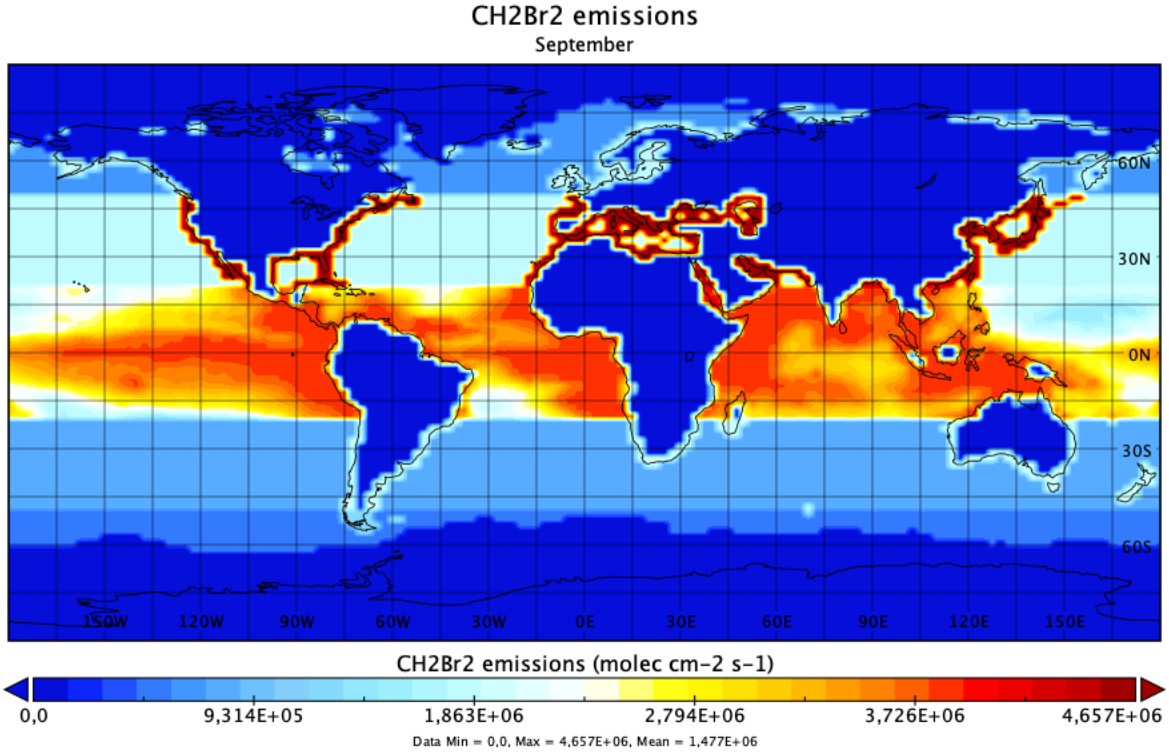

FIGURE 2.15: Global emission field ($molec/(cm^2s^1)$) of CH_2Br_2 estimated by Ordóñez et al. (2012) for September.

2.5.3 Br-VSLS seasonality in the UTLS and comparison limitations

This section presents a summary of the results of the Br-VSLS distribution based on the before mentioned observations and model results. For a comprehensive discussion of all the results, see Jesswein et al. (2022). For the investigation of the seasonal distribution of the Br-VSLS, we combined the measurements from the different missions. Tegtmeier et al., 2020 recently speculated a small positive trend in tropical Br-VSLS between 1979 and 2013 of 0.017 ± 0.012 ppt Br per decade. However, in this analysis, we did not consider a trend in Br-VSLS. The combined data set was split by season (DJF: December, January, February; MAM: March, April, May; JJA: June, July, August; SON: September, October, November). Likewise, this was done for the model data. Only model data for the years and month, for which observations are available, have been taken into account for the comparison.

Altitude-latitude cross sections

On a global scale, observations and model results were analysed in an altitude-latitude cross section for every season. Observational and model data are binned in 10° latitude intervals from 90° S to 90° N and vertically in pressure intervals between 1000 hPa and 50 hPa. The bin size decreases logarithmically with increasing altitude. This results in bin sizes of 180 hPa to

8.5 hPa, which corresponds to an altitude resolution of around 1.3 km. The altitude-latitude cross section of the four seasons from observations, model results from TOMCAT and CAM-Chem, and the difference between the respective model results and observations, are shown in Figure 2.16 for CH_2Br_2 and 2.17 for $CHBr_3$. In the following, we will discuss only some key aspects regarding the distribution of CH_2Br_2 and $CHBr_3$.

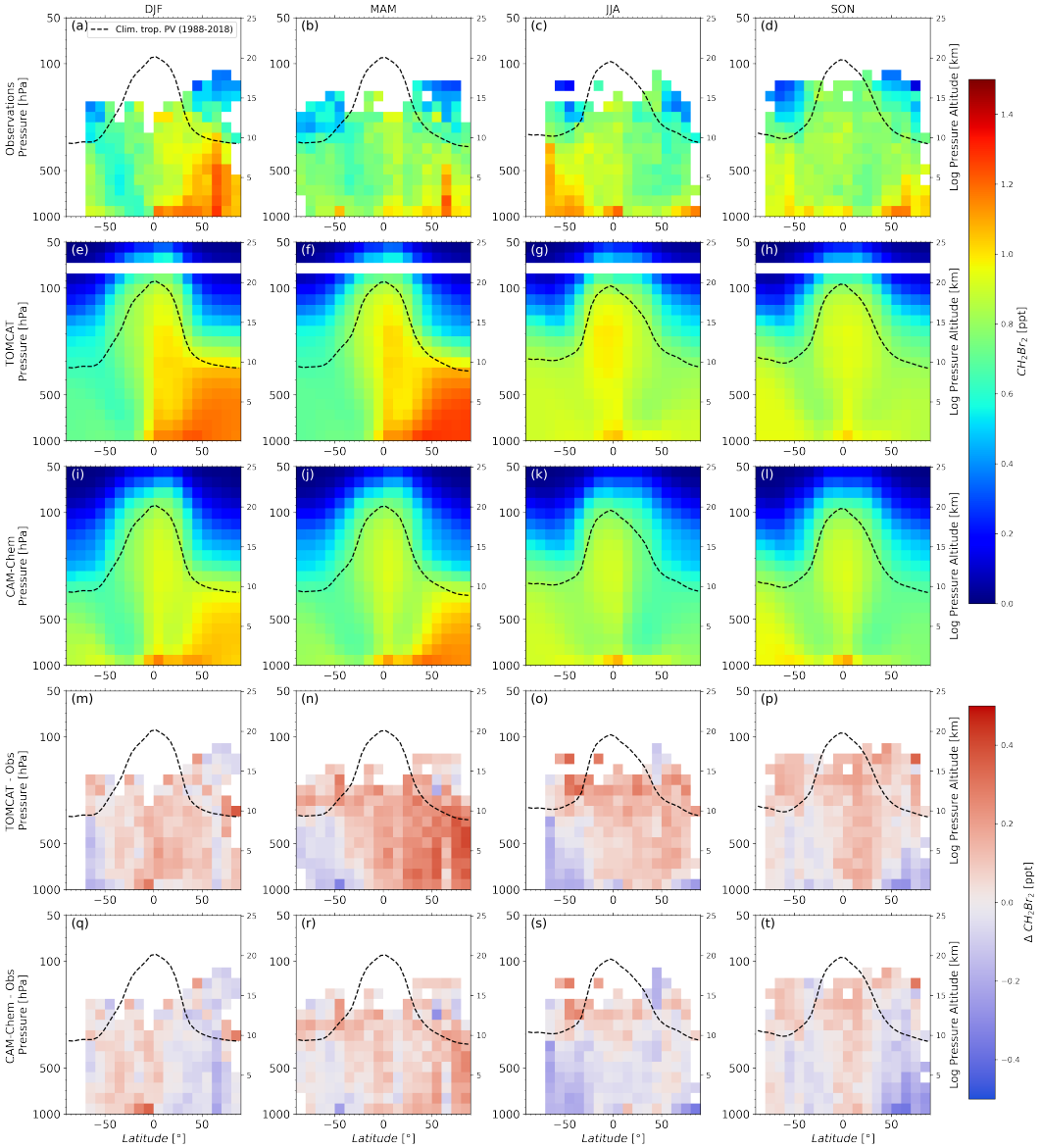

FIGURE 2.16: Zonal mean distributions of CH_2Br_2 as a function of latitude and pressure. The data are separated by season. The top row (a–d) shows observational data. The second and third row (e–h and i–l) show model results of TOMCAT and CAM-Chem, respectively. The fourth and fifths row (m–p and q–t) show differences between the respective model and the observations. The dynamical tropopause (dashed lines) has been derived from the ERA-Interim reanalysis, providing a climatological (1988–2018) zonal mean tropopause. The figure is taken from Jesswein et al. (2022).

The tropospheric distribution of CH_2Br_2 shows a clear seasonality in both hemispheres with largest mixing ratios in hemispheric winter, reaching almost up to the tropopause at high-latitudes. Mixing ratios are lowest in hemispheric summer. The mixing ratios are generally larger in the NH, probably caused by more coastal regions and thus more source

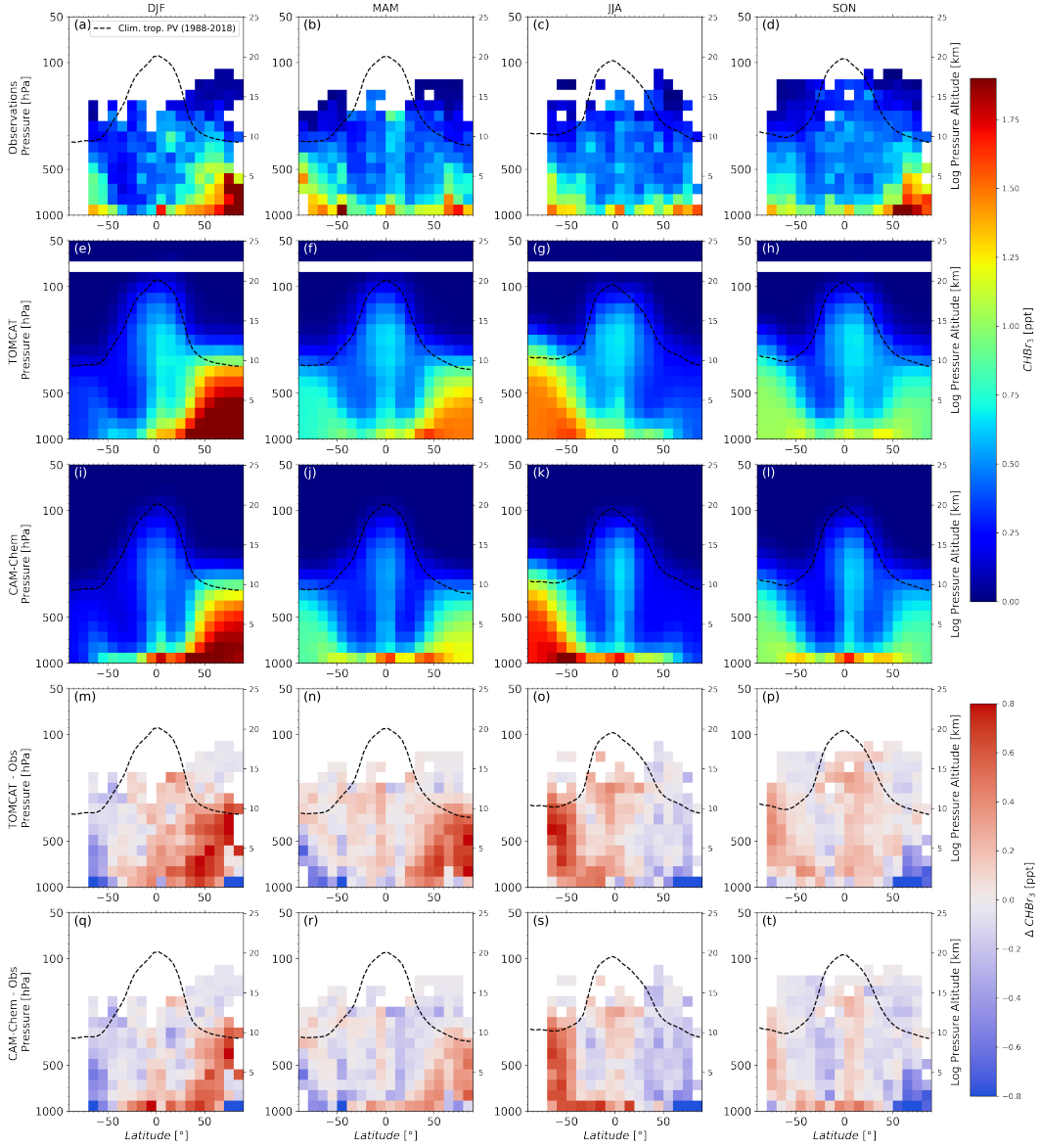

FIGURE 2.17: As in Fig. 2.16 but for $CHBr_3$. The figure is taken from Jesswein et al. (2022).

regions. In the lowermost stratosphere, the seasonal distribution of CH_2Br_2 shows somewhat greater differences in hemispheric autumn and spring. The distribution in hemispheric spring is quite similar. However, the distribution in hemispheric autumn shows bigger differences with lowermost stratospheric mixing ratios by up to 0.3 ppt smaller in the SH. The Ex-UTLS exhibits an influx of tropospheric air (flushing) in the NH summer to early autumn (e.g. Hoor, Fischer, and Lelieveld, 2005; Bönisch et al., 2009, and section 1.2.1). This is revealed by the observation of CH_2Br_2 in SON with elevated mixing ratios in the NH lowermost stratosphere. Mixing ratios in MAM in the SH lowermost stratosphere do not show an equivalent flushing of the SH lowermost stratosphere. This distribution difference may be an indication of the different strength of tropospheric air mixing into the lowermost stratosphere of the two hemispheres. Support for this assumption is provided by e.g. Konopka et al. (2015), who diagnosed an asymmetry of the NH and SH subtropical jets as transport barriers. The NH subtropical jet in NH summer showed the strongest weakening (see Fig. 1 and references in Konopka et al., 2015).

The distribution of the SH lowermost stratosphere are best presented in spring and autumn with observations up to high-latitudes and well into the lowermost stratosphere, but data coverage is still not as good as in the NH lowermost stratosphere. Unfortunately, observations in SH autumn (MAM) show larger differences between those from the TOGA instrument and the two whole air samplers, which could be tracked down to two flights of the ATom–4 mission. This is displayed in Fig. 2.18. Only the MAM distribution is shown, but in addition to using all data (a), the distribution is also shown using only TOGA measurements from ATom (b) or only WAS and PFP observations from ATom (c). Large differences can be seen in the SH lowermost stratosphere, although the remaining distribution looks similar. Mixing ratios are larger and in the range of around 0.4–0.8 ppt including only TOGA data from ATom (Fig. 2.18b). This would suggest a flushing of the lowermost stratosphere similar to that in northern hemispheric autumn (e.g. Bönisch et al., 2009). Mixing ratios are much smaller when using WAS and PFP data (Fig. 2.18c), below around 0.4 ppt. This would indicate a strong isolation of the SH lowermost stratosphere, which would be in agreement to the finding of Shuckburgh, d'Ovidio, and Legras (2009), who investigated a strong seasonal cycle in the strength of the barriers at the subtropical jet, where mixing follows a mostly zonal pattern and the subtropical jet acts as a barrier in SH autumn. There is no clear explanation of the differences between the in-situ instrument and the WASs observation during ATom–4 yet. Thus, on the basis of these observations it is not possible to make a conclusive statement about the strength of the transport in the autumn lowermost stratosphere of the SH.

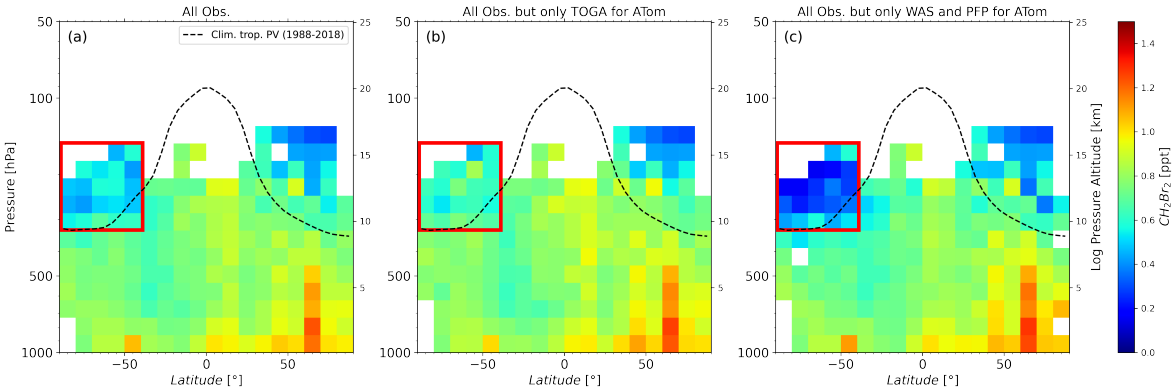

FIGURE 2.18: Zonal mean distribution of CH_2Br_2 for March, April, and May. Panel (a) presents the distribution of CH_2Br_2 as in Fig. 2.16, in (b) data from all missions were used, but only TOGA observations from ATom were included, and in (c) data from all missions were used, but only WAS and PFP observations from ATom were included. The red rectangle indicates the region where observations from different techniques differed substantially from one another. The figure is taken from Jesswein et al. (2022).

Comparison of model results and observations show positive and negative bias dependent on season and latitude. CH_2Br_2 model results show a pronounced seasonality in the NH, although largest values were indicated in spring instead of winter. This leads to a larger overestimation in MAM in the NH, much larger in TOMCAT than in CAM-Chem. Both models underestimate NH high-latitudes near-ground mixing ratios of CH_2Br_2 in summer and autumn, strongest in SON. Hossaini et al. (2016) showed a comparison of different models and ground-based stations in which the models do not reproduce the seasonality at coastal stations such as Mace Head (Ireland). Observations used in this thesis are predominantly over open ocean and coastal regions (e.g. with near shore basis during WISE and SouthTRAC) and may have similar near-surface signatures to coastal stations as in Hossaini

et al. (2016). Both models do not show a pronounced seasonality of CH_2Br_2 in the SH and thus underestimate the elevated mixing ratios in southern hemispheric winter (JJA). The Ordóñez et al. (2012) emission estimates are based on aircraft campaigns and some available observations in the marine boundary layer, most of which are in the NH. Issues regarding the emission flux estimates in the SH are thus consequences of missing aircraft observations in the SH (especially south of 40° S for all seasons) (Ordóñez et al., 2012). In addition, the Ordóñez et al. (2012) emission inventory does not consider Br-VSLSs originating from sea ice regions, which are possible sources according to, e.g., Abrahamsson et al. (2018).

The observational distribution of $CHBr_3$ shows larger variability and a less pronounced seasonality. $CHBr_3$ is much shorter in lifetime than CH_2Br_2 (8–23 days compared to 80–890 days). Jia et al. (2019) linked larger mixing ratios to regions of convergence or low wind speeds and the impact of localized elevated emissions varies significantly, making it difficult to interpret the distribution. Having this in mind, the distribution in the NH shows overall larger mixing rations in autumn and winter than spring and summer. In the SH, the seasonality is not very pronounced with only slightly smaller mixing ratios in summer, although missing observational data at high-latitudes limit the examination of the seasonal distribution, especially in SH summer and winter. Nonetheless, the less pronounced seasonality in the SH is in good agreement with findings of Hossaini et al. (2016), where ground-based NOAA/GML measurements from Cape Grim (Tasmania, Australia) and the Palmer Station (Antarctica), on the same scale as the aircraft measurements e.g. from PFP, also show a less pronounced seasonality. Lowermost stratosphere distributions in both hemispheres look similar with very low mixing ratios close to zero, which is because of the shorter lifetime of $CHBr_3$.

Both models generally capture the tropospheric seasonality on both hemispheres. Near-ground mixing ratios may not be representative and thus comparable to model results, as these are largely from coastal areas. The high-latitudes of both hemisphere were underestimated in summer and autumn with up to 0.6 ppt differences to the model results in the SH and up to 0.9 ppt in the NH. Winter and spring of both hemisphere were overestimated by up to 0.8 ppt (excluded the larger differences at near-ground). Model estimates of TOMCAT and CAM-Chem overall agree well within the lowermost stratosphere of both hemispheres.

Upper-tropospheric latitudinal distribution

The distributions of the two major Br-VSLS were also investigated in the upper troposphere, as air can be transported across the extratropical tropopause into the stratosphere (e.g. Gettelman et al., 2011). For this, observational and model data in the 10 K range below the local tropopause were compared. Data have been separated into low-latitudes (0–30°), mid-latitudes (30–60°), and high-latitudes (60–90°) for both hemispheres. The results of CH_2Br_2 and $CHBr_3$ for all seasons and latitude ranges can be found in Table 1 and 2 in Jesswein et al. (2022). As an example for hemispheric winter, the mixing ratios for CH_2Br_2 and $CHBr_3$ are shown graphically in Figure 2.19 (figures of the other seasons can be found in the supporting information of Jesswein et al. (2022)).

The upper-tropospheric distribution of CH_2Br_2 shows a similar seasonality in both hemisphere with larger mixing ratios in winter and spring and smaller mixing ratios in summer and autumn. The tendency of increased tropopause mixing ratios with increased latitude, due to the increase in lifetime with latitude as photochemical breakdown becomes slower with higher latitudes especially during winter, was found both in the NH and SH and confirms the findings of Keber et al. (2020) at least in the NH. In all seasons the mixing ratios are larger at NH mid- and high-latitudes than at the SH mid- and high-latitudes, reflecting the difference in the ratio of ocean and land mass of the NH and SH and thus the size of coastal areas. Both models quantitatively reproduce the larger CH_2Br_2 mixing ratios in

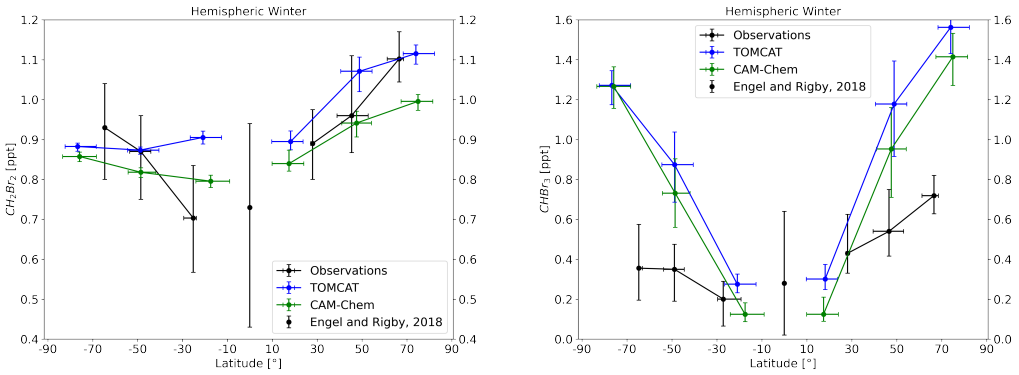

(A) (B)

FIGURE 2.19: Latitude cross section of tropopause representative mixing ratios of CH_2Br_2 (A) and $CHBr_3$ (B) using all observation (black) and model results (blue for TOMCAT and green for CAM-Chem) for both hemispheres in winter. Data are binned into three latitude bins for each hemisphere: high-latitudes (90°–60°), mid-latitudes (60°–30°), and low-latitudes (30°–0°) and only for data within the 10 K below the dynamical tropopause. Latitudinal position of observational and model bins may differ due to different spatial data coverage of observations and models. Also included are the reference mixing ratios for the tropical tropopause (Engel and Rigby, 2018). The figure is taken from Jesswein et al. (2022).

hemispheric winter and spring and smaller mixing ratios in summer and autumn at mid- and high-latitudes. Low-latitude mixing ratios are less well captured by the models. TOMCAT estimates are generally larger than CAM-Chem estimates, which could be due to differences in transport and the efficiency of the photochemical decomposition in the models when using the same emission scenario. Overall, CAM-Chem estimates are closer to the observations with exceptions in SH winter and spring mid- and high-latitudes.

Upper-tropospheric distributions of $CHBr_3$ are more variable with a less clear seasonality compared to CH_2Br_2, especially in the SH. In the NH, mixing ratios show an increase with latitude, most pronounced in winter and spring. Mixing ratios dip down in NH summer mid-latitudes, which can also be seen in SH spring. In all other southern hemispheric seasons, mixing ratios increase with latitude, strongest in SH summer. For both models, mixing ratios increase with latitude for almost all seasons with the largest values in hemispheric winter and spring. Only in hemispheric summer do values decrease from low- to mid-latitudes. Mid- and high-latitude mixing ratios are highly overestimated by the model in hemispheric winter. In addition, high-latitude values are overestimated in spring and autumn. Although CAM-Chem upper-tropospheric distributions are similar to TOMCAT distributions, they show smaller values for all latitudes and are generally closer to observational data. An exception can be found in SH high-latitudes in summer, where observational mixing ratios are largest and model estimates are smallest. Further, SH high-latitude observations are smallest in winter. As the high-latitude observations are much more limited during these seasons, a certain caution is necessary with regard to their interpretation, and further observations are needed to verify these deviations from model results.

Mid-latitude UTLS vertical profiles

The lowermost stratosphere of both hemispheres has been best sampled in the seasons of autumn and spring (see e.g. Fig 2.16). It was thus possible to take a closer look at the

	Gradients [%/K]			
	Spring		Autumn	
	SH	NH	SH	NH
CH_2Br_2	1.12	1.23	1.27	0.59
$CHBr_3$	2.63	2.97	4.42 [a]	2.25

[a] Gradient from TP to (10–20) K

TABLE 2.2: Vertical gradients across the tropopause in the Northern Hemisphere (NH) and Southern Hemisphere (SH) spring and autumn from tropopause (TP) mixing ratios from the 10 K bin below the dynamical tropopause up to the 20–30 K bin above the dynamical tropopause.

mid-latitude vertical profiles of CH_2Br_2 and $CHBr_3$ during these seasons. For this, the observations were binned in 10 K intervals of Θ up to the tropopause. From 10 K below the local tropopause, data have been binned in $\Delta\Theta$ coordinates, as $\Delta\Theta$ coordinates reduce the variability of the profile near the tropopause and within the lowermost stratosphere (e.g. Keber et al., 2020). Both coordinates were combined by aligning 0 K of $\Delta\Theta$ with the median tropopause in Θ. The mixing ratios are averaged over equivalent latitude* of 40–60° of the respective hemisphere. To keep the key results clear, profiles can be found in Jesswein et al., 2022. Vertical gradients for spring and autumn profiles from tropopause values up to 30 K $\Delta\Theta$ are listed in table 2.2. A steep gradient across the tropopause, e.g. of a tracer of tropospheric origin, can be attributed to a stronger transport barrier, whereas a shallow gradient may reveal transport processes.

The vertical profiles of hemispheric spring look similar with upper tropospheric mixing ratios of CH_2Br_2 close to 1 ppt and decreasing towards the tropopause. Further, lowermost stratospheric profiles of both hemispheres are very similar. The vertical gradients of $CHBr_3$ profiles are larger than for CH_2Br_2 and mixing ratios drop to values close to 0 in both hemisphere at about 30–40 K of $\Delta\Theta$. The vertical profiles of hemispheric autumn differ much more. Larger differences between NH and SH autumn profiles can be found above the dynamical tropopause, where CH_2Br_2 shows a larger vertical gradient up to 30 K of $\Delta\Theta$ in the SH than in the NH (see table 2.2). In fact, the vertical gradient in smallest in NH autumn with 0.59 %/K. The vertical profile of CH_2Br_2 in SH autumn is displayed separately in Figure 2.20. Two more profiles were added in $\Delta\Theta$ coordinates, one profile excluding TOGA observations and one profile excluding WAS and PFP observations. A much steeper gradient is obtained when excluding TOGA observations, supporting the assumption of a strong transport barrier, e.g. the subtropical jet and little exchange between the stratosphere and troposphere at the edges of the jets (e.g. Gettelman et al., 2011). Little change to the profile can be observed when excluding WAS and PFP observations. The larger number of TOGA observations shifts the median towards larger values. However, the gradient is still larger than in the NH, which suggests a larger transport barrier than in the NH. Hemispherical differences are also apparent from the autumn vertical profiles of $CHBr_3$. In the lowermost stratosphere, the vertical gradient is much larger in the SH than in the NH with values going down to almost 0 ppt or even below the limit of detection and thus the gradient can only be derived up to 20 K of $\Delta\Theta$. In contrast, NH lowermost stratospheric values are steadily decreasing and are above 0.02 ppt even at 90 K of $\Delta\Theta$, provided that the observations in the NH contain measurements of the GhOST-MS in NCI mode and the detection limit therefore lower.

The mid-latitude profiles are finally compared to model results of TOMCAT and CAM-Chem. The comparison are shown as a function of $\Delta\Theta$ only and thus from 10 K below the local tropopause and into the lowermost stratosphere. As not all model results contain tropopause information, $\Delta\Theta$ for both models was derived relative to the climatological tropopause. Further, instead of equivalent latitude, geographic latitude was used for the model data. Figure 2.21 shows exemplary the vertical profiles from observations and from the two models TOMCAT and CAM-Chem for hemispheric autumn. Hemispheric spring profiles can be found in Jesswein et al. (2022) and are only briefly discussed here. Mean absolute percentage differences (MAPD) between observational and the respective model profile are listed in table 2.3.

		Spring		Autumn	
		SH	NH	SH	NH
CH_2Br_2	TOMCAT	18	26	25[a]	20
	CAM-Chem	9	17	15[a]	6
$CHBr_3$	TOMCAT	21[b]	69[b]	89[b]	22[b]
	CAM-Chem	26[b]	15[b]	65[b]	26[b]

[a] between 0-40 K of $\Delta\Theta$
[b] between -10-40 K of $\Delta\Theta$

TABLE 2.3: Median absolute percentage differences (%) of to the respective model to the observational mid latitude vertical profiles (40° - 60° eq. lat*) in hemispheric spring and autumn. Vertical profiles from 10 K below the dynamic tropopause to the lowermost stratosphere (if not additionally marked otherwise).

The vertical profiles of CH_2Br_2 of TOMCAT and CAM-Chem in hemispheric spring agree well to the vertical profiles from the observational data. CAM-Chem results are overall closer to the observation on both hemispheres with MAPDs under 20 %, and TOMCAT deviations slightly larger up to 26 %. $CHBr_3$ profiles of the models are in good agreement with the observations below $\Delta\Theta$ of around 40 K. Above, both models estimated complete depletion of $CHBr_3$, whereas observations show values within the range of 0.02–0.04 ppt up to around 90 K of $\Delta\Theta$. Deviations below $\Delta\Theta$ of 40 K are slightly smaller for TOMCAT in the SH but in the NH, TOMCAT shows large deviations of 69 % and CAM-Chem substantially smaller deviation of 15 %.

Vertical profiles in hemispheric autumn are in good agreement in the NH but larger differences can be found in the SH. Both models estimated the NH profiles of CH_2Br_2 well with MAPDs below 20 % with CAM-Chem closer to the observations. In the SH, the models deviate more form the observations, especially in the lowest 40 K above the tropopause with MAPDs up to 25 %. TOMCAT profiles are generally larger in mixing ratios and show larger deviations. Above 40 K of $\Delta\Theta$, there is better agreement between models and observations but with much larger variability in the observational profile, which is probably partly due to the different results of the instruments during ATom–4. The NH $CHBr_3$ profile of TOMCAT is in slightly better agreement to the observations than the profile of CAM-Chem (22 % to 26 %). Both models did not estimate the steep gradient of $CHBr_3$ across the dynamical tropopause, seen in the observational data. Above 20 K of $\Delta\Theta$, a comparison with model profiles was not possible because a missing observational data.

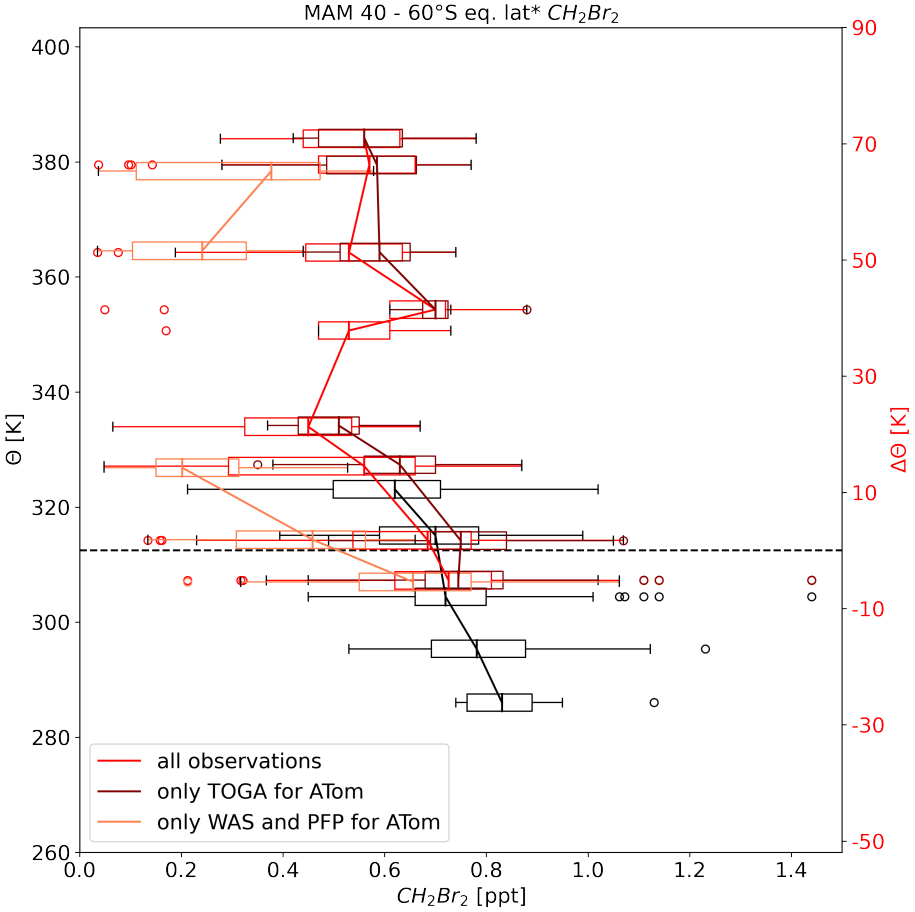

FIGURE 2.20: Vertical profile of CH_2Br_2 for SH autumn. Observations were averaged over 40–60° of equivalent latitude*. Data are displayed as a function of potential temperature for tropospheric values (black) and potential temperature difference to the local tropopause for values from 10 K below the tropopause and above (red). Shown are the medians with the boxes representing the interquartile range (IQR), with whiskers as the 1.5 × IQR, and circles are single observations outside the whiskers (outliers). Profile using all observations is in red, profile using all observation but with only TOGA observations from ATom in dark red, and profile using all observations but with only flask observations in light red. The dashed black line shows the median dynamical tropopause derived from the times and locations of the observation. The figure is taken from Jesswein et al. (2022).

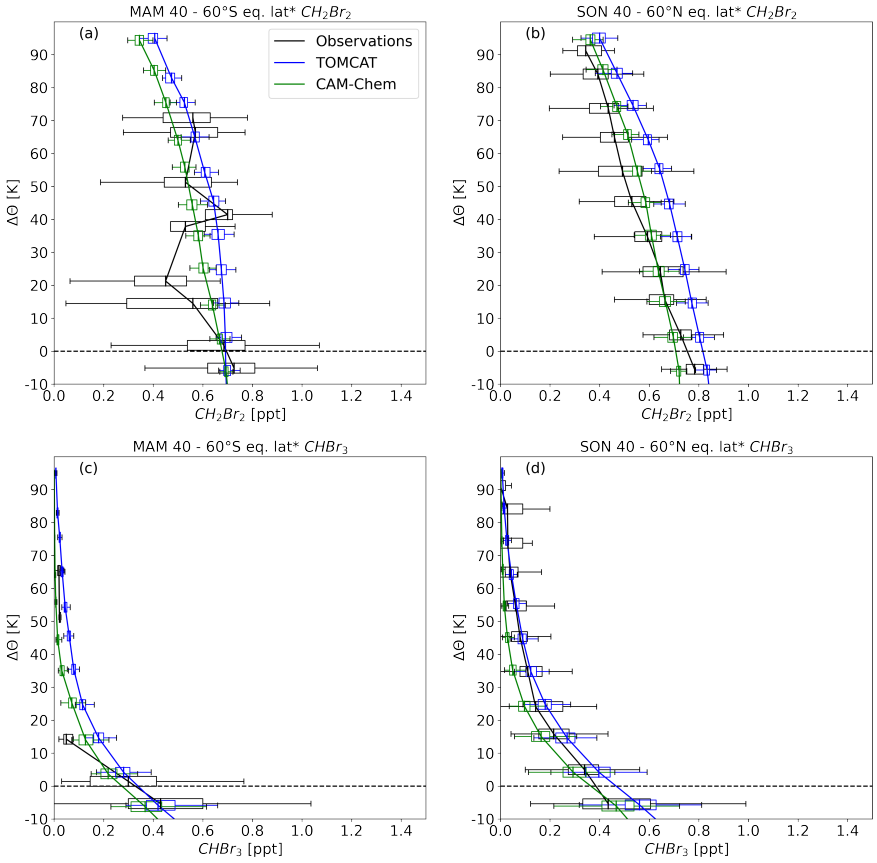

FIGURE 2.21: Hemispheric autumn vertical profiles of (a, b) CH_2Br_2 and (c, d) $CHBr_3$. Observations were averaged over 40–60° of equivalent latitude*. Data are displayed as a function of ΔΘ to the local tropopause (black). Also shown are model results from TOMCAT (blue) and CAM-Chem (green) as a function of ΔΘ to the climatological tropopause. Profiles show medians with the boxes representing the interquartile range (IQR) and whiskers as the 1.5 × IQR. Outliers are not included for a better illustration. The figure is taken from Jesswein et al. (2022).

Chapter 3

Summary and Outlook

3.1 Summary

The aim of this thesis was to draw conclusions about the global distribution of chlorinated and brominated substances based on measurements carried out during aircraft campaigns. The focus is on the area of the upper tropopsphere and lower stratosphere of both hemispheres and the investigation of possible differences in terms of chemical composition and transport aspects. For this purpose, the GhOST instrument on board several aircraft missions of the HALO aircraft was used with the most recent HALO mission SouthTRAC conducted in the period of this thesis, expanding the data base in the Southern Hemisphere. These data have been applied in this work for studies of inorganic chlorine and mean age of air in the respective hemisphere late winter to early spring, resulting in two publications (Jesswein et al., 2021; Wagenhäuser et al., 2022). Further, to study the global seasonal distribution of brominated short-lived substances, observations from the HIPPO and ATom mission were added to the data base with results collated in a third publication (Jesswein et al., 2022). Chronologically, they were published in the order Jesswein et al. (2021), Jesswein et al. (2022), and Wagenhäuser et al. (2022).

In the first publication, inner-vortex inorganic chlorine (Cl_y) was derived and compared in late winter to early spring between the Northern and Southern Hemisphere (Jesswein et al., 2021). Measurements were allocated to the respective vortex, vortex boundary region, and mid-latitudes, using an extended method by Greenblatt et al. (2002). This method uses high resolution N_2O measurements for the air mass classification to detect even small scale features like vortex filaments. The air mass classification works well with strong gradients of the source gases when the classified region changes, but shows its weakness near the tropopause, where the N_2O profiles of the vortex and the mid-latitudes overlap and a distinction is not possible anymore. Cl_y of the Northern and Southern Hemisphere was compared on the basis of GhOST measurements from two HALO campaigns, the SouthTRAC campaign in 2019 and the PGS campaign in 2015/2016. Both campaigns took place during similar seasons, with the SouthTRAC campaign in the Southern Hemisphere and the PGS campaign in the Northern Hemisphere, but with the GhOST-MS operated in different ionization modes. Thus, Cl_y is calculated differently for both campaigns, either semi-directly from the GhOST-MS measurements of the major organic source gases and mean age of air (for SouthTRAC) or indirectly using a correlation adapted from observations of balloon flights in the Arctic polar vortex in 2009 and 2011 (for PGS). Both methods are compared based on SouthTRAC observations. For this, measurements of the GhOST-MS were up-sampled to the time resolution of the GhOST-ECD, using simultaneous accurate measurements of CFC-12 in both channels. Further, mean age of air was derived using SF_6 measurements of the GhOST-ECD, which are used for Cl_y determination. The semi-direct and indirect method agree well, despite the time interval of 10 years and the fact, that the scaled correlation is based on observations in the Northern Hemisphere. In 2019, the Antarctic vortex was weakened and shifted towards the eastern South Pacific and South America

as a result of an uncommon minor stratospheric warming event (e.g. Wargan et al., 2020; Safieddine et al., 2020). Even though this caused a reduction of the ozone hole compared to the previous year, i.e. only 20 % of the 2018 ozone hole in mid-September (Wargan et al., 2020), about up to 50 % of the total chlorine could be found in the inorganic form inside the vortex during SouthTRAC and only 15 % of total chlorine could be found in inorganic form at mid-latitudes below about 390 K of potential temperature. At comparable levels above the tropopause and comparable season in the Northern Hemisphere, only around 40 % of total chlorine was found in inorganic form and roughly 20 % in the mid-latitudes. The difference inside the respective vortex amounts to up 540 ppt more Cl_y in the Antarctic vortex. This difference is substantially larger than reported inter-annual variations published by Strahan et al. (2014). Regarding the difference at lower stratospheric mid-latitudes, Cl_y values were higher during PGS. Closer to the tropopause, difference from calculated Cl_y during SouthTRAC and PGS become smaller so that no hemispherical difference can be seen.

Mean age of air is required for the determination of Cl_y with the given methods (semi-direct and indirect), as it is used to calculate the total amount of chlorine entering the stratosphere. In the second publication, an improved method to derive mean age of air from observational tracer mixing ratios is presented, considering additional extra-tropical input into the stratosphere next to tropical input (exTR-TR method) (Wagenhäuser et al., 2022). This advanced method was compared with the method considering only the tropical input to the stratosphere (TR-only method), which was also used for derived mean age of air in Jesswein et al. (2021). The new exTR-TR method has resulted in fewer negative values near the tropopause compared to the TR-only method. Differences of derived mean age of air between the TR-only and exTR-TR method maximised at about 0.31 years in the Northern Hemisphere and 0.42 years in the Southern Hemisphere. As shown for Cl_y in Jesswein et al. (2021), the SouthTRAC and PGS campaigns were used to investigate inter-hemispheric differences at similar season, but now for mean age in the air. The new exTR-TR method revealed overall older air in the Northern Hemisphere lowermost stratosphere during PGS than in the Southern Hemisphere during SouthTRAC (on average 0.5 ± 0.3 years older). Only above around 65 K of $\Delta\Theta$, the pattern changed with older air at mid-latitudes during PGS, but older air at high-latitudes during SouthTRAC. Larger values of mean age of air in the Northern Hemisphere mid-latitude stratosphere can be associated to mixing with old vortex air, whereas in the Southern Hemisphere there is a distinct separation of vortex and mid-latitudes with strong gradients of mean age of air in between. Differences below around 65 K of $\Delta\Theta$, which can be identified with the use of the exTR-TR method, are not clearly evident in the TR-only method, as it disregards the inter-hemispheric gradient in tropospheric SF_6 mixing ratios. This leads to biases in mean age determination of Northern and Southern Hemisphere. Cl_y can be considered a conservative tracer over a short period of time and correlates with mean age of air. The less pronounced differences in the lowermost stratosphere Cl_y in Jesswein et al. (2021) from the SouthTRAC and PGS campaign are thus likewise masked by the biases of mean age of air in both hemispheres. For future Cl_y determination, usage of the exTR-TR method is recommended.

Finally, in the third publication, the global seasonal distribution of the two major short-lived substances CH_2Br_2 and $CHBr_3$ are derived and compared to model results of the TOMCAT and CAM-Chem model (Jesswein et al., 2022). In contrast to the long-lived chlorinated and brominated substances, these short-lived substances are mainly of natural origin and are not regulated under the Montreal Protocol. Their relative contribution to the loss of ozone will rise with the decline of the long-lived substances. To have a seasonal and global perspective of these substances, observational data of four HALO missions (TACTS, PGS, WISE, and SouthTRAC), together with two global scale missions (HIPPO and ATom) were used, leading to a data base for the time period of 2009 to 2019 and with a broad latitude

range in both hemispheres. Focusing on zonal mean distributions, CH_2Br_2 showed a similar seasonality in the troposphere and upper troposphere in both hemispheres with larger mixing ratios in respective winter and spring and smaller mixing ratios in summer and autumn. Mixing ratios are slightly larger in the Northern Hemisphere, in good agreement with larger emissions from more coastal areas in the Northern Hemisphere. $CHBr_3$ showed overall a larger variability and a less clear seasonality, but with more elevated mixing ratios in northern hemispheric autumn and winter, a feature not very pronounced in the Southern Hemisphere. The mixing ratios at the extratropical tropopause are systematically larger than those at the tropical tropopause in both hemispheres at all times of the year. The lower coverage of observational data in the Southern Hemisphere limited the comparison of the UTLS distributions to spring and autumn of both hemispheres. Both substances showed similar lowermost stratospheric distributions in hemispheric spring. In hemispheric autumn, however, larger differences could be found, e.g. with up to 0.3 ppt more CH_2Br_2 in the Northern Hemispheres. Hemispheric spring and autumn were further analysed by mid-latitude vertical profiles up into the lower stratosphere. Again, similar profiles are evident in the hemispheric spring, and profiles in hemispheric autumn differ much more. Southern hemispheric profiles of CH_2Br_2 and $CHBr_3$ decreased more rapidly across the tropopause and into the stratosphere than northern hemispheric profiles. Further, the CH_2Br_2 profile in southern hemispheric autumn shows larger variability. This leads to the assumption that the transport barrier in southern hemispheric autumn is stronger and prevents the flushing of the lowermost stratosphere, an event that occurs in northern hemispheric summer and autumn. Unfortunately, the observational data in southern hemispheric autumn shows larger discrepancies between the instruments during one of the ATom missions and further observations are needed to confirm the hemispheric differences in the respective lowermost stratosphere.

The observed seasonal distribution of CH_2Br_2 was only partly reproduced by the two models. In the Southern Hemisphere, the models did not show a pronounced seasonality of CH_2Br_2. This is probably due to the used emission scenario of Ordóñez et al. (2012), where in the high-latitudes the distribution is presented more homogeneous due to the scarcity of observational data used for deriving the scenario, especially for the southern hemispheric high-latitudes. For $CHBr_3$, both models systematically overestimate hemispheric winter and spring mixing ratios in the free troposphere and slightly underestimate hemispheric summer and autumn. Generally, mixing ratios in the TOMCAT model are larger than in the CAM-Chem model, which could be due to differences in transport and photochemical decomposition efficiency in the models (both models use the Ordóñez et al. (2012) scenario). Model and observational data close to the tropopause agree well for CH_2Br_2 for all seasons and both hemispheres. Modeled mixing ratios of $CHBr_3$ are significantly higher than observed mixing ratios in hemispheric winter mid- and high-latitudes. Especially large deviation from model results are found in southern hemispheric high-latitudes in winter and summer. However, the number of observations is very low at southern hemispheric high-latitudes and do not extend beyond 70° S. More observations are needed for a more meaningful conclusion about the model deviations for that region. Mid-latitude vertical profiles of CH_2Br_2 and $CHBr_3$ from TOMCAT and CAM-Chem agree well with observations, but with CAM-Chem predominantly closer to the observations as TOMCAT results are generally larger than CAM-Chem results. Only the vertical profiles in southern hemispheric autumn were not captured by the models with vertical gradients from the observational data much steeper than modeled gradients. Thus, the models do not show the differences in the hemispheres as seen in the observations for each autumn lowermost stratosphere. Vertical gradients in the hemispheric spring, on the other hand, are more similar to each other.

3.2 Outlook

The Montreal Protocol is one of, if not, the most successful international agreements regarding environmental protection. It has now been in place for more than 30 years, leading to ongoing reduction of long-lived substances that contribute to ozone depletion. The extent of ozone destruction and thus the size of the ozone hole in the hemispheric polar vortex is determined not only by the halogen loading but also by dynamic aspects (e.g., temperature), and both have to be accounted. Observationally derived estimates of Cl_y inside the respective vortex, such as those made in the present work, need to be continued to monitor impacts and compliance with the Montreal Protocol. In addition, continued observations provide a likely better understanding of the ozone hole variation with decreasing halogen loading. Furthermore, differences in Cl_y inside the Arctic and Antarctic vortex, are based on only one winter in each hemisphere. Due to the variations within the Arctic and Antarctic vortices, further sampling over several years would lead to a more meaningful conclusion.

The presented methods for the determination of Cl_y rely on accurate estimations of mean age of air. The new exTR-TR method, presented in this work, accounts for tropical and extra-tropical input into the stratosphere. More realistic values of transport times, especially in the lowermost stratosphere, were derived with this method, compared to the method considering only tropical input into the stratosphere. In Jesswein et al. (2021), the old TR-only method was used, whereas future Cl_y determination should use the new ExTR-TR method.

As long-lived substances decline, unregulated short-lived substances gain importance. The two major brominated VSLS, CH_2Br_2 and $CHBr_3$, with dominant oceanic sources show seasonally varying distributions on both hemisphere, although mixing ratios are slightly larger in the Northern Hemisphere. The number of observations on which this work is based is still substantially smaller in the Southern Hemisphere. Differences that have been shown in the lowermost stratosphere in hemispheric autumn require further investigation for confirmation. The comparison of observed Br-VSLS distribution to model results shows room for improvement for both, transport and chemical processes inside the models as well as refined emission scenarios. Especially for the latter, a stronger consideration of the seasonality of CH_2Br_2 sources in both hemispheres could lead to an improvement, whereas for $CHBr_3$, there is systematically over- and underestimation depending on the season, which masks the strong variability of $CHBr_3$.

An new data set of the major long-lived and short-lived substances is expected from the GhOST instrument on board the planned HALO mission PHILEAS (Probing HIgh Latitude Export of air from the Asian Summer Monsoon), scheduled for 2023. The Asian summer monsoon is thought to be one of the main pathways by which tropospheric air masses move rapidly into the UTLS. A large-scale anticyclonic circulation in the UTLS traps lifted polluted air over Asia. As the circulation becomes weaker and more unstable, the temporally isolated system is disturbed and frequent but irregular eddy shedding occurs, which leads to the transport of polluted air from inside the anticyclone to the extratropical lower stratosphere. One of the key research questions addressed by the group in which I am doing my graduate work is the investigation of the chemical composition during these eddy shedding events as well as the pathways and time scales of transport of halogenated substances from the monsoon anticyclone into the UTLS. In addition, the data from this mission expand the data base for the seasonal distribution of short-lived substances in a geographic area that has not yet been covered. However, as the Southern Hemisphere remains significantly less covered in terms of in situ observations, a mission similar to SouthTRAC is needed for the other seasons and should be the focus of future mission planning.

Appendix A

Scientific background

A.1 Potential temperature

The potential temperature is the temperature an air parcel would have, if brought down to a reference pressure level adiabatically. This is typically the pressure at sea level or 1000 hPa. It can be derived via the equation of entropy of an ideal gas as the entropy does not change during adiabatic processes.

$$\Theta = T * (\frac{p_0}{p})^{\frac{R}{cp}} \tag{A.1}$$

Where T is the ambient air temperature, p_0 the reference pressure (usually 1000 hPa), p the ambient pressure, R the gas constant, and c_p the specific heat capacity.

A.2 Stratospheric transport diagnostic

The given form of the Green's function is equivalent to the analytic expression derived by Hall and Plumb (1994). The age sprectrum is given as:

$$G(z, t') = \frac{z}{2\sqrt{\pi K t'^3}} * \exp(\frac{z}{2H} - \frac{Kt'}{4H^4} - \frac{z^2}{4Kt'}) \tag{A.2}$$

with K being the one-dimensional diffusion coefficient, z the altitude, and H the scale height of the air density. In order to be a correctly defined PDF, the age spectrum must fulfill the normalization condition.

$$\int_0^\infty G(\vec{x}, t, t')\mathrm{d}t' = 1 \tag{A.3}$$

The moments can thus be properly derived. The first moment of the PDF is the mean AoA

$$\Gamma(\vec{x}, t') = \int_0^\infty t' G(\vec{x}, t, t')\mathrm{d}t'. \tag{A.4}$$

and the second moment the variance and thus an estimate of the spread around the mean AoA (width of the age spectrum).

$$\Delta^2(\vec{x}, t') = \frac{1}{2}\int_0^\infty (t' - \Gamma(\vec{x}, t))^2 G(\vec{x}, t, t')\mathrm{d}t' \tag{A.5}$$

Appendix B

Distribution of halogenated trace gases in the UTLS

B.1 Iterative filter procedure for air mass classification

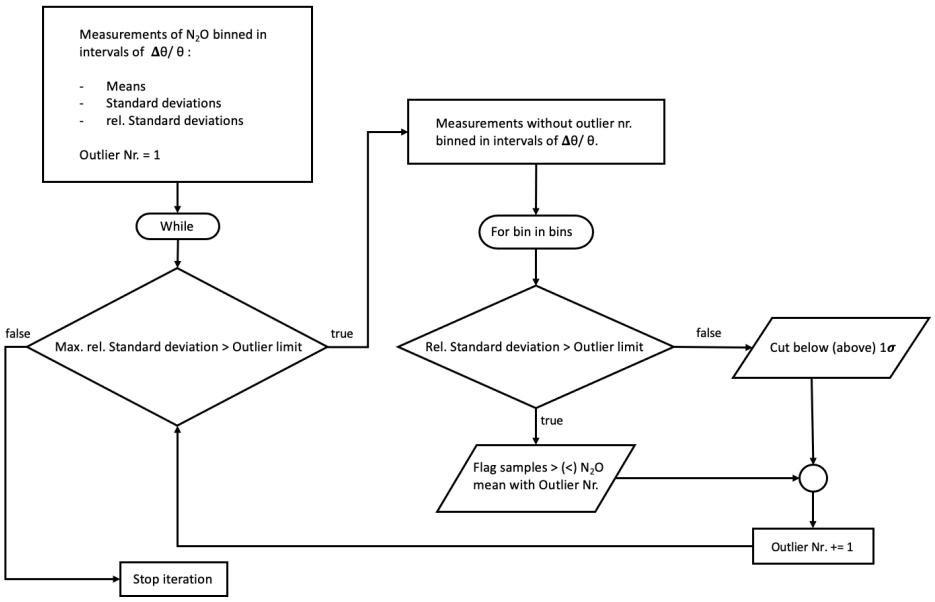

FIGURE B.1: Flowchart for the outlier identification to generate the vortex profile and mid-latitude profile. The figure is taken from the supporting information of Jesswein et al. (2021).

B.2 Up-sampling GhOST-MS measurements

Up-sampling was done by using simultaneous measurement of CFC-12 with the GhOST-MS and GhOST-ECD channels. The correlation between CFC-12 measurements of the two channels for all flights is linear over the whole range of mixing ratios (coefficient of determination of R^2 = 0.968). For each long-lived chlorinated source gas, a linear or polynomial fit is calculated based on the correlation with CFC-12. The fit functions are then used to calculate the up-sampled mixing ratios by using the CFC-12 observations from the GhOST-ECD. Up-sampled mixing ratios are thus on a time resolution of 1 min.

B.3 Ordóñez et al. (2012) scenario

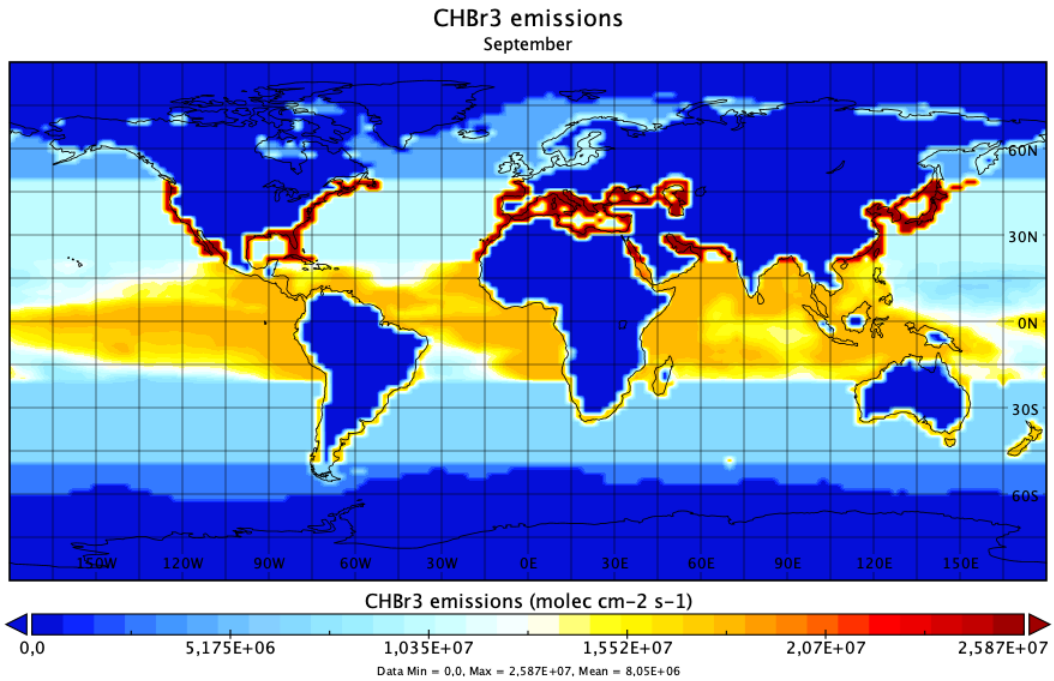

FIGURE B.2: Global emission field ($molec/(cm^2 s^1)$) of $CHBr_3$ estimated by Ordóñez et al. (2012) for September.

Bibliography

Abrahamsson, Katarina et al. (2018). "Organic bromine compounds produced in sea ice in Antarctic winter". In: *Nature Communications* 9.1, p. 5291. DOI: 10.1038/s41467-018-07062-8. URL: https://doi.org/10.1038/s41467-018-07062-8.

Anderson, J. et al. (2000). "Halogen Occultation Experiment confirmation of stratospheric chlorine decreases in accordance with the Montreal Protocol". In: *Journal of Geophysical Research: Atmospheres* 105.D4, pp. 4483–4490. DOI: https://doi.org/10.1029/1999JD901075. URL: https://agupubs.onlinelibrary.wiley.com/doi/abs/10.1029/1999JD901075.

Apel, E. C. et al. (Mar. 2015). "Upper tropospheric ozone production from lightning NO_x-impacted convection: Smoke ingestion case study from the DC3 campaign". In: *Journal of Geophysical Research: Atmospheres* 120.6, pp. 2505–2523. DOI: 10.1002/2014jd022121. URL: https://doi.org/10.1002/2014jd022121.

Asher, E. et al. (2019). "Novel approaches to improve estimates of short-lived halocarbon emissions during summer from the Southern Ocean using airborne observations". In: *Atmospheric Chemistry and Physics* 19.22, pp. 14071–14090. DOI: 10.5194/acp-19-14071-2019. URL: https://acp.copernicus.org/articles/19/14071/2019/.

Atlas, E. (2016). *Advanced Whole Air Sampler (AWAS) for HIAPER. UCAR/NCAR - Earth Observing Laboratory*. DOI: 10.5065/D65X270F.

Ball, W. T. et al. (2018). "Evidence for a continuous decline in lower stratospheric ozone offsetting ozone layer recovery". In: *Atmospheric Chemistry and Physics* 18.2, pp. 1379–1394. DOI: 10.5194/acp-18-1379-2018. URL: https://acp.copernicus.org/articles/18/1379/2018/.

Ball, W. T. et al. (2019). "Stratospheric ozone trends for 1985–2018: sensitivity to recent large variability". In: *Atmospheric Chemistry and Physics* 19.19, pp. 12731–12748. DOI: 10.5194/acp-19-12731-2019. URL: https://acp.copernicus.org/articles/19/12731/2019/.

Ball, W. T. et al. (2020). "Inconsistencies between chemistry–climate models and observed lower stratospheric ozone trends since 1998". In: *Atmospheric Chemistry and Physics* 20.16, pp. 9737–9752. DOI: 10.5194/acp-20-9737-2020. URL: https://acp.copernicus.org/articles/20/9737/2020/.

Barletta, B. et al. (2019). *ATom: L2 Halocarbons and Hydrocarbons from the UC-Irvine Whole Air Sampler (WAS)*. en. DOI: 10.3334/ORNLDAAC/1751. URL: https://daac.ornl.gov/cgi-bin/dsviewer.pl?ds_id=1751.

Barnes, Paul W. et al. (June 2019). "Ozone depletion, ultraviolet radiation, climate change and prospects for a sustainable future". In: *Nature Sustainability* 2.7, pp. 569–579. DOI: 10.1038/s41893-019-0314-2. URL: https://doi.org/10.1038/s41893-019-0314-2.

Birner, T. and H. Bönisch (2011). "Residual circulation trajectories and transit times into the extratropical lowermost stratosphere". In: *Atmospheric Chemistry and Physics* 11.2, pp. 817–827. DOI: 10.5194/acp-11-817-2011. URL: https://acp.copernicus.org/articles/11/817/2011/.

Bönisch, H. et al. (2009). "Quantifying transport into the lowermost stratosphere using simultaneous in-situ measurements of SF_6 and CO_2". In: *Atmospheric Chemistry and Physics* 9.16, pp. 5905–5919. DOI: 10.5194/acp-9-5905-2009. URL: https://acp.copernicus.org/articles/9/5905/2009/.

Brewer, A. W. (1949). "Evidence for a world circulation provided by the measurements of helium and water vapour distribution in the stratosphere". In: *Quarterly Journal of the Royal Meteorological Society* 75.326, pp. 351–363. DOI: https://doi.org/10.1002/qj.49707532603. URL: https://rmets.onlinelibrary.wiley.com/doi/abs/10.1002/qj.49707532603.

Brinckmann, S. et al. (2012). "Short-lived brominated hydrocarbons – observations in the source regions and the tropical tropopause layer". In: *Atmospheric Chemistry and Physics* 12.3, pp. 1213–1228. DOI: 10.5194/acp-12-1213-2012. URL: https://acp.copernicus.org/articles/12/1213/2012/.

Burkholder, J. B. et al. (2019). "Chemical Kinetics and Photochemical Data for Use in Atmospheric Studies, Evaluation No. 19," in: *JPL Publication 19-5, Jet Propulsion Laboratory, Pasadena*, URL: http://jpldataeval.jpl.nasa.gov.

Burkholder, J. B. et al. (2022). "Annex: Summary of Abundance, Lifetimes, ODPs, REs, GWPs, and GTPs". In: 278. Geneva, Switzerland: World Meteorological Organization.

Butchart, Neal (2014). "The Brewer-Dobson circulation". In: *Reviews of Geophysics* 52.2, pp. 157–184. DOI: https://doi.org/10.1002/2013RG000448. URL: https://agupubs.onlinelibrary.wiley.com/doi/abs/10.1002/2013RG000448.

Butler, A. H. and D. I. V. Domeisen (2021). "The wave geometry of final stratospheric warming events". In: *Weather and Climate Dynamics* 2.2, pp. 453–474. DOI: 10.5194/wcd-2-453-2021. URL: https://wcd.copernicus.org/articles/2/453/2021/.

Butler, A. H. et al. (2017). "A sudden stratospheric warming compendium". In: *Earth System Science Data* 9.1, pp. 63–76. DOI: 10.5194/essd-9-63-2017. URL: https://essd.copernicus.org/articles/9/63/2017/.

Carpenter, L. J. and P. S. Liss (Aug. 2000). "On temperate sources of bromoform and other reactive organic bromine gases". In: *Journal of Geophysical Research: Atmospheres* 105.D16, pp. 20539–20547. DOI: 10.1029/2000jd900242. URL: https://doi.org/10.1029/2000jd900242.

Carpenter, Lucy Jane et al. (2014). "Chapter 1: Update on Ozone-Depleting Substances (ODSs) and Other Gases of Interest to the Montreal Protocol". English. In: *Scientific Assessment of Ozone Depletion*. Ed. by Christine A. Ennis. Global Ozone Research and Monitoring Project Report 55. World Meteorological Organization (WMO), pp. 21–125. ISBN: 978996-6076014.

Charlton, Andrew J and Lorenzo M Polvani (Feb. 2007). "A new look at stratospheric sudden warmings. Part I: Climatology and modeling benchmarks". en. In: *J. Clim.* 20.3, pp. 449–469. DOI: http://doi.org/10.1175/JCLI3996.1.

Charney, J. G. and P. G. Drazin (1961). "Propagation of planetary-scale disturbances from the lower into the upper atmosphere". In: *Journal of Geophysical Research (1896-1977)* 66.1, pp. 83–109. DOI: https://doi.org/10.1029/JZ066i001p00083. URL: https://agupubs.onlinelibrary.wiley.com/doi/abs/10.1029/JZ066i001p00083.

Chipperfield, M. P. (2006). "New version of the TOMCAT/SLIMCAT off-line chemical transport model: Intercomparison of stratospheric tracer experiments". In: *Royal Meteorological Society* 132.617, pp. 1179–1203. DOI: 10.1256/qj.05.51. URL: https://rmets.onlinelibrary.wiley.com/doi/abs/10.1256/qj.05.51.

Chipperfield, Martyn P. et al. (2018). "On the Cause of Recent Variations in Lower Stratospheric Ozone". In: *Geophysical Research Letters* 45.11, pp. 5718–5726. DOI: https://doi.org/10.1029/2018GL078071. URL: https://agupubs.onlinelibrary.wiley.com/doi/abs/10.1029/2018GL078071.

Clarmann, T. von and S. Johansson (2018). "Chlorine nitrate in the atmosphere". In: *Atmospheric Chemistry and Physics* 18.20, pp. 15363–15386. DOI: 10.5194/acp-18-15363-2018. URL: https://acp.copernicus.org/articles/18/15363/2018/.

Daniel, J. S. et al. (1996). "On the age of stratospheric air and inorganic chlorine and bromine release". In: *Journal of Geophysical Research: Atmospheres* 101.D11, pp. 16757–16770. DOI: https://doi.org/10.1029/96JD01167. URL: https://agupubs.onlinelibrary.wiley.com/doi/abs/10.1029/96JD01167.

Dee, D. P. et al. (Apr. 2011). "The ERA-Interim reanalysis: Configuration and performance of the data assimilation system". In: *Quarterly Journal of the Royal Meteorological Society* 137, 553–597. DOI: 10.1002/qj.828.

DLR (2022a). *SouthTRAC Scientific Objectives*. URL: https://www.pa.op.dlr.de/southtrac/science/scientific-objectives/ (visited on 12/03/2022).

— (2022b). *The Basis HALO Measurement and Sensor System (BAHAMAS)*. URL: https://www.halo.dlr.de/instrumentation/basis.html.

Dobson, Gordon Miller Bourne, D. N. Harrison, and J. Lawrence (1929). "Measurements of the amount of ozone in the Earth's atmosphere and its relation to other geophysical conditions.—Part III". In: *Proceedings of the Royal Society of London. Series A, Containing Papers of a Mathematical and Physical Character* 122.790, pp. 456–486. DOI: 10.1098/rspa.1929.0034. URL: https://royalsocietypublishing.org/doi/abs/10.1098/rspa.1929.0034.

Engel, A. et al. (2006). "Highly resolved observations of trace gases in the lowermost stratosphere and upper troposphere from the Spurt project: an overview". In: *Atmospheric Chemistry and Physics* 6.2, pp. 283–301. DOI: 10.5194/acp-6-283-2006. URL: https://acp.copernicus.org/articles/6/283/2006/.

Engel, A. et al. (2018). "Update on Ozone-Depletion Substances (ODSs) and other Gases of Interest to the Montreal Protocol". In: 58. Geneva, Switzerland: World Meteorological Organization. Chap. 1.

Engel, Andreas et al. (2002). "Temporal development of total chlorine in the high-latitude stratosphere based on reference distributions of mean age derived from CO2 and SF6". In: *Journal of Geophysical Research: Atmospheres* 107.D12, ACH 1–1–ACH 1–11. DOI: https://doi.org/10.1029/2001JD000584. URL: https://agupubs.onlinelibrary.wiley.com/doi/abs/10.1029/2001JD000584.

Farman, J. C., B. G. Gardiner, and J. D. Shanklin (May 1985). "Large losses of total ozone in Antarctica reveal seasonal ClOx/NOx interaction". In: *Nature* 315.6016, pp. 207–210. DOI: 10.1038/315207a0. URL: https://doi.org/10.1038/315207a0.

Fernandez, R. P. et al. (2014). "Bromine partitioning in the tropical tropopause layer: implications for stratospheric injection". In: *Atmospheric Chemistry and Physics* 14.24, pp. 13391–13410. DOI: 10.5194/acp-14-13391-2014. URL: https://acp.copernicus.org/articles/14/13391/2014/.

Fernandez, R. P. et al. (2017). "Impact of biogenic very short-lived bromine on the Antarctic ozone hole during the 21st century". In: *Atmospheric Chemistry and Physics* 17.3, pp. 1673–1688. DOI: 10.5194/acp-17-1673-2017. URL: https://acp.copernicus.org/articles/17/1673/2017/.

Froidevaux, L. et al. (2006). "Temporal decrease in upper atmospheric chlorine". In: *Geophysical Research Letters* 33.23. DOI: https://doi.org/10.1029/2006GL027600. URL: https://agupubs.onlinelibrary.wiley.com/doi/abs/10.1029/2006GL027600.

Froidevaux, L. et al. (2015). "Global OZone Chemistry And Related trace gas Data records for the Stratosphere (GOZCARDS): methodology and sample results with a focus on HCl, H_2O, and O_3". In: *Atmospheric Chemistry and Physics* 15.18, pp. 10471–10507. DOI: 10.5194/acp-15-10471-2015. URL: https://acp.copernicus.org/articles/15/10471/2015/.

Froidevaux, L. et al. (2019). "Evaluation of CESM1 (WACCM) free-running and specified dynamics atmospheric composition simulations using global multispecies satellite data

records". In: *Atmospheric Chemistry and Physics* 19.7, pp. 4783–4821. DOI: 10.5194/acp-19-4783-2019. URL: https://acp.copernicus.org/articles/19/4783/2019/.

Gettelman, A. et al. (Aug. 2011). "THE EXTRATROPICAL UPPER TROPOSPHERE AND LOWER STRATOSPHERE". In: *Reviews of Geophysics* 49.3. DOI: 10.1029/2011rg000355. URL: https://doi.org/10.1029/2011rg000355.

Greenblatt, Jeffrey B. et al. (2002). "Defining the polar vortex edge from an N2O:potential temperature correlation". In: *Journal of Geophysical Research* 107.D20, SOL 10–1 –10–9. DOI: 10.1029/2001JD000575.

Grooß, J.-U. et al. (2014). "Nitric acid trihydrate nucleation and denitrification in the Arctic stratosphere". In: *Atmospheric Chemistry and Physics* 14.2, pp. 1055–1073. DOI: 10.5194/acp-14-1055-2014. URL: https://acp.copernicus.org/articles/14/1055/2014/.

Hall, Timothy M. and R. Alan Plumb (1994). "Age as a diagnostic of stratospheric transport". In: *Journal of Geophysical Research: Atmospheres* 99.D1, pp. 1059–1070. DOI: https://doi.org/10.1029/93JD03192. URL: https://agupubs.onlinelibrary.wiley.com/doi/abs/10.1029/93JD03192.

Hall, Timothy M. and Michael J. Prather (1993). "Simulations of the trend and annual cycle in stratospheric CO2". In: *Journal of Geophysical Research: Atmospheres* 98.D6, pp. 10573–10581. DOI: https://doi.org/10.1029/93JD00325. URL: https://agupubs.onlinelibrary.wiley.com/doi/abs/10.1029/93JD00325.

Hartmann, D. L. et al. (1989). "Potential Vorticity and Mixing in the South Polar Vortex During Spring". In: *Journal of Geophysical Research* 94.D9, pp. 11,625–11,640. DOI: 10.1029/JD094iD09p11625.

Hauck, M. et al. (2019). "Deriving stratospheric age of air spectra using an idealized set of chemically active trace gases". In: *Atmospheric Chemistry and Physics* 19.7, pp. 5269–5291. DOI: 10.5194/acp-19-5269-2019. URL: https://acp.copernicus.org/articles/19/5269/2019/.

Hauck, M. et al. (2020). "A convolution of observational and model data to estimate age of air spectra in the northern hemispheric lower stratosphere". In: *Atmospheric Chemistry and Physics* 20.14, pp. 8763–8785. DOI: 10.5194/acp-20-8763-2020. URL: https://acp.copernicus.org/articles/20/8763/2020/.

Hegglin, M. I. et al. (2009). "A global view of the extratropical tropopause transition layer from Atmospheric Chemistry Experiment Fourier Transform Spectrometer O_3, H_2O, and CO". In: *Journal of Geophysical Research: Atmospheres* 114.D7. DOI: 10.1029/2008JD009984. URL: https://agupubs.onlinelibrary.wiley.com/doi/abs/10.1029/2008JD009984.

Hegglin, Michaela I. and Theodore G. Shepherd (2007). "O3-N2O correlations from the Atmospheric Chemistry Experiment: Revisiting a diagnostic of transport and chemistry in the stratosphere". In: *Journal of Geophysical Research: Atmospheres* 112.D19. DOI: https://doi.org/10.1029/2006JD008281. URL: https://agupubs.onlinelibrary.wiley.com/doi/abs/10.1029/2006JD008281.

Hersbach, Hans et al. (2020). "The ERA5 global reanalysis". In: *Quarterly Journal of the Royal Meteorological Society* 146.730, pp. 1999–2049. DOI: 10.1002/qj.3803. URL: https://rmets.onlinelibrary.wiley.com/doi/abs/10.1002/qj.3803.

Holloway, A.M. and R.P. Wayne (2010). *Atmospheric Chemistry*. Royal Society of Chemistry. ISBN: 9781847558077. URL: https://books.google.de/books?id=WI906EYHkb4C.

Holton, James R et al. (1995). "Stratosphere-troposphere exchange". In: *Rev. Geophys.* 33.4, p. 403. DOI: 10.1029/2011rg000355.

Hoor, P., H. Fischer, and J. Lelieveld (2005). "Tropical and extratropical tropospheric air in the lowermost stratosphere over Europe: A CO-based budget". In: *Geophysical Research Letters* 32, p. L07802. DOI: 10.1029/2004GL022018.

Hoor, P. et al. (2004). "Seasonality and extent of extratropical TST derived from in-situ CO measurements during SPURT". In: *Atmospheric Chemistry and Physics* 4.5, pp. 1427–1442.

DOI: 10.5194/acp-4-1427-2004. URL: https://acp.copernicus.org/articles/4/1427/2004/.

Hossaini, R. et al. (2013). "Evaluating global emission inventories of biogenic bromocarbons". In: *Atmospheric Chemistry and Physics* 13.23, pp. 11819–11838. DOI: 10.5194/acp-13-11819-2013. URL: https://acp.copernicus.org/articles/13/11819/2013/.

Hossaini, R. et al. (2015). "Efficiency of short-lived halogens at influencing climate through depletion of stratospheric ozone". In: *Nature Geoscience* 8.3, pp. 1427–1442. DOI: 10.1038/ngeo2363. URL: https://www.nature.com/articles/ngeo2363#citeas.

Hossaini, R. et al. (2016). "A multi-model intercomparison of halogenated very short-lived substances (TransCom-VSLS): linking oceanic emissions and tropospheric transport for a reconciled estimate of the stratospheric source gas injection of bromine". In: *Atmospheric Chemistry and Physics* 16.14, pp. 9163–9187. DOI: 10.5194/acp-16-9163-2016. URL: https://acp.copernicus.org/articles/16/9163/2016/.

Hossaini, Ryan et al. (June 2017). "The increasing threat to stratospheric ozone from dichloromethane". In: *Nature Communications* 8.1. DOI: 10.1038/ncomms15962. URL: https://doi.org/10.1038/ncomms15962.

Hossaini, Ryan et al. (2019). "Recent Trends in Stratospheric Chlorine From Very Short-Lived Substances". In: *Journal of Geophysical Research: Atmospheres* 124.4, pp. 2318–2335. DOI: https://doi.org/10.1029/2018JD029400. URL: https://agupubs.onlinelibrary.wiley.com/doi/abs/10.1029/2018JD029400.

Jesswein, M. et al. (2021). "Comparison of inorganic chlorine in the Antarctic and Arctic lowermost stratosphere by separate late winter aircraft measurements". In: *Atmospheric Chemistry and Physics* 21.23, pp. 17225–17241. DOI: 10.5194/acp-21-17225-2021. URL: https://acp.copernicus.org/articles/21/17225/2021/.

Jesswein, M. et al. (2022). "Global seasonal distribution of CH_2Br_2 and $CHBr_3$ in the upper troposphere and lower stratosphere". In: *Atmospheric Chemistry and Physics* 22.22, pp. 15049–15070. DOI: 10.5194/acp-22-15049-2022. URL: https://acp.copernicus.org/articles/22/15049/2022/.

Jia, Y. et al. (2019). "How marine emissions of bromoform impact the remote atmosphere". In: *Atmospheric Chemistry and Physics* 19.17, pp. 11089–11103. DOI: 10.5194/acp-19-11089-2019. URL: https://acp.copernicus.org/articles/19/11089/2019/.

Johnson, D. et al. (June 1995). "Detection of HBr and upper limit for HOBr: Bromine partitioning in the stratosphere". In: *Geophysical Research Letters - GEOPHYS RES LETT* 22, pp. 1373–1376. DOI: 10.1029/95GL01349.

Keber, T. et al. (2020). "Bromine from short-lived source gases in the extratropical northern hemispheric upper troposphere and lower stratosphere (UTLS)". In: *Atmospheric Chemistry and Physics* 20.7, pp. 4105–4132. DOI: 10.5194/acp-20-4105-2020. URL: https://acp.copernicus.org/articles/20/4105/2020/.

Kida, Hideji (1983). "General Circulation of Air Parcels and Transport Characteristics Derived from a Hemispheric GCM". In: *Journal of the Meteorological Society of Japan. Ser. II* 61.4, pp. 510–523. DOI: 10.2151/jmsj1965.61.4_510.

Klobas, J. E. et al. (2020). "Reformulating the bromine alpha factor and equivalent effective stratospheric chlorine (EESC): evolution of ozone destruction rates of bromine and chlorine in future climate scenarios". In: *Atmospheric Chemistry and Physics* 20.15, pp. 9459–9471. DOI: 10.5194/acp-20-9459-2020. URL: https://acp.copernicus.org/articles/20/9459/2020/.

Konopka, Paul et al. (2015). "Hemispheric asymmetries and seasonality of mean age of air in the lower stratosphere: Deep versus shallow branch of the Brewer-Dobson circulation". In: *Journal of Geophysical Research: Atmospheres* 120.5, pp. 2053–2066. DOI: https://doi.org/10.1002/2014JD022429. URL: https://agupubs.onlinelibrary.wiley.com/doi/abs/10.1002/2014JD022429.

Krause, J. et al. (2018). "Mixing and ageing in the polar lower stratosphere in winter 2015–2016". In: *Atmospheric Chemistry and Physics* 18.8, pp. 6057–6073. DOI: 10.5194/acp-18-6057-2018. URL: https://acp.copernicus.org/articles/18/6057/2018/.

Krüger, Kirstin, Barbara Naujokat, and Karin Labitzke (2005). "The Unusual Midwinter Warming in the Southern Hemisphere Stratosphere 2002: A Comparison to Northern Hemisphere Phenomena". In: *Journal of the Atmospheric Sciences* 62.3, pp. 603 –613. DOI: 10.1175/JAS-3316.1. URL: https://journals.ametsoc.org/view/journals/atsc/62/3/jas-3316.1.xml.

Lamarque, J.-F. et al. (2012). "CAM-chem: description and evaluation of interactive atmospheric chemistry in the Community Earth System Model". In: *Geoscientific Model Development* 5.2, pp. 369–411. DOI: 10.5194/gmd-5-369-2012. URL: https://gmd.copernicus.org/articles/5/369/2012/.

Lary, D. J. (1997). "Catalytic destruction of stratospheric ozone". In: *Journal of Geophysical Research: Atmospheres* 102.D17, pp. 21515–21526. DOI: https://doi.org/10.1029/97JD00912. URL: https://agupubs.onlinelibrary.wiley.com/doi/abs/10.1029/97JD00912.

Laube, J. C. et al. (2022). "Update on Ozone-Depletion Substances (ODSs) and other Gases of Interest to the Montreal Protocol". In: 278. Geneva, Switzerland: World Meteorological Organization. Chap. 1.

Leedham, E. C. et al. (2013). "Emission of atmospherically significant halocarbons by naturally occurring and farmed tropical macroalgae". In: *Biogeosciences* 10.6, pp. 3615–3633. DOI: 10.5194/bg-10-3615-2013. URL: https://bg.copernicus.org/articles/10/3615/2013/.

Leedham Elvidge, E. et al. (2018). "Evaluation of stratospheric age of air from CF_4, C_2F_6, C_3F_8, CHF_3, HFC-125, HFC-227ea and SF_6; implications for the calculations of halocarbon lifetimes, fractional release factors and ozone depletion potentials". In: *Atmospheric Chemistry and Physics* 18.5, pp. 3369–3385. DOI: 10.5194/acp-18-3369-2018. URL: https://acp.copernicus.org/articles/18/3369/2018/.

Liang, Q. et al. (2010). "Finding the missing stratospheric Br_y: a global modeling study of $CHBr_3$ and CH_2Br_2". In: *Atmospheric Chemistry and Physics* 10.5, pp. 2269–2286. DOI: 10.5194/acp-10-2269-2010. URL: https://acp.copernicus.org/articles/10/2269/2010/.

Loeffel, S. et al. (2022). "The impact of sulfur hexafluoride SF_6 sinks on age of air climatologies and trends". In: *Atmospheric Chemistry and Physics* 22.2, pp. 1175–1193. DOI: 10.5194/acp-22-1175-2022. URL: https://acp.copernicus.org/articles/22/1175/2022/.

Mahieu, E. et al. (2014). "Recent Northern Hemisphere stratospheric HCl increase due to atmospheric circulation changes". In: *Nature* 515.22, pp. 104–107. DOI: https://doi.org/10.1038/nature13857. URL: https://www.nature.com/articles/nature13857.

Maiss, Manfred and Carl A. M. Brenninkmeijer (1998). "Atmospheric SF6: Trends, Sources, and Prospects". In: *Environmental Science & Technology* 32.20, pp. 3077–3086. DOI: 10.1021/es9802807. URL: https://doi.org/10.1021/es9802807.

Marsing, Andreas et al. (2019). "Chlorine partitioning in the lowermost Arctic vortex during the cold winter 2015/2016". In: *Atmospheric Chemistry and Physics* 19, pp. 10757–10772. DOI: 10.5194/acp-19-10757-2019.

McCulloch, Archie et al. (1999). "Global emissions of hydrogen chloride and chloromethane from coal combustion, incineration and industrial activities: Reactive Chlorine Emissions Inventory". In: *Journal of Geophysical Research: Atmospheres* 104.D7, pp. 8391–8403. DOI: https://doi.org/10.1029/1999JD900025. URL: https://agupubs.onlinelibrary.wiley.com/doi/abs/10.1029/1999JD900025.

McIntyre, M. E. and T. N. Palmer (Oct. 1983). "Breaking planetary waves in the stratosphere". In: *Nature* 305.5935, pp. 593–600. DOI: 10.1038/305593a0. URL: https://doi.org/10.1038/305593a0.

McIntyre, M.E and T.N Palmer (1984). "The 'surf zone' in the stratosphere". In: *Journal of Atmospheric and Terrestrial Physics* 46.9, pp. 825–849. ISSN: 0021-9169. DOI: https://doi.org/10.1016/0021-9169(84)90063-1. URL: https://www.sciencedirect.com/science/article/pii/0021916984900631.

Molina, L. T. and M. J. Molina (1987). "Production of chlorine oxide (Cl2O2) from the self-reaction of the chlorine oxide (ClO) radical". In: *The Journal of Physical Chemistry* 91.2, pp. 433–436. DOI: 10.1021/j100286a035. URL: https://doi.org/10.1021/j100286a035.

Molina, M. J. and F. S. Rowland (1974). "Stratospheric sink for chlorofluoromethanes: chlorine atomic-catalysed destruction of ozone". In: *Nature* 249.

Monks, S. A. et al. (2017). "The TOMCAT global chemical transport model v1.6: description of chemical mechanism and model evaluation". In: *Geoscientific Model Development* 10.8, pp. 3025–3057. DOI: 10.5194/gmd-10-3025-2017. URL: https://gmd.copernicus.org/articles/10/3025/2017/.

Montzka, Stephen A. et al. (1996). "Decline in the Tropospheric Abundance of Halogen from Halocarbons: Implications for Stratospheric Ozone Depletion". In: *Science* 272.5266, pp. 1318–1322. DOI: 10.1126/science.272.5266.1318. URL: https://www.science.org/doi/abs/10.1126/science.272.5266.1318.

Müller, S. et al. (2015). "In situ detection of stratosphere-troposphere exchange of cirrus particles in the midlatitudes". In: *Geophysical Research Letters* 42.3, pp. 949–955. DOI: https://doi.org/10.1002/2014GL062556. URL: https://agupubs.onlinelibrary.wiley.com/doi/abs/10.1002/2014GL062556.

Nash, Eric R. et al. (1996). "An objective determination of the polar vortex using Ertel's potential vorticity". In: *Journal of Geophysical Research: Atmospheres* 101.D5, pp. 9471–9478. DOI: https://doi.org/10.1029/96JD00066. URL: https://agupubs.onlinelibrary.wiley.com/doi/abs/10.1029/96JD00066.

Navarro, Maria A. et al. (2015). "Airborne measurements of organic bromine compounds in the Pacific tropical tropopause layer". In: *Proceedings of the National Academy of Sciences* 112.45, pp. 13789–13793. DOI: 10.1073/pnas.1511463112. URL: https://www.pnas.org/doi/abs/10.1073/pnas.1511463112.

Newman, Paul A., S. Randolph Kawa, and Eric R. Nash (2004). "On the size of the Antarctic ozone hole". In: *Geophysical Research Letters* 31.21. DOI: https://doi.org/10.1029/2004GL020596. URL: https://agupubs.onlinelibrary.wiley.com/doi/abs/10.1029/2004GL020596.

NOAA (2023). *NOAA Global Monitoring Laboratory - halocarbons and other atmospheric trace species*. URL: https://gml.noaa.gov/hats/graphs/graphs.html (visited on 03/13/2023).

Obersteiner, Florian et al. (2016). "A versatile, refrigerant- and cryogen-free cryofocusing–thermodesorption unit for preconcentration of traces gases in air". In: *Atmospher Measurement Techniques* 9, pp. 5265–5279. DOI: 10.5194/amt-9-5265-2016.

Oelhaf, Hermann et al. (2019). "POLSTRACC: Airborne Experiment for Studying the Polar Stratosphere in a Changing Climate with the High Altitude and Long Range Research Aircraft (HALO)". In: *Bulletin of the American Meteorological Society* 100.12, pp. 2634 – 2664. DOI: 10.1175/BAMS-D-18-0181.1. URL: https://journals.ametsoc.org/view/journals/bams/100/12/bams-d-18-0181.1.xml.

Ordóñez, C. et al. (2012). "Bromine and iodine chemistry in a global chemistry-climate model: description and evaluation of very short-lived oceanic sources". In: *Atmospheric Chemistry and Physics* 12.3, pp. 1423–1447. DOI: 10.5194/acp-12-1423-2012. URL: https://acp.copernicus.org/articles/12/1423/2012/.

Pan, L. L. et al. (2017). "The Convective Transport of Active Species in the Tropics (CONTRAST) Experiment". In: *Bulletin of the American Meteorological Society* 98.1, pp. 106–128. DOI: 10.1175/BAMS-D-14-00272.1. URL: https://journals.ametsoc.org/view/journals/bams/98/1/bams-d-14-00272.1.xml.

Patra, P. K. et al. (2011). "TransCom model simulations of CH_4 and related species: linking transport, surface flux and chemical loss with CH_4 variability in the troposphere and lower stratosphere". In: *Atmospheric Chemistry and Physics* 11.24, pp. 12813–12837. DOI: 10.5194/acp-11-12813-2011. URL: https://acp.copernicus.org/articles/11/12813/2011/.

Patra, Prabir K. et al. (2000). "Chlorine partitioning in the stratosphere based on in situ measurements". In: *Tellus B: Chemical and Physical Meteorology* 52.3, pp. 934–946. DOI: 10.3402/tellusb.v52i3.17076. URL: https://doi.org/10.3402/tellusb.v52i3.17076.

Plumb, I. C., P. F. Vohralik, and K. R. Ryan (1999). "Normalization of correlations for atmospheric species with chemical loss". In: *Journal of Geophysical Research* 104.D9, pp. 11,723–11,732.

Plumb, R. Alan (2002). "Stratospheric Transport". In: *Journal of the Meteorological Society of Japan. Ser. II* 80.4B, pp. 793–809. DOI: 10.2151/jmsj.80.793.

— (2007). "Tracer interrelationships in the stratosphere". In: *Reviews of Geophysics* 45.4. DOI: https://doi.org/10.1029/2005RG000179. URL: https://agupubs.onlinelibrary.wiley.com/doi/abs/10.1029/2005RG000179.

Portmann, R. W., J. S. Daniel, and A. R. Ravishankara (2012). "Stratospheric ozone depletion due to nitrous oxide: influences of other gases". In: *Philosophical Transactions of the Royal Society B: Biological Sciences* 367.1593, pp. 1256–1264. DOI: 10.1098/rstb.2011.0377. URL: https://doi.org/10.10982Frstb.2011.0377.

Prinn, R. G. et al. (2018). "History of chemically and radiatively important atmospheric gases from the Advanced Global Atmospheric Gases Experiment (AGAGE)". In: *Earth System Science Data* 10.2, pp. 985–1018. DOI: 10.5194/essd-10-985-2018. URL: https://essd.copernicus.org/articles/10/985/2018/.

Quack, B. et al. (2007). "Oceanic distribution and sources of bromoform and dibromomethane in the Mauritanian upwelling". In: *Journal of Geophysical Research: Oceans* 112.C10006, pp. 1–13. DOI: 10.1029/2006JC003803.

Rapp, M. et al. (2020). "SOUTHTRAC-GW: An airborne field campaign to explore gravity wave dynamics at the world's strongest hotspot". In: *Bulletin of the American Meteorological Society*, pp. 1 –60. DOI: 10.1175/BAMS-D-20-0034.1.

Ravishankara, A. R. et al. (1993). "Atmospheric Lifetimes of Long-Lived Halogenated Species". In: *Science* 259.5092, pp. 194–199. DOI: 10.1126/science.259.5092.194. URL: https://www.science.org/doi/abs/10.1126/science.259.5092.194.

Ray, Eric A. et al. (2017). "Quantification of the SF6 lifetime based on mesospheric loss measured in the stratospheric polar vortex". In: *Journal of Geophysical Research: Atmospheres* 122.8, pp. 4626–4638. DOI: https://doi.org/10.1002/2016JD026198. URL: https://agupubs.onlinelibrary.wiley.com/doi/abs/10.1002/2016JD026198.

Riese, M. et al. (2012). "Impact of uncertainties in atmospheric mixing on simulated UTLS composition and related radiative effects". In: *Journal of Geophysical Research: Atmospheres* 117.D16. DOI: https://doi.org/10.1029/2012JD017751. URL: https://agupubs.onlinelibrary.wiley.com/doi/abs/10.1029/2012JD017751.

Rowland, F. S. and Mario J. Molina (1975). "Chlorofluoromethanes in the environment". In: *Reviews of Geophysics* 13.1, pp. 1–35. DOI: https://doi.org/10.1029/RG013i001p00001. URL: https://agupubs.onlinelibrary.wiley.com/doi/abs/10.1029/RG013i001p00001.

Safieddine, Sarah et al. (2020). "Antarctic Ozone Enhancement During the 2019 Sudden Stratospheric Warming Event". In: *Geophysical Research Letters* 47.14, e2020GL087810.

DOI: https://doi.org/10.1029/2020GL087810. URL: https://agupubs.onlinelibrary.wiley.com/doi/abs/10.1029/2020GL087810.

Sala, S. et al. (2014). "Deriving an atmospheric budget of total organic bromine using airborne in situ measurements from the western Pacific area during SHIVA". In: *Atmospheric Chemistry and Physics* 14, pp. 6903–6923. DOI: 10.5194/acp-14-6903-2014.

Salby, Murry L. and Patrick F. Callaghan (2007). "Influence of planetary wave activity on the stratospheric final warming and spring ozone". In: *Journal of Geophysical Research: Atmospheres* 112.D20. DOI: https://doi.org/10.1029/2006JD007536. URL: https://agupubs.onlinelibrary.wiley.com/doi/abs/10.1029/2006JD007536.

Schoeberl, Mark R. and Dennis L. Hartmann (1991). "The Dynamics of the Stratospheric Polar Vortex and Its Relation to Springtime Ozone Depletion". In: *Science* 251.4989, pp. 46–52. DOI: 10.1126/science.251.4989.46.

Schoeberl, Mark R. et al. (1992). "The structure of the polar vortex". In: *Journal of Geophysical Research: Atmospheres* 97.D8, pp. 7859–7882. DOI: https://doi.org/10.1029/91JD02168. URL: https://agupubs.onlinelibrary.wiley.com/doi/abs/10.1029/91JD02168.

Seinfeld, J and S Pandis (2016). *Atmospheric Chemistry and Physics: From Air Pollution to Climate Change*. A Wiley-Interscience publication. Wiley, p. 1112.

Shuckburgh, Emily, Francesco d'Ovidio, and Bernard Legras (2009). "Local Mixing Events in the Upper Troposphere and Lower Stratosphere. Part II: Seasonal and Interannual Variability". In: *Journal of the Atmospheric Sciences* 66.12, pp. 3695–3706. DOI: 10.1175/2009JAS2983.1. URL: https://journals.ametsoc.org/view/journals/atsc/66/12/2009jas2983.1.xml.

Simmonds, P. G. et al. (2020). "The increasing atmospheric burden of the greenhouse gas sulfur hexafluoride (SF_6)". In: *Atmospheric Chemistry and Physics* 20.12, pp. 7271–7290. DOI: 10.5194/acp-20-7271-2020. URL: https://acp.copernicus.org/articles/20/7271/2020/.

Sinnhuber, B.-M. et al. (2009). "The contribution of anthropogenic bromine emissions to past stratospheric ozone trends: a modelling study". In: *Atmospheric Chemistry and Physics* 9.8, pp. 2863–2871. DOI: 10.5194/acp-9-2863-2009. URL: https://acp.copernicus.org/articles/9/2863/2009/.

Solomon, Susan (1999). "Stratospheric ozone depletion: A review of concepts and history". In: *Reviews of Geophysics* 37.3, pp. 275–316. DOI: https://doi.org/10.1029/1999RG900008. URL: https://agupubs.onlinelibrary.wiley.com/doi/abs/10.1029/1999RG900008.

Spencer, John E. and F. S. Rowland (Jan. 1978). "Bromine nitrate and its stratospheric significance". In: *The Journal of Physical Chemistry* 82.1, pp. 7–10. DOI: 10.1021/j100490a002. URL: https://doi.org/10.1021/j100490a002.

Stohl, A. et al. (2003). "Stratosphere-troposphere exchange: A review, and what we have learned from STACCATO". In: *Journal of Geophysical Research: Atmospheres* 108.D12. DOI: https://doi.org/10.1029/2002JD002490. URL: https://agupubs.onlinelibrary.wiley.com/doi/abs/10.1029/2002JD002490.

Strahan, S. E., M. Loewenstein, and J. R. Podolske (1999). "Climatology and small-scale structure of lower stratospheric N2O based on in situ observations". In: *Journal of Geophysical Research: Atmospheres* 104.D2, pp. 2195–2208. DOI: https://doi.org/10.1029/1998JD200075. URL: https://agupubs.onlinelibrary.wiley.com/doi/abs/10.1029/1998JD200075.

Strahan, S. E. et al. (2014). "Inorganic chlorine variability in the Antarctic vortex and implications for ozone recovery". In: *Journal of Geophysical Research: Atmospheres* 119.24, pp. 14,098–14,109. DOI: https://doi.org/10.1002/2014JD022295. URL: https://agupubs.onlinelibrary.wiley.com/doi/abs/10.1002/2014JD022295.

Strahan, S. E. et al. (2015). "Modulation of Antarctic vortex composition by the quasi-biennial oscillation". In: *Geophysical Research Letters* 42.10, pp. 4216–4223. DOI: https://doi.org/

10.1002/2015GL063759. URL: https://agupubs.onlinelibrary.wiley.com/doi/abs/10.1002/2015GL063759.

Strahan, Susan E. and Anne R. Douglass (2018). "Decline in Antarctic Ozone Depletion and Lower Stratospheric Chlorine Determined From Aura Microwave Limb Sounder Observations". In: *Geophysical Research Letters* 45.1, pp. 382–390. DOI: https://doi.org/10.1002/2017GL074830. URL: https://agupubs.onlinelibrary.wiley.com/doi/abs/10.1002/2017GL074830.

Strunk, M. et al. (2000). "CO_2 and SF_6 as stratospheric age tracers: Consistency and the effect of mesospheric SF_6-loss". In: *Geophysical Research Letters* 27.3, pp. 341–344. DOI: https://doi.org/10.1029/1999GL011044. URL: https://agupubs.onlinelibrary.wiley.com/doi/abs/10.1029/1999GL011044.

Sturges, W. T. et al. (1993). "Bromoalkane production by Antarctic ice algae". In: *Tellus B: Chemical and Physical Meteorology* 45.2, pp. 120–126. DOI: 10.3402/tellusb.v45i2.15586. URL: https://doi.org/10.3402/tellusb.v45i2.15586.

Tegtmeier, S. et al. (2020). "Variability and past long-term changes of brominated very short-lived substances at the tropical tropopause". In: *Atmospheric Chemistry and Physics* 20.11, pp. 7103–7123. DOI: 10.5194/acp-20-7103-2020. URL: https://acp.copernicus.org/articles/20/7103/2020/.

Thompson, Chelsea R. et al. (2022). "The NASA Atmospheric Tomography (ATom) Mission: Imaging the Chemistry of the Global Atmosphere". In: *Bulletin of the American Meteorological Society* 103.3, E761 –E790. DOI: 10.1175/BAMS-D-20-0315.1. URL: https://journals.ametsoc.org/view/journals/bams/103/3/BAMS-D-20-0315.1.xml.

Tritscher, Ines et al. (2021). "Polar Stratospheric Clouds: Satellite Observations, Processes, and Role in Ozone Depletion". In: *Reviews of Geophysics* 59.2, e2020RG000702. DOI: https://doi.org/10.1029/2020RG000702. URL: https://agupubs.onlinelibrary.wiley.com/doi/abs/10.1029/2020RG000702.

UNEP (2019). *Handbook for the Montreal Protocol on Substances that Deplete the Ozone Layer*. United Nations Environment Programme Nairobi, Kenya: UNEP Ozone Secretariat. ISBN: 978-9966-076-59-5.

— (2023). *About Montreal protocol*. URL: https://www.unep.org/ozonaction/who-we-are/about-montreal-protocol (visited on 03/13/2023).

Volk, C. M. et al. (1997). "Evaluation of source gas lifetimes from stratospheric observations". In: *Journal of Geophysical Research: Atmospheres* 102.D21, pp. 25543–25564. DOI: https://doi.org/10.1029/97JD02215. URL: https://agupubs.onlinelibrary.wiley.com/doi/abs/10.1029/97JD02215.

Wagenhäuser, T. et al. (2022). "Mean age from observations in the lowermost stratosphere: an improved method and interhemispheric differences". In: *EGUsphere* 2022, pp. 1–26. DOI: 10.5194/egusphere-2022-1197. URL: https://egusphere.copernicus.org/preprints/egusphere-2022-1197/.

Walker, S. J., R. F. Weiss, and P. K. Salameh (2000). "Reconstructed histories of the annual mean atmospheric mole fractions for the halocarbons CFC-11 CFC-12, CFC-113, and carbon tetrachloride". In: *Journal of Geophysical Research: Oceans* 105.C6, pp. 14285–14296. DOI: https://doi.org/10.1029/1999JC900273. URL: https://agupubs.onlinelibrary.wiley.com/doi/abs/10.1029/1999JC900273.

Wallington, T J et al. (1994). "The environmental impact of CFC replacements HFCs and HCFCs". In: *Environ. Sci. Technol.* 28.7, 320A–6A. DOI: 10.1021/es00056a714.

Wargan, Krzysztof et al. (2020). "The Anomalous 2019 Antarctic Ozone Hole in the GEOS Constituent Data Assimilation System With MLS Observations". In: *Journal of Geophysical Research: Atmospheres* 125.18. e2020JD033335 2020JD033335, e2020JD033335. DOI: https://doi.org/10.1029/2020JD033335. URL: https://agupubs.onlinelibrary.wiley.com/doi/abs/10.1029/2020JD033335.

Warwick, N. J. et al. (2006). "Global modeling of biogenic bromocarbons". In: *Journal of Geophysical Research: Atmospheres* 111.D24. DOI: https://doi.org/10.1029/2006JD007264. URL: https://agupubs.onlinelibrary.wiley.com/doi/abs/10.1029/2006JD007264.

Waugh, Darryn W. and William J. Randel (1999). "Climatology of Arctic and Antarctic Polar Vortices Using Elliptical Diagnostics". In: *Journal of the Atmospheric Sciences* 56.11, pp. 1594 –1613. DOI: 10.1175/1520-0469(1999)056<1594:COAAAP>2.0.CO;2. URL: https://journals.ametsoc.org/view/journals/atsc/56/11/1520-0469_1999_056_1594_coaaap_2.0.co_2.xml.

Wetzel, G. et al. (2015). "Partitioning and budget of inorganic and organic chlorine species observed by MIPAS-B and TELIS in the Arctic in March 2011". In: *Atmospheric Chemistry and Physics* 15.14, pp. 8065–8076. DOI: 10.5194/acp-15-8065-2015. URL: https://acp.copernicus.org/articles/15/8065/2015/.

WMO (1957). *Bulletin of the World Meteorological Organization*. Geneva, Switzerland.

— (2003). *Scientific Assessment of Ozone Depletion: 2002, Global ozone research and monitoring project report no. 47*, pp. 136–137.

Wofsy, S. C. (2011). "HIAPER Pole-to-Pole Observations (HIPPO): fine-grained, global-scale measurements of climatically important atmospheric gases and aerosols". In: *Philosophical Transactions of the Royal Society A: Mathematical, Physical and Engineering Sciences* 369.1943, pp. 2073–2086. DOI: 10.1098/rsta.2010.0313. URL: https://royalsocietypublishing.org/doi/abs/10.1098/rsta.2010.0313.

Wofsy, S.C. et al. (2021). *ATom: Merged Atmospheric Chemistry, Trace Gases, and Aerosols, Version 2*. en. DOI: 10.3334/ORNLDAAC/1925. URL: https://daac.ornl.gov/cgi-bin/dsviewer.pl?ds_id=1925.

Wofsy, Steven C., Michael B. McElroy, and Yuk Ling Yung (1975). "The chemistry of atmospheric bromine". In: *Geophysical Research Letters* 2.6, pp. 215–218. DOI: https://doi.org/10.1029/GL002i006p00215. URL: https://agupubs.onlinelibrary.wiley.com/doi/abs/10.1029/GL002i006p00215.

World Meteorological Organization, National Oceanic, National Aeronautics Atmospheric Administration United Nations Environment Programme, and European Commission Space Administration (2018). *Scientific Assessment of Ozone Depletion: 2018 - Global Ozone Research and Monitoring Project Report No. 58*. Geneva, Switzerland. URL: https://wedocs.unep.org/20.500.11822/32140.

Yung, Y. L. et al. (1980). "Atmospheric bromine and ozone perturbations in the lower stratosphere". In: *J. Atmos. Sci.* 37, pp. 339–353. DOI: 10.1175/1520-0469(1980)037<0339:ABAOPI>2.0.CO;2.

Ziska, F. et al. (2013). "Global sea-to-air flux climatology for bromoform, dibromomethane and methyl iodide". In: *Atmospheric Chemistry and Physics* 13.17, pp. 8915–8934. DOI: 10.5194/acp-13-8915-2013. URL: https://acp.copernicus.org/articles/13/8915/2013/.

Paper I: Comparison of inorganic chlorine in the Antarctic and Arctic lowermost stratosphere by separate late winter aircraft measurements

Published as:

Jesswein, M., Bozem, H., Lachnitt, H.-C., Hoor, P., Wagenhäuser, T., Keber, T., Schuck, T., and Engel, A.: *Comparison of inorganic chlorine in the Antarctic and Arctic lowermost stratosphere by separate late winter aircraft measurements*, Atmos. Chem. Phys., 21, 17225–17241, 2021, DOI: https://doi.org/10.5194/acp-21-17225-2021

Author Contributions:

Markus Jesswein wrote the manuscript including the figures of the publication and prepared the answers to the referees during the revision process. Presented concepts were developed by Markus Jesswein in collaboration with Andreas Engel. The manuscript was proofread by Andreas Engel, Tanja Schuck, and Peter Hoor.

Markus Jesswein operated the GhOST instrument during the SouthTRAC research campaign, together with Thomas Wagenhäuser, Timo Keber, Tanja Schuck, and Andreas Engel. Markus Jesswein evaluated and interpreted the data of the SouthTRAC campaign.

Markus Jesswein processed both AGAGE and HALO (PGS and SouthTRAC) data, developed and applied the air mass classification as well as derived Cl_y in collaboration with Andreas Engel.

Heiko Bozem, Hans-Christoph Lachnitt, and Peter Hoor were active part during both PGS and SouthTRAC with the TRIHOP and UMAQS instruments.

All co-authors contributed to the preparation of the manuscript in many useful discussions.

Frankfurt am Main .....

Markus Jesswein

Atmos. Chem. Phys., 21, 17225–17241, 2021
https://doi.org/10.5194/acp-21-17225-2021

Atmospheric Chemistry and Physics
Open Access
EGU

Comparison of inorganic chlorine in the Antarctic and Arctic lowermost stratosphere by separate late winter aircraft measurements

Markus Jesswein[1], Heiko Bozem[2], Hans-Christoph Lachnitt[2], Peter Hoor[2], Thomas Wagenhäuser[1], Timo Keber[1], Tanja Schuck[1], and Andreas Engel[1]

[1]University of Frankfurt, Institute for Atmospheric and Environmental Sciences, Frankfurt, Germany
[2]Johannes Gutenberg University of Mainz, Institute for Atmospheric Physics, Mainz, Germany

Correspondence: Markus Jesswein (jesswein@iau.uni-frankfurt.de)

Received: 28 April 2021 – Discussion started: 28 May 2021
Revised: 15 October 2021 – Accepted: 21 October 2021 – Published: 29 November 2021

Abstract. Stratospheric inorganic chlorine (Cl_y) is predominantly released from long-lived chlorinated source gases and, to a small extent, very short-lived chlorinated substances. Cl_y includes the reservoir species (HCl and $ClONO_2$) and active chlorine species (i.e., ClO_x). The active chlorine species drive catalytic cycles that deplete ozone in the polar winter stratosphere. This work presents calculations of inorganic chlorine (Cl_y) derived from chlorinated source gas measurements on board the High Altitude and Long Range Research Aircraft (HALO) during the Southern Hemisphere Transport, Dynamic and Chemistry (SouthTRAC) campaign in austral late winter and early spring 2019. Results are compared to Cl_y in the Northern Hemisphere derived from measurements of the POLSTRACC-GW-LCYCLE-SALSA (PGS) campaign in the Arctic winter of 2015/2016. A scaled correlation was used for PGS data, since not all source gases were measured. Using the SouthTRAC data, Cl_y from a scaled correlation was compared to directly determined Cl_y and agreed well. An air mass classification based on in situ N_2O measurements allocates the measurements to the vortex, the vortex boundary region, and midlatitudes. Although the Antarctic vortex was weakened in 2019 compared to previous years, Cl_y reached 1687 ± 19 ppt at 385 K; therefore, up to around 50 % of total chlorine was found in inorganic form inside the Antarctic vortex, whereas only 15 % of total chlorine was found in inorganic form in the southern midlatitudes. In contrast, only 40 % of total chlorine was found in inorganic form in the Arctic vortex during PGS, and roughly 20 % was found in inorganic form in the northern midlatitudes. Differences inside the two vortices reach as much as 540 ppt, with more Cl_y in the Antarctic vortex in 2019 than in the Arctic vortex in 2016 (at comparable distance to the local tropopause). To our knowledge, this is the first comparison of inorganic chlorine within the Antarctic and Arctic polar vortices. Based on the results of these two campaigns, the differences in Cl_y inside the two vortices are substantial and larger than the interannual variations previously reported for the Antarctic.

1 Introduction

The Antarctic ozone hole is a recurring event that was first documented by Farman et al. (1985) and has been observed annually since the 1980s. Polar ozone depletion is predominantly driven by anthropogenic chlorine and bromine from long-lived halogenated species (Molina and Rowland, 1974; Engel et al., 2018b). The primary mechanisms for the depletion of ozone (O_3) in the polar stratosphere are the catalytic cycles with halogen-containing free radicals as chain carriers (Molina et al., 1987). Chlorine substances involved in rapid ozone depletion are Cl, Cl_2, ClO, and ClOOCl and can be summarized as ClO_x. Additionally, hydrogen chloride (HCl) and chlorine nitrate ($ClONO_2$) contribute to ozone depletion as they enable the production of active chlorine through heterogeneous reactions on polar stratospheric clouds (PSCs) during polar winter with low temperatures (e.g., Crutzen and Arnold, 1986; Molina et al., 1987; Solomon, 1999). They are therefore called reservoir species. Chemically active chlorine (ClO_x) and the reservoir gases together form the to-

tal inorganic chlorine (Cl_y), also called available chlorine. Equivalent effective stratospheric chlorine (EESC) is a simple metric that sums the effect of ozone-depleting substances (ODSs) as an equivalent amount of inorganic chlorine in the stratosphere (Newman et al., 2007; Daniel et al., 1995). Changes to the EESC are mainly due to Cl_y, as Br_y makes up a smaller fraction (Strahan et al., 2014).

The size of the Antarctic ozone hole varies and depends on the amount of Cl_y and on stratospheric temperature and dynamics (e.g., Newman et al., 2004). However, Cl_y data are sparse in the polar stratosphere, and there are few measurements of total organic chlorine (CCl_y) in this area. In contrast, there are many more observations from, e.g., remote sensing instruments of nitrous oxide (N_2O), which can be used to determine Cl_y. A common tool to determine Cl_y is the usage of scaled correlations. Strahan et al. (2014) used Microwave Limb Sounder (MLS) N_2O measurements and a scaled correlation between N_2O and Cl_y from Schauffler et al. (2003) to show that inter-annual variability of Cl_y for 2004–2012 (-200 to $+150$ ppt) can be up to 10 times larger than the expected 20–22 ppt yr^{-1} decline rate due to the Montreal Protocol. Strahan and Douglass (2018) again used MLS measurements of O_3, HCl, and N_2O to show that Antarctic Cl_y levels have decreased by 223 ± 93 ppt over a 9-year period (2013–2016 compared to 2003–2007), equivalent to an annual rate of 25 ± 10 ppt yr^{-1} (~ 0.8 % yr^{-1}). It is thus important to know whether and how correlations can be transferred from another time period and possibly another region (i.e., the other hemisphere). Due to the phase-out of the long-lived chlorinated species, Cl_y shows a long-term negative trend (e.g., Newman et al., 2007), whereas N_2O exhibits a positive trend (Engel et al., 2018b). This leads to a changing relationship between Cl_y and N_2O with time that must be taken into account. The concept of mean arrival time (Γ^*) can be used to normalize correlations of chemically active tracers and scale them to the time of interest (Plumb et al., 1999). The normalized correlations do not change with time and the resulting scaled correlations are used to calculate Cl_y.

Ozone destruction in the stratosphere is closely linked to the polar vortex. Due to a temperature difference and consequently to a latitudinal pressure gradient between the polar and midlatitude stratosphere (e.g., Schoeberl and Hartmann, 1991), a state with a strong westerly wind in the stratosphere is established (polar night jet). This jet acts as a transport barrier, leading to strong latitudinal gradients of potential vorticity and long-lived substances like N_2O (e.g., Hartmann et al., 1989). This isolation of the vortex leads to different concentrations of trace gases within the vortex compared to those in the stratosphere of the midlatitudes. The effect is further enhanced by diabatic descent over the winter, leading to substantially different distributions of trace gases inside and outside the vortex on the same potential temperature (Θ) surface. The polar vortex core can thus be described as a quasi-isolated vessel, separated from the midlatitude stratosphere by the vortex boundary region. In order to differentiate between air masses inside and outside the vortex, a classification of the measurements is needed.

In this study, inorganic chlorine (Cl_y) was quantified in the Arctic and Antarctic vortex. Calculations of Cl_y are based only on long-lived chlorinated substances. There is an additional contribution to total stratospheric chlorine from the very short-lived chlorinated substances. Engel et al. (2018b) estimated a contribution of 115(75–169) ppt from very short-lived substances for 2016. Hossaini et al. (2019) estimated a contribution of about 111 ± 22 ppt, of which 13 ± 4.6 ppt are already in inorganic form, which is not considered in this analysis. A new air mass classification system was used for this purpose, based on high-resolution in situ measurements during the campaigns, to map measurements to the vortex, vortex boundary region, and midlatitudes. Results of the Southern Hemisphere Transport, Dynamic and Chemistry (SouthTRAC) campaign from the Antarctic winter and spring 2019 are used to compare Cl_y of the Southern Hemisphere with Cl_y of the Northern Hemisphere from measurements of the POLSTRACC-GW-LCYCLE-SALSA (PGS) campaign in the Arctic winter of 2015/2016. An overview of the atypical Antarctic vortex 2019 can be found in Wargan et al. (2020). The evolution of the 2015/2016 Arctic vortex is reported in Manney and Lawrence (2016). Since not all source gases were measured during PGS, a scaled correlation was used and showed the capability of this method as a proxy for sparse data in comparison to the determination from the source gases used for SouthTRAC measurements. Section 2 is a brief introduction to the SouthTRAC campaign and the observations used for this study. Section 3 explains the identification of the vortex, vortex boundary, and midlatitude region. The derivation of inorganic chlorine and the comparison of the methods, the distribution during the late Antarctic winter of 2019, and the comparison of Arctic and Antarctic Cl_y are all discussed in Sect 4. Section 5 sums up and concludes the findings.

2 The SouthTRAC campaign

In late winter and early spring of 2019, the Southern Hemisphere Transport, Dynamics, and Chemistry (SouthTRAC) campaign took place to investigate dynamical and chemical composition aspects of the Antarctic upper troposphere and lower stratosphere (UTLS) and gravity waves up to the mesosphere (Rapp et al., 2020). Flights were performed with the German High Altitude and LOng Range Research Aircraft (HALO), which is capable of reaching an altitude of around 14.5 km or 420 K potential temperature. To meet the dynamical and chemical objectives (see https://www.pa.op.dlr.de/southtrac/home/science/scientific-objectives/, last access: 22 November 2021), the aircraft was based in Rio Grande, Argentina (RGA, 53° S, 67° W). Thus, regions of gravity wave breaking (southern Atlantic and eastern Pacific) and Antarctica were in the range of the aircraft. The cam-

paign was split into two phases. The first phase took place from 6 September to 9 October 2019 to target the dynamical objectives (e.g., Rapp et al., 2020). The second phase took place from 2 to 15 November 2019 to sample polar vortex remnants, as well as perform other tasks. Furthermore, the transfer flights were part of the scientific flights and provide additional information for all objectives.

HALO performed 23 scientific flights with in total 183 hours of measurement time. Nine of these flights were transfer flights from Oberpfaffenhofen (EDMO), Germany, to Rio Grande (RGA), Argentina, and back via Sal (SID), Cabo Verde, and Buenos Aires (EZE), Argentina (see Fig. 1a). Within the first transfer from EDMO to RGA, there was an additional local flight operated from SID. The remaining flights were local flights, with 10 in the first phase and 3 in the second phase. The second phase was terminated early due to technical problems but still provided 27 h of measurements. Thus, it was possible to investigate a region of around 36–70° S and 32–84° W (see Fig. 1b). The airplane reached a maximum potential temperature of 409 K during the campaign.

The following is a brief explanation of the meteorological data and the instruments and types of measurements used for this work.

2.1 Meteorological data

HALO was equipped with a wide range of in situ and remote sensing instruments. In addition to the scientific instruments installed for the measurement campaign, the Basic Halo Measurements and Sensor System (BAHAMAS) is part of HALO. BAHAMAS is installed permanently and provides meteorological and aircraft parameters along the flight trajectory (DLR, 2020).

The local tropopause information along the flight tracks of HALO was created using the Chemical Lagrangian Model of the Stratosphere (CLaMS) (e.g., Grooß et al., 2014). The underlying meteorological data are taken from ECMWF ERA-5 (Hersbach et al., 2020). In this work, the potential vorticity (PV)-based dynamical tropopause is used (e.g., Gettelman et al., 2011), taking 2 PVU (potential vorticity unit) for the dynamical tropopause. Since the PV tropopause is not physically meaningful in the tropics, the potential temperature level of 380 K was taken as the tropopause if the 2 PVU level lies above.

2.2 Halocarbons and SF_6

The Gas chromatograph for Observational Studies using Tracers (GhOST) is a two-channel gas chromatographic instrument. The first channel combines an isothermally operated gas chromatograph (GC) with an electron capture detector (ECD) to measure SF_6 and CFC-12 at a time resolution of 1 min (hereinafter referred to as GhOST-ECD). A similar setup was used during the SPURT campaign (Bönisch et al., 2009; Engel et al., 2006). The second channel is a combination of temperature programmed GC with a quadrupole mass spectrometer (QP-MS, hereinafter referred to as GhOST-MS). Because of very small mole fractions of the halocarbons, a cryogenic pre-concentration system is installed prior to the GC (Obersteiner et al., 2016; Sala et al., 2014). GhOST was operated successfully during several aircraft campaigns to mainly target brominated halocarbon species, as discussed in Keber et al. (2020). For the SouthTRAC campaign, the ionization mode was changed from negative chemical ionization (NCI) to electron impact ionization (EI) to record full mass spectra. For each substance, one molecular fragment is selected for which the chromatographic peak is not disturbed by other substances. Furthermore, the MS was operated in selected ion monitoring (SIM), scanning pre-selected mass fractions at a preset retention time window. A larger sample volume is needed in EI mode compared to NCI mode. The change of ionization decreased the time resolution from 4 to 6 min per measurement cycle, of which 147 s are needed for sampling air. The performance of the GhOST-MS channel for the chlorinated substances used in this work is shown in Table 1. Displayed are the precisions and detection limits measured shortly before the campaign in the laboratory. Additionally, based on in-flight calibration, precision during the flight can also be calculated. As the conditions in the airplane are more variable than in a laboratory, especially when changing the flight level, this affects the precision of the measurements. The frequency of calibration measurements during a flight is much lower than in the laboratory, making it less stable than the laboratory value. Therefore, precision drops for most of the substances by up to a factor of 4. The exceptions are CFC-11, CFC-113, and methyl chloroform. Methyl chloroform shows a significantly better precision during the campaign, whereas the precision of CFC-12 and CFC-113 measurements was much poorer. It is difficult to determine exactly what the poorer precisions of these two substances can be attributed to. The chromatographic peak of CFC-11 is very narrow, and variable environmental conditions (due to changes in altitude, pressure, and temperature in the cabin) have an influence on the peak shape. The amount of water in the analysis system is also important and is kept as low as possible by drying before pre-concentration. As the chromatographic peak of CFC-113 is close to the chromatographic peak of water, small changes in water can affect the chromatographic peak of CFC-113. CFC-12 and SF_6 with the GhOST-ECD channel were measured with a precision of 0.2 % and 0.64 %, respectively. The instrument was tested for nonlinearities and memory effect, and correction was done where necessary (see Sala et al., 2014, for details). Mixing ratios in this work are reported as dry mixing ratios on AGAGE (Advanced Global Atmospheric Gases Experiment) scales.

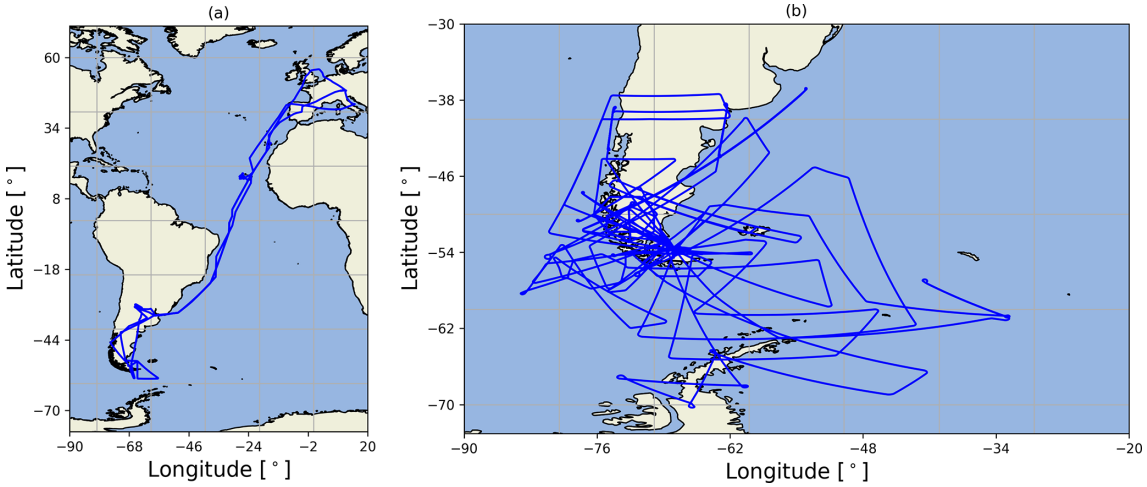

Figure 1. Flight tracks of HALO of **(a)** the transfers from and to Oberpfaffenhofen, Germany (48° N, 11° E) and **(b)** during the two phases with the base in Rio Grande, Argentina (53° S, 67° W).

Table 1. Chlorinated species measured with the GhOST-MS. The precisions and limit of detections (LODs) of GhOST were determined in the laboratory shortly before the SouthTRAC (ST) campaign, and mean precision was calculated during the flights.

		Laboratory		ST
Name	Formula	Prec. (%)	LOD (ppt)	Prec. (%)
CFC-11	CCl3F	0.22	0.36	1.13
CFC-12	CCl2F2	0.30	0.47	0.71
CFC-113	C2Cl3F3	0.64	0.18	2.93
Methyl chloride	CH3Cl	0.39	0.76	1.11
Tetrachloromethane	CCl4	0.44	0.22	0.98
Methyl chloroform	CH3CCl3	8.67	0.53	3.76
HCFC-22	CHClF2	0.41	1.31	0.84
HCFC-141b	C2H3Cl2F	0.82	0.39	1.23
HCFC-142b	C2H3ClF	0.84	0.50	1.63

2.3 N_2O

Measurements of N_2O were performed with the University of Mainz Airborne Quantum Cascade Laser-spectrometer (UMAQS), which also provided data for CH_4, CO, CO_2, and OCS during SouthTRAC. The instrument is based on direct absorption spectroscopy using a continuous-wave quantum cascade laser with a sweep rate of 2 kHz (Müller et al., 2015). During SouthTRAC the instrument was calibrated in situ against two standards of different concentrations, which are compared against primary standards (NOAA) prior to and after campaign phases.

Under typical flight conditions at flight level, N_2O was measured with an overall uncertainty of 0.6 ppb relative to the calibration standards. The noise of the 1 Hz data was 0.1 ppb (1σ). Note that this is an upper limit since the data are corrected post-flight for drift effects based on the in-flight calibrations.

3 Defining vortex, vortex boundary, and midlatitude region

Chlorine activation tends to occur in the coldest regions of the stratosphere and is therefore typically co-located with the polar vortex. Furthermore, as the polar night jet acts as a barrier, air composition is different inside and outside the vortex. High concentrations of reactive halogenated substances can be maintained inside the vortex because there is little mixing with the surrounding area. During the HALO flights, the aircraft encountered air masses with different characteristics due to their origin. To make systematic conclusions about the distribution of trace gases, a reliable, accurate method of separating the measurements in terms of their region of origin is needed. For this reason, the following describes how air masses have been classified using highly resolved in situ measurements.

3.1 Air mass classification by in situ measurements

The maximum gradient of PV is a commonly used indicator to define the location of the vortex edge, also known as the Nash criterion (Nash et al., 1996). PV is a model-derived quantity. Although the underlying meteorological reanalyses have a fairly high resolution these days (e.g., Hersbach et al., 2020), small-scale features like vortex filaments with different chemical compositions may not be well resolved. In this work, an extended version of the vortex definition by Greenblatt et al. (2002) is used instead. The technique by Greenblatt et al. (2002) uses the tight correlation between N_2O and potential temperature to determine the inner edge of the vortex boundary. N_2O can be measured in situ with

a high time resolution to reveal small-scale structures in the atmosphere. As already mentioned in Sect. 1, air inside the polar vortex has a substantially different composition regarding trace gases than air outside the vortex. A tracer like N_2O exhibits a horizontal gradient across the vortex edge in the stratosphere with lower mixing ratios inside the vortex and higher mixing ratios outside the vortex. In addition, N_2O has small variability inside the vortex on constant isentropic surfaces (variability of about 6 ppb Greenblatt et al., 2002). This is an indication of well-mixed air inside the polar vortex due to the long isolation in polar winter. The vertical profile of N_2O in the midlatitudes shows a weak gradient but a high variability as it is influenced by both tropical and polar air (Krause et al., 2018; Marsing et al., 2019). In between there is a transition region (vortex boundary region), which is influenced by the vortex as well as by midlatitudes. Towards tropopause altitudes, the transport barrier of the polar vortex disappears and a classification is not possible.

Based on the method of Greenblatt et al. (2002), one flight is chosen to generate a vortex reference profile. This flight should ideally be completely in the vortex. However, during the SouthTRAC campaign there was no flight that only sampled vortex air. In addition, there is an interest in not only distinguishing between vortex and non-vortex air, but also in assigning the campaign measurements to the vortex, vortex boundary region, and midlatitudes. For this reason, several flights were used to create reference profiles for the vortex and midlatitudes. The composition of the lowermost stratosphere is affected by diabatic descent inside and outside the polar vortex and quasi-isentropic mixing with air from lower latitudes. In addition, mixing at the extratropical tropopause affects the lowest 20–25 K above the local tropopause (Hoor et al., 2004, 2005). Therefore, classification was done with two vertical coordinates, potential temperature (Θ) and potential temperature above the local tropopause ($\Delta\Theta$).

The vortex reference profile (see Fig. 2) was generated from all flights that are assumed to contain measurements within vortex air. Data from these flights were pre-filtered by taking only the measurements polewards of 60° S equivalent latitude (Butchart and Remsberg, 1986) and 20 K above the local tropopause. With an iterative filter procedure (see Appendix A) the lower envelope of the remaining measurements is obtained and is used to generate the vortex profile function (Werner et al., 2010). For the midlatitude profile (see Fig. 2), all flights were taken into account, focusing only on measurements between 40 and 60° S equivalent latitude and again 20 K above the local tropopause. This time, the upper envelope of the measurements was evaluated by the iteration procedure to build a reference profile function for the midlatitudes. As an intermediate step to the final profiles, the measurements of the lower and upper envelope are binned in 5 K intervals of Θ or $\Delta\Theta$ (see Fig. S2c and d). Mean values of the binned profiles are then used to generate a polynomial fit function for the vortex profile and the midlatitude profile (Fig. S3). The two reference profiles in Θ coordinates are displayed in Fig. 2a, and the two reference profiles in $\Delta\Theta$ coordinates are displayed in Fig. 2b.

In general, it cannot be assumed that a single N_2O vortex profile can be representative for the entire winter. Subsidence of the vortex air by several kilometers due to radiative cooling (Schoeberl and Hartmann, 1991) leads to a changing N_2O profile throughout the polar winter. In the lower stratosphere of the Southern Hemisphere, descent generally stops around mid-October (Manney et al., 1994). However, N_2O data of the SouthTRAC flights did not reveal strong diabatic descent during the time of the campaign (below $\Theta = 400$ K). Therefore, only one reference vortex profile was generated for the campaign.

A vortex and midlatitude reference N_2O data set (N_2O_{vor} and N_2O_{mid}) can be calculated from Θ or $\Delta\Theta$ by using the fit function for the vortex and midlatitude profiles for every measurement point of the UMAQS instrument for all flights. The following then applies for each N_2O measurement: if the mixing ratio is below the respective N_2O_{vor} plus the prescribed vortex cutoff, then it is assigned to the vortex. Otherwise, if the mixing ratio is above the respective N_2O_{mid} minus the associated variability, then it is assigned to the midlatitudes. Mixing ratios above the respective N_2O_{vor} plus the prescribed vortex cutoff and below the respective N_2O_{mid} minus the associated variability are assigned to the boundary region. Measurements for which the respective N_2O_{vor} plus the prescribed vortex cutoff and the N_2O_{mid} minus the associated variability overlap cannot be uniquely classified and are assigned to both the vortex and the midlatitudes in later analysis. For the prescribed vortex cutoff, the value of 20 ppb proposed by Greenblatt et al. (2002) was used. The associated variability of the midlatitude profile was set to 15 ppb, as the variability in N_2O in the midlatitudes is roughly 10 % (Strahan et al., 1999).

3.2 Overview of the sample regions

In 2019, extraordinary meteorological conditions led to a sudden rise in stratospheric temperatures over Antarctica. This minor sudden stratospheric warming (minor SSW) event affected the shape, location, and strength of the polar vortex. From mid-August to early September 2019, the polar vortex was displaced and weakened towards the eastern South Pacific and South America (Safieddine et al., 2020; Wargan et al., 2020). The SouthTRAC campaign flights took place from early September to early October and in the first half of November; thus, they took place shortly after the minor SSW event and captured the late winter evolution of the Antarctic polar vortex.

Figure 3 displays an overview of air mass classification of the local flights of the SouthTRAC campaign (classification in Θ coordinates). Measurements below 20 K of $\Delta\Theta$ are not classified and are not taken into account here. There are no N_2O measurements available from flight ST08 on 11 September, and thus no classification was possible. Vortex

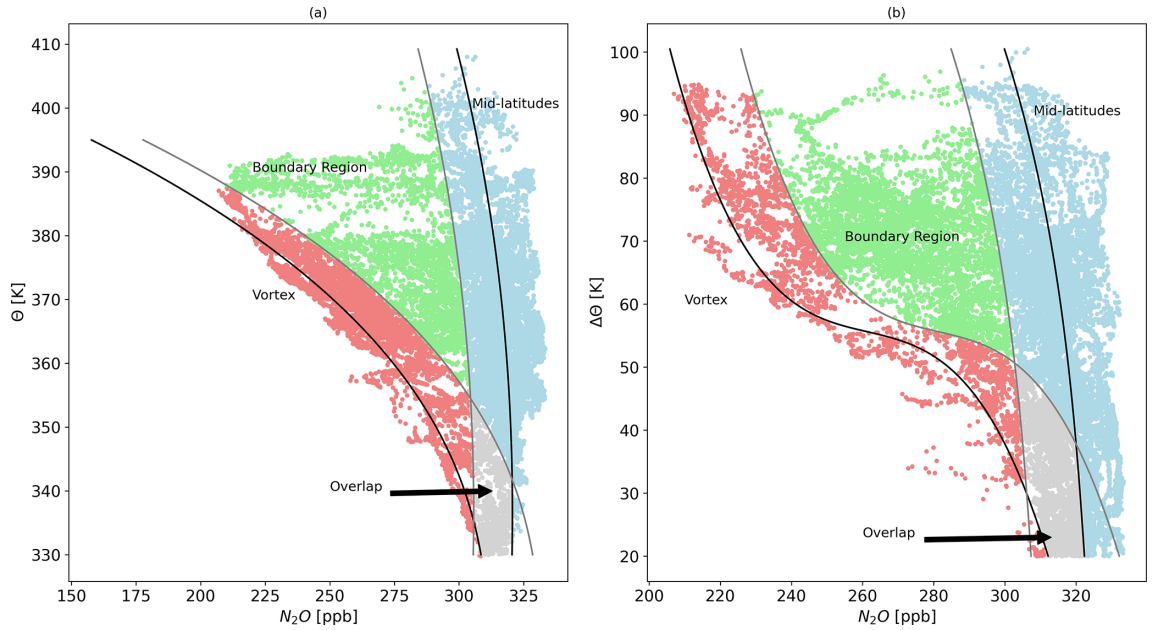

Figure 2. Midlatitude and vortex profiles (black) of N_2O versus **(a)** potential temperature (Θ) and **(b)** potential temperature difference ($\Delta\Theta$) from the local PV tropopause. The vortex cutoff criterion (see main text for details) of 20 ppb is illustrated by the grey profile on the right side of the vortex profile. Midlatitude variability of 15 ppb is illustrated with the grey profile on the left side of the midlatitude profile. In between these is the vortex boundary region. The overlap region is declared for the area where the vortex cutoff and midlatitude variability cross. Additionally, N_2O measurements classified to the respective region are displayed. Vortex measurements are in red, vortex boundary region measurements are in green, midlatitude measurements are in blue, and overlapping measurements are in grey.

air sampling varies from flight to flight depending on the objective of each flight. The vortex and boundary regions were sampled in both phases of the campaign. The first phase includes some flights that predominantly sampled the vortex or vortex boundary region (e.g., flight ST15 on 29 September or flight ST16 on 30 September). In general, vortex air represents about 23 % of flight time in the stratosphere and vortex boundary air about 14 %. More than half (56 %) of the flight time in the stratosphere was in midlatitude air. The use of the $\Delta\Theta$ coordinates for the air mass classification leads to similar percentage division (not shown here).

4 Inferred inorganic chlorine

4.1 Up-sampling GhOST-MS measurements

The GhOST-MS measurements have a time resolution of 6 min of which the enrichment and therefore the sampling of air takes around 147 s. With a maximum cruising speed of around 258 m/s, this means that air is sampled along a distance of approximately 38 km per measurement during enrichment. This could lead to a rather coarse resolution where fine structures like filaments and small-scale dynamical perturbations are sometimes not well resolved.

Measuring CFC-12 in both the ECD and MS channels of the instrument allows the measurements of the organic source gases to be up-sampled by using the better-resolved measurements of CFC-12 from the ECD channel. Measurements of CFC-12 in the ECD channel not only have a higher time resolution of 1 min, but they also have better precision than data from the MS channel. As shown in Fig. 4, the correlation between CFC-12 measurements of the two channels for all flights is linear over the whole range of mixing ratios, with a coefficient of determination of $R^2 = 0.968$. Firstly, for each organic source gas, a linear or polynomial fit function is calculated based on the correlation with CFC-12 measurements in the GhOST-MS channel for all flights (correlations contained in the supporting information). Secondly, these fit functions are then used together with the CFC-12 measurements of the ECD channel to calculate the up-sampled mixing ratios of the organic source gases. Flight ST14 from 26 September in Fig. 5 is an example to demonstrate the benefits of the up-sampling. Displayed are the original measurements of CFC-11 of the MS channel as well as the up-sampled CFC-11 values. The background colors indicate to which region the samples can be assigned (classification in Θ coordinates), as described in Sect. 3. The up-sampled values show higher variability and follow the classification well by region. Especially with the sharp gradients, e.g., at 04:10 and 05:50 UTC in Fig. 5, the original lower-resolution data did not capture the transitions well between the regimes compared to the up-sampled data. In the following, the up-sampled data are used for further evaluation.

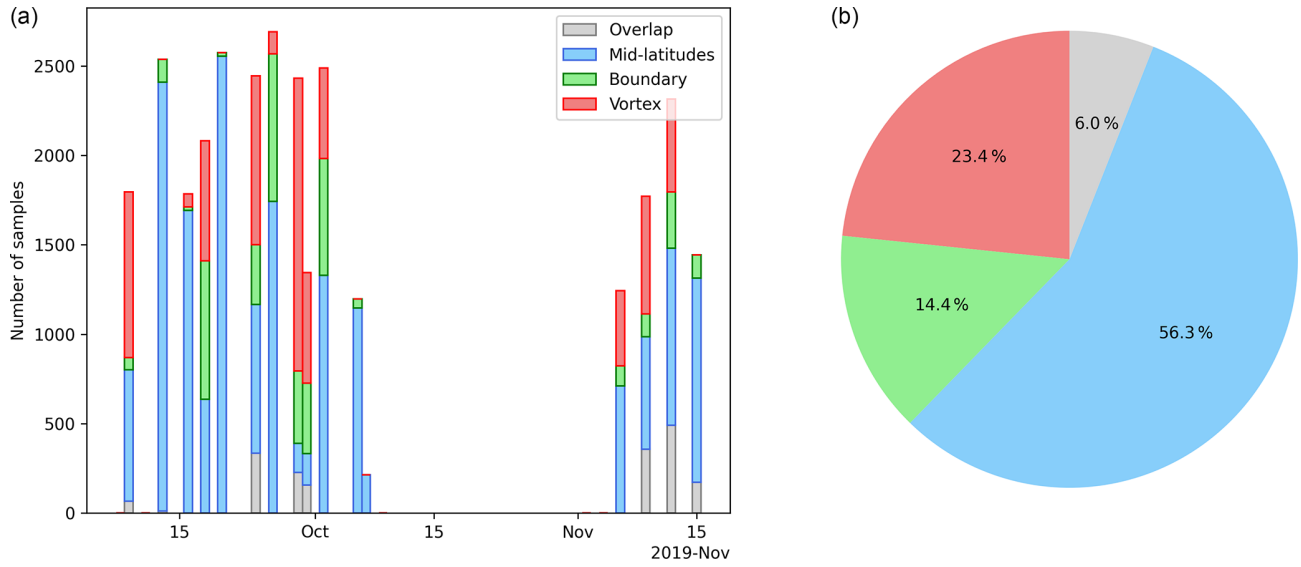

Figure 3. Air sampling statistics of the SouthTRAC campaign. **(a)** The number of classified measurements. Each column represents a single scientific flight. Stacked bars indicate vortex (red), vortex boundary (green), midlatitudes (blue), and undefined (grey) amounts. **(b)** Percentage of each region in the total of all measurements in the scope of the classification (above $\Delta\Theta$ of 20 K).

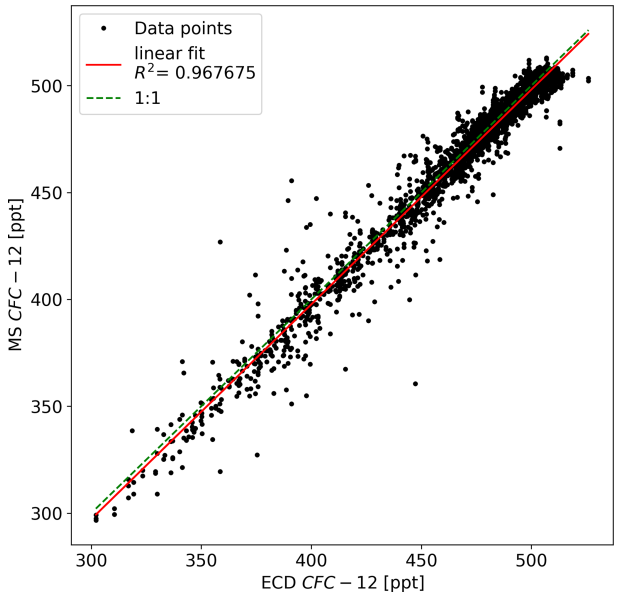

Figure 4. Correlation between CFC-12 measured in the GhOST-MS channel and in the GhOST-ECD channel.

4.2 Semi-direct and indirect calculation of inorganic chlorine

Organic chlorine (CCl_y) can be calculated directly from the up-sampled GhOST-MS measurements. Thus, Cl_y can be calculated from Eq. (1) if the mixing ratios of the major chlorine-containing substances at the stratospheric entry point (Cl_{total}) are known.

$$\chi_{Cl_y} = \chi_{Cl_{total}} - \chi_{CCl_y} \quad (1)$$

Air enters the stratosphere predominantly through the tropical tropopause layer (TTL). During transport into and within the stratosphere, an air parcel exhibits irreversible mixing and cannot be regarded as conserved (Hall and Plumb, 1994). Instead, an air parcel in the stratosphere consists of a multitude of components with different transit times, representing their travel times since they entered the stratosphere. The distribution of the transit times is called the age spectrum G, and the first moment is the mean age Γ (Hall and Plumb, 1994). The concept of the age spectrum can be used to determine mean age values based on observations of chemically inert tracers in the stratosphere. For this purpose, in addition to the age spectrum, tropospheric time series of the inert tracers are required (Engel et al., 2002). This was done for the SouthTRAC campaign by using SF_6 measurements of the GhOST-ECD and tropospheric time trends taken from the AGAGE (Advanced Global Atmospheric Gases Experiment) Network (Prinn et al., 2018). Since only the mean age is given, a width parameterization is used to derive the age spectrum by using the ratio of moments (Δ^2/Γ). Hauck et al. (2019) showed that the ratio of moments undergoes seasonal variability and is probably much larger than previously implemented values (e.g., Engel et al., 2002; 0.7 years). A ratio of moments of 1.25 years is chosen here. The age spectrum, together with the tropospheric time trend of the substances of interest, can be used to calculate the stratospheric mixing ratio that would be present without chemical degradation, which thus represents the entry mixing ratio. In the following, Cl_y derived from the difference between the esti-

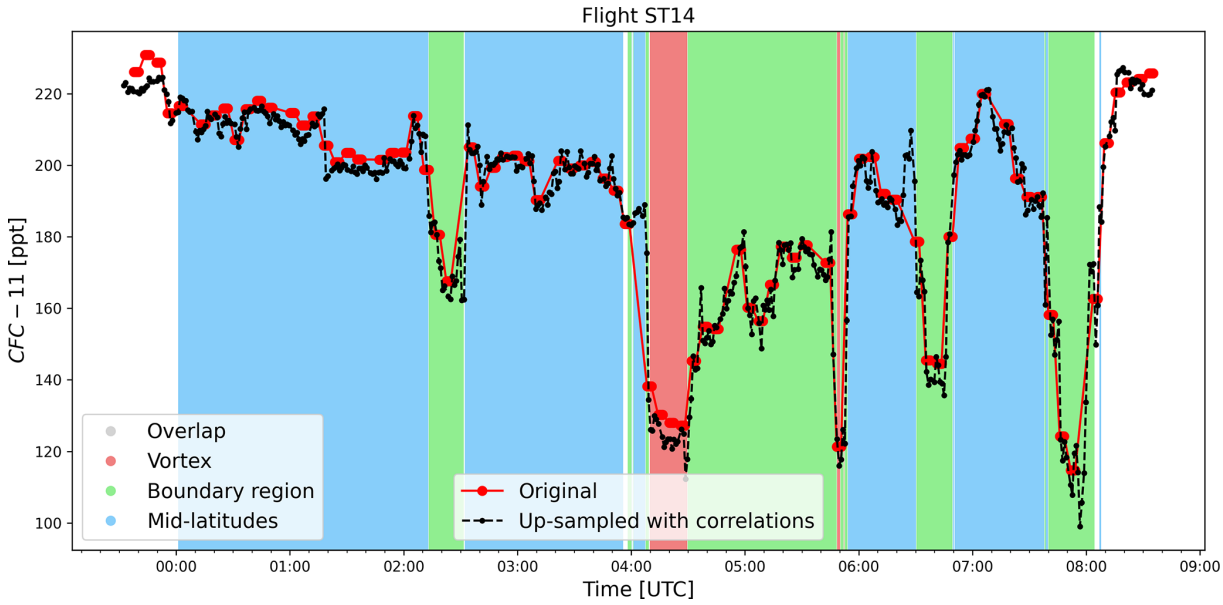

Figure 5. CFC-11 measured in the GhOST-MS during flight ST14 on 26 September 2019. Original data are shown in red, and measurements up-sampled using CFC-12 from the ECD channel are shown in black. Background colors indicate in which region the samples were taken using the air mass classification in Θ coordinates.

mated entry mixing ratios and observed CCl_y from the in situ measurements (see Eq. 1) is referred to as the semi-direct calculation of Cl_y.

For the case where measurements of all major chlorine-containing substances are not available, Cl_y has in the past been calculated indirectly based on correlations derived from previous measurement campaigns. This also applies to Cl_y from the Northern Hemisphere used later in this paper (see Sect. 4.4). For instance Wetzel et al. (2015) and Marsing et al. (2019) used Cl_y based on a correlation derived from two balloon flights inside the Arctic polar vortex in 2009 and 2011 from a cryogenic whole-air sampler (Engel et al., 2002). In order to account for tropospheric trends, the correlations between CFC-12 and the other long-lived substances were adapted with a modified method described in Plumb et al. (1999) using the mean arrival time Γ^* to derive a correlation function valid for the respective time when the correlation is applied. Plumb et al. (1999) showed that the age spectrum of an inert tracer is not well suited to describe the propagation of chemically active tracers into and through the stratosphere. They introduced a modified age spectrum, called the normalized arrival time distribution G^*, which combines chemical loss and transport. The mean arrival time Γ^* represents the first moment of this distribution. The mean arrival time Γ^* for all the relevant chlorine substances can be parameterized in terms of stratospheric lifetime τ and mean age Γ (Plumb et al., 1999). Using G^* instead of G and therefore Γ^* instead of Γ is better suited for chemically active tracers because the tail of the transit time distribution is less weighted, especially for substances with shorter stratospheric lifetimes (Engel et al., 2018a; Ostermöller et al., 2017). To transfer the correlations from the balloon observations in 2009 and 2011 to the measurements during SouthTRAC in 2019, the observed mixing ratios are first divided by the respective estimated entry values to derive the normalized mixing ratios. The entry values are calculated by the modified age spectrum and tropospheric time trends from the AGAGE Network for the time of the balloon measurements. Multiplying the normalized mixing ratios by the entry mixing ratio for the time during SouthTRAC then allows a comparison to the directly determined correlations during SouthTRAC. Here, we compare the directly observed correlation from SouthTRAC to the indirectly determined correlations based on previous balloon observations transferred to 2019. Note that the indirectly determined values are based on observations that were not only performed about 10 years earlier but that were also from the Northern Hemisphere instead of the Southern Hemisphere. Figure 6 displays scaled correlations from the balloon observations (red) and correlations from the SouthTRAC data (black) of three long-lived substances against CFC-12. The balloon-based correlations correspond well to the correlations measured during the SouthTRAC campaign. Thus, the balloon-based correlations can be used to determine CCl_y from CFC-12 alone. As already mentioned earlier, Cl_{total} is also needed for the calculation of Cl_y (see Eq. 1). The mean age values derived for the balloon measurements are used for this purpose, and Cl_{total} is calculated for the conditions during SouthTRAC. Cl_y is then derived as the difference between Cl_{total} and CCl_y.

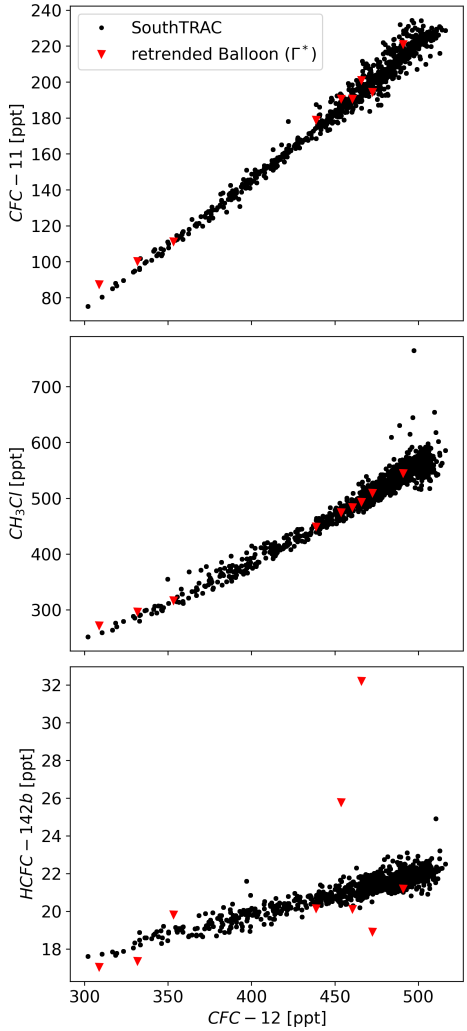

Figure 6. Correlation between CFC-12 and CFC-11, between CFC-12 and CH_3Cl, and between CFC-12 and HCFC-142b. The raw measurements by GhOST-MS are shown in black, and the balloon observations scaled to the time of the SouthTRAC campaign using mean arrival time are shown in red.

With the good agreement between observed correlations and scaled correlations from the balloon measurements and the previously described determination of Cl_y, we explore whether Cl_y can be successfully estimated from CFC-12 alone. Therefore, a correlation function for the conditions during Antarctic late winter 2019 has then been derived for the indirect calculation of Cl_y as a function of CFC-12 mixing ratios (Eq. 2). The coefficients for the correlation function with CFC-12 as the reference substance based on the balloon measurements can be taken from Table 2. In addition, the fit coefficients are given if one wants to use N_2O as the reference. N_2O shows a compact correlation with long-lived chlorinated substances and has been used in many publications for the determination of Cl_y (e.g., Schauffler et al., 2003; Strahan et al., 2014; Strahan and Douglass, 2018). Using CFC-12 from the GhOST-ECD channel and N_2O from the UMAQS instrument, we obtain comparable values for Cl_y (see Fig. S7 in the supporting information). In the following, CFC-12 from the GhOST-ECD channel is used as the reference in Eq. (2) for the indirect determination of inorganic chlorine.

$$\chi_{Cl_y} = c_0 + c_1 \chi_{ref} + c_2 (\chi_{ref})^2 \quad (2)$$

Figure 7 shows semi-directly and indirectly determined inorganic chlorine as a function of mean age. Cl_y values were binned in intervals of 0.2 years, and the mean values are displayed. For both methods, inorganic chlorine increases with mean age of air as more molecules of the organic source gases are converted to the inorganic form. The difference between the two methods is rather small, with less than around 30 ppt difference between 1 and 4 years of mean age and a maximum difference of about 65 ppt at 5 years of mean age. Recent research suggests that SF_6-based mean age is biased because its suggested lifetime has been overestimated (e.g., Ray et al., 2017). As a guideline, Fig. 7 additionally shows a corrected mean age of air using one of the linear fit functions from Leedham Elvidge et al. (2018), based on a comparison of SF_6-based mean age with a combined mean age based on five alternative age tracers. The fundamental picture does not change, however, and thus we use the uncorrected mean age of air. The small deviation over the entire range of mean age indicates that adapted correlations from previous measurement campaigns and also from the Northern Hemisphere lead to comparable values in inorganic chlorine determined for the Southern Hemisphere. Hence the metric can be used for the calculations of Cl_y in the case where only measurements of CFC-12 are available. Since it was possible during SouthTRAC to measure the organic source gases, the Cl_y determined semi-directly from the measurements was used for further evaluation. However, the good comparability of the two methods offers the possibility to compare Cl_y from different measurement campaigns, which differ regarding the number of measured chlorinated substances (see Sect. 4.4). With the semi-directly determined Cl_y during SouthTRAC, correlation functions can be determined. Table 2 contains the coefficients for the correlation functions based on CFC-12 and N_2O as references. The correlation functions are limited to the minimum mixing ratio of the respective reference substance taken during the SouthTRAC campaign.

4.3 Chlorine partitioning in the Antarctic winter 2019 lower stratosphere

Since inorganic chlorine plays a major role in ozone depletion, it is worth investigating its distribution in the Antarctic stratosphere. For the analysis only measurements polewards of 40° equivalent latitude are used. As a vertical coordinate Θ was chosen. All measurements have been binned into 5 K potential temperature bins between 270 and 420 K (see Fig. 8). Bins that contain fewer than five data points are

Table 2. Coefficients of the correlation function to indirectly derive Cl_y with the respective reference substance for the time of the SouthTRAC campaign (2019.75). Calculation of Cl_y with CFC-12 or N_2O and coefficients based on the balloon observations in 2009 and 2011 (Balloon) and coefficients based on the SouthTRAC measurements (SouthTRAC).

Data source	χ_{ref}	c_0 [ppt]	c_1	c_2 [ppt^{-1}]
Balloon	CFC-12	2965.27	−2.80700	-6.06944×10^{-3}
Balloon	N_2O	2990.74	−2.16187	-2.10586×10^{-2}
SouthTRAC (limited to about 300 ppt)	CFC-12	3024.26	−2.61888	-6.87717×10^{-3}
SouthTRAC (limited to about 250 ppb)	N_2O	3884.40	−8.02682	-1.14510×10^{-2}

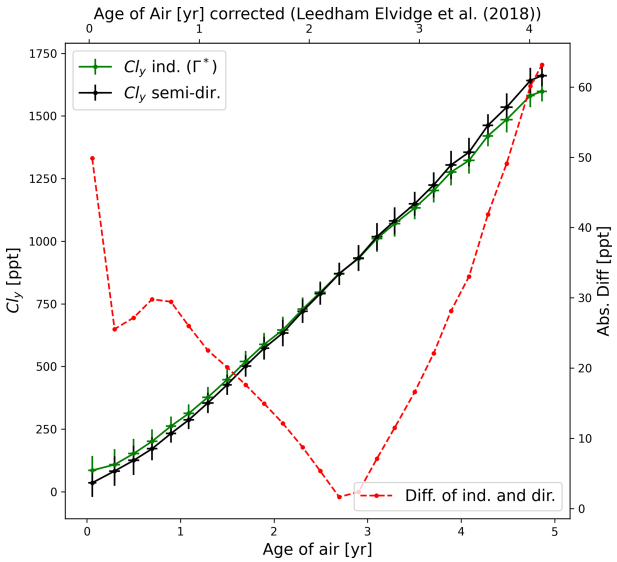

Figure 7. Indirectly (green) determined Cl_y based on balloon observations in 2009 and 2011 and semi-directly (black) determined Cl_y as a function of age of air (bottom axis) and corrected age of air (top) using a linear fit $y = 0.85x - 0.02$ from Leedham Elvidge et al. (2018). The absolute difference between these methods is shown in red.

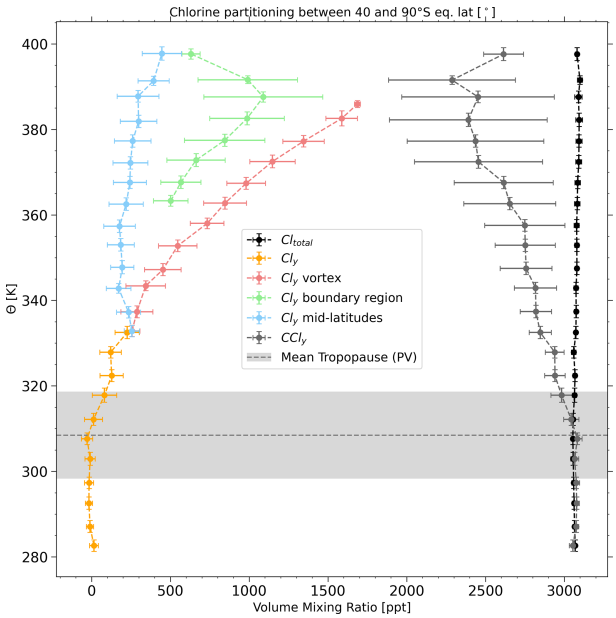

Figure 8. Vertical profiles of Cl_y, Cl_y by region from 20 K above the local tropopause, CCl_y, and Cl_{total} averaged over 40–90° S equivalent latitude for all flights during SouthTRAC. The data are displayed as a function of potential temperature. Vertical and horizontal error bars denote 1σ variability. The dashed line shows the averaged PV-based dynamical tropopause with the 1σ variability as a shaded area.

not included in the analysis. The uncertainties represented by the error bars are the 1σ standard deviations of the means. Up to the potential temperature at which air mass classification begins, the Cl_y is estimated based on all measurements. From the potential temperature at which air mass classification begins, Cl_y is estimated separately in each region. Measurements within the overlap area in the classification (see Fig. 2) are counted both as vortex and midlatitude measurements.

In Fig. 8, the inferred Cl_y throughout the troposphere is close to zero and increases in the tropopause region. The tropospheric measurements during SouthTRAC are thus consistent with Cl_{total} derived from ground-based AGAGE measurements. The vertical profiles of vortex, vortex boundary, and midlatitude declared measurements show different gradients. In the midlatitudes, the inorganic chlorine hardly increases between 330 and 380 K, with values between 171 ± 78 and 260 ± 117 ppt, whereas the increase is stronger between 380 and 400 K, reaching a value of 446 ± 124 ppt. The profile of the vortex boundary region increases in the range from 502 ± 110 up to 1090 ± 377 ppt in the Θ interval of 360 to 395 K. The variability of the vortex boundary profile increases with height. This is partly due to the air mass classification, since the range of values in the vortex boundary region increases with increasing potential temperature (see Fig. 2). Inorganic chlorine within the vortex could be ob-

tained from Θ between 330 to 385 K. Cl_y inside the vortex increases significantly up to a value of 1687 ± 19 ppt. Thus, in late winter and early spring at the highest measured potential temperatures, about half of the recorded chlorine is found in inorganic form. Despite this amount of inorganic chlorine in the lower stratosphere, the total polar ozone column was higher than usual in September 2019. As a result of the minor SSW event, chlorine deactivation began earlier in 2019, and the ozone hole was about 10×10^6 km^2 in size and thus only 20 % of that in mid-September 2018 (Wargan et al., 2020).

4.4 Comparison of Cl_y in the Antarctic (SouthTRAC) and Arctic (PGS) polar winter

To compare Cl_y in the Antarctic polar vortex and in the Arctic polar vortex, measurements performed on the HALO aircraft during the PGS campaign were used. PGS consisted of the three partial missions POLSTRACC (Polar Stratosphere in a Changing Climate), GW-LCYCLE (Investigation of the Life cycle of gravity waves), and SALSA (Seasonality of Air mass transport and origin in the Lowermost Stratosphere) to probe stratospheric air during the Arctic winter in 2015/2016 (Oelhaf et al., 2019). Flights of the PGS campaign were conducted from 17 December 2015 until 18 March 2016 and can be separated into two main phases. For this study, only the flights from the second main phase from 26 February to 18 March are investigated, since they took place in a comparable period (later winter). The separation into vortex, vortex boundary, and midlatitude measurements is based on the above-mentioned method using N_2O measurements performed by the TRIHOP instrument on board HALO during PGS (Krause et al., 2018) (see Fig. S6 in the Supplement). In Sect. 4.2, the indirect method for the determination of Cl_y, where a direct measurement of all relevant chlorinated substances is not possible, was shown to provide values comparable to those obtained by the semi-direct method. During PGS, CFC-12 was measured with the ECD channel, but the MS channel was in NCI mode and could not measure all chlorinated substances. Cl_y was therefore calculated using the indirect method and CFC-12 measurements from the GhOST-ECD channel during PGS. As for SouthTRAC, the scaled correlations from observations of the cryogenic whole-air sampling on two balloon flights inside the Arctic polar vortex in 2009 and 2011 were used (correlation function for the Arctic winter 2015/2016 can be taken from the Supplement).

Figure 9 displays the mean vertical profiles of Cl_y inside the vortex and Cl_{total} of the respective hemisphere. Measurements from the individual campaigns have been binned into 5 K potential temperature (a) and potential temperature difference to the local tropopause (b). The PV-based dynamical tropopause was used for PGS, as was done for the SouthTRAC analysis. The mean PV-based tropopause was at 306 K during PGS, only slightly lower than that during SouthTRAC at 308 K. Independent of the vertical coordinate, total chlorine (Cl_{total}) in the lower stratosphere decreased from the time of PGS (2015/2016) to the time of SouthTRAC (2019). The difference between Cl_{total} from controlled substances during PGS and that during SouthTRAC is about 60 ± 9.6 ppt. This difference can be explained by a combination of temporal trends of controlled substances and interhemispheric gradients. Using the rate of decline from Engel et al. (2018b) of -12.7 ± 0.9 ppt yr^{-1} for the controlled substances, a difference of about 45 ppt is expected due to the time difference between the two campaigns. The remaining difference of about 15 ppt can be explained by the higher Cl_{total} in the Northern Hemisphere.

Using Θ as the vertical coordinate (Fig. 9a), vertical profiles of vortex classified Cl_y of PGS and SouthTRAC show different results. Although the Cl_y vortex profiles are similar until around 350 K, the SouthTRAC profile increased more steeply, reaching values more than 444 ppt larger than those during PGS at the same potential temperatures. Differences are slightly larger when using ΔΘ as the vertical coordinate (Fig. 9b). Although the two Cl_y profiles lie close together between 20 and 50 K ΔΘ, the differences between them increase to 540 ppt at 65 K ΔΘ. The fraction of total chlorine in the form of Cl_y during PGS at the same distance from the local tropopause as the maximum SouthTRAC Cl_y fraction is about 20 % in the midlatitudes (not shown) and about 40 % inside the vortex (Fig. 9b).

Figure 10 shows the difference between PGS and SouthTRAC Cl_y in a latitude–altitude cross section. Equivalent latitude* was used as a horizontal coordinate, i.e., the geographic latitude for all tropospheric observations and equivalent latitude for all stratospheric ones (Keber et al., 2020); ΔΘ was used as a vertical coordinate. Since the tropopause height of the two hemispheres is different and changes with the season, the tropopause relative coordinate ΔΘ accounts for tropopause variability and allows for better comparison of Cl_y. The data have been binned in 5° latitude and 5 K of potential temperature relative to the local tropopause. Only bins which contain at least five data points were considered in this analysis. The difference was calculated by subtracting each Southern Hemispheric latitude–altitude bin from the equivalent Northern Hemispheric latitude–altitude bin. Values in the troposphere differ only slightly. In the lower stratosphere, a separation into two areas can be seen. In the lower stratosphere at higher latitudes, overall higher mixing ratios were derived during SouthTRAC in comparison to PGS. There are two bins with substantially higher values during SouthTRAC, with around 900 ppt more Cl_y between 80 and 90 K of ΔΘ and 65 to 70° equivalent latitude. This difference is much larger than the difference when comparing vortex classified measurements (Fig. 9). Thus, it is very likely that vortex core and vortex edge values are compared due to the different Arctic and Antarctic vortex size, stability, and strength of the transport barrier. Therefore, performing the comparison in equivalent latitude and potential temperature coordinates removes only some of the sources of discrepancy. The

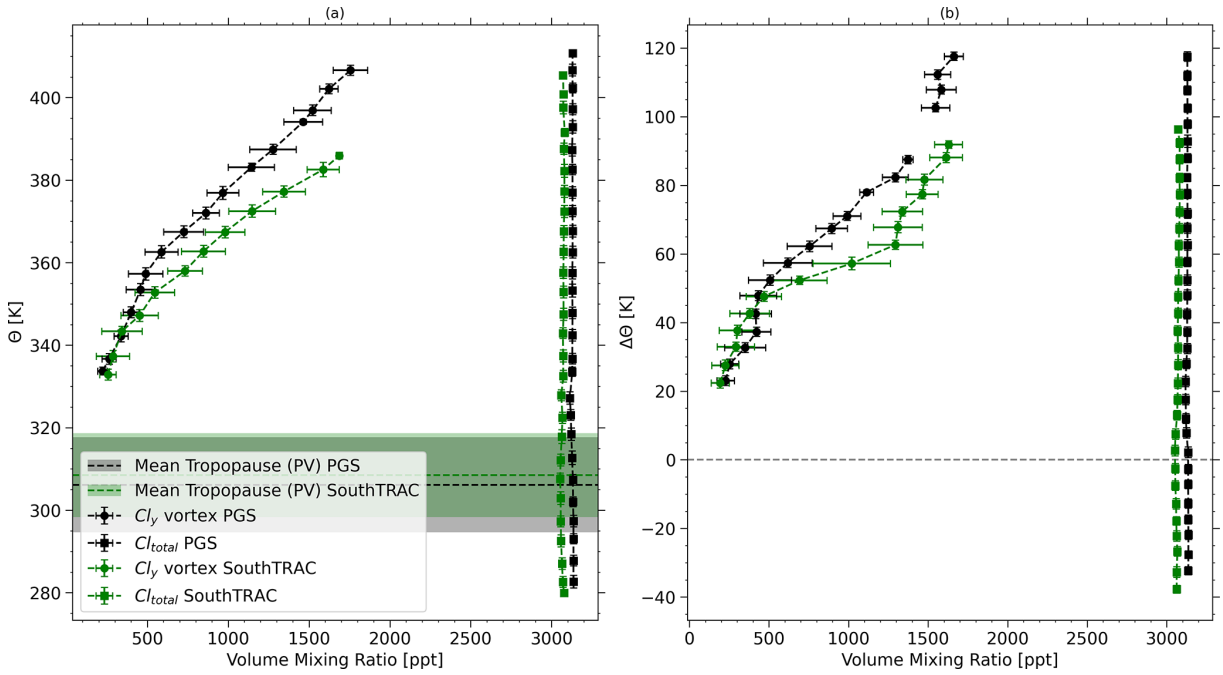

Figure 9. (a) Comparison of the vertical profiles of Cl_y inside the respective vortex where classification was possible and total chlorine from PGS (black) and SouthTRAC (green). Data are averaged over 40 to 90° equivalent latitude of the respective hemisphere and are displayed as a function of potential temperature. Vertical and horizontal error bars denote 1σ variability. PV tropopause for PGS (black) and SouthTRAC (green) are displayed as dashed horizontal lines with the 1σ variability as shaded areas. Panel **(b)** is the same data as **(a)** but as a function of potential temperature relative to the local tropopause (PV) displayed with a dashed grey line.

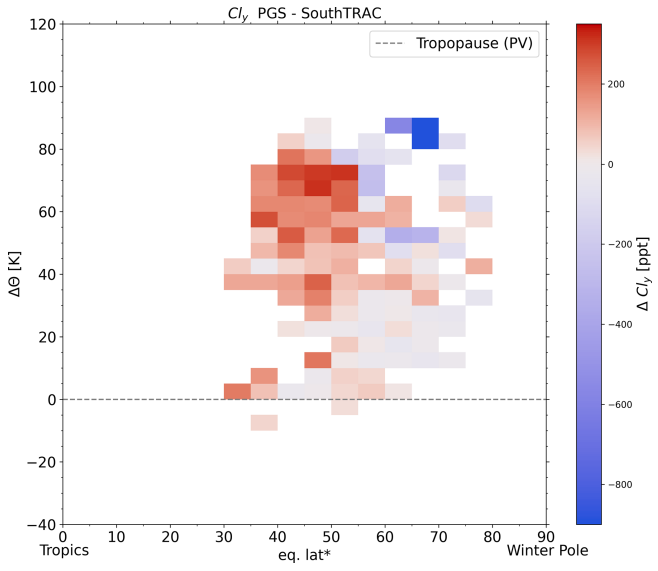

Figure 10. Difference of the latitude–altitude cross section of Cl_y from PGS and SouthTRAC. Data are binned using equivalent latitude* and $\Delta\Theta$.

stratosphere of the midlatitudes shows consistently higher Cl_y values during PGS. The highest values of Cl_y reached are 315 ppt higher during PGS between 65 and 70 K of $\Delta\Theta$ and 40 to 45° equivalent latitude. The already-mentioned difference of Cl_{total} between PGS and SouthTRAC amounts to 60 ± 9.6 ppt. This maximum difference of 60 ± 9.6 ppt will only propagate completely to Cl_y when all chlorine is converted to the inorganic form. Taking into account the difference in Cl_{total} between the two campaigns would reduce the observed differences in the midlatitudes, where mixing ratios of Cl_y were higher during PGS, but would increase the differences in the high latitudes, where higher Cl_y was derived for SouthTRAC. The observed differences in Cl_y are thus clearly larger than can be explained by the temporal difference in Cl_{total}. Possible reasons for the observed differences can be derived from the hemispheric difference of the Brewer–Dobson circulation using the age of air as a common metric for transport. Konopka et al. (2015) showed that the age of air is always younger north of 60° N than south of 60° S in the corresponding season. Older air will be higher in Cl_y as a larger fraction of total chlorine has already been converted to the inorganic form. Therefore, the observed differences in Cl_y, with higher Cl_y values in the southern high latitudes than in the northern high latitudes (see Figs. 9 and 10), are consistent with the differences in the age of air found by Konopka et al. (2015). In addition, Engel et al. (2018b)

updated the long-term total column HCl and $ClONO_2$ (representing Cl_y) record reported by Mahieu et al. (2014) in the stratosphere at Jungfraujoch (46.5° N) and at Lauder (45° S) through the end of 2016. A negative trend of Cl_y is observed at both stations but with a non-significant trend for the Jungfraujoch data over the last decade and a slightly larger negative trend from the Lauder data. In addition, trends between 1997 and 2016 are given at both stations, with $-0.42 \pm 0.23\,\%\,yr^{-1}$ and $-0.51 \pm 0.12\,\%\,yr^{-1}$ for HCl and $-0.60 \pm 0.39\,\%\,yr^{-1}$ and $-0.74 \pm 0.59\,\%\,yr^{-1}$ for $ClONO_2$ at Jungfraujoch station and Lauder station, respectively. Furthermore, the Global Ozone Chemistry And Related trace gas Data records for the Stratosphere (GOZCARDS) shows short-term lower-stratospheric HCl trends that are negative at southern latitudes and slightly positive (marginal significance) at northern midlatitudes between 2005 and 2015/2018 (Froidevaux et al., 2015, 2019). Although the trends given are indicative of the interhemispheric differences in Cl_y decline, they do not explain the difference in Cl_y at midlatitudes of 200 ppt or more shown in Fig. 10. The lowest 20 K above the local tropopause show in general minor differences between the two hemispheres. There are two exceptions. A bin between 0 and 5 K of $\Delta\Theta$ and 30 to 35° equivalent latitude and a bin between 10 and 15 K of $\Delta\Theta$ and 45 to 50° equivalent latitude both have around 200 ppt more Cl_y during PGS. However, this Θ range is in general affected by cross-tropopause mixing in both hemispheres, leading to generally small differences in the extratropical tropopause layer.

5 Summary and conclusion

This study is based on high-resolution measurements of chlorinated hydrocarbons and N_2O taken during the SouthTRAC campaign in the Antarctic lower stratosphere in late austral winter 2019. Extending the method of Greenblatt et al. (2002), it was possible to allocate the measurements to the vortex, vortex boundary region, and midlatitudes. The classification of air masses based on high-resolution in situ measurements of N_2O offers the possibility to detect and account for even small structures and follows the sharp gradient between the regimes well. However, the weakness of this air mass classification appears near the tropopause, where it was difficult to make a distinction between vortex, vortex boundary, and midlatitudes.

Inorganic chlorine was calculated semi-directly from the GhOST-MS measurements of the major organic source gases and mean age and indirectly using a correlation adapted from observations of balloon flights in the Arctic polar vortex in 2009 and 2011. In order to compare the indirect method to the semi-direct method, first the measurements of the GhOST-MS were up-sampled to a higher time resolution. The simultaneous accurate measurements of CFC-12 in the GhOST-MS and GhOST-ECD channels were used. The indirect method shows good agreement with the semi-direct method despite a time interval of 10 years and the use of measurements of the Northern Hemisphere. Thus, the indirect method serves as a good alternative calculation of inorganic chlorine in case not all organic source gases are measured.

The year 2019 was special for the Antarctic polar vortex, with extraordinary meteorological conditions, which led to a minor sudden stratospheric warming. The Antarctic polar vortex was weakened and shifted towards the eastern South Pacific and South America during SouthTRAC (e.g., Wargan et al., 2020; Safieddine et al., 2020). Despite a weakened vortex, up to 50 % of the total chlorine could be found in inorganic form inside the vortex at the highest $\Delta\Theta$ levels of 75 K above the tropopause. Furthermore, inorganic chlorine for midlatitudes and the vortex boundary region could be derived during SouthTRAC, with only about 15 % of the total chlorine in inorganic form in the midlatitudes.

Measurements from the PGS campaign, which took place in the Arctic polar winter 2015/2016, were used to compare Arctic and Antarctic Cl_y. To our knowledge, a comparison of Cl_y of the Arctic and Antarctic vortex has not been published previously. For PGS, Cl_y was calculated using the indirect method based on scaled correlation from the observations of balloon flights in the Arctic polar vortex in 2009 and 2011. Additionally, region classification was done using N_2O measurements, as for the Southern Hemisphere data. In contrast to the Antarctic polar vortex in 2019, the Arctic polar vortex in 2015/2016 was one of the strongest compared to previous years (Matthias et al., 2016). At a comparable level of $\Delta\Theta$ inside the vortex, only around 40 % of total chlorine was found in inorganic form, whereas roughly 20 % was found at midlatitudes. Inside the respective vortex, the amount of Cl_y was higher during SouthTRAC than during PGS by up to 540 ppt (at the same $\Delta\Theta$ level). Trends due to the Montreal Protocol are estimated to be negative at about $-20\,ppt\,yr^{-1}$, which is not evident in this comparison. The differences in Cl_y values inside the two vortices are substantial and even larger than the inter-annual variations reported by Strahan et al. (2014) for the Antarctic. For the comparison of the Arctic and Antarctic Cl_y in this study, only one winter in each hemisphere was investigated. Furthermore, the respective campaigns only show a part of the winter seasons. These intervals do not correspond completely. For a more meaningful conclusion about the Cl_y loading in the two polar vortices, further sampling at different seasons and over several years would be required.

Investigating the difference of Cl_y in a latitude–altitude cross section from PGS and SouthTRAC, higher values at higher latitudes were found for SouthTRAC, whereas higher values for the midlatitude lower stratosphere were found for PGS. In the troposphere and near the tropopause, differences become smaller. Cl_y increases with increasing mean age of air, for which Konopka et al. (2015) derived similar hemispheric differences based on model simulations using meteorological reanalysis data. A comparison of the available

data with chemical transport models should be the subject of further studies. Furthermore, such interhemispheric differences should also be captured by chemistry climate models, which are used not only to understand past changes but also to predict future changes in chemical composition. The higher values from SouthTRAC at higher latitudes may reflect the difference in spatial extent, isolation, and location of the Southern Hemisphere vortex. The Arctic vortex exhibits larger variability as it is more affected by weather systems or wave activity. The Antarctic vortex on the other hand is larger and stronger and is typically less affected by wave disturbances.

Appendix A: Filter procedure for vortex and midlatitude profiles

A filter procedure was used to derive the lower envelope for the vortex profile and the upper envelope for the midlatitude profile. Figure S1 in the Supplement displays the procedure for the task using either $\Delta\Theta$ or Θ as the vertical coordinate. The process is initialized by binning the N_2O measurements into intervals of e.g., $\Delta\Theta$. The bin size must be adjusted to the number of measurements available for the vortex and midlatitude profile to make the filter procedure work properly. For every bin, the mean value, standard deviation, and relative standard deviation are calculated. This is necessary as the condition for the filter needs a binned profile to begin with. While the maximum relative standard deviation is larger than the preset outlier limit, the measurements that are not flagged as outliers are binned in intervals of $\Delta\Theta$ (this is done twice in the first iteration step, since the binned profile is already needed for the initialization and no outliers are set for the beginning of the filtering process). Every bin is checked, whether the relative standard deviation is larger than the outlier limit. In this case, all measurements of N_2O which are higher (or lower, if the upper envelope is requested) than the mean of the respective bin are flagged as outliers and removed from further iterations. The iteration process stops when the maximum relative standard deviation is below the preset outlier limit.

For the vortex profile, bin size was set to 2 K. The variability of N_2O on a constant Θ surface inside the vortex is about 6 ppb (Greenblatt et al., 2002). For the range of N_2O mixing ratios in this work, 6 ppb corresponds roughly to about 3 % and was thus set as the outlier limit. Four iterations were done to get the lower envelope (grey samples in Fig. S2a and b in the supporting information). For the midlatitude profile, the bin size was set to 2 K. Strahan et al. (1999) showed that the variability of N_2O in the Southern Hemisphere lower stratosphere of the midlatitudes is approximately between 5 and 15 % (see plate 6 therein). Therefore, a value of about 10 % is set for the outlier limit, which leads to two iteration steps for the remaining measurements. For the profiles only measurements which are not marked as outliers are used.

Data availability. The observational data of the HALO flights during the SouthTRAC campaign are available via the HALO database https://halo-db.pa.op.dlr.de (DLR, 2021).

Supplement. The supplement related to this article is available online at: https://doi.org/10.5194/acp-21-17225-2021-supplement.

Author contributions. MJ and AE performed the study, and MJ wrote the paper. Measurements were performed by MJ, TK, TS, TW, and AE for GhOST and HB, HCL, and PH for UMAQS. All authors contributed to the final paper.

Competing interests. At least one of the (co-)authors is a member of the editorial board of *Atmospheric Chemistry and Physics*.

Disclaimer. Publisher's note: Copernicus Publications remains neutral with regard to jurisdictional claims in published maps and institutional affiliations.

Acknowledgements. This work was done at the University of Frankfurt. The authors would like to thank the DLR staff for the operation of the HALO and the support during the campaign and also the coordinators and colleagues for a productive cooperation during the campaign. We further thank Jens-Uwe Grooß from the Forschungszentrum Jülich for the calculation of the tropopause and equivalent latitude for the HALO campaigns. The authors would further like to thank the site operators at the Cape Grim, Mace Head, Trinidad Head, Ragged Point, and Cape Matatula stations. AGAGE is supported principally by NASA (USA) grants to MIT and SIO and also by BEIS (UK) and NOAA (USA) grants to Bristol University, CSIRO and BoM (Australia), FOEN grants to Empa (Switzerland), NILU (Norway), SNU (South Korea), CMA (China), NIES (Japan), and Urbino University (Italy). The authors would like to thank the editor, Marc von Hobe, and the two reviewers, Michelle Santee and an anonymous reviewer, for their helpful comments.

Financial support. This research has been supported by the Bundesministerium für Bildung und Forschung (grant no. 01LG1908B) and the Deutsche Forschungsgemeinschaft (grant nos. EN367/13-1, EN367/14-1, EN367/16-1, EN367/17-1, HO4225/15-1, and HO4225/14-1).

This open-access publication was funded by the Goethe University Frankfurt.

Review statement. This paper was edited by Marc von Hobe and reviewed by Michelle Santee and one anonymous referee.

References

Bönisch, H., Engel, A., Curtius, J., Birner, Th., and Hoor, P.: Quantifying transport into the lowermost stratosphere using simultaneous in-situ measurements of SF_6 and CO_2, Atmos. Chem. Phys., 9, 5905–5919, https://doi.org/10.5194/acp-9-5905-2009, 2009.

Butchart, N. and Remsberg, E. E.: The Area of the Stratospheric Polar Vortex as a Diagnostic for Tracer Transport on an Isentropic Surface, J. Atmos. Sci., 43, 1319–1339, https://doi.org/10.1175/1520-0469(1986)043<1319:TAOTSP>2.0.CO;2, 1986.

Crutzen, P. J. and Arnold, F.: Nitric acid cloud formation in the cold Antarctic stratosphere: a major cause for the springtime "ozone hole", Nature, 324, 651–655, https://doi.org/10.1038/324651a0, 1986.

Daniel, J. S., Solomon, S., and Albritton, D. L.: On the evaluation of halocarbon radiative forcing and global warming potential, J. Geophys. Res., 100, 1271–1285, https://doi.org/10.1029/94JD02516, 1995.

DLR: The Basis HALO Measurement and Sensor System (BAHAMAS), available at: https://www.halo.dlr.de/instrumentation/basis.html (last access: 25 August 2021), 2020.

Engel, A., Strunk, M., Müller, M., Haase, H. P., Levin, I., and Schmidt, U.: Temporal development of total chlorine in the high-latitude stratosphere based on reference distributions of mean age derived from CO_2 and SF_6, J. Geophys. Res., 107, ACH 1-1–ACH 1–8, https://doi.org/10.1029/2001JD000584, 2002.

Engel, A., Bönisch, H., Brunner, D., Fischer, H., Franke, H., Günther, G., Gurk, C., Hegglin, M., Hoor, P., Königstedt, R., Krebsbach, M., Maser, R., Parchatka, U., Peter, T., Schell, D., Schiller, C., Schmidt, U., Spelten, N., Szabo, T., Weers, U., Wernli, H., Wetter, T., and Wirth, V.: Highly resolved observations of trace gases in the lowermost stratosphere and upper troposphere from the Spurt project: an overview, Atmos. Chem. Phys., 6, 283–301, https://doi.org/10.5194/acp-6-283-2006, 2006.

Engel, A., Bönisch, H., Ostermöller, J., Chipperfield, M. P., Dhomse, S., and Jöckel, P.: A refined method for calculating equivalent effective stratospheric chlorine, Atmos. Chem. Phys., 18, 601–619, https://doi.org/10.5194/acp-18-601-2018, 2018a.

Engel, A., Rigby, M., Burkholder, J., Fernandez, R., Froidevaux, L., Hall, B., Hossaini, R., Saito, T., Vollmer, M., and Yao, B.: Ozone-Depleting Substances (ODSs) and Other Gases of Interest to the Montreal Protocol, in: Scientific Assessment of Ozone Depletion: 2018, Global Ozone Research and Monitoring, chap. 1, World Meteorological Organization, Geneva, Switzerland, 2018b.

Farman, J. C., Gardiner, B. G., and Shanklin, J. D.: Large losses of total ozone in Antarctica reveal seasonal ClO_x / NO_x interaction, Nature, 315, 207–210, https://doi.org/10.1038/315207a0, 1985.

Froidevaux, L., Anderson, J., Wang, H.-J., Fuller, R. A., Schwartz, M. J., Santee, M. L., Livesey, N. J., Pumphrey, H. C., Bernath, P. F., Russell III, J. M., and McCormick, M. P.: Global OZone Chemistry And Related trace gas Data records for the Stratosphere (GOZCARDS): methodology and sample results with a focus on HCl, H_2O, and O_3, Atmos. Chem. Phys., 15, 10471–10507, https://doi.org/10.5194/acp-15-10471-2015, 2015.

Froidevaux, L., Kinnison, D. E., Wang, R., Anderson, J., and Fuller, R. A.: Evaluation of CESM1 (WACCM) free-running and specified dynamics atmospheric composition simulations using global multispecies satellite data records, Atmos. Chem. Phys., 19, 4783–4821, https://doi.org/10.5194/acp-19-4783-2019, 2019.

German Aerospace Center (DLR): The High Altitude and LOng Range database (HALO-DB), DLR, available at: https://halo-db.pa.op.dlr.de, last access: 7 August 2021.

Gettelman, A., Hoor, P., Pan, L. L., Randel, W. J., Hegglin, M. I., and Birner, T.: The extratropical upper troposphere and lower stratosphere, Rev. Geophys., 49, RG3003, https://doi.org/10.1029/2011RG000355, 2011.

Greenblatt, J. B., Jost, H.-J., Loewenstein, M., Podolske, J. R., Bui, T. P., Hurst, D. F., Elkins, J. W., Herman, R. L., Webster, C. R., Schauffler, S. M., Atlas, E. L., Newman, P. A., Lait, L. R., Müller, M., Engel, A., and Schmidt, U.: Defining the polar vortex edge from an N_2O : potential temperature correlation, J. Geophys. Res., 107, SOL 10-1–SOL 10-9, https://doi.org/10.1029/2001JD000575, 2002.

Grooß, J.-U., Engel, I., Borrmann, S., Frey, W., Günther, G., Hoyle, C. R., Kivi, R., Luo, B. P., Molleker, S., Peter, T., Pitts, M. C., Schlager, H., Stiller, G., Vömel, H., Walker, K. A., and Müller, R.: Nitric acid trihydrate nucleation and denitrification in the Arctic stratosphere, Atmos. Chem. Phys., 14, 1055–1073, https://doi.org/10.5194/acp-14-1055-2014, 2014.

Hall, T. M. and Plumb, R. A.: Age as a diagnostic of stratospheric transport, J. Geophys. Res., 99, 1059–1070, 1994.

Hartmann, D. L., Chan, K. R., Gary, B. L., Schoeberl, M. R., Newman, P. A., Martin, R. L., Loewenstein, M., Podolske, J. R., and Strahan, S. E.: Potential Vorticity and Mixing in the South Polar Vortex During Spring, J. Geophys. Res., 94, 11625–11640, https://doi.org/10.1029/JD094iD09p11625, 1989.

Hauck, M., Fritsch, F., Garny, H., and Engel, A.: Deriving stratospheric age of air spectra using an idealized set of chemically active trace gases, Atmos. Chem. Phys., 19, 5269–5291, https://doi.org/10.5194/acp-19-5269-2019, 2019.

Hersbach, H., Bell, B., Berrisford, P., Hirahara, S., Horányi, A., Muñoz-Sabater, J., Nicolas, J., Peubey, C., Radu, R., Schepers, D., Simmons, A., Soci, C., Abdalla, S., Abellan, X., Balsamo, G., Bechtold, P., Biavati, G., Bidlot, J., Bonavita, M., De Chiara, G., Dahlgren, P., Dee, D., Diamantakis, M., Dragani, R., Flemming, J., Forbes, R., Fuentes, M., Geer, A., Haimberger, L., Healy, S., Hogan, R. J., Hólm, E., Janisková, M., Keeley, S., Laloyaux, P., Lopez, P., Lupu, C., Radnoti, G., de Rosnay, P., Rozum, I., Vamborg, F., Villaume, S., and Thépaut, J.-N.: The ERA5 global reanalysis, Q. J. Roy. Meteor. Soc., 146, 1999–2049, https://doi.org/10.1002/qj.3803, 2020.

Hoor, P., Gurk, C., Brunner, D., Hegglin, M. I., Wernli, H., and Fischer, H.: Seasonality and extent of extratropical TST derived from in-situ CO measurements during SPURT, Atmos. Chem. Phys., 4, 1427–1442, https://doi.org/10.5194/acp-4-1427-2004, 2004.

Hoor, P., Fischer, H., and Lelieveld, J.: Tropical and extratropical tropospheric air in the lowermost stratosphere over Europe: A CO-based budget, Geophys. Res. Lett., 32, L07802, https://doi.org/10.1029/2004GL022018, 2005.

Hossaini, R., Atlas, E., Dhomse, S. S., Chipperfield, M. P., Bernath, P. F., Fernando, A. M., Mühle, J., Leeson, A. A., Montzka, S. A., Feng, W., Harrison, J. J., Krummel, P., Vollmer, M. K., Reimann, S., O'Doherty, S., Young, D., Maione, M., Arduini, J., and Lunder, C. R.: Recent Trends in Stratospheric Chlorine From Very

Short-Lived Substances, J. Geophys. Res.-Atmos., 124, 2318–2335, https://doi.org/10.1029/2018JD029400, 2019.

Keber, T., Bönisch, H., Hartick, C., Hauck, M., Lefrancois, F., Obersteiner, F., Ringsdorf, A., Schohl, N., Schuck, T., Hossaini, R., Graf, P., Jöckel, P., and Engel, A.: Bromine from short-lived source gases in the extratropical northern hemispheric upper troposphere and lower stratosphere (UTLS), Atmos. Chem. Phys., 20, 4105–4132, https://doi.org/10.5194/acp-20-4105-2020, 2020.

Konopka, P., Ploeger, F., Tao, M., Birner, T., and Riese, M.: Hemispheric asymmetries and seasonality of mean age of air in the lower stratosphere: Deep versus shallow branch of the Brewer-Dobson circulation, J. Geophys. Res.-Atmos., 120, 2053–2066, https://doi.org/10.1002/2014JD022429, 2015.

Krause, J., Hoor, P., Engel, A., Plöger, F., Grooß, J.-U., Bönisch, H., Keber, T., Sinnhuber, B.-M., Woiwode, W., and Oelhaf, H.: Mixing and ageing in the polar lower stratosphere in winter 2015–2016, Atmos. Chem. Phys., 18, 6057–6073, https://doi.org/10.5194/acp-18-6057-2018, 2018.

Leedham Elvidge, E., Bönisch, H., Brenninkmeijer, C. A. M., Engel, A., Fraser, P. J., Gallacher, E., Langenfelds, R., Mühle, J., Oram, D. E., Ray, E. A., Ridley, A. R., Röckmann, T., Sturges, W. T., Weiss, R. F., and Laube, J. C.: Evaluation of stratospheric age of air from CF_4, C_2F_6, C_3F_8, CHF_3, HFC-125, HFC-227ea and SF_6; implications for the calculations of halocarbon lifetimes, fractional release factors and ozone depletion potentials, Atmos. Chem. Phys., 18, 3369–3385, https://doi.org/10.5194/acp-18-3369-2018, 2018.

Mahieu, E., Chipperfield, M. P., Notholt, J., Reddmann, J., Anderson, J., Bernath, P. F., Blumenstock, T., Coffey, M. T., Dhomse, S. S., Feng, W., Franco, B., Froidevaux, L., Griffith, D. W., Hannigan, J. W., Hase, F., Hossaini, R., Jones, N. B., Morino, I., Murata, I., Nakajima, H., Palm, M., Paton-Walsh, C., Russell III, J. M., Schneider, M., Servais, C., Smale, D., and Walker, K. A.: Recent Northern Hemisphere stratospheric HCl increase due to atmospheric circulation changes, Nature, 515, 104–107, https://doi.org/10.1038/nature13857, 2014.

Manney, G. L. and Lawrence, Z. D.: The major stratospheric final warming in 2016: dispersal of vortex air and termination of Arctic chemical ozone loss, Atmos. Chem. Phys., 16, 15371–15396, https://doi.org/10.5194/acp-16-15371-2016, 2016.

Manney, G. L., Zurek, R. W., O'Neal, A., and Swinbank, R.: On the Motion of Air through the Stratospheric Polar Vortex, J. Atmos. Sci., 51, 2973–2994, https://doi.org/10.1175/1520-0469(1994)051<2973:OTMOAT>2.0.CO;2, 1994.

Marsing, A., Jurkat-Witschas, T., Grooß, J.-U., Kaufmann, S., Heller, R., Engel, A., Hoor, P., Krause, J., and Voigt, C.: Chlorine partitioning in the lowermost Arctic vortex during the cold winter 2015/2016, Atmos. Chem. Phys., 19, 10757–10772, https://doi.org/10.5194/acp-19-10757-2019, 2019.

Matthias, V., Dörnbrack, A., and Stober, G.: The extraordinarily strong and cold polar vortex in the early nothern winter 2015/2016, Geophys. Res. Lett., 43, 287–294, https://doi.org/10.1002/2016GL071676, 2016.

Molina, M. J. and Rowland, F. S.: Stratospheric sink for chlorofluoromethanes: chlorine atomic-catalysed destruction of ozone, Nature, 249, 810–812, https://doi.org/10.1038/249810a0, 1974.

Molina, M. J., Tso, T., Molina, L. T., and Wang, F. C.-Y.: Antarctic Stratospheric Chemistry of Chlorine Nitrate, Hydrogen Chloride, and Ice: Release of Active Chlorine, Science, 238, 1253–1257, https://doi.org/10.1126/science.238.4831.1253, 1987.

Müller, S., Hoor, P., Berkes, F., Bozem, H., Klingebiel, M., Reutter, P., Smit, H. G. J., Wendisch, M., Spichtinger, P., and Borrmann, S.: In situ detection of stratosphere-troposphere exchange of cirrus particles in the midlatitudes, Geophys. Res. Lett., 42, 949–955, https://doi.org/10.1002/2014GL062556, 2015.

Nash, E. R., Newman, P. A., Rosenfield, J. E., and Schoeberl, M. R.: An objective determination of the polar vortex using Ertel's potential vorticity, J. Geophys. Res., 101, 9471–9478, 1996.

Newman, P. A., Kawa, S. R., and Nash, E. R.: On the size of the Antarctic ozone hole, Geophys. Res. Lett., 31, L21104, https://doi.org/10.1029/2004GL020596, 2004.

Newman, P. A., Daniel, J. S., Waugh, D. W., and Nash, E. R.: A new formulation of equivalent effective stratospheric chlorine (EESC), Atmos. Chem. Phys., 7, 4537–4552, https://doi.org/10.5194/acp-7-4537-2007, 2007.

Obersteiner, F., Bönisch, H., Keber, T., O'Doherty, S., and Engel, A.: A versatile, refrigerant- and cryogen-free cryofocusing–thermodesorption unit for preconcentration of traces gases in air, Atmos. Meas. Tech., 9, 5265–5279, https://doi.org/10.5194/amt-9-5265-2016, 2016.

Oelhaf, H., Sinnhuber, B.-M., Woiwode, W., Bönisch, H., Bozem, H., Engel, A., Fix, A., Friedl-Vallon, F., Grooß, J.-U., Hoor, P., Johansson, S., Jurkat-Witschas, T., Kaufmann, S., Krämer, M., Krause, J., Kretschmer, E., Lörks, D., Marsing, A., Orphal, J., Pfeilsticker, K., Pitts, M., Poole, L., Preusse, P., Rapp, M., Riese, M., Rolf, C., Ungermann, J., Voigt, C., Volk, C. M., Wirth, M., Zahn, A., and Ziereis, H.: POLSTRACC: Airborne Experiment for Studying the Polar Stratosphere in a Changing Climate with the High Altitude and Long Range Research Aircraft (HALO), B. Am. Meteorol. Soc., 100, 2634–2664, https://doi.org/10.1175/BAMS-D-18-0181.1, 2019.

Ostermöller, J., Bönisch, H., Jöckel, P., and Engel, A.: A new time-independent formulation of fractional release, Atmos. Chem. Phys., 17, 3785–3797, https://doi.org/10.5194/acp-17-3785-2017, 2017.

Plumb, I. C., Vohralik, P. F., and Ryan, K. R.: Normalization of correlations for atmospheric species with chemical loss, J. Geophys. Res., 104, 11723–11732, 1999.

Prinn, R. G., Weiss, R. F., Arduini, J., Arnold, T., DeWitt, H. L., Fraser, P. J., Ganesan, A. L., Gasore, J., Harth, C. M., Hermansen, O., Kim, J., Krummel, P. B., Li, S., Loh, Z. M., Lunder, C. R., Maione, M., Manning, A. J., Miller, B. R., Mitrevski, B., Mühle, J., O'Doherty, S., Park, S., Reimann, S., Rigby, M., Saito, T., Salameh, P. K., Schmidt, R., Simmonds, P. G., Steele, L. P., Vollmer, M. K., Wang, R. H., Yao, B., Yokouchi, Y., Young, D., and Zhou, L.: History of chemically and radiatively important atmospheric gases from the Advanced Global Atmospheric Gases Experiment (AGAGE), Earth Syst. Sci. Data, 10, 985–1018, https://doi.org/10.5194/essd-10-985-2018, 2018.

Rapp, M., Kaifler, B., Dörnbrack, A., Gisinger, S., Mixa, T., Reichert, R., Kaifler, N., Knobloch, S., Eckert, R., Wildmann, N., Giez, A., Krasauskas, L., Preusse, P., Geldenhuys, M., Riese, M., Woiwode, W., Friedl-Vallon, F., Sinnhuber, B.-M., de la Torre, A., Alexander, P., Hormaechea, J. L., Janches, D., Garhammer, M., Chau, J. L., Conte, F. F., Hoor, P., and Engel, A.: SOUTHTRAC-GW: An airborne field campaign to explore gravity wave dynamics at the world's strongest hotspot, B. Am.

Meteorol. Soc., 102, 1–60, https://doi.org/10.1175/BAMS-D-20-0034.1, 2020.

Ray, E. A., Moore, F. L., Elkins, J. W., Rosenlof, K. H., Laube, J. C., Röckmann, T., Marsh, D. R., and Andrews, A. E.: Quantification of the SF_6 lifetime based on mesospheric loss measured in the stratospheric polar vortex, J. Geophys. Res.-Atmos., 122, 4626–4638, https://doi.org/10.1002/2016JD026198, 2017.

Safieddine, S., Bouillon, M., Paracho, A.-C., Jumelet, J., Tencé, F., Pazmino, A., Goutail, F., Wespes, C., Bekki, S., Boynard, A., Hadji-Lazaro, J., Coheur, P.-F., Hurtmans, D., and Clerbaux, C.: Antarctic Ozone Enhancement During the 2019 Sudden Stratospheric Warming Event, Geophys. Res. Lett., 47, https://doi.org/10.1029/2020GL087810, 2020.

Sala, S., Bönisch, H., Keber, T., Oram, D. E., Mills, G., and Engel, A.: Deriving an atmospheric budget of total organic bromine using airborne in situ measurements from the western Pacific area during SHIVA, Atmos. Chem. Phys., 14, 6903–6923, https://doi.org/10.5194/acp-14-6903-2014, 2014.

Schauffler, S. M., Atlas, E. L., Donnelly, S. G., Andrews, A., Montzka, S. A., Elkins, J. W., Hurst, D. F., Romashkin, P. A., Dutton, G. S., and Stroud, V.: Chlorine budget and partitioning during the Stratospheric Aersol and Gas Experiment (SAFE) III Ozone Loss and Validation Experiment (SOLVE), J. Geophys. Res., 108, ACH 7-1–ACH 7-18, https://doi.org/10.1029/2001JD002040, 2003.

Schoeberl, M. R. and Hartmann, D. L.: The Dynamics of the Stratospheric Polar Vortex and Its Relation to Springtime Ozone Depletion, Science, 251, 46–52, https://doi.org/10.1126/science.251.4989.46, 1991.

Solomon, S.: Stratospheric ozone depletion: A review of concepts and history, Rev. Geophys., 37, 275–316, https://doi.org/10.1029/1999RG900008, 1999.

Strahan, S. E. and Douglass, A. R.: Decline in Antarctic Ozone Depletion and Lower Stratospheric Chlorine Determined From Aura Microwave Limb Sounder Observations, Geophys. Res. Lett., 45, 382–390, https://doi.org/10.1002/2017GL074830, 2018.

Strahan, S. E., Loewenstein, M., and Podolske, J. R.: Climatology and small-scale structure of lower stratospheric N_2O based on in situ observations, J. Geophys. Res.-Atmos., 104, 2195–2208, https://doi.org/10.1029/1998JD200075, 1999.

Strahan, S. E., Douglass, A. R., Newman, P. A., and Steenrod, S. D.: Inorganic chlorine variability in the Antarctic vortex and implications for ozone recovery, J. Geophys. Res., 119, 14098–14109, https://doi.org/10.1002/2014JD022295, 2014.

Wargan, K., Weir, B., Manney, G. L., Cohn, S. E., and Livesey, N. J.: The Anomalous 2019 Antarctic Ozone Hole in the GEOS Constituent Data Assimilation System With MLS Observations, J. Geophys. Res., 125, e2020JD033335, https://doi.org/10.1029/2020JD033335, 2020.

Werner, A., Volk, C. M., Ivanova, E. V., Wetter, T., Schiller, C., Schlager, H., and Konopka, P.: Quantifying transport into the Arctic lowermost stratosphere, Atmos. Chem. Phys., 10, 11623–11639, https://doi.org/10.5194/acp-10-11623-2010, 2010.

Wetzel, G., Oelhaf, H., Birk, M., de Lange, A., Engel, A., Friedl-Vallon, F., Kirner, O., Kleinert, A., Maucher, G., Nordmeyer, H., Orphal, J., Ruhnke, R., Sinnhuber, B.-M., and Vogt, P.: Partitioning and budget of inorganic and organic chlorine species observed by MIPAS-B and TELIS in the Arctic in March 2011, Atmos. Chem. Phys., 15, 8065–8076, https://doi.org/10.5194/acp-15-8065-2015, 2015.

Paper II: Global seasonal distribution of CH_2Br_2 and $CHBr_3$ in the upper troposphere and lower stratosphere

Published as:

Jesswein, M., Fernandez, R. P., Berná, L., Saiz-Lopez, A., Grooß, J.-U., Hossaini, R., Apel, E. C., Hornbrook, R. S., Atlas, E. L., Blake, D. R., Montzka, S., Keber, T., Schuck, T., Wagenhäuser, T., and Engel, A.: *Global seasonal distribution of CH_2Br_2 and $CHBr_3$ in the upper troposphere and lower stratosphere*, Atmos. Chem. Phys., Atmos. Chem. Phys., 22, 15049–15070, 2022, DOI: https://doi.org/10.5194/acp-22-15049-2022

Author Contributions:

Markus Jesswein wrote the manuscript including the figures of the publication and prepared the answers to the referees during the revision process. The manuscript and the answers to the referees were proofread by the co-authors.

Markus Jesswein operated the GhOST instrument during the SouthTRAC research campaign, together with Thomas Wagenhäuser, Timo Keber, Tanja Schuck, and Andreas Engel. Markus Jesswein evaluated and interpreted the data of the SouthTRAC campaign.

Eric Apel, Rebecca Honbrook, Eliot Atlas, Donald Blake, and Stephen Monzka provided observational data from the HIPPO and ATom mission.

Markus Jesswein processed HALO, HIPPO, and ATom data and evaluated the results.

Ryan Hossaini, Rafael P. Fernandez, Lucas Berná, Alfonso Saiz-Lopez, and Jens-Uwe Grooß conducted the model simulations and provided the resulting data as well as help for interpretation.

All co-authors contributed to the preparation of the manuscript in many useful discussions.

Frankfurt am Main .....

Markus Jesswein

Atmos. Chem. Phys., 22, 15049–15070, 2022
https://doi.org/10.5194/acp-22-15049-2022

Atmospheric Chemistry and Physics
Open Access
EGU

Global seasonal distribution of CH_2Br_2 and $CHBr_3$ in the upper troposphere and lower stratosphere

Markus Jesswein[1], Rafael P. Fernandez[2], Lucas Berná[3], Alfonso Saiz-Lopez[4], Jens-Uwe Grooß[5], Ryan Hossaini[6], Eric C. Apel[7], Rebecca S. Hornbrook[7], Elliot L. Atlas[8], Donald R. Blake[9], Stephen Montzka[10], Timo Keber[1], Tanja Schuck[1], Thomas Wagenhäuser[1], and Andreas Engel[1]

[1]Institute for Atmospheric and Environmental Sciences, University of Frankfurt, Frankfurt, Germany
[2]Institute for Interdisciplinary Science (ICB), National Research Council (CONICET), FCEN-UNCuyo, Mendoza, Argentina
[3]Atmospheric and Environmental Studies Group (GEAA), National Technological University (UTN-FR Mendoza), Mendoza, Argentina
[4]Department of Atmospheric Chemistry and Climate, Institute of Physical Chemistry Rocasolano, CSIC, Madrid, Spain
[5]Institute of Energy and Climate Research – Stratosphere (IEK-7), Forschungszentrum Jülich, Jülich, Germany
[6]Lancaster Environment Centre, Lancaster University, Lancaster, UK
[7]Atmospheric Chemistry Observations & Modeling Laboratory, National Center for Atmospheric Research, Boulder, CO, USA
[8]University of Miami, Miami, FL, USA
[9]Department of Chemistry, University of California, Irvine, Irvine, CA, USA
[10]Global Monitoring Laboratory, NOAA, Boulder, CO, USA

Correspondence: Markus Jesswein (jesswein@iau.uni-frankfurt.de)

Received: 1 July 2022 – Discussion started: 19 July 2022
Revised: 3 November 2022 – Accepted: 5 November 2022 – Published: 25 November 2022

Abstract. Bromine released from the decomposition of short-lived brominated source gases contributes as a sink of ozone in the lower stratosphere. The two major contributors are CH_2Br_2 and $CHBr_3$. In this study, we investigate the global seasonal distribution of these two substances, based on four High Altitude and Long Range Research Aircraft (HALO) missions, the HIAPER Pole-to-Pole Observations (HIPPO) mission, and the Atmospheric Tomography (ATom) mission. Observations of CH_2Br_2 in the free and upper troposphere indicate a pronounced seasonality in both hemispheres, with slightly larger mixing ratios in the Northern Hemisphere (NH). Compared to CH_2Br_2, $CHBr_3$ in these regions shows larger variability and less clear seasonality, presenting larger mixing ratios in winter and autumn in NH midlatitudes to high latitudes. The lowermost stratosphere of SH and NH shows a very similar distribution of CH_2Br_2 in hemispheric spring with differences well below 0.1 ppt, while the differences in hemispheric autumn are much larger with substantially smaller values in the SH than in the NH. This suggests that transport processes may be different in both hemispheric autumn seasons, which implies that the influx of tropospheric air ("flushing") into the NH lowermost stratosphere is more efficient than in the SH. The observations of $CHBr_3$ support the suggestion, with a steeper vertical gradient in the upper troposphere and lower stratosphere in SH autumn than in NH autumn. However, the SH database is insufficient to quantify this difference. We further compare the observations to model estimates of TOMCAT (Toulouse Off-line Model of Chemistry And Transport) and CAM-Chem (Community Atmosphere Model with Chemistry, version 4), both using the same emission inventory of Ordóñez et al. (2012). The pronounced tropospheric seasonality of CH_2Br_2 in the SH is not reproduced by the models, presumably due to erroneous seasonal emissions or atmospheric photochemical decomposition efficiencies. In contrast, model simulations of $CHBr_3$ show a pronounced seasonality in both hemispheres, which is not confirmed by observations. The distributions

of both species in the lowermost stratosphere of the Northern and Southern hemispheres are overall well captured by the models with the exception of southern hemispheric autumn, where both models present a bias that maximizes in the lowest 40 K above the tropopause, with considerably lower mixing ratios in the observations. Thus, both models reproduce equivalent flushing in both hemispheres, which is not confirmed by the limited available observations. Our study emphasizes the need for more extensive observations in the SH to fully understand the impact of CH_2Br_2 and $CHBr_3$ on lowermost-stratospheric ozone loss and to help constrain emissions.

1 Introduction

Reactive gases containing chlorine and bromine are very efficient in destroying stratospheric ozone in catalytic reaction cycles. The relative efficiency of bromine is 60–65 times higher than that of chlorine (e.g. Sinnhuber et al., 2009; WMO, 2018). A more recent study reports a 74 times higher efficiency of bromine (Klobas et al., 2020). Thus, although the amount of bromine in the stratosphere is much smaller than that of chlorine, bromine plays an important role in stratospheric ozone chemistry. Major contributors to stratospheric bromine are the four major halons H-1211 ($CBrClF_2$), H-1301 ($CBrF_3$), H-1202 (CBr_2F_2), and H-2402 ($CBrF_2CBrF_2$), all originating from anthropogenic sources. Furthermore, methyl bromide (CH_3Br) is a major contributor, which has both natural and anthropogenic sources. Additionally, the so-called "very short-lived substances" (VSLSs), with lifetimes shorter than 6 months, can contribute bromine to the stratosphere and thus lead to ozone loss. Bromine VSLSs (Br-VSLSs in the following) contributed about a quarter to stratospheric bromine in 2016 with a total of 5 (3–7) ppt (parts per trillion) (Engel et al., 2018). The contribution is partly in the form of organic source gases (source gas injection; SGI) providing 2.2 (0.8–4.2) ppt Br and in inorganic form as photochemically decomposed species (product gas injection; PGI) with 2.7 (1.7–4.2) ppt Br (Engel et al., 2018). Once in the lowermost stratosphere (LMS), released bromine from VSLSs can affect the ozone abundance and distribution. Especially in the midlatitude LMS, bounded by the 380 K potential temperature surface at the top and the extratropical tropopause at the bottom (e.g. Hoor et al., 2005), bromine-driven ozone loss cycles gain importance (e.g. Daniel et al., 1999; Salawitch et al., 2005). It is also a region where ozone changes have a relatively large radiative effect (Hossaini et al., 2015, and references therein).

Transport of source gases into the LMS can occur via different pathways. Transport associated with the global-scale stratospheric Brewer–Dobson circulation (BDC) brings older air from the stratospheric overworld into the upper troposphere and lower stratosphere (UTLS) via the deep branch with long transit times, as well as air from the tropics and subtropics into the UTLS via the shallow branch with shorter transit times (Birner and Bönisch, 2011). On the other hand, air can be transported directly into the LMS via the extratropical tropopause by troposphere-to-stratosphere transport (TST). Kunkel et al. (2019) describe in more detail the processes for stratosphere–troposphere exchange (STE) in the midlatitudes, for example due to Rossby wave breaking and tropopause folds along jet streams. Furthermore, Kunkel et al. (2019) suggested that air masses potentially enter the stratosphere in ridges of baroclinic waves at the anticyclonic side of the jets above the outflow of warm conveyor belts (whereby the significance of this process still needs to be assessed). Previous studies estimated that the contribution of extratropical tropospheric air to the LMS shows a pronounced seasonality. Hoor et al. (2005) used CO in situ measurements to infer a fraction of 35 % extratropical tropospheric air in winter and spring LMS composition over Europe, whereas the fraction rises to 55 % in summer and autumn. A similar seasonality but with much higher extratropical fractions was found by Bönisch et al. (2009) using in situ measurements of CO_2 and SF_6. Extratropical tropospheric fractions of up to 90 % were found in October and the lowest fraction below 20 % in April. Hegglin et al. (2009) used O_3, H_2O, and CO measurements from the Atmospheric Chemistry Experiment Fourier Transformation Spectrometer (ACE-FTS) on Canada's SCISAT-1 satellite to investigate the global behaviour of the extratropical tropopause transition layer (ExTL), which is the finite chemical transition layer across the tropopause and into the LMS. Major findings were a shallower transition layer in the Southern Hemisphere (SH) with a weaker troposphere–stratosphere transport compared to the Northern Hemisphere (NH) and an overall smaller seasonal variation. Hegglin and Shepherd (2007) showed that "flushing" of the LMS with younger air from the tropics is most evident in NH summer and autumn and is weaker in the SH. These results are confirmed by the CO tracer distribution in Hegglin et al. (2009).

The different transport paths have an influence on the distribution of Br-VSLSs, especially in the LMS of each hemisphere. This study focuses on bromoform ($CHBr_3$) and dibromomethane (CH_2Br_2), which are the most abundant Br-VSLSs. The local lifetime of CH_2Br_2 ranges from 150 to 890 d and that of $CHBr_3$ between 17 to 88 d, depending on location and season (see Sect. 4, Table 3 for seasonally resolved local lifetimes). The main sources of these Br-VSLSs are open-ocean and coastal regions via the metabolism of marine organisms such as phytoplankton and macro-algae (e.g. Carpenter and Liss, 2000; Quack et al., 2007; Leedham et al., 2013). Sturges et al. (1993) and Abrahamsson

et al. (2018) suggested that winter sea ice could potentially be an additional source of Br-VSLSs. Anthropogenic sources are water chlorination (e.g. Worton et al., 2006; Maas et al., 2021) and industrial discharge of chlorinated effluents to seawater (Quivet et al., 2022; Maas et al., 2019; Hamed et al., 2017; Boudjellaba et al., 2016; Sam Yang, 2001). The contribution of treated water may have an impact on a local scale only, and the significance of theses sources on a global scale remains unclear (e.g. Quivet et al., 2022; Liu et al., 2011). Studies of the observation-based distribution, especially when looking at stratospheric input of Br-VSLSs, have focused predominantly on the tropics and the NH. The current best estimates of tropical tropopause values of CH_2Br_2 and $CHBr_3$ are given in Engel et al. (2018) ranging from 0.81 (0.59–0.98) ppt to 0.64 (0.32–0.89) ppt CH_2Br_2 from the level of 0 clear-sky radiative heating (LZRH) to the tropical tropopause (TTP) and 0.36 (0.05–0.72) ppt to 0.19 (0.01–0.54) ppt $CHBr_3$ from LZRH to TTP (Wofsy, 2011; Sala et al., 2014; Navarro et al., 2015; Pan et al., 2017). A recent study by Keber et al. (2020) reported aircraft measurements of Br-VSLSs at the tropopause and LMS in NH midlatitudes to high latitudes during winter and late summer to early autumn. They reported systematically higher mixing ratios of $CHBr_3$ at the extratropical tropopause than those at the TTP. A similar, although less pronounced feature was found for CH_2Br_2. This increase was more pronounced in winter, when lifetimes increase at higher latitudes. In addition, Keber et al. (2020) compared their observations with model estimates using different emission scenarios. Although no scenario was able to capture the tropical and extratropical values from their observations, the Ordóñez et al. (2012) scenario showed an overall good agreement, especially for CH_2Br_2.

As Keber et al. (2020) already pointed out, there are still some knowledge gaps regarding the distribution of the Br-VSLSs in the upper atmosphere, as they only show observations of the NH in winter and late summer to early autumn. Especially the data coverage in the SH is sparse. It is expected that the distribution of the Br-VSLSs in the SH may differ from the NH distribution, due to fewer source regions like coastal ocean regions. Here we expand the analysis of Keber et al. (2020) to a global view of the two major Br-VSLSs. For that, besides using the observations already used in Keber et al. (2020), namely the High Altitude and Long Range Research Aircraft (HALO) missions TACTS (Transport and Composition in the Upper Troposphere/Lowermost Stratosphere), PGS, and WISE (Wave-driven ISentropic Exchange), we also use observations from the southern hemispheric HALO mission SouthTRAC (Southern Hemisphere Transport, Dynamics, and Chemistry) from September to November 2019. Furthermore, we use observations from the HIAPER Pole-to-Pole Observations (HIPPO) mission and the Atmospheric Tomography (ATom) mission, both of which include data from the Northern and Southern hemispheres, to investigate the global seasonal distribution of the Br-VSLSs. Observations are compared with two global models, namely CAM-Chem (Community Atmosphere Model with Chemistry, version 4) and TOMCAT (Toulouse Off-line Model of Chemistry And Transport), both using the same emission scenario of Ordóñez et al. (2012). In Sect. 2, we give a brief overview of the missions and instruments used for this analysis, followed by an introduction to the meteorological data and the models against which we compare the observations in Sect. 3. The distribution of CH_2Br_2 and $CHBr_3$ from observations and model simulations is discussed in Sect. 4. We start with the broader global distribution by presenting seasonal zonal mean mixing ratios from both hemispheres from the ground to the lower stratosphere, moving on to a closer look at near-tropopause mixing ratios, and finally focus on the vertical distribution in the midlatitudes of NH and SH. Lastly, we summarize the conclusion and provide an outlook in Sect. 5.

2 Measurements

2.1 HALO missions

In this work, we use data from four missions conducted with the High Altitude and Long Range Research Aircraft (HALO). HALO is a Gulfstream V (GV) aircraft and can reach altitudes of up to 15 km. The first mission is the TACTS (Transport and Composition in the Upper Troposphere/Lowermost Stratosphere) mission, conducted in August and September 2012 with flights covering an area from the Cabo Verde islands to the Norwegian archipelago of Spitsbergen and over Europe and the Atlantic Ocean. The base of all flights was Oberpfaffenhofen (Germany) (Fig. 1, blue tracks). The second mission was PGS, consisting of three sub-missions: POLSTRACC (Polar Stratosphere in a Changing Climate), GW-LCYCLE (Investigation of the Life cycle of gravity waves), and SALSA (Seasonality of Air mass transport and origin in the Lowermost Stratosphere). The mission took place from December 2015 to March 2016 with flights mainly in the Arctic and covering Greenland, the North Atlantic, and Europe. Flights were conducted from Oberpfaffenhofen (Germany) and from Kiruna (Sweden) (Fig. 1, purple tracks) (Oelhaf et al., 2019). The third mission was the WISE (Wave-driven ISentropic Exchange) mission between September and October 2017. Flights were conducted mainly from Shannon (Ireland), covering an area above the Atlantic Ocean and western Europe (Fig. 1, green tracks). Finally, the SouthTRAC (Southern Hemisphere Transport, Dynamics, and Chemistry) mission took place from September to November 2019. It is the only one of the four HALO missions that covers the SH. In addition to the scientific transfer flights, which departed from Oberpfaffenhofen (Germany) via the Cabo Verde islands to South America, all other flights took place from Rio Grande (Argentina). Flights of the SouthTRAC mission cover the southern Pacific and southern Atlantic oceans near South America and Antarctica (Fig. 1, orange tracks).

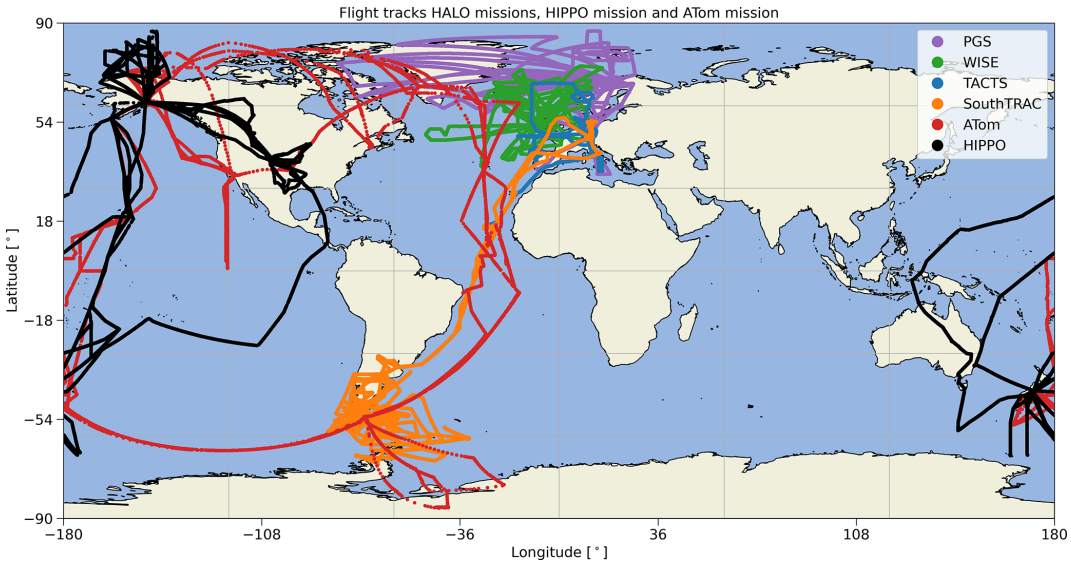

Figure 1. Flight tracks of the HALO missions TACTS (blue), WISE (green), PGS (purple), and SouthTRAC (orange) as well as flight tracks of the HIPPO mission (black) and ATom mission (red).

Data from the Gas chromatograph for Observational Studies using Tracers (GhOST) in situ instrument were used in this analysis. The instrument has two channels. The first channel couples an isothermally operated gas chromatograph (GC) with an electron capture detection (ECD) (GhOST-ECD), and the second channel couples a temperature-programmed GC with a quadrupole mass spectrometer (MS) (GhOST-MS) (see Jesswein et al. (2021) and references therein). For the SouthTRAC campaign, the GhOST-MS ionization mode was changed from negative chemical ionization (NCI) to electron impact ionization (EI) to record broader mass spectra, leading to different detection limits for the Br-VSLSs compared to previous campaigns. In this work, only measurements of the MS channels are used. The measurements of CH_2Br_2 and $CHBr_3$ are on the NOAA-2003 scale, thus consistent with NOAA/ESRL observations.

2.2 HIPPO mission

The HIPPO mission measured cross sections of trace gases over the Pacific Basin and North American mainland (170–80° W) (Fig. 1 black tracks), covering a latitudinal range from the North Pole (85° N) to the coastal region of Antarctica (65° S) (Wofsy, 2011). The mission was split into seasonal segmented deployments, which took place in January 2009 (HIPPO-1), October to November 2009 (HIPPO-2), March to April 2010 (HIPPO-3), June to July 2011 (HIPPO-4), and August to September 2011 (HIPPO-5). The platform used for the observations was the NSF/NCAR High-performance Instrumented Airborne Platform for Environmental Research (HIAPER) Gulfstream V (GV) aircraft.

Data from two whole air samplers (WASs) were combined in this analysis. The University of Miami operated the Advanced Whole Air Sampler (AWAS), storing air samples in pressurized stainless steel canisters (Atlas, 2016). The second sampler operated during HIPPO was the NOAA Whole Air Sampler (NWAS), which stores samples in pressurized glass flasks. Subsequently, the samples were analysed using ground-based laboratory GC–MS (gas chromatograph–mass spectrometer) systems. Results from both laboratories were provided on a scale consistent with NOAA/ESRL ground-based station results (see Hossaini et al., 2013, 2016).

2.3 ATom mission

The ATom mission was split into four parts, which took place in July to August 2016 (ATom-1), January to February 2017 (ATom-2), September to October 2017 (ATom-3), and April to May 2018 (ATom-4). Thus, all seasons were covered within a 2-year time period. In each season, flights started and ended in Palmdale (California, USA) with a route to the western Arctic, south to the South Pacific, east to the Atlantic, and north to Greenland, returning across central North America (Wofsy et al., 2021) (Fig. 1, red tracks). The platform for the ATom mission was the NASA DC-8 aircraft, which is capable of reaching an altitude of around 12 km (Thompson et al., 2022).

As with the HIPPO mission, data from two WASs were used for this analysis. The University of Carlifornia – Irvine (UC-Irvine) research group operated one whole air sampler (hereafter referred to as WAS), storing air in stainless steel canisters. Samples were analysed in the laboratory using GC with flame ionization detection (FID), ECD, and MS (Barletta et al., 2019). In addition, the NOAA/GML's Programmable Flask Package Whole Air Sampler (PFP) was operated using glass flasks. The air samples were analysed

at the NOAA's Global Monitoring Division laboratory for trace gases by GC-MS and at the Institute of Arctic and Alpine Research (INSTAAR) Stable Isotope Lab for isotopes of methane. Beside the two WASs, the NCAR Trace Organic Gas Analyzer (TOGA) was operated during ATom. TOGA is an in situ instrument, combining a GC with an MS (Apel et al., 2015), similar to the GhOST-MS. Asher et al. (2019) used ATom-2 observations among others to improve estimates of short-lived halocarbon emissions during summer from the Southern Ocean using airborne observations. The two whole air samplers and the TOGA instrument shared approximately half of the sampling period, generally presenting a good correlation and consistency in mole fractions for CH_2Br_2 and $CHBr_3$ (Asher et al., 2019).

3 Models and meteorological data

3.1 TOMCAT

The TOMCAT (Toulouse Off-line Model of Chemistry And Transport) is an Eulerian offline three-dimensional chemistry transport model (CTM) (Chipperfield, 2006; Monks et al., 2017). The model uses a hybrid vertical sigma–pressure coordinate ($\sigma - p$) with 60 vertical levels from the ground up to around 60 km. The horizontal resolution was set to $2.8° \times 2.8°$ (latitude $\times$ longitude). The CTM is forced by meteorological fields (winds, temperature, and humidity) taken from the European Centre for Medium-Range Weather Forecasts ERA5 reanalysis (Hersbach et al., 2020). The internal model step was 30 min and monthly means of the tracers are generated for this study. A similar setup was previously used to study NH Br-VSLSs in Keber et al. (2020), beside using ERA-Interim data instead of ERA5. In addition, the configuration used here reads an offline monthly varying climatological OH concentration field, developed for the TransCom-CH_4 project (Patra et al., 2011). In this study, the VSLS emission scenario of Ordóñez et al. (2012), which includes monthly variability in emissions, was used with TOMCAT. Model output is available for the period from 2009 to 2019.

3.2 CAM-Chem

CAM-Chem (Community Atmosphere Model with Chemistry, version 4) is a three-dimensional chemistry climate model (CCM) and a component of the NCAR Community Earth System Model (CESM) (Lamarque et al., 2012). The WACCM (Whole Atmosphere Community Climate Model) physics module for the stratosphere is included, and it uses the chemical mechanism of MOZART (Model for OZone and Related chemical Tracers) with different possibilities of complexity for tropospheric and stratospheric chemistry. The model includes a detailed treatment of tropospheric Br-VSLS sources and chemistry described in Fernandez et al. (2014) and Fernandez et al. (2017). The horizontal resolution was set to $0.96° \times 1.25°$ (latitude $\times$ longitude) and 56 hybrid vertical levels from the surface to around 40 km. The model setup is similar to the one used in Navarro et al. (2015), using the NASA Goddard Global Modeling and Assimilation Office (GMAO) GEOS5-generated meteorology. The model step was 5 min but monthly means of the tracers are used for this study. As with the TOMCAT model, the monthly varying emission scenario of Ordóñez et al. (2012) was used, with fixed emissions of the VSLSs during the whole modelling period (available from 2009–2019).

3.3 Meteorological data

Aeroplanes modified for scientific observations are equipped with on-board instruments to gather meteorological and aircraft parameters along the flight tracks. In addition, local tropopause information along the flight tracks as well as equivalent latitude were derived using the Chemical Lagrangian Model of the Stratosphere (CLaMS) (e.g. Grooß et al., 2014) with underlying ECMWF reanalysis. For the SouthTRAC, PGS, HIPPO, and ATom mission, the underlying meteorological field are taken from the ERA5 reanalysis, whereas for TACTS and WISE, the underlying fields are from the ERA-Interim reanalysis (Dee et al., 2011).

For this work, the potential vorticity (PV)-based dynamical tropopause is used (e.g. Gettelman et al., 2011). The commonly used value of 2 PVU (potential vorticity unit) was used for the dynamical tropopause; this condition was replaced by the potential temperature level of 380 K in the tropics when the 2 PVU level is above (e.g. Keber et al., 2020; Jesswein et al., 2021). We additionally used the same PV-based climatological tropopause information as in Keber et al. (2020), which is based on the ERA-Interim reanalysis.

4 Results

4.1 Analysis methods

In the course of this work, we progressively move from a more global view of the distribution of the tracers to a more detailed view of the UTLS in the midlatitudes of both hemispheres. For the global view (Sect. 4.2), we use latitude as the horizontal coordinate and pressure as the vertical coordinate and thus get a detailed perspective of the troposphere from the ground up to the tropopause and the LMS. As we then look more closely at the area around the tropopause and into the stratosphere, we change the vertical coordinate using potential temperature (Θ) and potential temperature difference to the local tropopause ($\Delta\Theta$) instead of pressure (starting from Sect. 4.3). Transport in the free atmosphere is predominantly isentropic, making Θ a very useful coordinate. Furthermore, Θ allows for better vertical resolution as it increases more rapidly with height in stable layers. Finally, the focus moves towards the UTLS of the midlatitudes in the course of the analysis (Sect. 4.4). We switch from the examination in latitude only to a combined coordinate already

used in Keber et al. (2020) and Jesswein et al. (2021). Latitude is used for tropospheric observations, whereas equivalent latitude is used for stratospheric ones. The equivalent latitude (Butchart and Remsberg, 1986) is a commonly used horizontal coordinate for studying tracers in the stratosphere and assigns PV to latitude based on the area (of the polar cap) enclosed by the specific isopleth of PV on a given potential temperature contour (Pan et al., 2012). The combined coordinate is referred to as equivalent latitude*. In all sub-analyses (Sects. 4.2–4.4), the observations are compared with the model data. The model results are only used for the years and months for which observations are available and have been zonally averaged (consistent with Keber et al., 2020).

4.2 Altitude–latitude cross sections

We combined the measurements from the different missions, leaving aside that the Br-VSLSs may have shown a weak positive trend (e.g. tropical mean 0.017 ± 0.012 ppt Br per decade for 1979–2013 from Tegtmeier et al., 2020). Observations and model results were split by season (DJF: December, January, February; MAM: March, April, May; JJA: June, July, August; SON: September, October, November). The data are binned in 10° latitude intervals from 90° S to 90° N. In the vertical we have binned the data between 1000 and 50 hPa into 20 bins. The bin size decreases logarithmically with increasing altitude and thus lower pressure. Thus, the size of the bins varies from about 180 hPa near the ground to 8.5 hPa in the lower stratosphere, which corresponds to an altitude resolution of about 1.3 km.

Figures 2 and 3 show the distributions of CH_2Br_2 and $CHBr_3$ for the observations (a–d), the TOMCAT model (e–h), the CAM-Chem model (i–l), and the differences between the respective model and the observations (m–t). The merged observational data set allows for a comprehensive representation of the tropospheric distribution except for the southern high latitudes (greater than 70° S) in summer and winter. Furthermore, the LMS of both hemispheres is much better covered by observations in spring and autumn.

The distributions of CH_2Br_2 in the troposphere (Fig. 2a–d) show a general increase in mixing ratios with increasing latitude, which is most pronounced in hemispheric winter. Increased mixing ratios almost reach the tropopause for this season. The tropospheric distributions show a clear seasonality in both hemispheres with the largest values observed in hemispheric winter and the smallest values in hemispheric summer in the lower troposphere. There is a slight asymmetry towards generally higher mixing ratios in the NH, particularly for the 70° N bin. The NH has more coastal regions, which are assumed to be one of the main sources of Br-VSLSs, which could explain the asymmetry of tropospheric mixing ratios. A rather striking difference between the NH and SH is observed in the LMS in autumn and spring. While the distribution of CH_2Br_2 in hemispheric spring is quite similar in both hemispheres, the distribution in hemispheric autumn differs with smaller values in the SH compared to the NH. Mixing ratios above the subtropical and extratropical tropopause are up to 0.3 ppt smaller in the SH. High mixing ratios of tropospheric tracers in the LMS observations during NH autumn have been explained by a strong influx of tropospheric air during NH summer and autumn (flushing of the LMS) (e.g. Hoor et al., 2005; Bönisch et al., 2009). It could be argued that this is an indication of the different strength of tropospheric air mixing into the LMS of the two hemispheres. The subtropical jet acts as a transport barrier and Konopka et al. (2015) diagnosed a hemispheric asymmetry of the subtropical jet with a most pronounced weakening in the NH summer (see Fig. 1 and references in Konopka et al., 2015).

Even though SH observations are available for all seasons from the different missions, the SH database remains much smaller than the NH database. Unfortunately, MAM measurements during ATom-4 show quite large differences between the results from TOGA and both whole air samplers (WAS and PFP) but only for observations of the SH LMS. Figure 4 displays the altitude–latitude cross section of the observations for MAM, taking all observations (a) and thus being similar to Fig. 2b as well as using all observations but only TOGA measurements from ATom (b) and using all observations but only the whole air samplers for ATom (c). Although there is little difference in the rest of the atmosphere due to the use of TOGA or WAS/PFP, the difference in the SH LMS during MAM is clear (see Fig. 4 observations inside red rectangles). Using the TOGA data (Fig. 4b), values are larger in the range of around 0.4–0.8 ppt, which would suggest a flushing of the LMS similar to that in northern hemispheric autumn (e.g. Bönisch et al., 2009). Values are much smaller when using WAS and PFP data (Fig. 4c) below around 0.4 ppt. This would indicate a strong isolation of the SH lower stratosphere. Indeed, Shuckburgh et al. (2009) investigated a strong seasonal cycle in the strength of the barriers at the subtropical jet, where in MAM in the SH, mixing follows a mostly zonal pattern and the subtropical jet acts as a barrier. They further stated that observed mixing is of the greatest magnitude in the NH in any season. The representation of the southern hemispheric UTLS in MAM is based on fewer observations than, e.g., southern hemispheric UTLS in spring where the SouthTRAC campaign took place. The SouthTRAC campaign contributes to a substantial portion of the spring UTLS observations in the SH. For a more meaningful result especially in SH autumn, but also in winter and summer, further measurements are necessary and should be a focus of future campaigns.

The model results show a general good agreement to the observations in the annual mean. Positive or negative bias to the observations are not very pronounced or consistent. Instead, negative or positive bias is dependent on season and latitude. For the case of CH_2Br_2, the largest lower-tropospheric values in the NH observations are in winter,

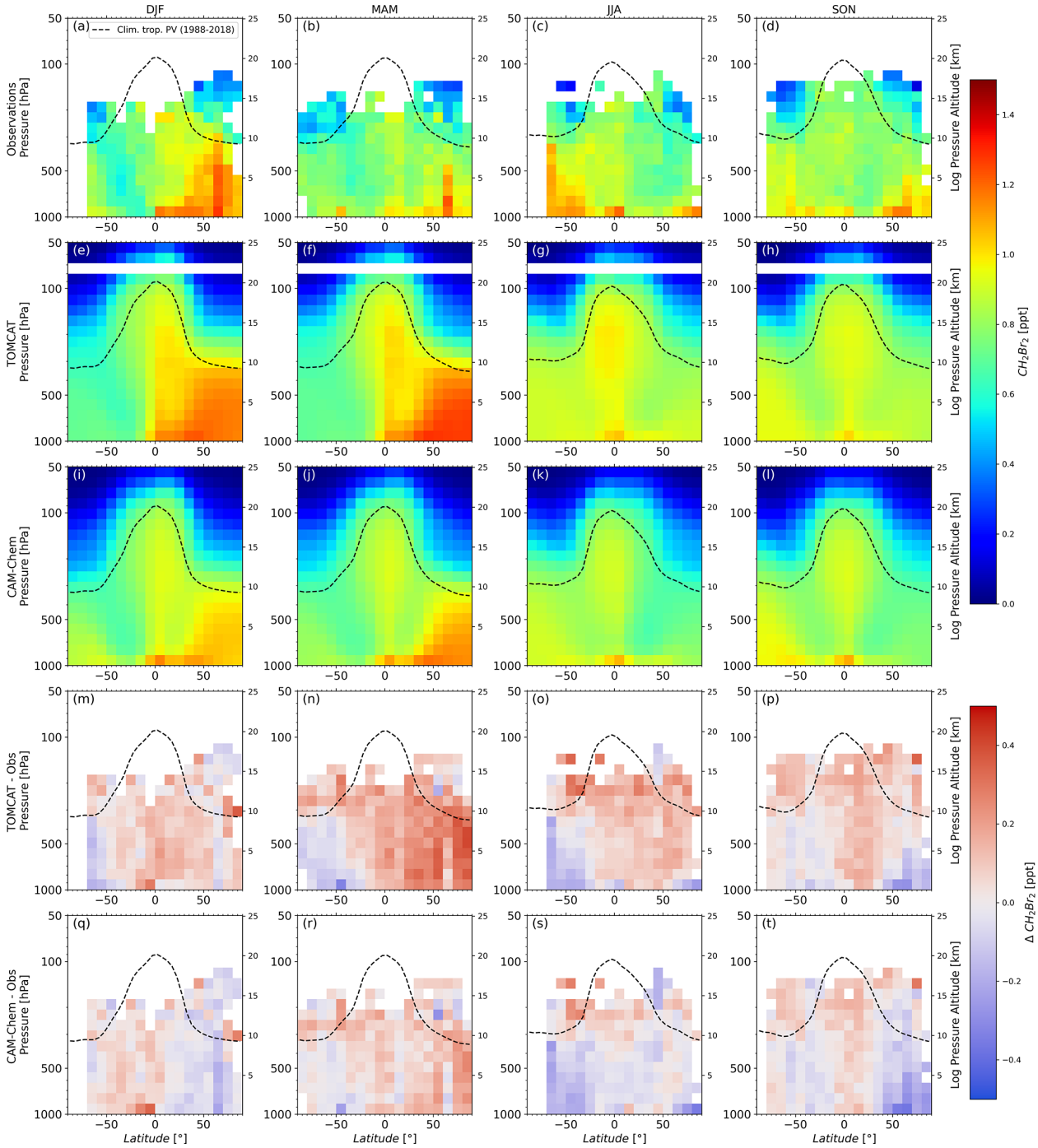

Figure 2. Altitude–latitude cross section of CH_2Br_2. The data are separated by season and displayed as a function of latitude and pressure. Top row **(a–d)** shows observational data. Second and third row **(e–h** and **i–l)** show model results of TOMCAT and CAM-Chem, respectively. Fourth and fifths row **(m–p** and **q–t)** show differences between the respective model and the observations. The dynamical tropopause (dashed lines) has been derived from the ERA-Interim reanalysis, providing a climatological (1988–2018) zonal mean tropopause. The slightly coarser vertical resolution of TOMCAT combined with the bin size leads to missing TOMCAT data between 68 and 80 hPa.

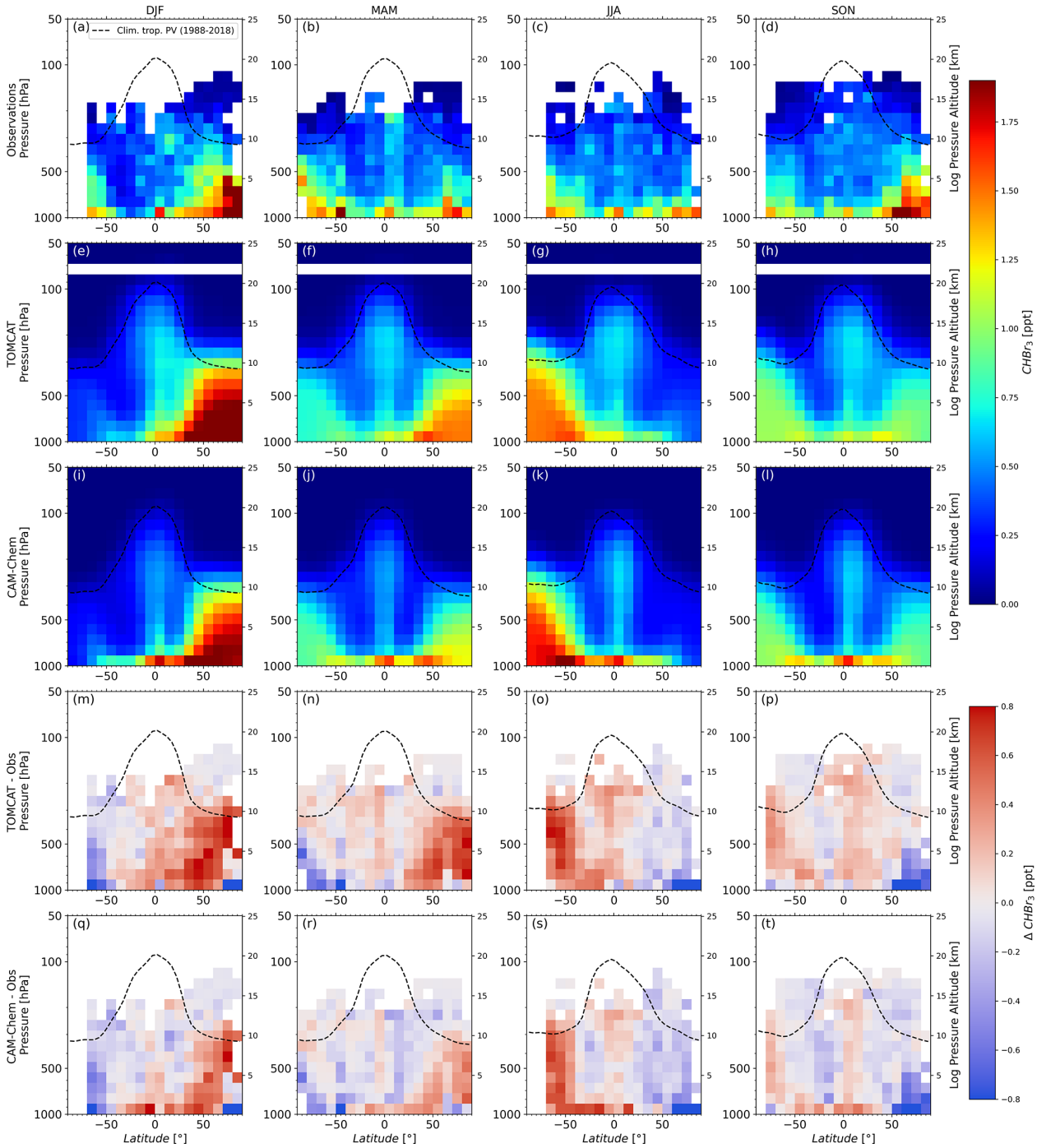

Figure 3. As in Fig. 2 but for $CHBr_3$.

whereas models show the largest values in spring. This may arise from a possible incorrect seasonal representation in the Ordóñez et al. (2012) emission scenario. Furthermore, TOMCAT values in the free troposphere are larger than in CAM-Chem, despite using the same emission scenario. Thus, overestimation in MAM in the NH is larger within TOMCAT with differences to observations of up to about 0.4 ppt. Both models underestimate NH high-latitude values of CH_2Br_2 in SON by up to 0.3 ppt. Hossaini et al. (2016) showed a comparison of different models and ground-based stations in which the models do not reproduce the seasonality at coastal stations such as Mace Head (Ireland) (see Fig. 3 therein). The observations used in this work were conducted predominantly over ocean and coastal regions (e.g. nearshore bases

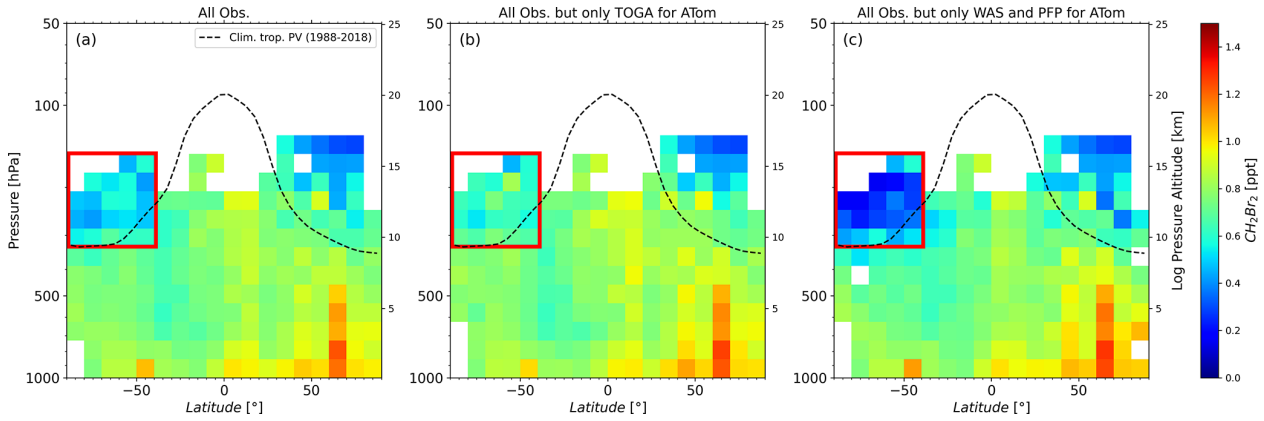

Figure 4. Altitude–latitude cross section of CH_2Br_2 for March, April, and May. Panel **(a)** presents the distribution of CH_2Br_2 as in Fig. 2, whereas in **(b)** data from all missions were used, but only TOGA observations from ATom were included, and in **(c)** data from all missions were used, but only WAS and PFP observations from ATom were included. The red rectangle indicates the region where observations from different techniques differed substantially from one another.

such as during the WISE campaign) and may have similar signatures to the coastal stations shown in Hossaini et al. (2016). Neither model shows the pronounced seasonal pattern of CH_2Br_2 in the SH with elevated values in the southern hemispheric winter. This may be due to the emission scenario of Ordóñez et al. (2012), which was used in both models. The top–down emission estimates of the bromocarbons in the Ordóñez et al. (2012) scenario are based on aircraft campaigns and some available observations in the marine boundary layer, most of which are from the NH. Ordóñez et al. (2012) already identified the issue regarding the emission flux estimates in the SH as a consequence of missing aircraft observations in the SH (especially south of 40° S for all seasons). In addition, the Ordóñez et al. (2012) emission inventory does not consider Br-VSLSs arising from sea ice regions, which are possible sources of Br-VSLSs according to, e.g., Abrahamsson et al. (2018).

As noted before, $CHBr_3$ has a much shorter atmospheric lifetime than CH_2Br_2. Consequently, the global tropospheric distributions from the observations of $CHBr_3$ show larger variability and a less pronounced seasonality. Jia et al. (2019) used simulations to demonstrate that uniform background emissions of $CHBr_3$ from the ocean result in a highly variable distribution in the atmosphere with larger values in regions of convergence or low wind speed and that the impact of localized elevated emissions on the distribution varies significantly from campaign to campaign. Thus, the interpretation of $CHBr_3$ airborne observations is challenging. Nonetheless, the NH shows larger values in autumn and winter compared to spring and summer, a feature that is captured by both models, although the modelled wintertime maxima are more pronounced than in the observations and much less pronounced in autumn. Near-ground observations, however, may not be representative as they are largely from coastal areas. Based on the limited existing observations in the SH, the seasonality is not very pronounced with slightly smaller values in summer high latitudes and slightly larger near-ground values in autumn followed by winter. SH high-latitude ground-based NOAA/GML measurements presented in Hossaini et al. (2016) like the one from Cape Grim (Tasmania, Australia) and the Palmer Station (Antarctica), which are on a consistent scale as aircraft measurements, e.g. from PFP, also show a less pronounced seasonality. Furthermore, measurements of these stations reveal that models did not capture the observed seasonality for coastal stations (see Fig. 3 in Hossaini et al., 2016). Observations and model comparison from this study demonstrate a similar discrepancy as seen in Hossaini et al. (2016) at high latitudes of the SH with an underestimation in summer and autumn, where differences for tropospheric observations range between about 0.2 and 0.6 ppt, and overestimation mainly in winter high latitudes which reaches up to 0.8 ppt. Both models overestimate NH tropospheric values in winter and spring by up to 0.8 ppt except for near-ground values at high latitudes, which are much larger in the observational data (2–5 ppt difference to the observations above 80° N). In summer and autumn, the models underestimate high-latitude values (differences to observations of about 0.2 ppt and up to 0.9 ppt near the ground). Especially in the NH there is a larger frequency of observations over the northern Atlantic Ocean (see Fig. 1). For example, the flights of the WISE campaigns took place predominantly from Shannon (Ireland), close to known coastline source regions of $CHBr_3$, which may have a greater influence on the atmospheric distribution than photochemical decay (e.g. Carpenter et al., 2005; Hossaini et al., 2016). $CHBr_3$ lower-stratospheric values are close to 0, as this substance has a shorter lifetime and is faster decomposed compared to CH_2Br_2. Model estimates of TOMCAT and CAM-Chem overall agree well within the LMS of both hemispheres.

4.3 Upper-tropospheric latitudinal distribution

Trace gases can enter the extratropical UTLS through several pathways. Beside the downward transport from the stratospheric overworld, there is a two-way exchange across the extratropical tropopause and an isentropic exchange, often in the vicinity of the subtropical jet (e.g. Gettelman et al., 2011, and references therein). The amount of total bromine likely differs depending on how and where air enters the LMS and, consequently, the characteristics of the contributing input regions.

To investigate the distributions of the two major Br-VSLSs in the upper troposphere as a function of latitude, we binned the observational data according to latitude and to potential temperature relative to the local tropopause. Only data in the 10 K range below the local dynamical tropopause are included, to characterize the possible input region. For the models, only data in the 10 K range below the climatological PV-based tropopause are included. Data have been separated into low latitudes (0–30°), midlatitudes (30–60°), and high latitudes (60–90°) for both hemispheres. Results for CH_2Br_2 and $CHBr_3$ are listed in Tables 1 and 2, respectively, and the hemispheric winter CH_2Br_2 results are shown in Fig. 5 (graphical representations of the other seasons and seasonal cycle of each latitudinal band can be found in the Supplement). Engel et al. (2018) reported typical tropical tropopause mixing ratios compiled from different measurement campaigns with mixing ratios in the upper tropical tropopause layer (upper TTL) of 0.73 (0.43–0.94) ppt CH_2Br_2 and 0.28 (0.02–0.64) ppt $CHBr_3$.

As shown in Table 1, low-latitude CH_2Br_2 values in both hemispheres during all seasons are well within the range reported by Engel et al. (2018) although with slightly higher mixing ratios. Keber et al. (2020) showed a clear tendency for an increase in tropopause mixing ratios with latitude in the NH, most pronounced in winter (see Fig. 5). This is likely due to the increase in lifetimes with latitude, as photochemical breakdown becomes slower with higher latitudes especially during winter. Our extended data set confirms the findings of Keber et al. (2020). In addition, we show that the SH upper-tropospheric distribution looks similar to that of the NH. Mixing ratios in NH winter and spring are slightly larger than in SH winter and spring, whereas mixing ratios in the respective hemispheric summer are close to each other across all latitudes. Larger differences are observed in the low and midlatitudes of NH and SH during autumn, with larger values in the NH than in the SH. However, the high latitudes of each autumn differ only to a small extent.

Both models qualitatively reproduce the larger CH_2Br_2 values in hemispheric winter and spring and smaller values in summer and autumn at high and midlatitudes (see Fig. S3 in the Supplement). However, both models overestimate low-latitude values for all seasons except for SH spring and NH winter. This overestimation in TOMCAT could already be seen in Keber et al. (2020) for the NH low latitudes for both

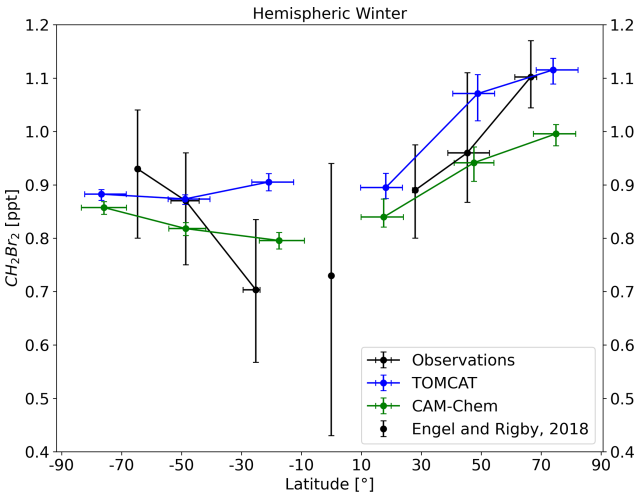

Figure 5. Latitude cross section of tropopause representative mixing ratios of CH_2Br_2 from observation (black) and model results (blue for TOMCAT and green for CAM-Chem) for both hemispheres in winter. Data are binned into three latitude bins for each hemisphere: high latitudes (60–90°), midlatitudes (30–60°), and low latitudes (0–30°) and only for data within the 10 K below the dynamical tropopause. Shown are the medians with the error bars representing the interquartile range (IQR). The median latitudinal position of observational and model bins may differ due to different spatial data coverage of observations and models. Also included is the reference mixing ratio for the tropical tropopause (Engel et al., 2018).

winter and late summer to early autumn, as well as in Hossaini et al. (2013) where the TOMCAT model was only compared with HIPPO data. In general, CAM-Chem values are slightly smaller than TOMCAT values except in SH summer and autumn high latitudes. In NH winter, the models are close to observations (observations in between the model results), but both models overestimate NH spring values. However, both models reproduce the observed increase in mixing ratios with latitude in NH winter and spring, with CAM-Chem showing slightly better agreement. The models simulate SH winter and spring well in the midlatitudes and high latitudes, with TOMCAT somewhat closer to the winter observations, but none of the models capture the observed latitudinal variations in winter. The largest values in the models are found at high latitudes in spring for both hemispheres where observations show the largest values in hemispheric winter high latitudes (see Table 1 for absolute values). Summer and autumn of both hemispheres are in better agreement with CAM-Chem, as TOMCAT deviates more from the observations. TOMCAT generally simulates smaller mixing ratios in the SH and larger mixing ratios in NH summer and autumn midlatitudes and high latitudes.

For $CHBr_3$ (see Table 2 and Figs. S2 and S4 in the Supplement), the upper-tropospheric distribution is much more variable and shows a less clear seasonality, especially in the SH. NH low-latitude values are slightly higher with a maxi-

Table 1. Averaged mole fractions (median in parts per trillion, ppt) of CH_2Br_2 and their corresponding range (25th to 75th percentiles) at high latitudes (60–90°), midlatitudes (30–60°), and low latitudes (0–30°) in the upper troposphere, e.g. within 10 K below the local dynamical tropopause for the Northern and Southern hemispheres.

	Southern Hemisphere			Northern Hemisphere		
CH_2Br_2	high latitudes	midlatitudes	low latitudes	low latitudes	midlatitudes	high latitudes
Observations	ppt (range)			ppt (range)		
Winter	0.93 (0.8–1.04)	0.87 (0.75–0.96)	0.7 (0.57–0.84)	0.89 (0.8–0.98)	0.96 (0.87–1.11)	1.1 (1.04–1.17)
Spring	0.87 (0.78–0.96)	0.81 (0.73–0.91)	0.86 (0.76–0.87)	0.74 (0.69–0.83)	0.84 (0.72–1.07)	0.92 (0.75–1.15)
Summer	0.73 (0.68–0.86)	0.68 (0.59–0.76)	0.68 (0.61–0.76)	0.64 (0.49–0.71)	0.7 (0.62–0.79)	0.72 (0.64–0.81)
Autumn	0.76 (0.67–0.82)	0.7 (0.6–0.8)	0.65 (0.57–0.73)	0.74 (0.72–0.77)	0.78 (0.75–0.82)	0.77 (0.71–0.84)
TOMCAT						
Winter	0.88 (0.87–0.89)	0.87 (0.86–0.88)	0.91 (0.89–0.92)	0.89 (0.87–0.92)	1.07 (1.02–1.11)	1.12 (1.09–1.14)
Spring	0.89 (0.87–0.91)	0.81 (0.79–0.83)	0.84 (0.82–0.87)	0.9 (0.87–0.92)	1.04 (0.99–1.09)	1.16 (1.13–1.19)
Summer	0.66 (0.65–0.67)	0.65 (0.64–0.69)	0.83 (0.8–0.86)	0.89 (0.87–0.9)	0.81 (0.8–0.83)	0.82 (0.81–0.83)
Autumn	0.69 (0.68–0.69)	0.7 (0.69–0.74)	0.86 (0.84–0.88)	0.88 (0.86–0.91)	0.84 (0.82–0.85)	0.83 (0.82–0.84)
CAM-Chem						
Winter	0.86 (0.84–0.87)	0.82 (0.8–0.83)	0.8 (0.78–0.81)	0.84 (0.82–0.87)	0.94 (0.91–0.97)	1.0 (0.97–1.01)
Spring	0.87 (0.85–0.89)	0.79 (0.77–0.81)	0.79 (0.77–0.81)	0.82 (0.8–0.83)	0.89 (0.84–0.93)	1.01 (0.98–1.03)
Summer	0.73 (0.71–0.75)	0.68 (0.67–0.7)	0.79 (0.76–0.82)	0.77 (0.74–0.79)	0.68 (0.67–0.69)	0.7 (0.68–0.71)
Autumn	0.73 (0.71–0.74)	0.7 (0.69–0.71)	0.79 (0.77–0.81)	0.81 (0.79–0.83)	0.71 (0.71–0.74)	0.72 (0.71–0.73)

Table 2. As in Table 1 but for $CHBr_3$.

	Southern Hemisphere			Northern Hemisphere		
$CHBr_3$	high latitudes	midlatitudes	low latitudes	low latitudes	midlatitudes	high latitudes
Observations	ppt (range)			ppt (range)		
Winter	0.36 (0.2–0.57)	0.35 (0.19–0.48)	0.2 (0.07–0.29)	0.43 (0.33–0.62)	0.54 (0.42–0.75)	0.72 (0.63–0.82)
Spring	0.45 (0.35–0.56)	0.33 (0.24–0.52)	0.41 (0.36–0.43)	0.35 (0.3–0.46)	0.49 (0.33–0.62)	0.5 (0.34–0.8)
Summer	0.57 (0.32–0.82)	0.3 (0.2–0.47)	0.3 (0.19–0.34)	0.32 (0.26–0.42)	0.27 (0.19–0.42)	0.37 (0.28–0.56)
Autumn	0.53 (0.38–0.76)	0.38 (0.26–0.57)	0.22 (0.17–0.28)	0.28 (0.2–0.33)	0.44 (0.33–0.6)	0.45 (0.35–0.63)
TOMCAT						
Winter	1.27 (1.17–1.34)	0.87 (0.69–1.04)	0.28 (0.23–0.33)	0.3 (0.25–0.37)	1.18 (0.91–1.39)	1.56 (1.43–1.68)
Spring	0.83 (0.75–0.89)	0.45 (0.33–0.59)	0.23 (0.19–0.28)	0.25 (0.21–0.31)	0.67 (0.52–0.82)	1.08 (0.99–1.18)
Summer	0.28 (0.24–0.3)	0.21 (0.19–0.24)	0.29 (0.24–0.39)	0.41 (0.33–0.49)	0.28 (0.25–0.31)	0.28 (0.25–0.3)
Autumn	0.64 (0.57–0.69)	0.4 (0.35–0.46)	0.29 (0.25–0.35)	0.41 (0.32–0.5)	0.55 (0.48–0.61)	0.73 (0.66–0.79)
CAM-Chem						
Winter	1.27 (1.16–1.36)	0.73 (0.56–0.9)	0.12 (0.09–0.18)	0.12 (0.09–0.21)	0.95 (0.71–1.16)	1.41 (1.27–1.53)
Spring	0.7 (0.61–0.77)	0.35 (0.26–0.45)	0.1 (0.07–0.14)	0.12 (0.09–0.15)	0.46 (0.33–0.57)	0.77 (0.7–0.86)
Summer	0.19 (0.17–0.22)	0.16 (0.14–0.18)	0.13 (0.09–0.21)	0.26 (0.17–0.33)	0.2 (0.17–0.21)	0.2 (0.19–0.21)
Autumn	0.64 (0.56–0.7)	0.33 (0.28–0.41)	0.13 (0.09–0.18)	0.22 (0.16–0.32)	0.44 (0.37–0.52)	0.66 (0.59–0.71)

mum in winter of 0.43 (0.33–0.62) ppt and maximum value in SH spring of 0.41 (0.36–0.43) ppt. NH values show an increase in mixing ratios with latitude, most pronounced in winter and spring. In NH summer, mixing ratios drop from low latitudes to midlatitudes and increase towards high latitudes again. Thus, the NH upper-tropospheric distribution of $CHBr_3$ does not show the behaviour described in Keber et al. (2020) with an increase towards midlatitudes and a decrease at higher latitudes. Keber et al. (2020) considered a combined data set for summer and early autumn, whereas in this analysis summer and autumn are considered separately. As the latitudinal distribution differs substantially in summer and autumn (see Table 2), the separate consideration of summer and autumn compared to the combined consideration as in Keber et al. (2020) can lead to differences in the interpretation of the observations. The behaviour of $CHBr_3$, which can be seen in the NH summer, is also observed in the SH spring as well. All other seasons of the SH show an increase in mix-

ing ratios with latitude but with the largest values in summer and autumn high latitudes with up to 0.57 (0.32–0.82) ppt in SH summer.

TOMCAT simulates an increase in mixing ratio with latitude for almost all seasons, with the largest values occurring in hemispheric winter. Only in hemispheric summer do values decrease from low latitudes to midlatitudes and then increase slightly in SH high latitudes and remain at the same level in the NH high latitudes. Mid- and high-latitude mixing ratios in the NH are highly overestimated in winter, spring, and to a smaller extent in autumn, a feature already observed in Fig. 3. In the SH, midlatitude mixing ratios are also overestimated in winter, spring, and autumn, which is also true for high-latitude spring and autumn. In contrast, the observed and modelled mixing ratios in the SH high latitudes in winter and summer show a different behaviour. In the observations, the high-latitude values are smallest in the winter and highest in the summer, which is a reversed behaviour of the model estimations (see Table 2 or Fig. S4). As the high-latitude observations are much more limited during these seasons (see Fig. 2 or Table S1 in the Supplement), we are careful about interpreting these differences and further observations are needed to verify these deviations from model results. CAM-Chem upper-tropospheric distributions are similar to TOMCAT distributions, although in general they show smaller values for all latitudes. Thus, $CHBr_3$ mixing ratios from CAM-Chem are somewhat closer to the observation in NH winter, spring, and autumn midlatitudes to high latitudes and deviate slightly more in NH summer, compared to TOMCAT. In the SH, spring and autumn distributions from CAM-Chem are closer to observations compared to winter and summer distributions. Like for TOMCAT, the seasonal variation within the high latitudes show a different behaviour in comparison to the observations, with an even smaller value from CAM-Chem in SH summer high latitudes. Overall, the distribution of $CHBr_3$ is highly variable, and both models simulate a similar latitudinal distribution, though with smaller values for CAM-Chem. The tug of war between rapid advective transport and local accumulation at the time of emission plays a decisive role. As already mentioned, Jia et al. (2019) showed that transport variations in the atmosphere itself produce a highly variable Br-VSLS distribution with elevated values not always reflecting strong localized sources.

4.4 Midlatitude UTLS vertical profiles

The observational coverage of the upper troposphere and especially the lower stratosphere is best in spring and autumn of the respective hemisphere. From the altitude–latitude cross sections (Sect. 4.1, Figs. 2 and 3), we already suspect larger differences in the LMS Br-VSLS distribution in hemispheric autumn than in hemispheric spring.

We thus took a closer look at the vertical profiles of CH_2Br_2 and $CHBr_3$ in the midlatitudes of the SH and NH during these seasons. The observations from the different missions were seasonally combined and have been binned in 10 K intervals of potential temperature and potential temperature difference to the local tropopause. Only bins with at least five observations are considered. For the profile in the free troposphere, data were binned in potential temperature (Θ). Data binned in potential temperature difference to the local tropopause ($\Delta\Theta$) show larger variability in the free troposphere (e.g. Keber et al., 2020). $\Delta\Theta$ coordinates are therefore not well suited for tropospheric data. As $\Delta\Theta$ coordinates reduce the variability of the profile near the tropopause and within the lowermost stratosphere (e.g. Keber et al., 2020), the profile continued from 10 K below the local tropopause into the stratosphere in $\Delta\Theta$ coordinates. The two vertical coordinates were combined by aligning 0 K of $\Delta\Theta$ with the median tropopause in Θ, observed during the measurements. Profiles in Θ coordinates may extend beyond the median tropopause even if the observations are declared as tropospheric ones. Tropopause Θ of these observations is much larger and corresponds to a higher tropopause, indicating that these observations may be subtropical in origin. The mixing ratios are averaged over equivalent latitude* of 40–60° of the respective hemisphere using box-and-whisker plots for the binned data (see Figs. 6 and 7). Vertical gradients for spring and autumn profiles for both hemispheres from tropopause values up to 30 K above the local tropopause are summarized in Table 3.

Figure 6 shows hemispheric spring profiles of CH_2Br_2 and $CHBr_3$. Upper-tropospheric values of CH_2Br_2 are very similar and close to 1 ppt in both hemispheres. The values at the tropopause are slightly larger (by 0.05–0.1 ppt) at the NH tropopause compared to the SH tropopause. The CH_2Br_2 profiles in the lowermost stratosphere of both hemispheres are very similar in their respective spring, beside an exceptional low value of 0.25 ppt at 90 K of $\Delta\Theta$ in the NH. Vertical gradients of $CHBr_3$ profiles are larger compared to CH_2Br_2, well in line with the much shorter lifetimes (see Table 3). Upper-tropospheric mixing ratios are slightly larger in SH midlatitudes (by roughly 0.16 ppt). However note that NH tropospheric values present a larger variability. In contrast, tropopause values are slightly larger in the NH than in the SH. Mixing ratios drop to values close to 0 in both hemispheres at about 30–40 K of Θ above the tropopause.

Figure 7 shows hemispheric autumn profiles of CH_2Br_2 and $CHBr_3$ with less similarity between SH and NH profiles than in hemispheric spring for both compounds. Upper-tropospheric values of CH_2Br_2 are slightly larger in the NH with a difference of up to 0.16 ppt to the SH. Tropopause values for hemispheric autumn (Fig. 7a and b) are slightly smaller compared to hemispheric spring values (Fig. 6a and b), but hemispheric differences in spring and autumn are comparable. Differences between NH and SH autumn become larger on the lowest levels above the dynamical tropopause; i.e. in the ExTL. CH_2Br_2 shows a larger vertical gradient up to 30 K of $\Delta\Theta$ in SH autumn than in NH autumn (see Table 3) reaching smallest value of 0.45 ppt between 20

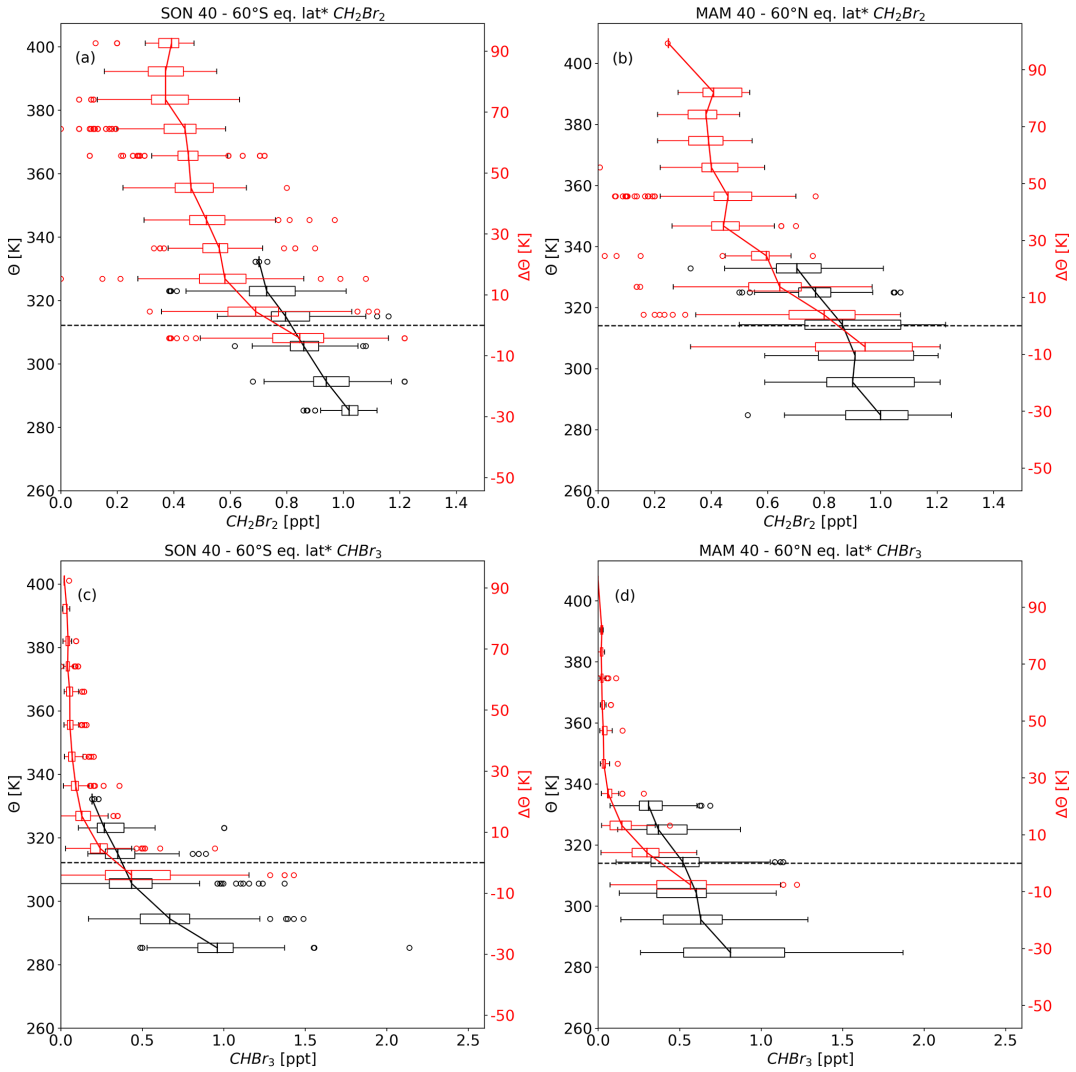

Figure 6. Hemispheric spring vertical profiles of **(a, b)** CH_2Br_2 and **(c, d)** $CHBr_3$. Observations were averaged over 40–60° of equivalent latitude*. Data are displayed as a function of potential temperature for tropospheric values (black) and potential temperature difference to the local tropopause for values from 10 K below the tropopause and above (red). Shown are the medians with the boxes representing the interquartile range (IQR), with whiskers as the 1.5 × IQR, and circles are single observations outside the whiskers (outliers). The dashed black line shows the median dynamical tropopause derived from the times and locations of the observation.

Table 3. Vertical gradients across the tropopause in the Northern Hemisphere (NH) and Southern Hemisphere (SH) spring and autumn from tropopause (TP) mixing ratios from the 10 K bin below the dynamical tropopause up to the 20–30 K bin above the dynamical tropopause. In addition, local lifetimes of CH_2Br_2 and $CHBr_3$ for the tropospheric tropics and northern hemispheric midlatitudes at 10 km, taken from Carpenter et al. (2014).

	Gradients [% K^{-1}]				Local lifetimes (d)				
	Spring		Autumn		Tropics	Midlatitudes			
	SH	NH	SH	NH		Winter	Spring	Summer	Autumn
CH_2Br_2	1.12	1.23	1.27	0.59	150	890	360	150	405
$CHBr_3$	2.63	2.97	4.42[a]	2.25	17	88	29	17	44

[a] Gradient from TP to 10–20 K.

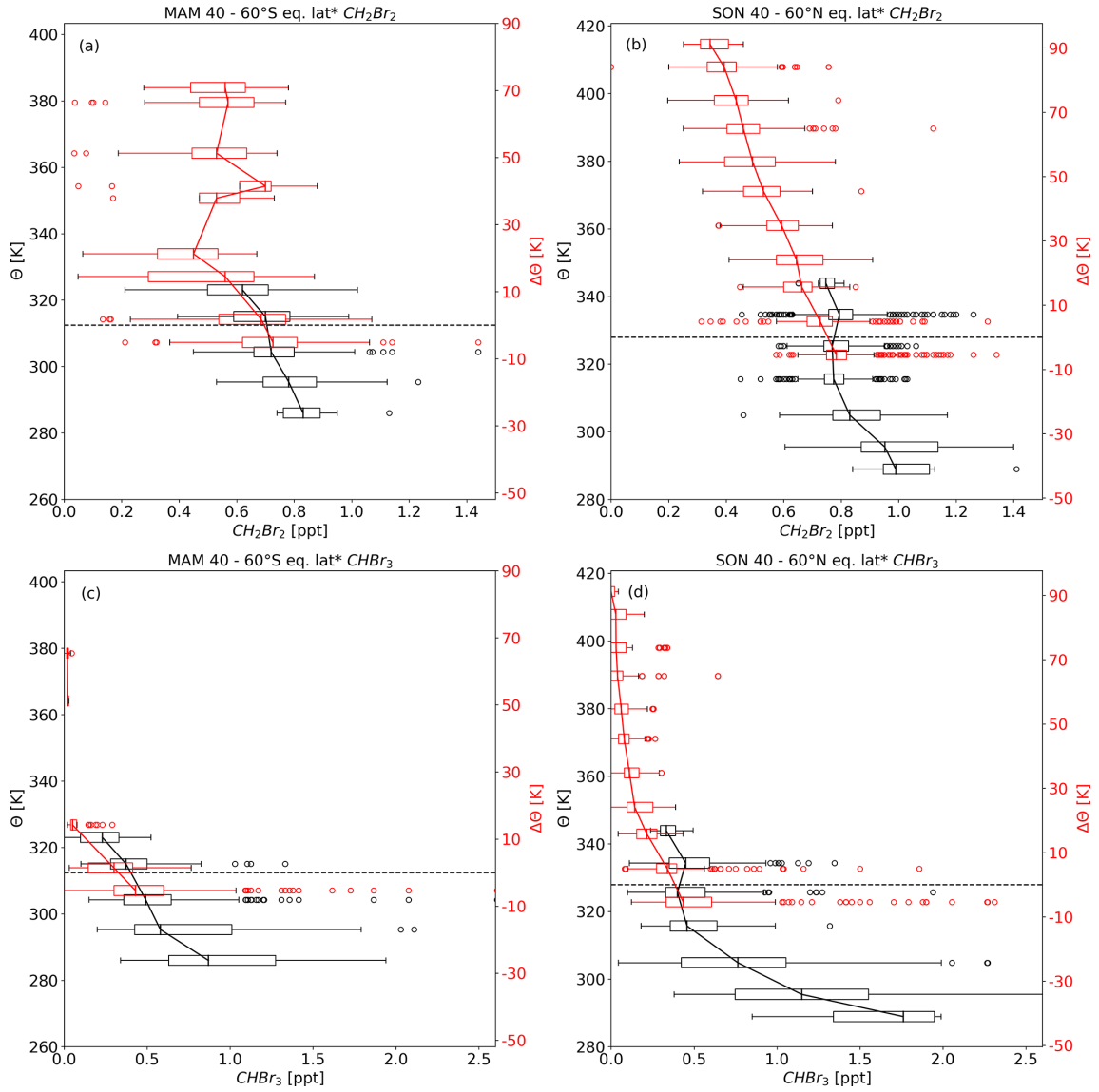

Figure 7. As in Fig. 6 but for hemispheric autumn.

and 30 K of $\Delta\Theta$. With a comparable distance to the dynamic tropopause, the value in the NH is 0.64 ppt. Between 40 and 70 K of $\Delta\Theta$, SH values range from 0.53 to 0.7 ppt associated with a large variability.

Figure 8 again shows the SH autumn vertical profile of CH_2Br_2, but two more profiles were included in $\Delta\Theta$ coordinates with one profile excluding TOGA observations and one profile excluding WAS and PFP observations. The profile including only TOGA from ATom is much closer to the profile using all observations, whereas the profile including only WAS and PFP observations from ATom shows a much steeper gradient across the tropopause and much smaller values. The larger number of TOGA observations shifts the median towards larger values. The profile without TOGA measurements would be in line with the assumption of a strong transport barrier, e.g. the subtropical jet and exchange between stratosphere and troposphere only at the edges of the jets (e.g. Fig. 1 in Gettelman et al., 2011), while the profile without WAS and PFP shows a less strong but still larger transport barrier than in the NH autumn profile (Fig. 7b). The NH profile also shows a much smaller gradient compared to NH spring and less variability, which may indicate a well-mixed LMS. This is also well in line with finding by, e.g., Bönisch et al. (2009), who showed a flushing of the lowermost stratosphere in summer and autumn.

Hemispherical differences can also be inferred from $CHBr_3$ vertical profiles. Larger differences can be seen in the upper troposphere with nearly double the amount in the NH compared to the SH. In contrast, hemispheric differences at the tropopause are small (close to 0.5 ppt for both

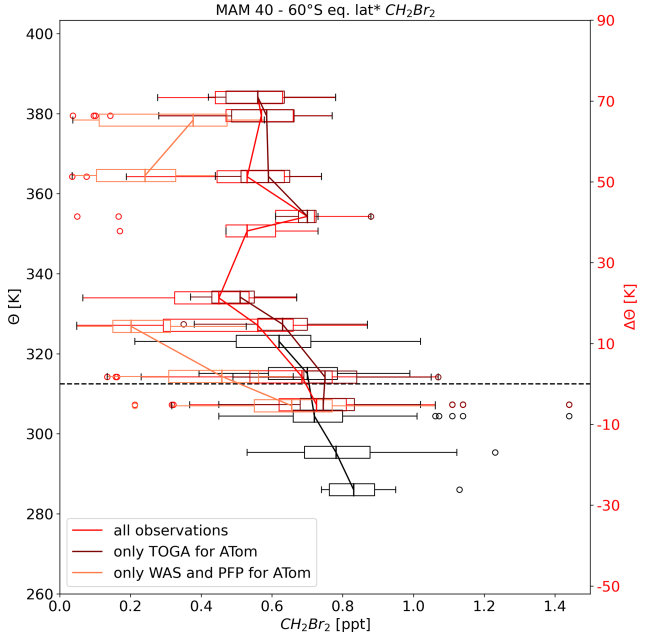

Figure 8. As in Fig. 7 but only CH_2Br_2 for SH autumn. Profile as a function of potential temperature difference to the local tropopause was split into three profiles. Profile using all observations is in red, similar to Fig. 7, profile using all observation but with only TOGA observations from ATom in dark red, and profile using all observations but with only flask observations in light red.

hemispheres). Regarding the LMS and especially the ExTL, the vertical gradient is much larger in the SH than in the NH. This implies that there is a stronger transport barrier in the SH when looking at $CHBr_3$. SH values drop to almost 0 in the first 20 K above the dynamical tropopause but to around 0.22 ppt at a comparable distance to the NH autumn tropopause. Furthermore, NH lowermost-stratospheric values are steadily decreasing and are above 0.02 ppt even at 90 K of $\Delta\Theta$.

We further compared the midlatitude profiles of CH_2Br_2 and $CHBr_3$ with model results of TOMCAT and CAM-Chem in Figs. 9 and 10. The comparisons are shown as a function of $\Delta\Theta$. Since there is no tropopause information for the TOMCAT model, we derived $\Delta\Theta$ as the difference between the climatological tropopause potential temperature and model potential temperature. For consistency, the climatological tropopause was used for CAM-Chem as well. Additionally, since equivalent latitude information is not available for the models, latitude was used instead. The mean absolute percentage differences (MAPDs) reported below are tabled in the Supplement.

For spring CH_2Br_2 (Fig. 9a and b), TOMCAT profiles overestimate the observations on average by about 0.12 ppt in the NH and 0.08 ppt in the SH, with a corresponding MAPD of about 26 % (NH) and 18 % (SH). The CAM-Chem profiles are closer to the observations. Particularly the NH profile within the lowest 20 K above the dynamical tropopause is close to the observations but deviates towards higher altitudes. Average differences in the NH are 0.06 ppt and an MAPD of 17 %, whereas in the SH, differences are on average 0.03 ppt with an MAPD of 9 %. For $CHBr_3$ (Fig. 9c and d), the comparison is only shown up to 40 K of $\Delta\Theta$, since this substance was almost completely depleted above. TOMCAT seems to overestimate NH $CHBr_3$ by on average 0.1 ppt, corresponding to an MAPD of 69 %. Differences are much smaller in the SH with 0.02 ppt and an MAPD of 21 %. CAM-Chem estimated the lowermost stratosphere well in the NH with an average difference of 0.02 ppt and an MAPD of 15 %. SH differences in CAM-Chem are on average 0.04 ppt with an MAPD of 26 %, thus slightly larger than TOMCAT differences. Both models estimated a nearly complete depletion of $CHBr_3$ in the SH lower stratosphere (above 40 K of $\Delta\Theta$). However, observations show a slight offset to the model estimations with values of 0.02–0.04 ppt up to 90 K of $\Delta\Theta$ (Fig. 9c).

Hemispheric autumn midlatitude profiles of CH_2Br_2 and $CHBr_3$ are displayed in Fig. 10. In NH autumn, the observed profiles and those of the models agree well. In the SH, however, the profiles diverge further as neither of the models reproduce the presumably stronger barrier at the tropopause described in Fig. 8. TOMCAT overestimates NH CH_2Br_2 up to 90 K of $\Delta\Theta$ on average by about 0.1 ppt (MAPD of 20 %). The difference between models and observations becomes much larger in SH autumn. In addition, the observational profile exhibits a high degree of variability, and the scatter of the individual bins increases due to the differences between the ATom instruments, as mentioned earlier. Although models are close to observations above 40 K of $\Delta\Theta$, average differences between 0 and 40 K of $\Delta\Theta$ are 0.12 ppt (MAPD of 25 %). CAM-Chem estimates are closer to the observations in the NH and differ on average by about 0.02 ppt corresponding to an MAPD of 6 %. However, CAM-Chem showed a similar profile to TOMCAT in the SH, although slightly smaller values in general and thus a smaller average difference between 0 and 40 K of $\Delta\Theta$ of 0.06 ppt and an MAPD of 15 %. Compared to NH spring, TOMCAT shows a $CHBr_3$ profile which is much closer to the observations in NH autumn. The average difference below 40 K of $\Delta\Theta$ is 0.06 ppt with a corresponding MAPD of 22 %. SH observations are limited and thus a comparison is only possible up to 20 K of $\Delta\Theta$. Although observations and model results of TOMCAT are close near the dynamical tropopause, the difference increases rapidly to 0.13 ppt between 10 and 20 K of $\Delta\Theta$. As the CAM-Chem profile is smaller in absolute values, the largest differences are around 0.08 ppt. Both models fail to capture the steeper gradient across the dynamical tropopause during SH autumn.

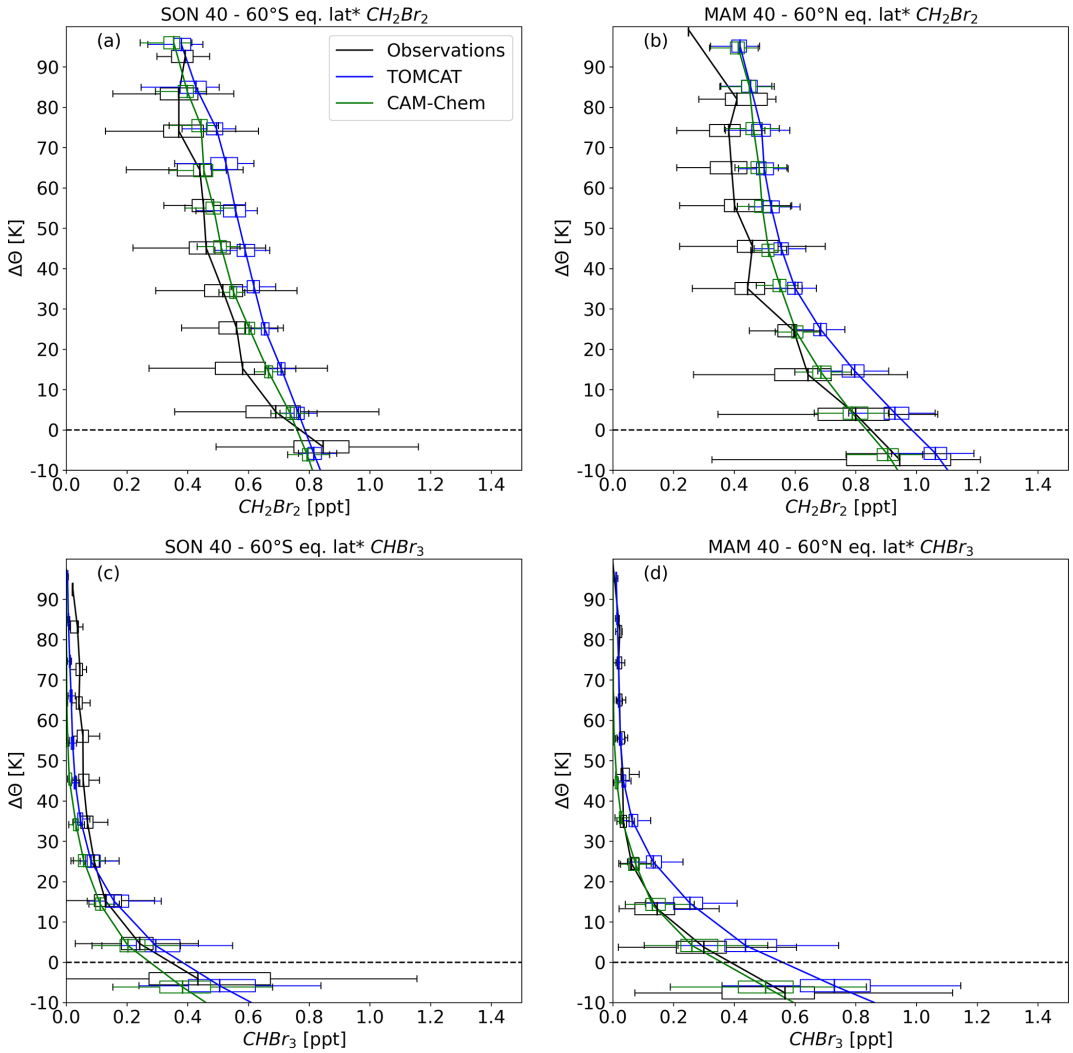

Figure 9. Hemispheric spring vertical profiles of **(a, b)** CH_2Br_2 and **(c, d)** $CHBr_3$. Observations were averaged over 40–60° of equivalent latitude*. Data are displayed as a function of potential temperature difference to the local tropopause (black). Also shown are model results from TOMCAT (blue) and CAM-Chem (green) as a function of potential temperature relative to the climatological tropopause. Profiles show medians with the boxes representing the interquartile range (IQR) and whiskers as the 1.5 × IQR. Outliers are not included for a better illustration.

5 Summary and conclusion

In the present work, we investigated the global seasonal distribution of the two major short-lived brominated substances CH_2Br_2 and $CHBr_3$. These natural substances with dominant oceanic origin gain importance because their relative contribution to the loss of ozone will rise as a result of the decline in the long-lived brominated substances of anthropogenic origin. We used data from four HALO missions: TACTS, WISE, PGS, and SouthTRAC. To further expand the data set, we included aircraft observations of the HIPPO and ATom missions. These are two global-scale missions, covering a wide latitude range in all seasons from the ground to the lowermost stratosphere. Zonal mean distributions were analysed by using latitude as the horizontal and pressure as the vertical coordinate (altitude–latitude cross sections). As the focus moved on to the tropopause region and lowermost stratosphere (upper-tropospheric distribution and vertical profiles), data are presented in potential temperature and further in a tropopause relative coordinate, namely the difference in potential temperature to the dynamical tropopause ($\Delta\Theta$). We further compared the observed distributions with two model distributions from TOMCAT and CAM-Chem, both using the Ordóñez et al. (2012) emission scenario, with emissions varying by season.

We found a similar tropospheric seasonality of CH_2Br_2 in both hemispheres, although with slightly larger mixing ratios in the NH. The larger values in the NH agree with expected hemispheric difference, as the main sources of many brominated VSLSs are believed to be stronger from coastal

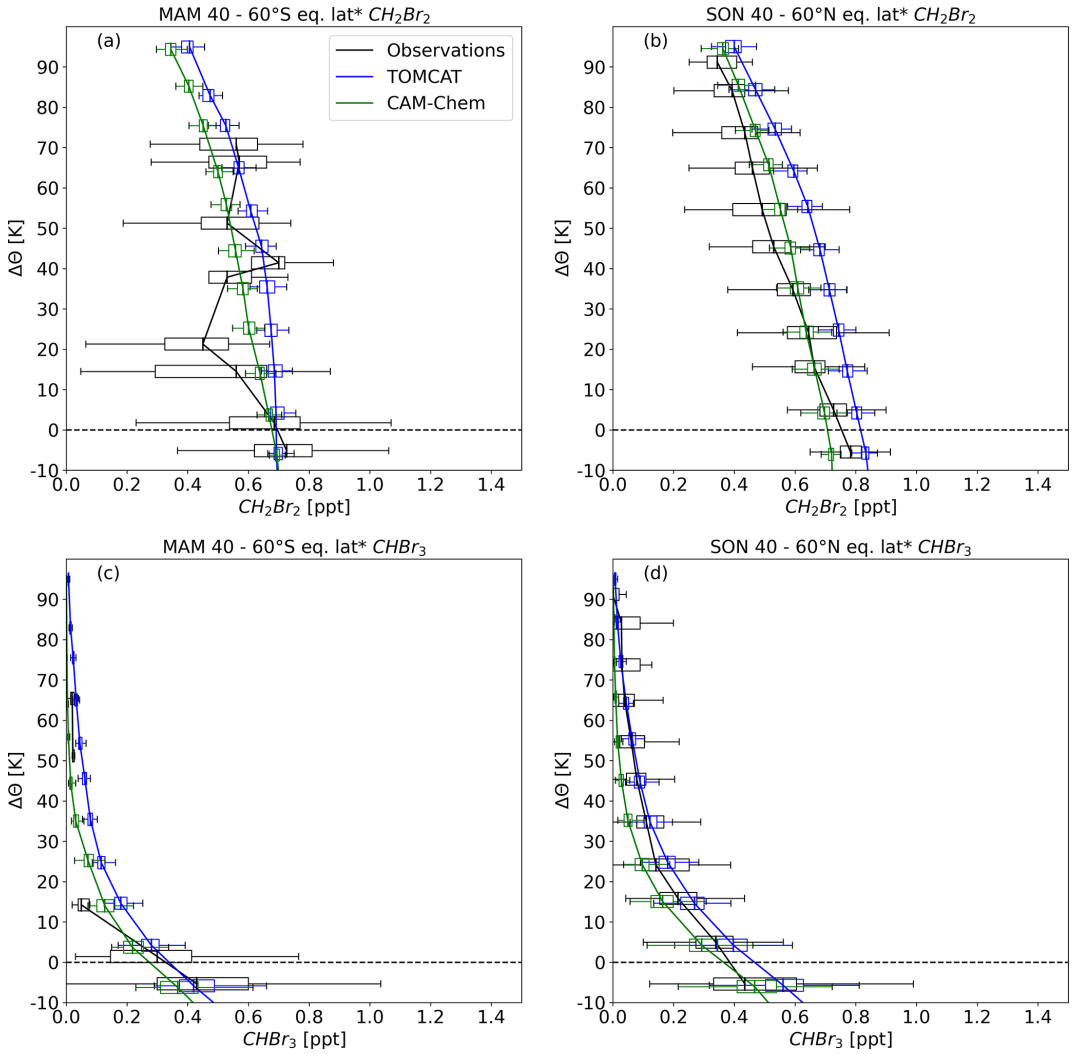

Figure 10. As in Fig. 9 but for hemispheric autumn.

ocean regions. The ratio of ocean and land mass of the NH and SH is different, causing the size of coastal areas to vary. The upper-tropospheric distributions of CH_2Br_2 also show that the seasonality is similar in both hemispheres with larger values in winter and spring and smaller values in summer and autumn. In addition, in all seasons the mixing ratios are larger at NH midlatitudes and high latitudes than at the SH midlatitudes and high latitudes. Global seasonal distribution of $CHBr_3$ shows larger variability and less clear seasonality. Although the NH mixing ratios seem to be larger in winter and spring than in summer and autumn, SH distributions show less seasonality with slightly larger values in autumn but overall smaller ones than in the NH. This may again be a result of the different ratio of ocean and land mass of both hemispheres. In good agreement with Keber et al. (2020), the mixing ratios at the extratropical tropopause are systematically larger than those at the tropical tropopause in both hemispheres at all times of the year. The comparison of the distributions in the UTLS was limited to hemispheric spring and autumn due to a lower coverage of the SH by observations. The LMS distributions in hemispheric spring are very similar (with differences well below 0.1 ppt) but differ considerably in hemispheric autumn (up to 0.3 ppt more in the NH). Midlatitude profiles of CH_2Br_2 and $CHBr_3$, extending into the lowest stratosphere in hemispheric spring, are also similar, whereas profiles in hemispheric autumn differ much more. In particular, SH profiles of CH_2Br_2 and $CHBr_3$ show much steeper gradients across the tropopause and into the stratosphere than NH profiles, and in the case of CH_2Br_2, SH observations present higher profile variability. This provides room for discussion as to whether the transport barrier in the SH autumn is significantly stronger, preventing the flushing of the lower stratosphere as it occurs in the NH summer and autumn. Unfortunately, in particular the observations in the lower stratosphere of the SH autumn show large differences between the different instruments on board the aircraft dur-

ing ATom-4. Even if differences in the hemispheric autumn are already recognizable here, more observations and further investigation are needed to confirm an interhemispheric difference in the respective autumn lowermost stratosphere. The SH is less sampled than the NH and the observations may not be representative of the general distribution for all seasons in the SH.

We further compared the observed and modelled distributions from TOMCAT and CAM-Chem. The observed seasonality of CH_2Br_2 was only partially reproduced by the models and was not very pronounced in the SH, probably due to the emission scenario used, which for the high latitudes presents a homogeneous distribution and less pronounced seasonal cycle due to the scarcity of observations used in the construction of the scenario. The lack of aircraft observations in the SH led to issues regarding the emission flux estimates. In the case of $CHBr_3$, both models systematically overestimate hemispheric winter and spring mixing ratios in the free troposphere and slightly underestimate hemispheric summer and autumn. In general, the mixing ratios in TOMCAT are larger than in CAM-Chem, which could be due to the differences in transport and the efficiency of the photochemical decomposition in the models when using the same emission scenario. Regarding upper-tropospheric distributions, the models reproduced the seasonality well with larger values in winter and spring and smaller values in summer and autumn. Model estimates are close to CH_2Br_2 observations for all seasons and both hemispheres, although the different flushing behaviour in the lower stratosphere between NH and SH is not captured by any of the models. Regarding $CHBr_3$, both models yield significantly higher values in hemispheric winter midlatitudes and high latitudes than observed. The high-latitude observations of $CHBr_3$ of the SH show a strong deviation from the models. Especially in winter and summer, the deviations are particularly large with observations showing reversed behaviour to the model simulations (largest values in summer and smallest values in winter). At these times of the year the flights do not reach such high latitudes ($< 70^\circ$ S) and the number of observations in the high latitudes is very limited. For a more meaningful conclusion for the SH high latitudes, additional observations are needed. Modelled midlatitude vertical profiles agree well with observed profiles for NH spring and autumn as well as for SH spring. TOMCAT profiles are always slightly higher in mixing ratios than CAM-Chem and differences were therefore predominantly smaller when comparing with CAM-Chem. Both models were not capable of reproducing SH autumn vertical profiles of CH_2Br_2. Vertical gradients of CH_2Br_2 and $CHBr_3$ across the tropopause in the respective autumn differ strongly from each other with steeper gradients in the SH autumn. Vertical gradients in the hemispheric spring, on the other hand, are more similar to each other.

Given these initial results of the global distribution of the two major Br-VSLSs, we reinforce the utility and need for further observations in the SH UTLS to further understand the seasonal distribution of theses species. Especially in the southern hemispheric UTLS, data coverage remains sparse in most seasons. First differences between the NH and SH could already be indicated based on the data used; thus extrapolating northern hemispheric observations to the SH is not possible. The representation of seasonal variability of Br-VSLS emissions and the efficiency of photochemical processes within the high latitudes need to be improved individually for the NH and SH to improve the agreement with current and future observations. In addition, it is of importance to generate a long-term global data set that can be used to determine if there is a trend in Br-VSLS abundance at the global and hemispheric scale.

Data availability. Observational data from the HALO missions are available via the HALO Database (https://halo-db.pa.op.dlr.de/, last access: 22 June 2022). ATom observational data are available at the Oak Ridge National Laboratory Distributed Active Archive Center (ORNL DAAC; https://doi.org/10.3334/ORNLDAAC/1925; Wofsy et al., 2021). HIPPO observational data are available at the Earth Observing Laboratory data archive (EOL data archive, Wofsy et al., 2017). Model data are available on request: please contact Ryan Hossaini (r.hossaini@lancaster.ac.uk) for TOMCAT model data and Rafael P. Fernandez (rpfernandez@mendoza-conicet.gob.ar) for CAM-Chem model data.

Supplement. The supplement related to this article is available online at: https://doi.org/10.5194/acp-22-15049-2022-supplement.

Author contributions. MJ, TK, TS, TW, and AE were involved in developing and operating the GhOST instrument. ELA and SM operated the instruments during HIPPO, and ECA, RSH, SM, and DRB operated the instruments during ATom. RH, RPF, ASL, and JUG provided model data and participated in the discussion regarding model comparison. MJ wrote the article with involvement of AE and TS in the analysis and writing process. All co-authors were involved in the discussion and iteration process of the article.

Competing interests. At least one of the (co-)authors is a member of the editorial board of *Atmospheric Chemistry and Physics*. The peer-review process was guided by an independent editor, and the authors also have no other competing interests to declare.

Disclaimer. Publisher's note: Copernicus Publications remains neutral with regard to jurisdictional claims in published maps and institutional affiliations.

Acknowledgements. Dough Kinnison is thanked for helping with the high-resolution SD-CAM-Chem setup.

Financial support. This research has been supported by the Bundesministerium für Bildung und Forschung (grant no. 01LG1908B), the Deutsche Forschungsgemeinschaft (grant nos. EN367/13-1, EN367/14-1, EN367/16-1, EN367/17-1), and DFG collaborative research program "The Tropopause Region in an Changing Atmosphere" TRR 301 – Project-ID 428312742, the National Center for Atmospheric Research (grant no. 1852977), the Consejo Nacional de Investigaciones Científicas y Técnicas (grant no. PICT 2019-2187), and the Natural Environment Research Council (grant no. NE/N014375/).

This open-access publication was funded by the Goethe University Frankfurt.

Review statement. This paper was edited by Aurélien Dommergue and reviewed by two anonymous referees.

References

Abrahamsson, K., Granfors, A., Ahnoff, M., Cuevas, C. A., and Saiz-Lopez, A.: Organic bromine compounds produced in sea ice in Antarctic winter, Nat. Commun., 9, 5291, https://doi.org/10.1038/s41467-018-07062-8, 2018.

Apel, E. C., Hornbrook, R. S., Hills, A. J., Blake, N. J., Barth, M. C., Weinheimer, A., Cantrell, C., Rutledge, S. A., Basarab, B., Crawford, J., Diskin, G., Homeyer, C. R., Campos, T., Flocke, F., Fried, A., Blake, D. R., Brune, W., Pollack, I., Peischl, J., Ryerson, T., Wennberg, P. O., Crounse, J. D., Wisthaler, A., Mikoviny, T., Huey, G., Heikes, B., O'Sullivan, D., and Riemer, D. D.: Upper tropospheric ozone production from lightning NO_x-impacted convection: Smoke ingestion case study from the DC3 campaign, J. Geophys. Res.-Atmos., 120, 2505–2523, https://doi.org/10.1002/2014jd022121, 2015.

Asher, E., Hornbrook, R. S., Stephens, B. B., Kinnison, D., Morgan, E. J., Keeling, R. F., Atlas, E. L., Schauffler, S. M., Tilmes, S., Kort, E. A., Hoecker-Martínez, M. S., Long, M. C., Lamarque, J.-F., Saiz-Lopez, A., McKain, K., Sweeney, C., Hills, A. J., and Apel, E. C.: Novel approaches to improve estimates of short-lived halocarbon emissions during summer from the Southern Ocean using airborne observations, Atmos. Chem. Phys., 19, 14071–14090, https://doi.org/10.5194/acp-19-14071-2019, 2019.

Atlas, E.: Advanced Whole Air Sampler (AWAS) for HIAPER, UCAR/NCAR – Earth Observing Laboratory, https://doi.org/10.5065/D65X270F, 2016.

Barletta, B., Biggs, B., Blake, D., Blake, N., Hoffman, A., Hughes, S., Meinardi, S., Vieznor, N., and Woods, C.: ATom: L2 Halocarbons and Hydrocarbons from the UC-Irvine Whole Air Sampler (WAS), https://doi.org/10.3334/ORNLDAAC/1751, 2019.

Birner, T. and Bönisch, H.: Residual circulation trajectories and transit times into the extratropical lowermost stratosphere, Atmos. Chem. Phys., 11, 817–827, https://doi.org/10.5194/acp-11-817-2011, 2011.

Bönisch, H., Engel, A., Curtius, J., Birner, Th., and Hoor, P.: Quantifying transport into the lowermost stratosphere using simultaneous in-situ measurements of SF_6 and CO_2, Atmos. Chem. Phys., 9, 5905–5919, https://doi.org/10.5194/acp-9-5905-2009, 2009.

Boudjellaba, D., Dron, J., Revenko, G., Demelas, C., and Boudenne, J.-E.: Chlorination by-product concentration levels in seawater and fish of an industrialised bay (Gulf of Fos, France) exposed to multiple chlorinated effluents, Sci. Total Environ., 541, 391–399, https://doi.org/10.1016/j.scitotenv.2015.09.046, 2016.

Butchart, N. and Remsberg, E. E.: The Area of the Stratospheric Polar Vortex as a Diagnostic for Tracer Transport on an Isentropic Surface, J. Atmos. Sci., 43, 1319–1339, https://doi.org/10.1175/1520-0469(1986)043<1319:TAOTSP>2.0.CO;2, 1986.

Carpenter, L. J. and Liss, P. S.: On temperate sources of bromoform and other reactive organic bromine gases, J. Geophys. Res.-Atmos., 105, 20539–20547, https://doi.org/10.1029/2000jd900242, 2000.

Carpenter, L. J., Wevill, D. J., O'Doherty, S., Spain, G., and Simmonds, P. G.: Atmospheric bromoform at Mace Head, Ireland: seasonality and evidence for a peatland source, Atmos. Chem. Phys., 5, 2927–2934, https://doi.org/10.5194/acp-5-2927-2005, 2005.

Carpenter, L. J., Reimann, S., Burkholder, J. B., Clerbaux, C., Hall, B. D., Hossaini, R., Laube, J. C., and Yvon-Lewis, S. A.: Ozone-Depleting Substances (ODSs) and Other Gases of Interest to the Montreal Protocol, Chap. 1, World Meteorological Organization, Geneva, Switzerland, 55, ISBN 978-9966-076-01-4, 2014.

Chipperfield, M. P.: New version of the TOMCAT/SLIMCAT offline chemical transport model: Intercomparison of stratospheric tracer experiments, Q. J. Roy. Meteor. Soc., 132, 1179–1203, https://doi.org/10.1256/qj.05.51, 2006.

Daniel, J. S., Solomon, S., and Portmann, R. W.: Stratospheric ozone depletion: The importance of bromine relative to chlorine, J. Geophys. Res.-Atmos., 104, 23871–23880, https://doi.org/10.1029/1999JD900381, 1999.

Dee, D. P., Uppala, S. M., Simmons, A. J., Berrisford, P., Poli, P., Kobayashi, S., Andrae, U., Balmaseda, M. A., Balsamo, G., Bauer, P., Bechtold, P., Beljaars, A. C. M., van de Berg, L., Bidlot, J., Bormann, N., Delsol, C., Dragani, R., Fuentes, M., Geer, A. J., Haimberger, L., Healy, S. B., Hersbach, H., Hòlm, E. V., Isaksen, L., Kållberg, P., Köhler, M., Matricardi, M., McNally, A. P., Monge-Sanz, B. M., Morcrette, J.-J., Park, B.-K., Peubey, C., de Rosnay, P., Tavalato, C., Thépaut, J.-N., and Vitart, F.: The ERA-Interim reanalysis: Configuration and performance of the data assimilation system, Q. J. Roy. Meteor. Soc., 137, 553–597, https://doi.org/10.1002/qj.828, 2011.

Engel, A., Rigby, M., Burkholder, J. B., Fernandez, R. P., Froidevaux, L., Hall, B. D., Hossaini, R., Saito, T., Vollmer, M. K., and Yao, B.: Update on Ozone-Depletion Substances (ODSs) and other Gases of Interest to the Montreal Protocol, Chap. 1, World Meteorological Organization, Geneva, Switzerland, 58, ISBN 978-1-7329317-1-8, 2018.

Fernandez, R. P., Salawitch, R. J., Kinnison, D. E., Lamarque, J.-F., and Saiz-Lopez, A.: Bromine partitioning in the tropical tropopause layer: implications for stratospheric injection, Atmos. Chem. Phys., 14, 13391–13410, https://doi.org/10.5194/acp-14-13391-2014, 2014.

Fernandez, R. P., Kinnison, D. E., Lamarque, J.-F., Tilmes, S., and Saiz-Lopez, A.: Impact of biogenic very short-lived bromine on the Antarctic ozone hole during the 21st century, Atmos. Chem. Phys., 17, 1673–1688, https://doi.org/10.5194/acp-17-1673-2017, 2017.

Gettelman, A., Hoor, P., Pan, L. L., Randel, W. J., Hegglin, M. I., and Birner, T.: The extratropical upper troposphere and lower stratosphere, Rev. Geophys., 49, https://doi.org/10.1029/2011RG000355, 2011.

Grooß, J.-U., Engel, I., Borrmann, S., Frey, W., Günther, G., Hoyle, C. R., Kivi, R., Luo, B. P., Molleker, S., Peter, T., Pitts, M. C., Schlager, H., Stiller, G., Vömel, H., Walker, K. A., and Müller, R.: Nitric acid trihydrate nucleation and denitrification in the Arctic stratosphere, Atmos. Chem. Phys., 14, 1055–1073, https://doi.org/10.5194/acp-14-1055-2014, 2014.

Hamed, M. A., Moustafa, M. E., Soliman, Y. A., El-Sawy, M. A., and Khedr, A. I.: Trihalomethanes formation in marine environment in front of Nuweibaa desalination plant as a result of effluents loaded by chlorine residual, The Egyptian Journal of Aquatic Research, 43, 45–54, https://doi.org/10.1016/j.ejar.2017.01.001, 2017.

Hegglin, M. I. and Shepherd, T. G.: O_3–N_2O correlations from the Atmospheric Chemistry Experiment: Revisiting a diagnostic of transport and chemistry in the stratosphere, J. Geophys. Res.-Atmos., 112, https://doi.org/10.1029/2006jd008281, 2007.

Hegglin, M. I., Boone, C. D., Manney, G. L., and Walker, K. A.: A global view of the extratropical tropopause transition layer from Atmospheric Chemistry Experiment Fourier Transform Spectrometer O_3, H_2O, and CO, J. Geophys. Res.-Atmos., 114, https://doi.org/10.1029/2008JD009984, 2009.

Hersbach, H., Bell, B., Berrisford, P., Hirahara, S., Horányi, A., Muñoz-Sabater, J., Nicolas, J., Peubey, C., Radu, R., Schepers, D., Simmons, A., Soci, C., Abdalla, S., Abellan, X., Balsamo, G., Bechtold, P., Biavati, G., Bidlot, J., Bonavita, M., De Chiara, G., Dahlgren, P., Dee, D., Diamantakis, M., Dragani, R., Flemming, J., Forbes, R., Fuentes, M., Geer, A., Haimberger, L., Healy, S., Hogan, R. J., Hólm, E., Janisková, M., Keeley, S., Laloyaux, P., Lopez, P., Lupu, C., Radnoti, G., de Rosnay, P., Rozum, I., Vamborg, F., Villaume, S., and Thépaut, J.-N.: The ERA5 global reanalysis, Q. J. Roy. Meteor. Soc., 146, 1999–2049, https://doi.org/10.1002/qj.3803, 2020.

Hoor, P., Fischer, H., and Lelieveld, J.: Tropical and extratropical tropospheric air in the lowermost stratosphere over Europe: A CO-based budget, Geophys. Res. Lett., 32, L07802, https://doi.org/10.1029/2004GL022018, 2005.

Hossaini, R., Mantle, H., Chipperfield, M. P., Montzka, S. A., Hamer, P., Ziska, F., Quack, B., Krüger, K., Tegtmeier, S., Atlas, E., Sala, S., Engel, A., Bönisch, H., Keber, T., Oram, D., Mills, G., Ordóñez, C., Saiz-Lopez, A., Warwick, N., Liang, Q., Feng, W., Moore, F., Miller, B. R., Marécal, V., Richards, N. A. D., Dorf, M., and Pfeilsticker, K.: Evaluating global emission inventories of biogenic bromocarbons, Atmos. Chem. Phys., 13, 11819–11838, https://doi.org/10.5194/acp-13-11819-2013, 2013.

Hossaini, R., Chipperfield, M. P., Montzka, S. A., Rap, A., Dhomse, S., and Feng, W.: Efficiency of short-lived halogens at influencing climate through depletion of stratospheric ozone, Nat. Geosci., 8, 1427–1442, https://doi.org/10.1038/ngeo2363, 2015.

Hossaini, R., Patra, P. K., Leeson, A. A., Krysztofiak, G., Abraham, N. L., Andrews, S. J., Archibald, A. T., Aschmann, J., Atlas, E. L., Belikov, D. A., Bönisch, H., Carpenter, L. J., Dhomse, S., Dorf, M., Engel, A., Feng, W., Fuhlbrügge, S., Griffiths, P. T., Harris, N. R. P., Hommel, R., Keber, T., Krüger, K., Lennartz, S. T., Maksyutov, S., Mantle, H., Mills, G. P., Miller, B., Montzka, S. A., Moore, F., Navarro, M. A., Oram, D. E., Pfeilsticker, K., Pyle, J. A., Quack, B., Robinson, A. D., Saikawa, E., Saiz-Lopez, A., Sala, S., Sinnhuber, B.-M., Taguchi, S., Tegtmeier, S., Lidster, R. T., Wilson, C., and Ziska, F.: A multi-model intercomparison of halogenated very short-lived substances (TransCom-VSLS): linking oceanic emissions and tropospheric transport for a reconciled estimate of the stratospheric source gas injection of bromine, Atmos. Chem. Phys., 16, 9163–9187, https://doi.org/10.5194/acp-16-9163-2016, 2016.

Jesswein, M., Bozem, H., Lachnitt, H.-C., Hoor, P., Wagenhäuser, T., Keber, T., Schuck, T., and Engel, A.: Comparison of inorganic chlorine in the Antarctic and Arctic lowermost stratosphere by separate late winter aircraft measurements, Atmos. Chem. Phys., 21, 17225–17241, https://doi.org/10.5194/acp-21-17225-2021, 2021.

Jia, Y., Tegtmeier, S., Atlas, E., and Quack, B.: How marine emissions of bromoform impact the remote atmosphere, Atmos. Chem. Phys., 19, 11089–11103, https://doi.org/10.5194/acp-19-11089-2019, 2019.

Keber, T., Bönisch, H., Hartick, C., Hauck, M., Lefrancois, F., Obersteiner, F., Ringsdorf, A., Schohl, N., Schuck, T., Hossaini, R., Graf, P., Jöckel, P., and Engel, A.: Bromine from short-lived source gases in the extratropical northern hemispheric upper troposphere and lower stratosphere (UTLS), Atmos. Chem. Phys., 20, 4105–4132, https://doi.org/10.5194/acp-20-4105-2020, 2020.

Klobas, J. E., Weisenstein, D. K., Salawitch, R. J., and Wilmouth, D. M.: Reformulating the bromine alpha factor and equivalent effective stratospheric chlorine (EESC): evolution of ozone destruction rates of bromine and chlorine in future climate scenarios, Atmos. Chem. Phys., 20, 9459–9471, https://doi.org/10.5194/acp-20-9459-2020, 2020.

Konopka, P., Ploeger, F., Tao, M., Birner, T., and Riese, M.: Hemispheric asymmetries and seasonality of mean age of air in the lower stratosphere: Deep versus shallow branch of the Brewer–Dobson circulation, J. Geophys. Res.-Atmos., 120, 2053–2066, https://doi.org/10.1002/2014jd022429, 2015.

Kunkel, D., Hoor, P., Kaluza, T., Ungermann, J., Kluschat, B., Giez, A., Lachnitt, H.-C., Kaufmann, M., and Riese, M.: Evidence of small-scale quasi-isentropic mixing in ridges of extratropical baroclinic waves, Atmos. Chem. Phys., 19, 12607–12630, https://doi.org/10.5194/acp-19-12607-2019, 2019.

Lamarque, J.-F., Emmons, L. K., Hess, P. G., Kinnison, D. E., Tilmes, S., Vitt, F., Heald, C. L., Holland, E. A., Lauritzen, P. H., Neu, J., Orlando, J. J., Rasch, P. J., and Tyndall, G. K.: CAM-chem: description and evaluation of interactive atmospheric chemistry in the Community Earth System Model, Geosci. Model Dev., 5, 369–411, https://doi.org/10.5194/gmd-5-369-2012, 2012.

Leedham, E. C., Hughes, C., Keng, F. S. L., Phang, S.-M., Malin, G., and Sturges, W. T.: Emission of atmospherically significant halocarbons by naturally occurring and farmed tropical macroalgae, Biogeosciences, 10, 3615–3633, https://doi.org/10.5194/bg-10-3615-2013, 2013.

Liu, Y., Yvon-Lewis, S., Hu, L., Salisbury, J., and O'Hern, J.: $CHBr_3$, CH_2Br_2, and $CHClBr_2$ in the U. S. coastal waters during the Gulf of Mexico and East Coast Carbon cruise, J. Geophys. Res.-Oceans, 116, https://doi.org/10.1029/2010JC006729, 2011.

Maas, J., Tegtmeier, S., Quack, B., Biastoch, A., Durgadoo, J. V., Rühs, S., Gollasch, S., and David, M.: Simulating the spread of disinfection by-products and anthropogenic bromoform emissions from ballast water discharge in Southeast Asia, Ocean Sci., 15, 891–904, https://doi.org/10.5194/os-15-891-2019, 2019.

Maas, J., Tegtmeier, S., Jia, Y., Quack, B., Durgadoo, J. V., and Biastoch, A.: Simulations of anthropogenic bromoform indicate high emissions at the coast of East Asia, Atmos. Chem. Phys., 21, 4103–4121, https://doi.org/10.5194/acp-21-4103-2021, 2021.

Monks, S. A., Arnold, S. R., Hollaway, M. J., Pope, R. J., Wilson, C., Feng, W., Emmerson, K. M., Kerridge, B. J., Latter, B. L., Miles, G. M., Siddans, R., and Chipperfield, M. P.: The TOMCAT global chemical transport model v1.6: description of chemical mechanism and model evaluation, Geosci. Model Dev., 10, 3025–3057, https://doi.org/10.5194/gmd-10-3025-2017, 2017.

Navarro, M. A., Atlas, E. L., Saiz-Lopez, A., Rodriguez-Lloveras, X., Kinnison, D. E., Lamarque, J.-F., Tilmes, S., Filus, M., Harris, N. R. P., Meneguz, E., Ashfold, M. J., Manning, A. J., Cuevas, C. A., Schauffler, S. M., and Donets, V.: Airborne measurements of organic bromine compounds in the Pacific tropical tropopause layer, P. Natl. Acad. Sci. USA, 112, 13789–13793, https://doi.org/10.1073/pnas.1511463112, 2015.

Oelhaf, H., Sinnhuber, B.-M., Woiwode, W., Bönisch, H., Bozem, H., Engel, A., Fix, A., Friedl-Vallon, F., Grooß, J.-U., Hoor, P., Johansson, S., Jurkat-Witschas, T., Kaufmann, S., Krämer, M., Krause, J., Kretschmer, E., Lörks, D., Marsing, A., Orphal, J., Pfeilsticker, K., Pitts, M., Poole, L., Preusse, P., Rapp, M., Riese, M., Rolf, C., Ungermann, J., Voigt, C., Volk, C. M., Wirth, M., Zahn, A., and Ziereis, H.: POLSTRACC: Airborne Experiment for Studying the Polar Stratosphere in a Changing Climate with the High Altitude and Long Range Research Aircraft (HALO), B. Am. Meteorol. Soc., 100, 2634–2664, https://doi.org/10.1175/BAMS-D-18-0181.1, 2019.

Ordóñez, C., Lamarque, J.-F., Tilmes, S., Kinnison, D. E., Atlas, E. L., Blake, D. R., Sousa Santos, G., Brasseur, G., and Saiz-Lopez, A.: Bromine and iodine chemistry in a global chemistry-climate model: description and evaluation of very short-lived oceanic sources, Atmos. Chem. Phys., 12, 1423–1447, https://doi.org/10.5194/acp-12-1423-2012, 2012.

Pan, L. L., Kunz, A., Homeyer, C. R., Munchak, L. A., Kinnison, D. E., and Tilmes, S.: Commentary on using equivalent latitude in the upper troposphere and lower stratosphere, Atmos. Chem. Phys., 12, 9187–9199, https://doi.org/10.5194/acp-12-9187-2012, 2012.

Pan, L. L., Atlas, E. L., Salawitch, R. J., Honomichl, S. B., Bresch, J. F., Randel, W. J., Apel, E. C., Hornbrook, R. S., Weinheimer, A. J., Anderson, D. C., Andrews, S. J., Baidar, S., Beaton, S. P., Campos, T. L., Carpenter, L. J., Chen, D., Dix, B., Donets, V., Hall, S. R., Hanisco, T. F., Homeyer, C. R., Huey, L. G., Jensen, J. B., Kaser, L., Kinnison, D. E., Koenig, T. K., Lamarque, J.-F., Liu, C., Luo, J., Luo, Z. J., Montzka, D. D., Nicely, J. M., Pierce, R. B., Riemer, D. D., Robinson, T., Romashkin, P., Saiz-Lopez, A., Schauffler, S., Shieh, O., Stell, M. H., Ullmann, K., Vaughan, G., Volkamer, R., and Wolfe, G.: The Convective Transport of Active Species in the Tropics (CONTRAST) Experiment, B. Am. Meteorol. Soc., 98, 106–128, https://doi.org/10.1175/BAMS-D-14-00272.1, 2017.

Patra, P. K., Houweling, S., Krol, M., Bousquet, P., Belikov, D., Bergmann, D., Bian, H., Cameron-Smith, P., Chipperfield, M. P., Corbin, K., Fortems-Cheiney, A., Fraser, A., Gloor, E., Hess, P., Ito, A., Kawa, S. R., Law, R. M., Loh, Z., Maksyutov, S., Meng, L., Palmer, P. I., Prinn, R. G., Rigby, M., Saito, R., and Wilson, C.: TransCom model simulations of CH_4 and related species: linking transport, surface flux and chemical loss with CH_4 variability in the troposphere and lower stratosphere, Atmos. Chem. Phys., 11, 12813–12837, https://doi.org/10.5194/acp-11-12813-2011, 2011.

Quack, B., Peeken, I., Petrick, G., and Nachtigall, K.: Oceanic distribution and sources of bromoform and dibromomethane in the Mauritanian upwelling, J. Geophys. Res.-Oceans, 112, 1–13, https://doi.org/10.1029/2006JC003803, 2007.

Quivet, E., Höhener, P., Temime-Roussel, B., Dron, J., Revenko, G., Verlande, M., Lebaron, K., Demelas, C., Vassalo, L., and Boudenne, J.-L.: Underestimation of Anthropogenic Bromoform Released into the Environment?, Environ. Sci. Technol., 56, 1522–1533, https://doi.org/10.1021/acs.est.1c05073, 2022.

Sala, S., Bönisch, H., Keber, T., Oram, D. E., Mills, G., and Engel, A.: Deriving an atmospheric budget of total organic bromine using airborne in situ measurements from the western Pacific area during SHIVA, Atmos. Chem. Phys., 14, 6903–6923, https://doi.org/10.5194/acp-14-6903-2014, 2014.

Salawitch, R. J., Weisenstein, D. K., Kovalenko, L. J., Sioris, C. E., Wennberg, P. O., Chance, K., Ko, M. K. W., and McLinden, C. A.: Sensitivity of ozone to bromine in the lower stratosphere, Geophys. Res. Lett., 32, 1–5, https://doi.org/10.1029/2004GL021504, 2005.

Sam Yang, J.: Bromoform in the effluents of a nuclear power plant: a potential tracer of coastal water masses, Hydrobiologia, 464, 99–105, https://doi.org/10.1023/A:1013922731434, 2001.

Shuckburgh, E., d'Ovidio, F., and Legras, B.: Local Mixing Events in the Upper Troposphere and Lower Stratosphere. Part II: Seasonal and Interannual Variability, J. Atmos. Sci., 66, 3695–3706, https://doi.org/10.1175/2009JAS2983.1, 2009.

Sinnhuber, B.-M., Sheode, N., Sinnhuber, M., Chipperfield, M. P., and Feng, W.: The contribution of anthropogenic bromine emissions to past stratospheric ozone trends: a modelling study, Atmos. Chem. Phys., 9, 2863–2871, https://doi.org/10.5194/acp-9-2863-2009, 2009.

Sturges, W. T., Sullivan, C. W., Schnell, R. C., Heidt, L. E., and Pollock, W. H.: Bromoalkane production by Antarctic ice algae, Tellus B, 45, 120–126, https://doi.org/10.3402/tellusb.v45i2.15586, 1993.

Tegtmeier, S., Atlas, E., Quack, B., Ziska, F., and Krüger, K.: Variability and past long-term changes of brominated very short-lived substances at the tropical tropopause, Atmos. Chem. Phys., 20, 7103–7123, https://doi.org/10.5194/acp-20-7103-2020, 2020.

Thompson, C. R., Wofsy, S. C., Prather, M. J., Newman, P. A., Hanisco, T. F., Ryerson, T. B., Fahey, D. W., Apel, E. C., Brock, C. A., Brune, W. H., Froyd, K., Katich, J. M., Nicely, J. M., Peischl, J., Ray, E., Veres, P. R., Wang, S., Allen, H. M., Asher, E., Bian, H., Blake, D., Bourgeois, I., Budney, J., Bui, T. P., Butler, A., Campuzano-Jost, P., Chang, C., Chin, M., Commane, R., Correa, G., Crounse, J. D., Daube, B., Dibb, J. E., DiGangi, J. P., Diskin, G. S., Dollner, M., Elkins, J. W., Fiore, A. M., Flynn, C. M., Guo, H., Hall, S. R., Hannun, R. A., Hills, A., Hintsa, E. J., Hodzic, A., Hornbrook, R. S., Huey, L. G., Jimenez, J. L., Keeling, R. F., Kim, M. J., Kupc, A., Lacey, F., Lait, L. R., Lamarque, J.-F., Liu, J., McKain, K., Meinardi, S., Miller, D.

O., Montzka, S. A., Moore, F. L., Morgan, E. J., Murphy, D. M., Murray, L. T., Nault, B. A., Neuman, J. A., Nguyen, L., Gonzalez, Y., Rollins, A., Rosenlof, K., Sargent, M., Schill, G., Schwarz, J. P., Clair, J. M. S., Steenrod, S. D., Stephens, B. B., Strahan, S. E., Strode, S. A., Sweeney, C., Thames, A. B., Ullmann, K., Wagner, N., Weber, R., Weinzierl, B., Wennberg, P. O., Williamson, C. J., Wolfe, G. M., and Zeng, L.: The NASA Atmospheric Tomography (ATom) Mission: Imaging the Chemistry of the Global Atmosphere, B. Am. Meteorol. Soc., 103, E761–E790, https://doi.org/10.1175/BAMS-D-20-0315.1, 2022.

WMO: Scientific Assesment of Ozone Depletion: 2018, Geneva, Switzerland, ISBN 978-1-7329317-1-8, 2018.

Wofsy, S., Daube, B., Jimenez, R., Kort, E., Pittman, J., Park, S., Commane, R., Xiang, B., Santoni, G., Jacob, D., Fisher, J., Pickett-Heaps, C., Wang, H., Wecht, K., Wang, Q., Stephens, B., Shertz, S., Watt, A., Romashkin, P., Campos, T., Haggerty, J., Cooper, W., Rogers, D., Beaton, S., Hendershot, R., Elkins, J., Fahey, D., Gao, R., Schwarz, J., Moore, F., Montzka, S., Perring, A., Hurst, D., Miller, B., Sweeney, C., Oltmans, S., Hintsa, E., Nance, D., Dutton, G., Watts, L., Spackman, J., Rosenlof, K., Ray, E., Hall, B., Zondlo, M., Diao, M., Keeling, R., Bent, J., Atlas, E., Lueb, R., and Mahoney, M. J.: HIPPO Combined Discrete Flask and GC Sample GHG, Halocarbon, and Hydrocarbon Data, Version 1.0, https://doi.org/10.3334/CDIAC/HIPPO_012, 2017.

Wofsy, S., Afshar, S., Allen, H., Apel, E., Asher, E., Barletta, B., Bent, J., Bian, H., Biggs, B., Blake, D., Blake, N., Bourgeois, I., Brock, C., Brune, W., Budney, J., Bui, T., Butler, A., Campuzano-Jost, P., Chang, C., Chin, M., Commane, R., Correa, G., Crounse, J., Cullis, P. D., Daube, B., Day, D., Dean-Day, J., Dibb, J., DiGangi, J., Diskin, G., Dollner, M., Elkins, J., Erdesz, F., Fiore, A., Flynn, C., Froyd, K., Gesler, D., Hall, S., Hanisco, T., Hannun, R., Hills, A., Hintsa, E., Hoffman, A., Hornbrook, R., Huey, L., Hughes, S., Jimenez, J., Johnson, B., Katich, J., Keeling, R., Kim, M., Kupc, A., Lait, L., McKain, K., Mclaughlin, R., Meinardi, S., Miller, D., Montzka, S., Moore, F., Morgan, E., Murphy, D., Murray, L., Nault, B., Neuman, J., Newman, P., Nicely, J., Pan, X., Paplawsky, W., Peischl, J., Prather, M., Price, D., Ray, E., Reeves, J., Richardson, M., Rollins, A., Rosenlof, K., Ryerson, T., Scheuer, E., Schill, G., Schroder, J., Schwarz, J., St. Clair, J., Steenrod, S., Stephens, B., Strode, S., Sweeney, C., Tanner, D., Teng, A., Thames, A., Thompson, C., Ullmann, K., Veres, P., Wagner, N., Watt, A., Weber, R., Weinzierl, B., Wennberg, P., Williamson, C., Wilson, J., Wolfe, G., Woods, C., Zeng, L., and Vieznor, N.: ATom: Merged Atmospheric Chemistry, Trace Gases, and Aerosols, Version 2, ORNL DAAC [data set], https://doi.org/10.3334/ORNLDAAC/1925, 2021.

Wofsy, S. C.: HIAPER Pole-to-Pole Observations (HIPPO): fine-grained, global-scale measurements of climatically important atmospheric gases and aerosols, Philos. T. Roy. Soc. A, 369, 2073–2086, https://doi.org/10.1098/rsta.2010.0313, 2011.

Worton, D. R., Sturges, W. T., Schwander, J., Mulvaney, R., Barnola, J.-M., and Chappellaz, J.: 20th century trends and budget implications of chloroform and related tri-and dihalomethanes inferred from firn air, Atmos. Chem. Phys., 6, 2847–2863, https://doi.org/10.5194/acp-6-2847-2006, 2006.

Paper III: Mean age from observations in the lowermost stratosphere: an improved method and inter-hemispheric differences

Published as:

Wagenhäuser, T., Jesswein, M., Keber, T., Schuck, T., and Engel, A.: *Mean age from observations in the lowermost stratosphere: an improved method and inter-hemispheric differences*, EGUsphere, 1–26, 2022, DOI: https://doi.org/10.5194/egusphere-2022-1197

Author Contributions:

Thomas Wagenhäuser wrote the manuscript including the figures of the publication and prepared the answers to the referees during the revision process. The manuscript was proof-read by the co-authors.

Presented concepts and results were developed by Thomas Wagenäuser in collaboration with Andreas Engel.

All authors contributed to the operation of the GhOST instrument with Markus Jesswein strongly involved during the SouthTRAC campaign together with Thomas Wagenhäuser.

Markus Jesswein provided processed HALO data for further analysis.

All co-authors contributed to the preparation of the manuscript in many useful discussions.

Frankfurt am Main .....

Markus Jesswein

https://doi.org/10.5194/egusphere-2022-1197
Preprint. Discussion started: 11 November 2022

Mean age from observations in the lowermost stratosphere: an improved method and interhemispheric differences

Thomas Wagenhäuser[1], Markus Jesswein[1], Timo Keber[1], Tanja Schuck[1], Andreas Engel[1]

[1]Institute for Atmospheric and Environmental Sciences, Goethe-University of Frankfurt, Frankfurt, Germany

Correspondence to: Thomas Wagenhäuser (wagenhaeuser@iau.uni-frankfurt.de)

Abstract. Age of stratospheric air is a concept commonly used to evaluate transport timescales in atmospheric models. The mean age can be derived from observations of a single long-lived trace gas species with a known tropospheric trend. Commonly, deriving mean age is based on the assumption that all air enters the stratosphere through the tropical (TR) tropopause. However, in the lowermost stratosphere (LMS) close to the extra-tropical (exTR) tropopause cross tropopause transport needs to be taken into account. We introduce the new exTR-TR method, which considers exTR input into the stratosphere in addition to TR input. We apply the exTR-TR method to in situ SF_6 measurements from three aircraft campaigns (PGS, WISE and SouthTRAC) and compare results to those from the conventional TR-only method. Using the TR-only method, negative mean age values are derived in the LMS close to the tropopause during the WISE campaign in northern hemispheric (NH) fall 2017. Using the new exTR-TR method instead, the number and extent of negative mean age values is reduced. With our new exTR-TR method we are thus able to derive more realistic values of typical transport times in the LMS from in situ SF_6 measurements. Absolute differences between both methods range from 0.3 to 0.4 years among the three campaigns. Interhemispheric differences in mean age are found when comparing seasonally overlapping campaign phases from the PGS and the SouthTRAC campaigns. On average, within the lowest 65 K potential temperature above the tropopause the NH LMS is 0.5 years ± 0.3 years older around March 2016 than the southern hemispheric (SH) LMS around September 2019. The derived differences between results from the exTR-TR method and the TR-only method, as well as interhemispheric differences are higher than the sensitivities of the exTR-TR method to parameter uncertainties, which are estimated to be below 0.22 years for all three campaigns.

1 Introduction

The lowermost stratosphere (LMS) is the lowest part of the extra tropical (exTR) stratosphere. Its upper boundary usually is defined as the 380 K isentrope, which approximates the lower boundary of the stratosphere in the tropics. The chemical composition of the LMS plays an important role in the climate system. Different transport paths and timescales determine the chemical composition of the LMS for a wide range of trace gases. The most prominent transport mechanism in the stratosphere is the Brewer-Dobson circulation (BDC), which transports air from the tropical (TR) tropopause to the exTR and polar stratosphere (Butchart, 2014). The residual circulation part of the BDC is characterized by two branches (Birner

https://doi.org/10.5194/egusphere-2022-1197
Preprint. Discussion started: 11 November 2022

and Bönisch, 2011; Plumb, 2002): One branch extends deep into the middle atmosphere and slowly transports air to high latitudes, where it eventually descends to lower altitudes. The shallow branch in the lower part of the stratosphere transports air poleward below the subtropical transport barrier and is characterized by comparably fast transport time scales. In addition to residual transport, air is transported within the stratosphere by bidirectional mixing. Both residual transport and mixing are induced by wave activity on different scales and are part of the BDC. In addition to the BDC, exTR cross-tropopause transport strongly affects the chemical composition of the LMS. This exTR transport mechanism is modulated by the subtropical jet (Gettelman et al., 2011).

Age of air is a widely used concept to describe tracer transport in the stratosphere (Waugh and Hall, 2002). In principle, infinitesimal fluid elements enter the stratosphere across a source region. The transit time (or "age") of each individual fluid element is the elapsed time since it last made contact to a source region. A macroscopic air parcel in the stratosphere consists of an infinite number of such fluid elements, each with its own transit time. The transit time distribution for the air parcel is called the "age spectrum" (Kida, 1983). Past studies were able to obtain information on age spectra from observations of multiple trace gases (Andrews et al., 1999, 2001; Bönisch et al., 2009; Hauck et al., 2020; Ray et al., 2022). The first moment of the age spectrum is the mean age of air. It can be derived from measurements of a single inert trace gas species with a monotonic trend in the troposphere. CO_2, SF_6 and a variety of "new" age tracers have been used in past studies to derive the mean age of air from observations (e.g. Engel et al., 2017; Leedham Elvidge et al., 2018).

Age of air from observations provides a stringent test for numerical models. The number of available trace gas observations that are suited to derive mean age is vastly higher than that to derive age spectra. In addition, deriving mean age relies on making less assumptions than does deriving age spectra. This makes mean age a valuable measure to compare models to observations. Still, observational estimates of mean age rely on several simplified assumptions, depending on the trace gas used, which significantly add to the uncertainty in mean age across large areas of the stratosphere. For example, in order to derive mean age from SF_6 measurements, commonly an infinite lifetime is assumed. In contrast, recent studies showed that a mesospheric sink of SF_6 leads to a significant bias towards higher ages especially on old mean age values derived from SF_6 observations (Leedham Elvidge et al., 2018; Loeffel et al., 2022). Another common assumption is that all air enters the stratosphere through the TR tropopause. However, Hauck et al. (2019, 2020) showed that in the vicinity of the tropopause, transport across the exTR tropopause is also important to adequately describe age spectra and mean age in the LMS. While the assumption of a single entry point is a good approximation for the stratosphere above about 380 K potential temperature θ, this is thus not the case for the LMS. Together with the interhemispheric gradient in tropospheric trace gas mixing ratios, this limits the ability to derive mean age of air in the LMS. Further improvements of the methods to derive the mean age of air from observations are thus desirable in order to provide robust real world estimates of transport time scales in sensitive regions of the atmosphere and be able to compare to model results.

With this work we focus on mean age of air in the LMS, where the old bias of SF_6 mean age is presumably low. We introduce an extended method that considers exTR input into the stratosphere in addition to TR input (hereafter exTR-TR method). In Sect. 2 we describe the concept and implementation of our new exTR-TR method. In Sect. 3 firstly we compare

https://doi.org/10.5194/egusphere-2022-1197
Preprint. Discussion started: 11 November 2022

results from the exTR-TR method to the conventional method, which only considers TR input (hereafter referred to as TR-only method). These results are based on in situ measurements taken during three aircraft campaigns. Secondly, we compare northern hemispheric (NH) and southern hemispheric (SH) mean age in the LMS based on these results. Thirdly, we present a sensitivity study on the exTR-TR method. We summarize our findings in Sect. 4.

2 Calculating Mean Age in the LMS considering multiple entry regions

2.1 General concept

A common approach to describe the mixing ratio $\chi(\boldsymbol{x})$ of a suitable age tracer at an arbitrary location $\boldsymbol{x}$ in the stratosphere is

$$\chi(\boldsymbol{x}) = \int_0^\infty \chi(\boldsymbol{x_0}, t') * G(\boldsymbol{x}, t')dt', \quad (1)$$

with $\chi(\boldsymbol{x_0}, t')$ being the tracer mixing ratio time series in the source region $\boldsymbol{x_0}$ as a function of transit time t' and the age spectrum $G(\boldsymbol{x}, t')$. The approach expressed in Eq. (1) is based on the assumption, that all fluid elements that enter the stratosphere at the same time have the same tracer mixing ratio. Albeit, in the real world there is no suitable age tracer with the same mixing ratio time series throughout the troposphere. Hence, the mixing ratio time series is likely to be different in different entry regions. By using Eq. (1), so far studies that derived the mean age of stratospheric air from measurements of one inert trace gas commonly relied on the assumption, that all air enters the stratosphere through the tropical (TR) tropopause (TR-only method), which appears valid for large parts of the stratosphere. In the LMS however, exTR input needs to be considered (Hauck et al., 2019, 2020).

We introduce the new exTR-TR method, which builds on an extended approach to derive mean age in the LMS from an inert monotonic tracer that considers exTR input into the stratosphere in addition to TR input. In a generalized way, our extended approach accounts for input into the stratosphere from *N* individual source regions $\boldsymbol{x}_i$ with individual mixing ratio time series $\chi(\boldsymbol{x}_i, t')$ by calculating a weighted mixing ratio time series. We use the origin fractions $f_i(\boldsymbol{x})$ as introduced by Hauck et al. (2020) as weights for each $\chi(\boldsymbol{x}_i)$. $f_i(\boldsymbol{x})$ is the fraction of air at $\boldsymbol{x}$, that entered the stratosphere through $\boldsymbol{x}_i$. By applying this assumption, Eq. (1) translates into Eq. (2):

$$\begin{aligned}\chi(\boldsymbol{x}) &= \int_0^\infty \sum_{i=0}^{N-1}\left(f_i(\boldsymbol{x}) * \chi(\boldsymbol{x}_i, t')\right) * G(\boldsymbol{x}, t')dt' \\ &= \sum_{i=0}^{N-1}\left(f_i(\boldsymbol{x}) * \int_0^\infty \chi(\boldsymbol{x}_i, t') * G(\boldsymbol{x}, t')dt'\right) \quad (2)\end{aligned}$$

Note that Eq. (2) is only valid if the sum of all origin fractions equals 1:

$$\sum_{i=0}^{N-1} f_i\,(\boldsymbol{x}) := 1 \quad (3)$$

There are currently no long term time series from measurements at the tropopause that are suited for mean age calculations. For this reason, we assume that each long term time series at each entry region i can be described by the tropical ground time series shifted by an individual constant t_{xi}:

$$\chi(\boldsymbol{x_i}) = \chi(\boldsymbol{x_{TR\ ground}}, t' - t_{xi}) \quad (4)$$

https://doi.org/10.5194/egusphere-2022-1197
Preprint. Discussion started: 11 November 2022

The negative sign points out, that looking at increasing transit times means looking backwards in time. In case of an ideal inert linear tracer with the y-intercept a and slope b and by applying Eq. (4), Eq. (2) can be transferred to Eq. (5) in order to calculate the mean age $\Gamma(\boldsymbol{x})$:

$$\Gamma(\boldsymbol{x}) = \frac{a-\chi(x)}{b} + t_m(\boldsymbol{x}), \tag{5}$$

with the weighted mean time shift $t_m(\boldsymbol{x}) = \sum_{i=0}^{N-1}(f_i(\boldsymbol{x}) * t_{xi})$.

In case of an ideal inert quadratic tracer with curvature c and a known ratio of moments $\lambda = \frac{\Delta^2}{\Gamma}$ with the width of the age spectrum Δ and again by applying Eq. (4), Eq. (2) can be transferred to Eq. (6) in order to calculate mean age:

$$\Gamma(\boldsymbol{x})_{1,2} = -\lambda + t_m(\boldsymbol{x}) + \frac{b}{2c} \pm \sqrt{\left(-\lambda + t_m(\boldsymbol{x}) + \frac{b}{2c}\right)^2 - \frac{a+bt_m(x)-\chi(x)}{c} - \sum_{i=0}^{N-1}[f_i(\boldsymbol{x}) * t_{xi}^2]}. \tag{6}$$

Details on deriving Eq. (5) and Eq. (6) are given in the Appendix A. Obviously, Eq. (5) and Eq. (6) can also be applied to the single entry region case, i.e. in context of the conventional TR-only method. This is equivalent to deriving mean age from an ideal inert linear tracer following Hall and Plumb (1994), respectively in the quadratic case following Volk et al. (1997).

Alternatively, instead of assuming ideal linearly or ideal quadraticly evolving tracer mixing ratios, G can be approximated by a mathematical function, e.g. an inverse Gaussian following (Hall and Plumb, 1994). Information on the width of the age spectrum needs to be included (like in the ideal quadratic tracer case). This way, Eq. (1) (TR-only) or Eq. (2) (exTR-TR) can be directly used to create a lookup table for Γ from a range of age spectra G as described in several studies (e.g. Fritsch et al., 2020; Leedham Elvidge et al., 2018; Ray et al., 2017). Mean age then is inferred from the best match between measured $\chi(\boldsymbol{x})$ and mixing ratios given in the lookup table. We refer to this approach as G-match approach in the following.

Our exTR-TR method will only work for inert monotonic tracers, e.g. SF_6-like tracers. Tracers that are characterized by seasonally varying trends in their mixing ratios, which propagate into the stratosphere, e.g. CO_2-like tracers, will lead to ambiguous mean age results in the LMS using the exTR-TR method. We tested calculating mean age from SF_6 measurements using Eq. (6) versus following the G-match approach and found only negligible differences for mean ages greater than one year. For lower mean ages the G-match approach leads to numerical issues that cause larger deviations. Therefore, we decided to use Eq. (6) for all mean age calculations in context of this study.

2.2 Implementation

The new exTR-TR method requires additional information compared to the conventional TR-only method. In order to account for input from different entry regions, firstly information on the fraction of air that originated from each entry region is essential. Secondly, the age tracer's mixing ratio time series at each entry region needs to be known. In the following we introduce a parameterization of the origin fractions published in Hauck et al. (2020). Further, we derive entry mixing ratio time series by shifting the tropical ground mixing ratio time series by a constant amount of time. The software implementation of the exTR-TR method is described in the supplementary information.

https://doi.org/10.5194/egusphere-2022-1197
Preprint. Discussion started: 11 November 2022

2.2.1 Parameterizations of origin fractions from CLaMS

Information on the fraction of air originating from different source regions is an essential input to our new exTR-TR method. We use the seasonally averaged origin fractions from the Chemical Lagrangian Model of the Stratosphere (CLaMS, e.g. Pommrich et al. (2014) published in Hauck et al. (2020). Hauck et al. (2020) derived such fractions based on origin tracers initiated at three tropopause sections in the model for extra tropical input from the Southern Hemisphere (30 to 90 °S, hereafter referred to as SH input), tropical input (30 °S to 30 °N, hereafter referred to as TR input) and extra tropical input from the Northern Hemisphere (30 to 90 °N, hereafter referred to as NH input). In total, there are 15 seasonal distributions of origin fractions $f_{i,seas}(\boldsymbol{x})$ published in Hauck et al. (2020) (see also their Fig. 2): Five seasonal sets (annual mean (ANN), December/January/February (DJF), March/April/May (MAM), June/July/August (JJA) and September/October/November (SON)) for each entry region (SH, TR, NH). (Hauck et al., 2020) found that cross-hemispheric transport is negligible, with origin fractions below 10 % from the extra tropics of the respective other hemisphere. Hence, in order to calculate the mean age at a given location in the stratosphere, we only consider the exTR origin fraction of the respective hemisphere and assume that the rest originates from the TR tropopause (i.e. $f_{TR} = 1 - f_{exTR}$). By doing so, the number of seasonal distributions of origin fractions reduces from 15 to 10.

In order to facilitate accessing the origin fractions from Hauck et al. (2020) and to reduce computational effort we designed a general mathematical parameterization function $\varphi_{i,seas}$ with 12 parameters to derive 2-D parameterizations for exTR origin fractions. The process of designing $\varphi_{i,seas}$ was guided by a non-physical but entirely geometrical approach. We chose the potential temperature difference to the local 2 PVU tropopause ($\Delta\Theta$) as the vertical coordinate, equivalent latitude (eq. lat., i.e. latitudes sorted by potential vorticity) as the horizontal coordinate. Details on the parameterizations and on how we derived them are given in the Appendix B. Figure 1 shows $\varphi_{i,seas}$ (top row), $f_{i,seas}(\boldsymbol{x})$ (middle row) and the absolute difference between $f_{i,seas}(\boldsymbol{x})$ and $\varphi_{i,seas}$ (bottom row) exemplarily for NH spring (March, April, May: MAM; left column), NH fall (September, October, November: SON; middle column) and SH spring (SON; right column). The remaining seven distributions are presented in the same way as Fig. 1 in the Supplementary Information (Fig. S1). The absolute differences between $\varphi_{i,seas}$ and $f_{i,seas}(\boldsymbol{x})$ shown in Fig. 1 are less than 10 % for NH MAM (panel (g)) and SH SON (panel (i)) and only exceed 10 % in a small region at the equator around 25 K above the tropopause for NH SON (panel (h)). The root mean squared difference (RMSD) is less than 3 % for all distributions shown in Fig. 1 and less than 4 % for all 10 distributions (including the seven distributions shown in Fig. S1).

https://doi.org/10.5194/egusphere-2022-1197
Preprint. Discussion started: 11 November 2022

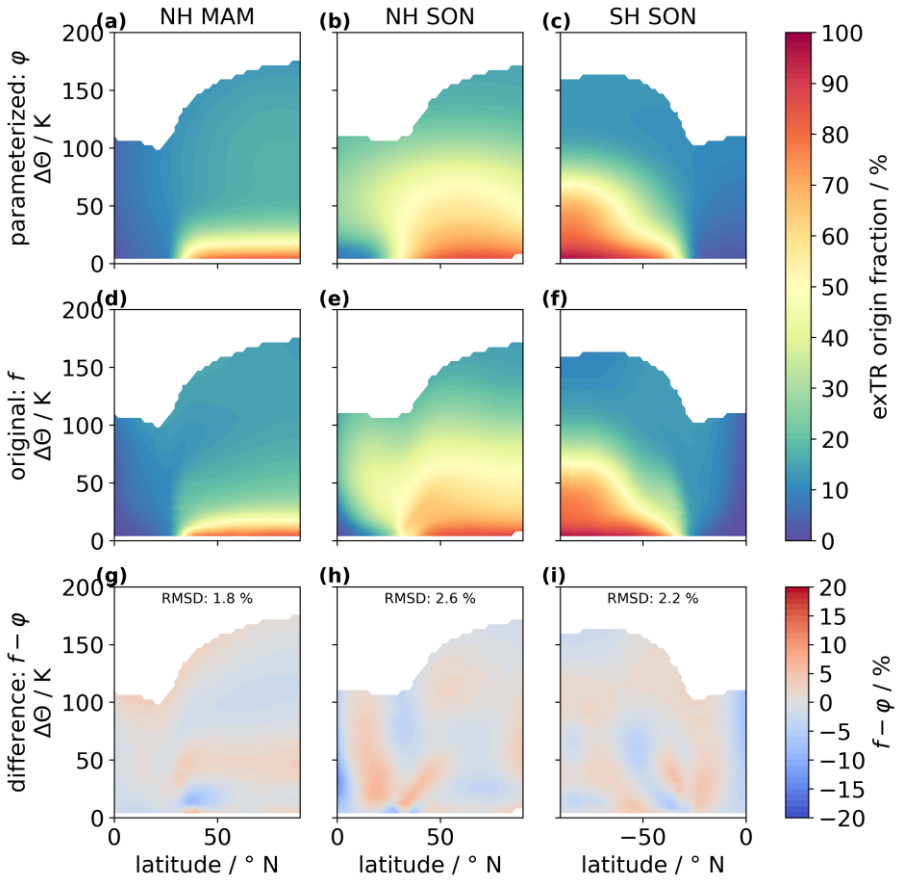

Figure 1. Comparing seasonal hemispheric extra tropical origin fractions parameterization ($\boldsymbol{\varphi}$, top row) and original CLaMS fractions from simulations from Hauck et al. (2020) (f, middle row). The difference is shown in the bottom row. Only three selected season-hemisphere combinations are shown here (NH MAM, left column; NH SON, middle column; SH SON, right column). The remaining distributions are shown in Fig. S1. Vertical coordinates are given in potential temperature above the 2 PVU tropopause (Δθ).

2.2.2 Entry region mixing ratio time series

Our new exTR-TR method uses a TR ground reference time series $\chi(\boldsymbol{x_{TR\ ground}}, t')$ together with constant time shift values t_{xi} in order to simulate reference time series in the three entry regions as defined by the origin fractions from Hauck et al. (2020) (see Eq. 4). This will work for inert monotonic tracers like SF_6. In contrast, the entry region mixing ratio time series of tracers like CO_2, which are characterized by a pronounced seasonality in the troposphere, most likely cannot be approximated satisfactorily with this approach. These tracers are thus not suited for deriving mean age with the exTR-TR method in the LMS. Here, at first we describe, which TR ground reference time series we use and secondly how we derived constant time shift values t_{xi}.

In this study, we use SF_6 as an age tracer. Simmonds et al. (2020) used ground measurements from the AGAGE (Advanced Global Atmospheric Gases Experiment) Network (Prinn et al., 2018) together with measurements of archived air samples and the two-dimensional AGAGE 12-box model (Cunnold et al., 1978, 1983; Rigby et al., 2013) to derive a monthly

https://doi.org/10.5194/egusphere-2022-1197
Preprint. Discussion started: 11 November 2022

resolved time series of SF_6 mixing ratios from the 1970s to 2018. We use the TR ground SF_6 mixing ratios of an updated version of this dataset, which has been extended until the end of 2019, as a reference time series $\chi(\boldsymbol{x}_{\boldsymbol{TR\ ground}}, t')$ for calculating the mean age of air.

In order to derive t_{xi} for each of the three entry regions we use the annual mean optimized three-dimensional SF_6 mixing ratios output from the Model for Ozone and Related Tracers (MOZART v4.5) for 1970 to 2008 published by Rigby et al. (2010, Supplement). Rigby et al. (2010) derived a new estimate of SF_6 emissions using the Emissions Database for Global Atmospheric Research (EDGAR v4) as a prior and optimizing the emissions using SF_6 ground measurements from the AGAGE Network including monitoring site data and archived sample measurements together with MOZART and meteorological data from the National Centers for Environmental Prediction/National Center for Atmospheric Reseach (NCEP/NCAR) reanalysis project. The annually-averaged, three-dimensional optimized SF_6 mixing ratio fields that we use to derive t_{xi} are part of their result. In our approach, we only considered the data from 1973 to 2008, since the data from 1970 to 1972 may be influenced by the start conditions of the model (Rigby et al., 2010). We calculated t_{xi} for each of the three entry regions following three steps:

(i) Calculate a mean TR ground SF_6 time series by using MOZART data between -30° to 30° N weighted by latitude.
(ii) For each grid cell and each year of the three-dimensional SF_6 field time series interpolate SF_6 mixing ratios to TR ground time using (i) and calculate time shift to TR ground.
(iii) For each entry region, calculate mean and standard deviations weighted by latitude and pressure for time shifts from (ii) for 1973 to 2008 altogether to eventually obtain t_{xi} and information on associated uncertainty.

The latitudinal extents of the entry regions that we calculated t_{xi} for are the same as for the origin fractions by Hauck et al. (2020). For the exTR entry regions, we included data between 500 hPa and 200 hPa. For the TR entry region, we included data between 300 hPa and 100 hPa. Table 1 lists t_{xi} and standard deviations for the three entry regions SH exTR, TR and NH exTR. Positive values of t_{xi} indicate, that the corresponding region lags behind TR ground SF_6 mixing ratios. Note that for NH exTR t_{xi} is negative. This means that this region precedes TR ground SF_6 mixing ratios. This finding is consistent with SF_6 source regions being located primarily in the northern hemisphere (Rigby et al., 2010).

We performed a Monte-Carlo simulation in order to test if t_{xi} can be considered to be constant over time for each entry region. Firstly, for each entry region we calculated weighted means and standard deviations for each year (instead for the whole time period like in (iii)). Figure 2 shows the resulting time shift time series from 1973 to 2008. Secondly, for each year, we took 10000 samples from a Gaussian distribution using those weighted means and standard deviations in order to create 10000 time series for each entry region. Thirdly, we applied a linear fit to each of the 10000 time series and calculated the mean and the standard deviation of the slope for each entry region. The resulting mean slopes, standard deviations and the ratio of mean slope and standard deviation are listed in Table 2. For NH exTR and TR the mean slopes deviate less than one standard deviation from zero. For SH exTR the mean slope deviates less than 1.2 standard deviations from zero. Hence, we do not detect a significant trend. These findings strengthen our confidence into our assumption that we can use the

https://doi.org/10.5194/egusphere-2022-1197
Preprint. Discussion started: 11 November 2022

constant time shifts t_{xi} listed in Table 1 together with $\chi(\boldsymbol{x_{TR\ ground}}, t')$ to describe the SF_6 entry mixing ratio time series reasonably well. In context of our exTR-TR method we assume that this also holds true for the subsequent decade from 2008 on. This decade is not covered by the model from Rigby et al. (2010) that we used to derive t_{xi}, however it is covered by $\chi(\boldsymbol{x_{TR\ ground}}, t')$ (updated from Simmonds et al., 2020). We emphasize that each t_{xi} as defined here is an integrated empirical measure. t_{xi} does neither contain useful information on transport paths nor on transit times from the TR ground to the entry regions. We only use t_{xi} to derive entry mixing ratio time series at locations, where suitable long term time series are not available from measurements.

Table 1: $\boldsymbol{t_{xi}}$ and standard deviations for SF_6 mixing ratio time series at three entry regions (NH 30°N-90°N, 500-200 hPa; TR 30°S-30°N, 300-100 hPa; SH 30°S-90°S, 500-200 hPa), weighted by latitude and pressure for the time period 1973-2008. These time shifts have been calculated relative to TR ground.

	t_{xi} / years	weighted standard deviation / years
NH exTR entry region	-0.4	0.156
TR entry region	0.12	0.15
SH exTR entry region	0.53	0.074

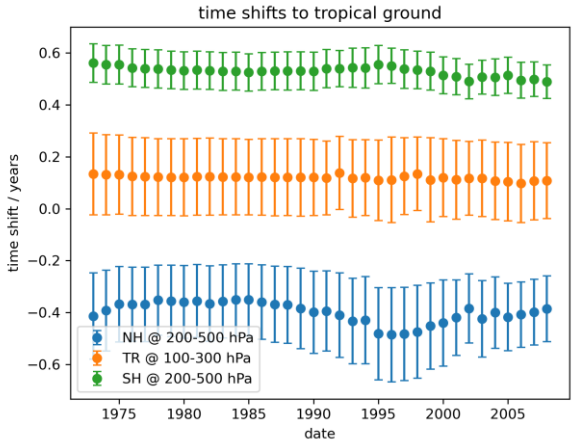

Figure 2. Annual mean time shifts and standard deviations for SF_6 mixing ratio time series at three entry regions, weighted by latitude and pressure. Based on three dimensional annual SF_6 model data output from Rigby et al. (2010).

https://doi.org/10.5194/egusphere-2022-1197
Preprint. Discussion started: 11 November 2022

Table 2: Mean slopes and slope standard deviation from Monte-Carlo simulation using the data shown in Fig. 2. Ratios of mean slopes and standard deviations have been calculated prior to rounding.

	mean time shift slope / years years-1	time shift slope standard deviation / years years-1	ratio of mean slope and standard deviation
NH exTR entry region	$-2 * 10^{-3}$	$3 * 10^{-3}$	-0.9
TR entry region	$-5 * 10^{-4}$	$3 * 10^{-3}$	-0.2
SH exTR entry region	$-1 * 10^{-3}$	$2 * 10^{-3}$	-1.1

2.3 Stratospheric observations of age tracer SF_6

We apply our new exTR-TR method to in situ measurements of SF_6 that were obtained during three HALO research campaigns. The first campaign, PGS (Oelhaf et al., 2019), is a combination of three missions: POLSTRACC (Polar Stratosphere in a Changing Climate), GW-LCYCLE (Investigation of the Life cycle of gravity waves) and SALSA (Seasonality of Air mass transport and origin in the Lowermost Stratosphere). PGS was split into two campaign phases, that were conducted in NH winter 2015/16 between December 13 and February 2, respectively NH early spring 2016 between February 26 and March 18. The second campaign, WISE (Wave-driven Isentropic Exchange, https://www.wise2017.de, last access: 05 May 2022), took place mainly in NH fall 2017 between September and October. The flight tracks of HALO during the PGS and during the WISE campaign are shown in Keber et al. (2020) Fig. 2 and Fig. 1b. They cover large parts of mid- and high latitudes in the NH. Thirdly, we consider data from the SouthTRAC (Southern Hemisphere Transport, Dynamics and Chemistry) campaign, which took place in SH spring 2019. The SouthTRAC campaign also was split into two campaign phases, conducted between September 6 and October 9 (Rapp et al., 2021), respectively between November 2 and November 15. The flight tracks for SouthTRAC, which covered a wide geographical area of the SH, are shown in Jesswein et al. (2021).

SF_6 and CFC-12 measurements were obtained in-flight in context of all three campaigns with a time resolution of one minute using the ECD channel of the two-channel Gas chromatograph for Observational Studies using Tracers (GhOST) instrument in a similar set-up as used in the SPURT campaign (Bönisch et al., 2009; Engel et al., 2006). SF_6 has been measured with a precision of 0.6 % (0.56 %) during SouthTRAC (PGS, WISE). CFC-12 has been measured with a precision of 0.23 % (0.2 %) during SouthTRAC (PGS, WISE). All measurements are reported relative to the AGAGE SIO-05 scale (Miller et al., 2008; Prinn et al., 2018; Rigby et al., 2010; Simmonds et al., 2020). Due to the better precision of CFC-12 measurements, the original SF_6 data was smoothed using a local SF_6 – CFC-12 correlation 10 minutes before and after each measurement following Krause et al. (2018), prior to calculating mean age values. The height of the dynamical 2 PVU tropopause (e.g. Gettelman et al., 2011) as well as eq. lat. coordinates were obtained via CLaMS driven by ERA-5 reanalysis along the flight tracks. With this study we exclusively focus on the LMS. Therefore, only tracer measurements at or above the dynamical tropopause were considered (i.e. with $\Delta\theta \geq 0\ K$). Tracer measurements and meteorological data are accessible via the HALO database (HALO consortium, 2021).

https://doi.org/10.5194/egusphere-2022-1197
Preprint. Discussion started: 11 November 2022

3 Results and discussion

We derive mean age in the LMS using in situ SF_6 measurements from three aircraft campaigns (see Sect. 2.3). Results are presented in a two dimensional tropopause-relative coordinate system. The potential temperature relative to the local dynamical tropopause (defined by the value of 2 PVU) Δθ is used as vertical coordinate. Horizontally, data are sorted by eq. lat. In order to visualize and compare our results, datasets were processed in a three-step process:

1. Mean age was calculated for each data point that was measured above the local 2 PVU tropopause.
2. For each campaign dataset, mean ages were averaged in Δθ – eq. lat. bins (5 K – 5 °). Only bins that contained at least five data points were considered.
3. The averaged mean ages have been corrected for mesospheric loss using a linear correction function by (Leedham Elvidge et al., 2018):

$$\Gamma_{corr} = 0.85 * \Gamma - 0.02\ years \quad (7)$$

3.1 Method comparison using campaign averaged results

We applied our new exTR-TR method for deriving mean age in the LMS considering exTR and TR input into the stratosphere to all three campaign datasets. Further, we applied the conventional TR-only method, which considers only TR input into the stratosphere, in order to compare the results from both methods. The results were averaged and corrected for mesospheric loss.

Figure 3 shows the resulting Δθ – eq. lat. distributions of averaged mean age mA for PGS (left column), WISE (middle column) and SouthTRAC (right column), derived using the conventional TR-only method $mA_{TR\text{-}only}$ (top row), using our new exTR-TR method $mA_{exTR\text{-}TR}$ (middle row), and the difference between the two methods $\Delta mA_{methods}$ (bottom row). There are negative values down to -0.54 years close to the tropopause below Δθ=10 K in the WISE dataset using the TR-only method (panel (b)). In the same region mean ages between -0.23 and 0.35 years are found using the new exTR-TR method (panel (e)). Mean ages below 0 as derived from the TR-only method do not allow for a reasonable interpretation regarding transport time scales in the LMS. In contrast, mean ages derived using our new exTR-TR method appear physically reasonable even close to the tropopause. During the WISE campaign low gradients in $mA_{exTR\text{-}TR}$ values reveal a well-mixed LMS (panel (e)), while during PGS and ST stronger gradients in $mA_{exTR\text{-}TR}$ are found (panels (d) and (f)).

The maximum absolute difference between average exTR-TR and TR-only method derived mean ages $|\Delta mA_{methods}|$ is with 0.31 years (WISE and PGS) and 0.42 years (SouthTRAC) on the same order of magnitude for all three campaigns, but in different direction for the SH (see also Fig. 3, bottom row). For all three campaigns $|\Delta mA_{methods}|$ is largest close to the tropopause at mid- and high latitudes and approaches zero years further up and closer to the equator. This distribution is similar to the distribution of exTR origin fractions from CLaMS. In fact, $|\Delta mA_{methods}|$ and the exTR origin fractions are highly correlated ($r > 0.99$ for all three campaigns). This results from the design of the exTR-TR method, which explicitly considers exTR input into the stratosphere.

https://doi.org/10.5194/egusphere-2022-1197
Preprint. Discussion started: 11 November 2022

Note that in the SH data from the SouthTRAC campaign mean ages are generally lower when derived using the exTR-TR method than when using the TR-only method. For NH data (WISE, PGS) the opposite is the case. This is a direct consequence from the TR ground mixing ratio time series being lagged by a positive (in the SH), respectively a negative (in the NH) empirical time shift to obtain the respective entry mixing ratio time series (see Table 1).

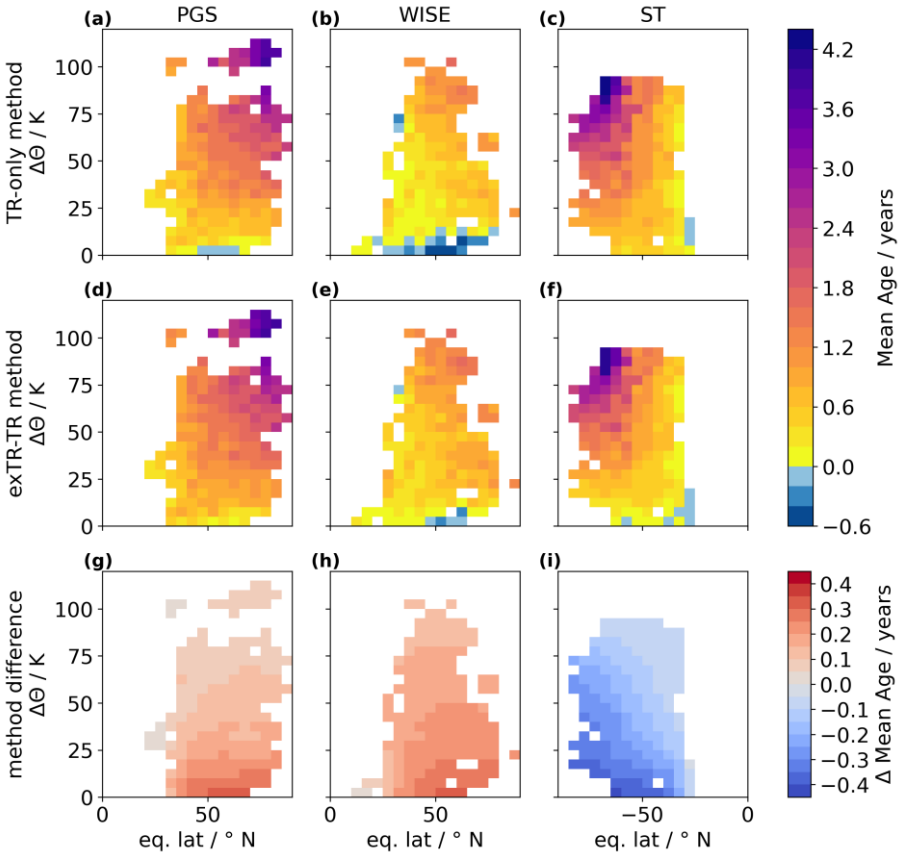

Figure 3. Comparison of methods to derive mean age in the LMS during PGS (left column), WISE (middle column) and SouthTRAC (right column). Results are shown for the TR-only method (top row) and the new exTR-TR method (middle row). The absolute differences between both methods are shown in the bottom row. Altitude is given in Δθ. Horizontally, data are sorted by eq. lat.

3.2 SouthTRAC and PGS campaign: SH vs NH late winter/early spring

Both the SouthTRAC and the PGS campaign involved flights during the respective hemisphere's late winter /early spring. We compare results from the SouthTRAC campaign phase 1 dataset (ST1) to results from the PGS campaign phase 2 dataset (PGS2) derived with the exTR-TR method. This selection is a compromise between including a high number of trace gas measurements and having a large seasonal overlap between both datasets. Again, the results were averaged and corrected for mesospheric loss.

https://doi.org/10.5194/egusphere-2022-1197
Preprint. Discussion started: 11 November 2022

Figure 4 shows $mA_{exTR\text{-}TR}$ for ST1 (panel (a)), for PGS2 (panel (b)) and the difference between the two $mA_{PGS2\text{-}ST1}$ (panel (c)). In order to calculate interhemispheric differences, the $mA_{exTR\text{-}TR}$ distribution from ST1 was converted from eq. lat. degrees North to eq. lat. degrees South by flipping it horizontally. Hence, the respective pole corresponds to 90 ° eq. lat. for both datasets in panel (c). Mean ages $mA_{exTR\text{-}TR}$ between -0.2 years and 0.1 years are found within the lowest 10 K above the tropopause during ST1 (panel (a)). During PGS2 $mA_{exTR\text{-}TR}$ between 0.2 years and 1.1 years are found in the equivalent region in the NH (panel (b)). The differences in mean age $mA_{PGS2\text{-}ST1}$ (panel (c)) reveal higher mean ages during PGS2 than during ST1 from the tropopause up to 65 K above the tropopause throughout mid- and high latitudes, with a few exceptions. On average, below $\Delta\theta$=65 K the LMS is 0.5 years ± 0.3 years older during PGS2 than during ST1. Above $\Delta\theta$=65 K a more complex picture is observed: At $\Delta\theta$-levels between 65 K and 85 K at latitudes between 40° and 55° the LMS is even older during PGS2 than during ST1 with $mA_{PGS2\text{-}ST1}$=0.7 years ± 0.4 years on average. In contrast, the opposite is the case at the same $\Delta\theta$-levels but at poleward latitudes higher than 55°: Mean ages during ST1 are older than during PGS2, with $mA_{PGS2\text{-}ST1}$ reaching values down to -2.1 years. A less clear picture emerges when comparing mean ages derived with the TR-only method (see Appendix C: Fig. C1). This could be explained by the fact, that the TR-only method disregards the interhemispheric gradient in SF_6 mixing ratios. In the LMS, the resulting mean age values thus are low biased in the NH, while they are old biased in the SH using the TR-only method. These biases happen to obscure interhemispheric differences in mean age in the LMS which have been detected using the new exTR-TR method on the same dataset.

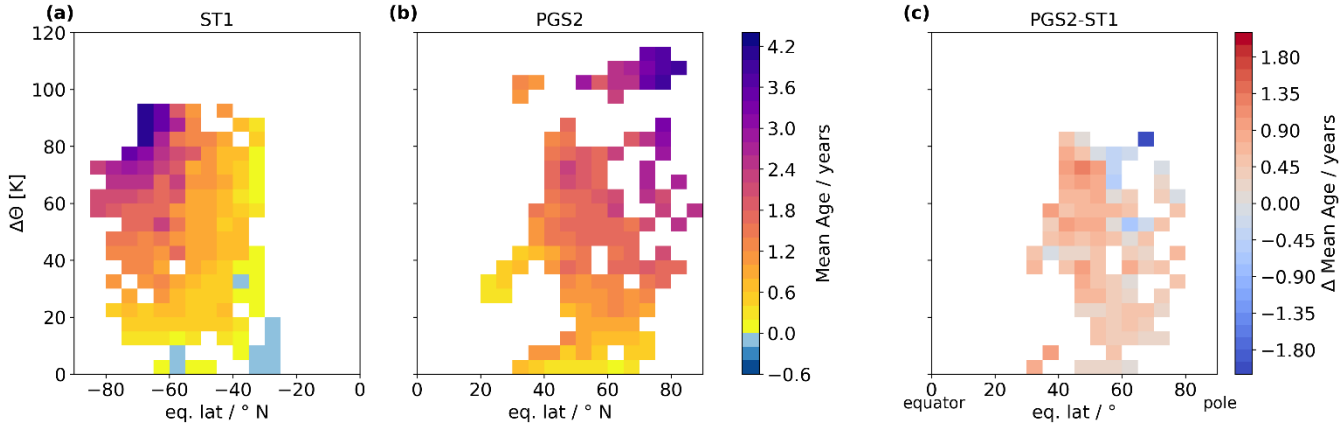

Figure 4. Comparison of mean age latitude-altitude distributions during SouthTRAC phase 1 (ST1) (a), PGS phase 2 (PGS2) (b). The hemispheric difference based on these two campaign phases is shown in panel (c). Altitude is given in $\Delta\theta$. Horizontally, data are sorted by eq. lat.

Our findings indicate, that on the one hand, during ST1 old air from higher altitudes descends in a confined way at high latitudes. There is a sharp vortex edge with a strong gradient in the SH. On the other hand, during PGS2 descending old air is mixed vertically and horizontally with young air in the LMS. The vortex edge is less sharp than during ST1, resulting in younger air at high latitudes and altitudes and older air outside the PGS2 vortex region compared to ST1.

These results cover only isolated time periods of less than two months for each campaign. In addition, as discussed by Jesswein et al. (2021) the extend of the respective polar vortices and therefore also the location of the respective vortex edge

https://doi.org/10.5194/egusphere-2022-1197
Preprint. Discussion started: 11 November 2022

are likely to be different for both hemispheres. Hence, different vortex characteristics contribute to the differences observed in Fig. 4. Nevertheless, our findings are in agreement with multiannual simulation results from Konopka et al. (2015), who found a pronounced minimum in wave forcing driving the shallow branch of the BDC in the midlatitudes of the lower stratosphere in the SH between June and October, opposed to a maximum in boreal spring in the NH.

3.3 Sensitivity study

3.3.1 Procedure

Our new exTR-TR method requires input of several parameters, which all have individual uncertainties. In the following, the sensitivity of the exTR-TR method to these uncertainties is investigated in context of three aircraft campaigns.

We identified seven uncertain parameters:

(i) extra tropical origin fraction; $f_{exTR,seas}(\boldsymbol{x})$

(ii) time shift to extra tropical entry region; t_{exTR}

(iii) time shift to tropical entry region; t_{TR}

(iv) measurement precision of age tracer mixing ratios; $\chi(\boldsymbol{x})$

(v) ratio of moments; λ

(vi) chemical depletion of age tracer SF_6

(vii) reference time series calibration scale uncertainty

Parameters (i) to (vi) may vary for each individual observational sample, making them eligible for a sensitivity analysis. In contrast, the uncertainty of the calibration scale of the reference time series (vii) affects all derived absolute mean ages not in an individual but in a consistent way. Therefore, we excluded it from the sensitivity analysis, albeit knowing that it contributes to the overall uncertainty in deriving mean age from tracers. Furthermore, we excluded the chemical depletion of SF_6 (vi) from the sensitivity analysis, since it is not yet well understood and subject of current comprehensive research (e.g. Loeffel et al., 2022). Leedham Elvidge et al. (2018) showed that younger mean age values derived from SF_6 measurements, which point to shorter transport paths, are less effected by the mesospheric sink than are older mean age values. Adequately addressing uncertainties in mean age due to the chemical depletion of SF_6 is beyond the scope of this paper, which focuses primarily on young air in the LMS.

Parameters (i) to (v) are suited for a sensitivity analysis within the scope of this study using a Monte-Carlo simulation. Since typical mean ages and origin fractions vary across different locations and seasons in the LMS, the sensitivity of the exTR-TR method is investigated and results are shown in the same two dimensional tropopause-relative coordinate system that is used for the results shown in Sects. 3.1 and 3.2: $\Delta\theta$ is used as vertical coordinate, while horizontally data are sorted by eq. lat. We conduct the sensitivity analysis by applying the following procedure to each of the three aircraft campaign datasets individually.

https://doi.org/10.5194/egusphere-2022-1197
Preprint. Discussion started: 11 November 2022

In order to obtain a reduced set of representative data and therefor reduce computational effort of the subsequent steps, SF_6 mixing ratios and dates of observation are averaged into 5 K Δθ and 5° eq. lat. bins. For each bin the following three steps are applied:

Step 1: For each uncertain parameter (i)-(v), a random number is drawn based on the parameter's best estimate and its uncertainty for that specific bin (see below for details). This is done 1000 times to create 1000 sets of parameters.

Step 2: These 1000 sets of parameters are used to calculate 1000 mean age values.

Step 3: The standard deviation of those 1000 mean age values is calculated to obtain an overall sensitivity value for this bin.

This way we derive the overall sensitivity. Further, we investigate the relative importance of the uncertain parameters (i)-(v). For this purpose, additional sensitivity calculations are done where only one uncertain parameter is varied while leaving the others at their best estimate.

3.3.2 Parameter uncertainties

Here we describe how uncertainties associated with parameters (i)-(v) are implemented in step 1 of the sensitivity analysis.

(i): The exTR origin fraction $f_{exTR}(\boldsymbol{x})$ varies spatially and over time. For each of the three aircraft campaigns the spatial distribution of uncertainties in $f_{exTR}(\boldsymbol{x})$ is derived from the parameterized origin fraction $\varphi_{i,seas}(\boldsymbol{x})$ (see Sect. 2.2.1) individually. Therefore, for each bin the mean absolute half difference ($MAHD_{seas}$) between $\varphi_{i,seas}(\boldsymbol{x})$ and $\varphi_{i,next\ seas}(\boldsymbol{x})$, respectively $\varphi_{i,previous\ seas}(\boldsymbol{x})$ is calculated. In addition, the root mean squared difference ($RMSD_{space}$) between each bin and its eight surrounding bins is calculated. Both measures, $MAHD_{seas}$ and $RMSD_{space}$ are combined in the root sum squared to finally derive the spatial distribution of uncertainties in the exTR origin fraction for each campaign. Random values are drawn from a Gaussian distribution using this root sum squared.

(ii), (iii): Obtaining t_{exTR} for the NH and for the SH tropopause and t_{TR} for the tropical tropopause regarding SF_6 from annually averaged three dimensional model output is described in Sect. 2.2.2. We use the weighted mean values and standard deviations given in Table 1 as input for a Gaussian distribution, from which random values are drawn.

(iv): The measurement precision of age tracer mixing ratios $\chi(\boldsymbol{x})$ is given campaign-wise in Sect. 2.3. Since we use smoothed SF_6 mixing ratios by considering local CFC-12 – SF_6 correlations for mean age calculations, here we apply the better measurement precision for CFC-12 mixing ratios to draw samples from a Gaussian distribution.

(v): Regarding the ratio of moments λ, random values are drawn from a triangular distribution with a minimum of $\lambda = 0.7$ years, a centre of $\lambda = 1.2$ years and a maximum of $\lambda = 2$ years.

3.3.3 exTR-TR method sensitivities during PGS, WISE and SouthTRAC

The sensitivities of the exTR-TR method to uncertainties in input parameters have been calculated following the procedure outlined above. The resulting distributions of sensitivity values are shown in Fig. 5. The most sensitive regions are found between 20-40 ° poleward of the equator below Δθ=20 K during all three aircraft campaigns with maximum values of

https://doi.org/10.5194/egusphere-2022-1197
Preprint. Discussion started: 11 November 2022

0.22 years (PGS, panel (a)), 0.19 years (WISE, panel (b)) and 0.16 years (SouthTRAC, panel (c)). Above Δθ=20 K, the sensitivity values are distributed evenly (standard deviation <0.02 years), with average values of 0.15 years (PGS) and 0.14 years (WISE and SouthTRAC). These sensitivities are lower than the differences between mean ages derived using the exTR-TR method and the TR-only method, which are found to be larger than 0.3 years close to the tropopause.

The contribution of the individual parameters (i)-(v) is shown in Fig. 6. Each row depicts isolated sensitivities to uncertainties in a single parameter with all other parameters being held at their best estimate. This allows us to test the relative importance of the individual parameters to the exTR-TR method's overall sensitivity. Most strikingly, uncertainties in the ratio of moments (parameter (v)) seem to contribute only to a negligible extend to the overall sensitivity (panels (m), (n), (o)). Measurement uncertainties in the stratospheric mixing ratio $\chi(\boldsymbol{x})$ contribute evenly distributed to the overall sensitivity to a moderate extend (panels (j), (k), (l)). Due to the slightly worse measurement precision during SouthTRAC and in addition due to the decelerating relative growth rate of SF_6 mixing ratios, the uncertainties in $\chi(\boldsymbol{x})$ have a stronger impact on the overall sensitivity during SouthTRAC than during the other two campaigns. In the upper part of the LMS (above Δθ=50 K), uncertainties in t_{TR} dominate the overall sensitivity (panels (g), (h), (i)). Below, uncertainties in t_{exTR} and in $f_{exTR}(\boldsymbol{x})$ gain importance (panels (a)-(f)). Note that for the SH uncertainties in t_{exTR} are low (see Table 1), which is reflected by contributing only to a minor to moderate extend to the overall sensitivity during the SouthTRAC campaign (panel (f)).

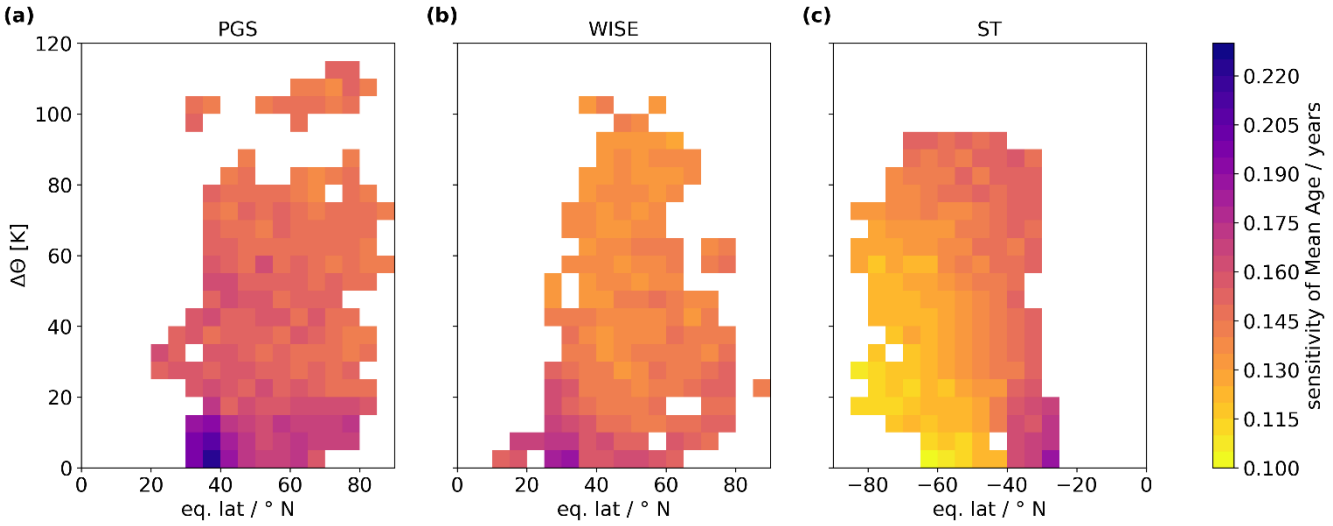

Figure 5. Latitude-altitude distribution of sensitivities of mean age from the exTR-TR method to uncertainties in all considered input parameters. Calculated for PGS (a), WISE (b) and SouthTRAC (c) campaign. Altitude is given in Δθ. Horizontally, data are sorted by eq. lat.

https://doi.org/10.5194/egusphere-2022-1197
Preprint. Discussion started: 11 November 2022

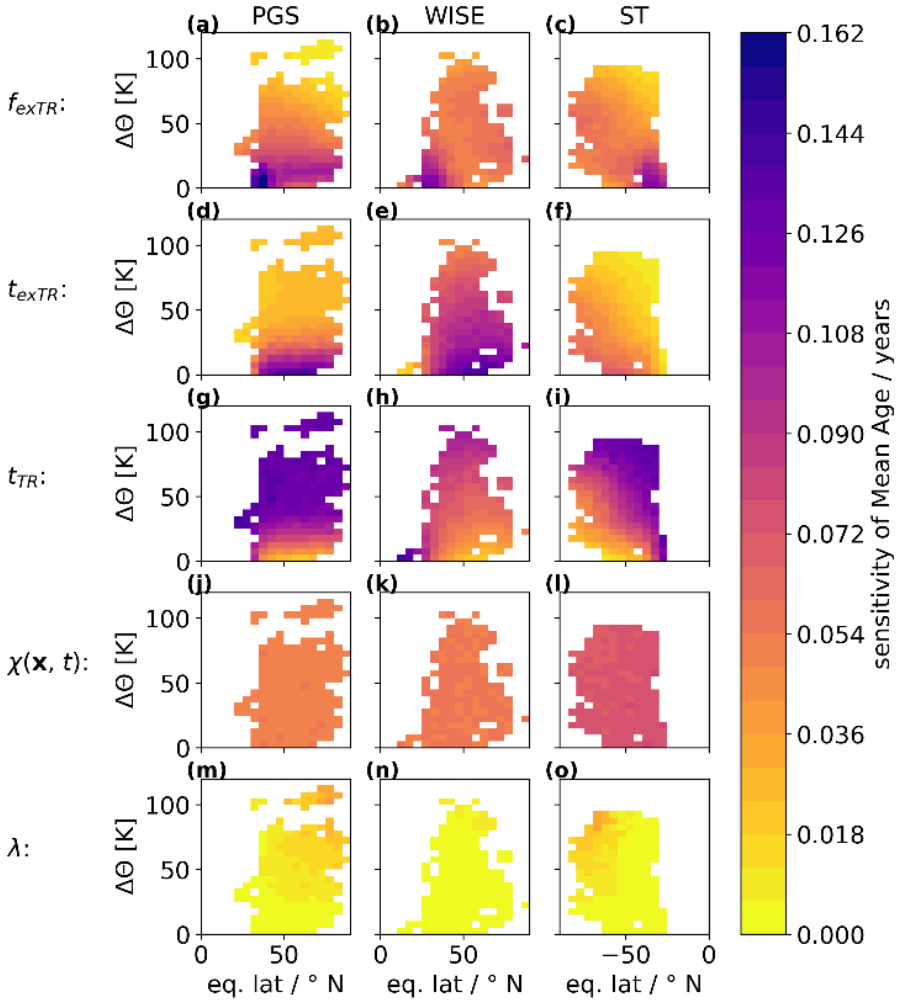

Figure 6. As Fig. 5, but each uncertain parameter is considered independently, assuming the others to be accurate. Uncertain parameters: exTR origin fraction (f_{exTR}, top row), time shift to exTR entry region (t_{exTR}, second row), time shift to TR entry region (t_{TR}, third row), SF_6 mixing ratio measurement uncertainty ($\boldsymbol{\chi}(\mathbf{x})$, forth row) and the ratio of moments (λ, bottom row).

4 Summary and Conclusions

In this work, the new exTR-TR method to derive stratospheric mean age of air in the LMS from observational tracer mixing ratio data is presented. In order to take exTR input into the stratosphere into account, our implementation of the exTR-TR method uses seasonally averaged exTR origin fractions from CLaMS (Hauck et al., 2020), for which we provide a parameterization, and a long term tracer mixing ratio time series for each entry region $\chi(\boldsymbol{x}_i, t')$. Following (Hauck et al., 2020), the entry regions are defined as a northern (90-30° N), a TR (30° N - 30° S) and a southern (30-90° S) tropopause section. Owing to the lack of continuous long term measurements of age tracers at the tropopause, we approximated $\chi(\boldsymbol{x}_i, t')$ by applying a constant empirical time shift t_{xi} to the available TR ground tracer mixing ratio time series for each entry

https://doi.org/10.5194/egusphere-2022-1197
Preprint. Discussion started: 11 November 2022

region. For the age tracer SF_6, individual t_{xi} were obtained in this study by averaging optimized three dimensional model output between 1973-2008 that was published by Rigby et al. (2010). We emphasize that the resulting t_{xi} are exclusively used to approximate $\chi(\boldsymbol{x}_i, t')$ and that they do not represent real-world transport times between TR ground and the entry regions.

We applied the exTR-TR method to in situ SF_6 measurements taken during three aircraft campaigns in different geographical regions and at different times: PGS in NH late winter/early spring 2016, WISE in NH fall 2017 and SouthTRAC in SH early spring 2019. The resulting mean age values were averaged into bins over multiple flights using tropopause-relative altitude and eq. lat. coordinates ($\Delta\theta$-bins of size 5 K, eq. lat. bins of size 5°). These averaged mean age values were corrected for mesospheric loss by applying a linear function published by Leedham Elvidge et al. (2018). In addition, the conventional TR-only method, which assumes that all air enters the stratosphere through the TR tropopause, was applied to the same data and the results were post-processed in the same way in order to compare the results. Using the conventional TR-only method negative mean age values are derived in the LMS close to the tropopause during the WISE campaign. Using the new exTR-TR method instead, the number and extend of negative mean age values is reduced. Maximum absolute differences between the resulting averaged mean age values from the two methods range from 0.31 years to 0.42 years among the three campaigns and go in different directions for the two hemispheres. With our new exTR-TR method we are thus able to derive more realistic values of typical transport times in the LMS from measurements. This allows comparison of the two hemispheres based on campaign data. We compared results derived using the exTR-TR method from PGS campaign phase 2 (PGS2) to SouthTRAC campaign phase 1 (ST1) in order to investigate hemispheric differences with a maximal seasonal overlap of the campaigns. On average, below $\Delta\theta$=65 K the LMS was 0.5 years ± 0.3 years older during PGS2 than during ST1 across all eq. lats that are covered by both datasets. We attribute this older LMS to mixing with old vortex air during PGS2, opposed to a more confined vortex edge with higher age gradients during ST1. Although these findings only cover an isolated time period of less than two months for each campaign and do not account for different polar vortex characteristics, they are in agreement with multiannual simulation results from Konopka et al. (2015), who found a pronounced minimum in wave forcing driving the shallow branch of the BDC in the midlatitudes of the lower stratosphere in the SH between June and October, opposed to a maximum in boreal spring in the NH.

The sensitivity of the exTR-TR method to uncertainties of six input parameters was investigated at different locations using a Monte Carlo approach. The mesospheric loss of SF_6 was excluded from this sensitivity analysis, since it is currently not well understood and beyond the scope of this work. The combined sensitivity was found to be less than 0.22 years for all locations for all three campaigns. The most sensitive region for each hemisphere was located between 20-40 ° poleward of the equator below $\Delta\theta$=20 K. This is related to the setup of the experiment with a boundary at 30° in each hemisphere. Uncertainties in the origin fractions and in t_{xi} have the largest isolated impact on the sensitivity of the exTR-TR method. Overall, these sensitivities are lower than the differences between mean ages derived using the exTR-TR method and the TR-only method. Hence, our new exTR-TR method yields mean age values that differ considerably from results obtained using the conventional TR-only method in the LMS. In future studies, the exTR-TR method could be used to improve

https://doi.org/10.5194/egusphere-2022-1197
Preprint. Discussion started: 11 November 2022

deriving estimates of total and inorganic chlorine from observations of organic chlorine in the LMS like in Jesswein et al. (2021).

Appendix A: Calculating mean age in the LMS considering multiple entry regions and an ideal tracer

In case of an ideal inert linear evolving tracer, the tropical ground time series as a function of transit time t' is given by

$$\chi\left(\boldsymbol{x}_{\boldsymbol{TR\ ground}}, t'\right) = a - bt'. \quad \text{(A1)}$$

The negative sign points out, that looking at increasing transit times means looking backwards in time.

Assuming a constant time shift t_{xi} for each entry region i, the tracer time series at $\boldsymbol{x_i}$ is

$$\chi(\boldsymbol{x_i}, t') = a - b * (t' - t_{xi}). \quad \text{(A2)}$$

Hence, by inserting Eq. (A2) into Eq. (2), the stratospheric mixing ratio can be expressed as

$$\chi(\boldsymbol{x}) = \int_0^\infty \sum_{i=0}^{N-1} \left(f_i(\boldsymbol{x}) * \left(a - b * (t' - t_{xi})\right)\right) * G(\boldsymbol{x}, t')dt'. \quad \text{(A3)}$$

Since the sum of all origin fractions equals 1, Eq. (A3) can also be written as

$$\chi(\boldsymbol{x}) = \int_0^\infty [a - bt' + b * \sum_{i=0}^{N-1}(f_i(\boldsymbol{x}) * t_{xi})] * G(\boldsymbol{x}, t')dt', \quad \text{(A4)}$$

which is equivalent to

$$\chi(\boldsymbol{x}) = a + b * \sum_{i=0}^{N-1}(f_i(\boldsymbol{x}) * t_{xi}) - b * \int_0^\infty t' * G(\boldsymbol{x}, t')dt'. \quad \text{(A5)}$$

The mean age Γ is the first moment of the age spectrum, given by

$$\Gamma(\boldsymbol{x}) = \int_0^\infty t' * G(\boldsymbol{x}, t')dt'. \quad \text{(A6)}$$

Inserting Eq. (A6) into Eq. (A5) yields:

$$\chi(\boldsymbol{x}) = a + b * \sum_{i=0}^{N-1}(f_i(\boldsymbol{x}) * t_{xi}) - b * \Gamma(\boldsymbol{x}). \quad \text{(A7)}$$

Equation (A7) can be solved for Γ, which yields

$$\Gamma(\boldsymbol{x}) = \frac{a-\chi(\boldsymbol{x})}{b} + \sum_{i=0}^{N-1}(f_i(\boldsymbol{x}) * t_{xi}), \quad \text{(A8)}$$

which is equivalent to Eq. (5).

In order to derive mean age from an ideal inert quadratic evolving tracer with multiple entry regions, we extended the equations given by (Volk et al., 1997). In this case the TR ground mixing ratio time series is given as a function of transit time by

$$\chi\left(\boldsymbol{x}_{\boldsymbol{TR\ ground}}, t'\right) = a - bt' + ct'^2. \quad \text{(A9)}$$

Assuming a constant time shift t_{xi} for each entry region i, the tracer time series at $\boldsymbol{x_i}$ is

$$\chi(\boldsymbol{x_i}, t') = a - b * (t' - t_{xi}) + c * (t' - t_{xi})^2. \quad \text{(A10)}$$

Hence, by inserting Eq. (A10) into Eq. (2), the stratospheric mixing ratio can be expressed as

$$\chi(\boldsymbol{x}) = \int_0^\infty \sum_{i=0}^{N-1}\left(f_i * (a - b * (t' - t_{xi}) + c * (t' - t_{xi})^2)\right) * G(\boldsymbol{x}, t')dt', \quad \text{(A11)}$$

which is equivalent to

https://doi.org/10.5194/egusphere-2022-1197
Preprint. Discussion started: 11 November 2022

$$\chi(\boldsymbol{x}) = \sum_{i=0}^{N-1}\left(f_i * \int_0^{\infty}(a - b * (t' - t_{xi}) + c * (t' - t_{xi})^2) * G(\boldsymbol{x}, t')dt'\right). \quad \text{(A12)}$$

Note that for better readability $f_i(\boldsymbol{x})$ is written as f_i.

By extracting constant factors from the integral and applying Eq. (A6), Eq. (A12) can also be written as

$$\begin{aligned}\chi(\boldsymbol{x}) &= \sum_{i=0}^{N-1}\left[f_i * \left(a + bt_{xi} - b * \int_0^{\infty} t' * G(\boldsymbol{x}, t')dt' + c * \int_0^{\infty}(t' - t_{xi})^2 * G(\boldsymbol{x}, t')dt'\right)\right] \\ &= \sum_{i=0}^{N-1}\left[f_i * \left(a + bt_{xi} - b\Gamma(\boldsymbol{x}) + c * \int_0^{\infty}(t' - t_{xi})^2 * G(\boldsymbol{x}, t')dt'\right)\right] \\ &= \sum_{i=0}^{N-1}\left[f_i * \left(a + bt_{xi} - b\Gamma(\boldsymbol{x}) + c * \int_0^{\infty}(t'^2 - 2t_{xi}t' + t_{xi}^2) * G(\boldsymbol{x}, t')dt'\right)\right] \\ &= \sum_{i=0}^{N-1}\left[f_i * \left(a + bt_{xi} - b\Gamma(\boldsymbol{x}) + c * \left(t_{xi}^2 + \int_0^{\infty}(t'^2 - 2t_{xi}t') * G(\boldsymbol{x}, t')dt'\right)\right)\right] \\ &= \sum_{i=0}^{N-1}\left[f_i * \left(a + bt_{xi} - b\Gamma(\boldsymbol{x}) + c * \left(t_{xi}^2 - 2t_{xi}\Gamma(\boldsymbol{x}) + \int_0^{\infty} t'^2 * G(\boldsymbol{x}, t')dt'\right)\right)\right]. \quad \text{(A13)}\end{aligned}$$

The width of the age spectrum Δ is the square root of the second centred moment of the age spectrum, which is given by

$$\Delta^2(\boldsymbol{x}) = \frac{1}{2}\int_0^{\infty}\left(t' - \Gamma(\boldsymbol{x})\right)^2 * G(\boldsymbol{x}, t') * dt'. \quad \text{(A14)}$$

Equation (A14) can be transformed to

$$\int_0^{\infty} t'^2 * G(\boldsymbol{x}, t')dt' = 2\Delta(\boldsymbol{x})^2 + \Gamma(\boldsymbol{x})^2. \quad \text{(A15)}$$

Inserting Eq. (A15) into Eq. (A13) yields

$$\chi(\boldsymbol{x}) = \sum_{i=0}^{N-1}\left[f_i * \left(a + bt_{xi} - b\Gamma(\boldsymbol{x}) + c * (t_{xi}^2 - 2t_{xi}\Gamma(\boldsymbol{x}) + \Gamma(\boldsymbol{x})^2 + 2\Delta(\boldsymbol{x})^2)\right)\right]. \quad \text{(A16)}$$

Since the sum of all origin fractions equals 1 and with the weighted mean time shift $t_m(\boldsymbol{x}) = \sum_{i=0}^{N-1}[f_i(\boldsymbol{x}) * t_{xi}]$, Eq. (A16) can also be written as:

$$\begin{aligned}\chi(\boldsymbol{x}) &= a - b\Gamma(\boldsymbol{x}) + c * (2\Delta(\boldsymbol{x})^2 + \Gamma(\boldsymbol{x})^2) + \sum_{i=0}^{N-1}\left[f_i * \left(bt_{xi} + c * \left(t_{xi}^2 - 2t_{xi}\Gamma(\boldsymbol{x})\right)\right)\right] \\ &= a + b * \left(t_m(\boldsymbol{x}) - \Gamma(\boldsymbol{x})\right) + c * \left(2\Delta(\boldsymbol{x})^2 + \Gamma(\boldsymbol{x})^2 + \sum_{i=0}^{N-1}\left[f_i * \left(t_{xi}^2 - 2t_{xi}\Gamma(\boldsymbol{x})\right)\right]\right) \\ &= a + b * \left(t_m(\boldsymbol{x}) - \Gamma(\boldsymbol{x})\right) + c * (2\Delta(\boldsymbol{x})^2 + \Gamma(\boldsymbol{x})^2 - 2t_m(\boldsymbol{x})\Gamma(\boldsymbol{x}) + \sum_{i=0}^{N-1}[f_i t_{xi}^2]) \quad \text{(A17)}\end{aligned}$$

Inserting the ratio of moments $\lambda = \Delta^2/\Gamma$ into Eq. (A17) yields the quadratic equation Eq. (A18):

$$\chi(\boldsymbol{x}) = a + b * \left(t_m(\boldsymbol{x}) - \Gamma(\boldsymbol{x})\right) + c * (2\lambda\Gamma(\boldsymbol{x}) + \Gamma(\boldsymbol{x})^2 - 2t_m(\boldsymbol{x})\Gamma(\boldsymbol{x}) + \sum_{i=0}^{N-1}[f_i t_{xi}^2]), \quad \text{(A18)}$$

which can be rearranged to

$$0 = \frac{a + bt_m(\boldsymbol{x}) - \chi(\boldsymbol{x})}{c} + \sum_{i=0}^{N-1}[f_i t_{xi}^2] + \Gamma(\boldsymbol{x}) * \left(2\lambda - \frac{b}{c} - 2t_m(\boldsymbol{x})\right) + \Gamma(\boldsymbol{x})^2, \quad \text{(A19)}$$

and finally solved for Γ:

$$\Gamma(\boldsymbol{x})_{1,2} = -\lambda + t_m + \frac{b}{2c} \pm \sqrt{\left(-\lambda + t_m + \frac{b}{2c}\right)^2 - \frac{a + bt_m - \chi(x)}{c} - \sum_{i=0}^{N-1}[f_i * t_{xi}^2]}. \quad \text{(A21)}$$

https://doi.org/10.5194/egusphere-2022-1197
Preprint. Discussion started: 11 November 2022

Appendix B: CLaMS origin fraction parameterizations

We designed a general mathematical parameterization function $\varphi_{i,seas}$ with 12 parameters to derive 2-D parameterizations for exTR origin fractions in $\Delta\Theta - eq.lat$ space. The process of designing $\varphi_{i,seas}$ was guided by a non-physical but entirely geometrical approach pursuing three priorities for all 10 considered $f_{i,seas}(\boldsymbol{x})$ at once:

(i) $\varphi_{i,seas}$ should be able to reproduce major geometrical features of the distributions.

(ii) The maximum difference to $f_{i,seas}(\boldsymbol{x})$ should be as low as possible.

(iii) The mean deviation to $f_{i,seas}(\boldsymbol{x})$ should be as low as possible.

In addition to the three priorities, the number of parameters needed to achieve (i), (ii) and (iii) should be preferably low. The resulting general mathematical parameterization function is a combination of Gaussian distributions and cumulative Gumbel distributions with 12 parameters in total:

$$\mathrm{peak1}(eq.lat, \Delta\Theta) = e^{-e^{-\frac{|eq.lat|-x_0}{x_1}}} * e^{-\left(\frac{\Delta\Theta-y_1}{y_0}\right)^2} \quad \text{(B1)}$$

$$\mathrm{peak2}(eq.lat, \Delta\Theta) = g_a * e^{-\left(\frac{eq.lat-g_{x1}}{g_{x0}}\right)^2} * e^{-\left(\frac{\Delta\Theta-g_{y1}}{g_{y0}}\right)^2} \quad \text{(B2)}$$

$$\mathrm{offset\_gumbel}(\Delta\Theta) = b_y * e^{-e^{-\frac{\Delta\Theta-e_0}{e_1}}} \quad \text{(B3)}$$

$$\varphi_{i,seas}(eq.lat, \Delta\Theta) = \mathrm{peak1}(eq.lat, \Delta\Theta) + \mathrm{peak2}(eq.lat, \Delta\Theta) + \mathrm{offset\_gumbel}(\Delta\Theta) \quad \text{(B4)}$$

The seasonally averaged $f_{i,seas}(\boldsymbol{x})$ data published by (Hauck et al., 2020) is gridded in 2° latitude and 37 vertical potential temperature levels between 280 K and 3000 K. Additionally, the potential temperature difference to the local tropopause ($\Delta\Theta$) is provided for each data point. In order to find optimal fitting parameters using a least-square fit, for each of the 10 considered $f_{i,seas}(\boldsymbol{x})$ we only considered data from the respective hemisphere and for the lower 20 vertical levels (i.e. 280 K to 480 K). The resulting parameters for each of the 10 considered $f_{i,seas}(\boldsymbol{x})$ are listed in Table B1. The python code for applying $\varphi_{i,seas}$ as given in Eq. (B4) and automatically including the information given in Table B1 is available from Wagenhäuser (2022a).

Table B1: Parameter values for extra tropical origin fractions $\boldsymbol{\varphi_{i,seas}}$ calculated with Eq. (B4) by hemisphere and season.

	x_0	x_1	y_0	y_1	b_y	e_0	e_1	g_{y0}	g_{y1}	g_a	g_{x0}	g_{x1}
NH ANN	31.012	4.873	33.943	-17.027	0.132	13.288	13.039	63.375	43.149	0.228	50.778	61.048
NH DJF	31.581	5.507	52.037	-20.088	0.107	36.32	9.341	77.047	82.829	0.132	73.343	50.228
NH MAM	31.786	3.858	33.519	-16.758	-669.405	-41.6	1.56	11043.854	85.872	669.578	6003.475	80.459
NH JJA	36.242	18.45	17.177	-5.66	0.142	10.948	4.301	-49.379	28.372	0.308	40.474	48.496
NH SON	26.958	8.66	40.786	-19.772	0.152	17.019	8.001	-53.255	52.041	0.366	58.629	59.063
SH ANN	30.434	4.033	-32.442	-15.257	0.13	75.493	12.132	41.952	44.968	0.488	66.713	-86.659
SH DJF	29.478	7.284	-48.731	-31.197	0.088	327.402	-3.53	59.583	49.447	0.355	59.492	-87.584

https://doi.org/10.5194/egusphere-2022-1197
Preprint. Discussion started: 11 November 2022

SH MAM	29.776	5.449	-44.403	-21.513	0.12	25.627	10.129	57.057	49.173	0.253	52.374	-59.583
SH JJA	30.733	3.882	-26.612	-9.583	0.136	67.734	8.593	31.786	43.443	0.381	58.274	-80.771
SH SON	30.296	4.814	-36.864	-14.732	0.135	30.789	49.448	37.568	45.222	0.585	36.574	-85.755

Appendix C: SouthTRAC phase 1 and PGS phase 2 campaign differences using the TR-only method

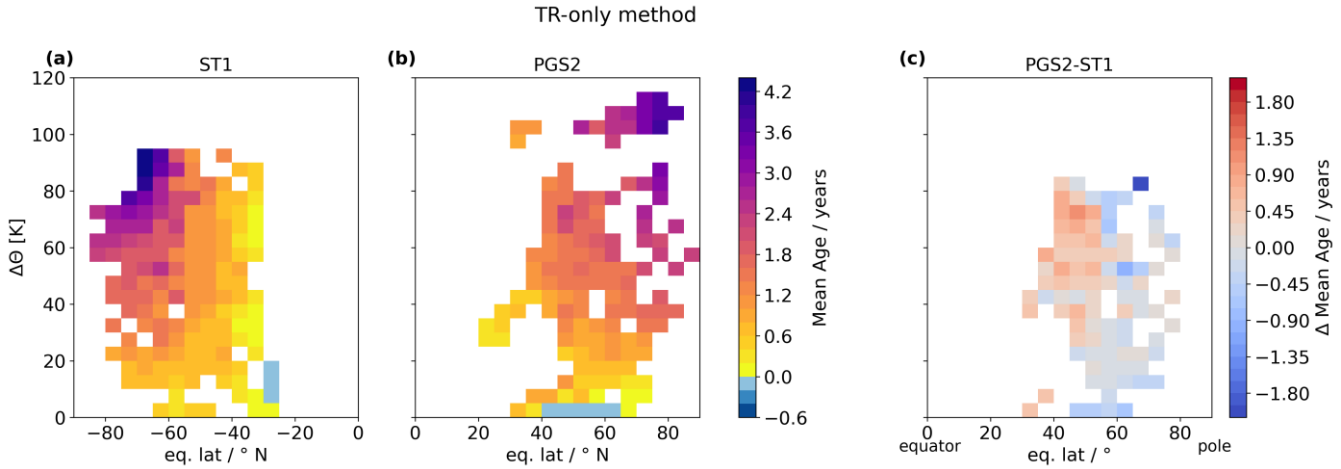

Figure C1: Same as Fig. 4, but mean ages have been derived using the conventional TR-only method instead.

Code and data availability

The Python software implementation of the exTR-TR method is available from Wagenhäuser and Engel (2022).

The Python software code repository "f_exTR" for deploying our parameterizations of the CLaMS origin fractions is available from Wagenhäuser (2022a).

The Python software code repository "sf6-timeshifts-from-rigby2010" for deriving SF_6 time shifts to tropical ground using model data from Rigby et al. (2010) (Sect. 2.2.2) is available from Wagenhäuser (2022b).

Tracer measurements, flight coordinates and mean age values derived using both the exTR-TR method and the TR-only method can be downloaded from Wagenhäuser et al. (2022).

Author contribution

TW developed the mathematical framework and Python software code for the exTR-TR method in close collaboration with AE. AE initiated this study. TW, MJ, TK, TS and AE operated the GhOST instrument during the SouthTRAC campaign. TW wrote the manuscript in collaboration with AE. All authors contributed to the final version of the manuscript.

https://doi.org/10.5194/egusphere-2022-1197
Preprint. Discussion started: 11 November 2022

Competing interests

The authors declare that they have no conflict of interest.

Acknowledgements

This research was supported under the Deutsche Forschungsgemeinschaft (DFG, German Research Foundation) Priority Program SPP 1294 "Atmospheric and Earth System Research with HALO" – "High Altitude and Long Range Research Aircraft" under project numbers EN367/5, EN367/8, EN367/11, EN 367/13, EN 367/14 and EN 367/16. Financial support also came from the DFG – TRR 301 – Project-ID 428312742. We would like to thank the DLR staff for the operation of the HALO and the support during all three campaigns. Many thanks also to all former master students at Goethe-University Frankfurt, who helped carrying out measurements during the campaigns. Moreover, we thank Jens-Uwe Grooß for facilitating access to model based Δθ and eq. lat. data along the flight tracks. We thank Matthew Rigby and Luke Western for providing updated AGAGE 12-box model output of SF_6 mixing ratios. We further thank Ronald Prinn, Ray Weiss, Paul Krummel, Dickon Young, Simon O'Doherty and Jens Mühle for facilitating access to the AGAGE data (agage.mit.edu). The AGAGE stations used in this paper are supported by the National Aeronautics and Space Administration (NASA) (grants NNX16AC98G to MIT, and NNX16AC97G and NNX16AC96G to SIO). Support also comes from the UK Department for Business, Energy & Industrial Strategy (BEIS) for MHD, the National Oceanic and Atmospheric Administration (NOAA) for RPB, and the Commonwealth Scientific and Industrial Research Organization (CSIRO) and the Bureau of Meteorology (Australia) for CGO.

References

Andrews, A. E., Boering, K. A., Daube, B. C., Wofsy, S. C., Hintsa, E. J., Weinstock, E. M. and Bui, T. P.: Empirical age spectra for the lower tropical stratosphere from in situ observations of CO2: Implications for stratospheric transport, J. Geophys. Res. Atmos., 104(D21), 26581–26595, doi:10.1029/1999JD900150, 1999.

Andrews, A. E., Boering, K. A., Wofsy, S. C., Daube, B. C., Jones, D. B., Alex, S., Loewenstein, M., Podolske, J. R. and Strahan, S. E.: Empirical age spectra for the midlatitude lower stratosphere from in situ observations of CO2: Quantitative evidence for a subtropical "barrier" to horizontal transport, J. Geophys. Res. Atmos., 106(D10), 10257–10274, doi:10.1029/2000JD900703, 2001.

Birner, T. and Bönisch, H.: Residual circulation trajectories and transit times into the extratropical lowermost stratosphere, Atmos. Chem. Phys., 11(2), 817–827, doi:10.5194/acp-11-817-2011, 2011.

Bönisch, H., Engel, A., Curtius, J., Birner, T. and Hoor, P.: Quantifying transport into the lowermost stratosphere using simultaneous in-situ measurements of SF6 and CO2, Atmos. Chem. Phys., 9(16), 5905–5919, doi:10.5194/acp-9-5905-2009, 2009.

https://doi.org/10.5194/egusphere-2022-1197
Preprint. Discussion started: 11 November 2022

Butchart, N.: The Brewer-Dobson circulation, Rev. Geophys., 52(2), 157–184, doi:10.1002/2013RG000448, 2014.

Cunnold, D., Alyea, F. and Prinn, R.: A methodology for determining the atmospheric lifetime of fluorocarbons, J. Geophys. Res., 83(C11), 5493, doi:10.1029/JC083iC11p05493, 1978.

Cunnold, D. M., Prinn, R. G., Rasmussen, R. A., Simmonds, P. G., Alyea, F. N., Cardelino, C. A. and Crawford, A. J.: The Atmospheric Lifetime Experiment: 4. Results for CF 2 Cl 2 based on three years data, J. Geophys. Res., 88(C13), 8401, doi:10.1029/JC088iC13p08401, 1983.

Engel, A., Bönisch, H., Brunner, D., Fischer, H., Franke, H., Günther, G., Gurk, C., Hegglin, M., Hoor, P., Königstedt, R., Krebsbach, M., Maser, R., Parchatka, U., Peter, T., Schell, D., Schiller, C., Schmidt, U., Spelten, N., Szabo, T., Weers, U., Wernli, H., Wetter, T. and Wirth, V.: Highly resolved observations of trace gases in the lowermost stratosphere and upper troposphere from the Spurt project: an overview, Atmos. Chem. Phys., 6(2), 283–301, doi:10.5194/acp-6-283-2006, 2006.

Engel, A., Bönisch, H., Ullrich, M., Sitals, R., Membrive, O., Danis, F. and Crevoisier, C.: Mean age of stratospheric air derived from AirCore observations, Atmos. Chem. Phys., 17(11), 6825–6838, doi:10.5194/acp-17-6825-2017, 2017.

Fritsch, F., Garny, H., Engel, A., Bönisch, H. and Eichinger, R.: Sensitivity of age of air trends to the derivation method for non-linear increasing inert SF6, Atmos. Chem. Phys., 20(14), 8709–8725, doi:10.5194/acp-20-8709-2020, 2020.

Gettelman, a., Hoor, P., Pan, L. L., Randel, W. J., Hegglin, M. I. and Birner, T.: The extratropical upper troposphere and lower stratosphere, Rev. Geophys., 49(3), RG3003, doi:10.1029/2011RG000355, 2011.

Hall, T. M. and Plumb, R. A.: Age as a diagnostic of stratospheric transport, J. Geophys. Res., 99(D1), 1059–1070, doi:10.1029/93JD03192, 1994.

HALO consortium: High Altitude and LOng Range database, , doi:10.17616/R39Q0T, 2021.

Hauck, M., Fritsch, F., Garny, H. and Engel, A.: Deriving stratospheric age of air spectra using an idealized set of chemically active trace gases, Atmos. Chem. Phys., 19(7), 5269–5291, doi:10.5194/acp-19-5269-2019, 2019.

Hauck, M., Bönisch, H., Hoor, P., Keber, T., Ploeger, F., Schuck, T. J. and Engel, A.: A convolution of observational and model data to estimate age of air spectra in the northern hemispheric lower stratosphere, Atmos. Chem. Phys., 20(14), 8763–8785, doi:10.5194/acp-20-8763-2020, 2020.

Jesswein, M., Bozem, H., Lachnitt, H. C., Hoor, P., Wagenhäuser, T., Keber, T., Schuck, T. and Engel, A.: Comparison of inorganic chlorine in the Antarctic and Arctic lowermost stratosphere by separate late winter aircraft measurements, Atmos. Chem. Phys., 21(23), 17225–17241, doi:10.5194/acp-21-17225-2021, 2021.

Keber, T., Bönisch, H., Hartick, C., Hauck, M., Lefrancois, F., Obersteiner, F., Ringsdorf, A., Schohl, N., Schuck, T., Hossaini, R., Graf, P., Jöckel, P. and Engel, A.: Bromine from short-lived source gases in the extratropical northern hemispheric upper troposphere and lower stratosphere (UTLS), Atmos. Chem. Phys., 20(7), 4105–4132, doi:10.5194/acp-20-4105-2020, 2020.

Kida, H.: General Circulation of Air Parcels and Transport Characteristics Derived from a hemispheric GCM, J. Meteorol. Soc. Japan. Ser. II, 61(2), 171–187, doi:10.2151/jmsj1965.61.2_171, 1983.

https://doi.org/10.5194/egusphere-2022-1197
Preprint. Discussion started: 11 November 2022

Konopka, P., Ploeger, F., Tao, M., Birner, T. and Riese, M.: Hemispheric asymmetries and seasonality ofmean age of air in the lower stratosphere: Deep versus shallow branch of the Brewer-Dobson circulation, J. Geophys. Res., 120(5), 2053–2066, doi:10.1002/2014JD022429, 2015.

Krause, J., Hoor, P., Engel, A., Plöger, F., Grooß, J. U., Bönisch, H., Keber, T., Sinnhuber, B. M., Woiwode, W. and Oelhaf, H.: Mixing and ageing in the polar lower stratosphere in winter 2015-2016, Atmos. Chem. Phys., 18(8), 6057–6073, doi:10.5194/acp-18-6057-2018, 2018.

Leedham Elvidge, E., Bönisch, H., Brenninkmeijer, C. A. M., Engel, A., Fraser, P. J., Gallacher, E., Langenfelds, R., Mühle, J., Oram, D. E., Ray, E. A., Ridley, A. R., Röckmann, T., Sturges, W. T., Weiss, R. F. and Laube, J. C.: Evaluation of stratospheric age of air from CF4, C2F6, C3F8, CHF3, HFC-125, HFC-227ea and SF6; Implications for the calculations of halocarbon lifetimes, fractional release factors and ozone depletion potentials, Atmos. Chem. Phys., 18(5), 3369–3385, doi:10.5194/acp-18-3369-2018, 2018.

Loeffel, S., Eichinger, R., Garny, H., Reddmann, T., Fritsch, F., Versick, S., Stiller, G. and Haenel, F.: The impact of sulfur hexafluoride SF6 sinks on age of air climatologies and trends, Atmos. Chem. Phys., 22(2), 1175–1193, doi:10.5194/acp-22-1175-2022, 2022.

Miller, B. R., Weiss, R. F., Salameh, P. K., Tanhua, T., Greally, B. R., Mühle, J. and Simmonds, P. G.: Medusa: A Sample Preconcentration and GC/MS Detector System for in Situ Measurements of Atmospheric Trace Halocarbons, Hydrocarbons, and Sulfur Compounds, Anal. Chem., 80(5), 1536–1545, doi:10.1021/ac702084k, 2008.

Oelhaf, H., Sinnhuber, B., Woiwode, W., Bönisch, H., Bozem, H., Engel, A., Fix, A., Friedl-Vallon, F., Grooß, J., Hoor, P., Johansson, S., Jurkat-Witschas, T., Kaufmann, S., Krämer, M., Krause, J., Kretschmer, E., Lörks, D., Marsing, A., Orphal, J., Pfeilsticker, K., Pitts, M., Poole, L., Preusse, P., Rapp, M., Riese, M., Rolf, C., Ungermann, J., Voigt, C., Volk, C. M., Wirth, M., Zahn, A. and Ziereis, H.: POLSTRACC: Airborne Experiment for Studying the Polar Stratosphere in a Changing Climate with the High Altitude and Long Range Research Aircraft (HALO), Bull. Am. Meteorol. Soc., 100(12), 2634–2664, doi:10.1175/BAMS-D-18-0181.1, 2019.

Plumb, R. A.: Stratospheric transport, J. Meteorol. Soc. Japan, 80(4 B), 793–809, doi:10.2151/jmsj.80.793, 2002.

Pommrich, R., Müller, R., Grooß, J.-U., Konopka, P., Ploeger, F., Vogel, B., Tao, M., Hoppe, C. M., Günther, G., Spelten, N., Hoffmann, L., Pumphrey, H.-C., Viciani, S., D'Amato, F., Volk, C. M., Hoor, P., Schlager, H. and Riese, M.: Tropical troposphere to stratosphere transport of carbon monoxide and long-lived trace species in the Chemical Lagrangian Model of the Stratosphere (CLaMS), Geosci. Model Dev., 7(6), 2895–2916, doi:10.5194/gmd-7-2895-2014, 2014.

Prinn, R. G., Weiss, R. F., Arduini, J., Arnold, T., DeWitt, H. L., Fraser, P. J., Ganesan, A. L., Gasore, J., Harth, C. M., Hermansen, O., Kim, J., Krummel, P. B., Li, S., Loh, Z. M., Lunder, C. R., Maione, M., Manning, A. J., Miller, B. R., Mitrevski, B., Mühle, J., O'Doherty, S., Park, S., Reimann, S., Rigby, M., Saito, T., Salameh, P. K., Schmidt, R., Simmonds, P. G., Steele, L. P., Vollmer, M. K., Wang, R. H., Yao, B., Yokouchi, Y., Young, D. and Zhou, L.: History of chemically and radiatively important atmospheric gases from the Advanced Global Atmospheric Gases Experiment

https://doi.org/10.5194/egusphere-2022-1197
Preprint. Discussion started: 11 November 2022

(AGAGE), Earth Syst. Sci. Data, 10(2), 985–1018, doi:10.5194/essd-10-985-2018, 2018.

Rapp, M., Kaifler, B., Dörnbrack, A., Gisinger, S., Mixa, T., Reichert, R., Kaifler, N., Knobloch, S., Eckert, R., Wildmann, N., Giez, A., Krasauskas, L., Preusse, P., Geldenhuys, M., Riese, M., Woiwode, W., Friedl-Vallon, F., Sinnhuber, B.-M., Torre, A. de la, Alexander, P., Hormaechea, J. L., Janches, D., Garhammer, M., Chau, J. L., Conte, J. F., Hoor, P. and Engel, A.: SOUTHTRAC-GW: An Airborne Field Campaign to Explore Gravity Wave Dynamics at the World's Strongest Hotspot, Bull. Am. Meteorol. Soc., 102(4), E871–E893, doi:10.1175/BAMS-D-20-0034.1, 2021.

Ray, E. A., Moore, F. L., Elkins, J. W., Rosenlof, K. H., Laube, J. C., Röckmann, T., Marsh, D. R. and Andrews, A. E.: Quantification of the SF6 lifetime based on mesospheric loss measured in the stratospheric polar vortex, J. Geophys. Res., 122(8), 4626–4638, doi:10.1002/2016JD026198, 2017.

Ray, E. A., Atlas, E. L., Schauffler, S., Chelpon, S., Pan, L., Bönisch, H. and Rosenlof, K. H.: Age spectra and other transport diagnostics in the North American monsoon UTLS from SEAC4RS in situ trace gas measurements, Atmos. Chem. Phys., 22(10), 6539–6558, doi:10.5194/acp-22-6539-2022, 2022.

Rigby, M., Mühle, J., Miller, B. R., Prinn, R. G., Krummel, P. B., Steele, L. P., Fraser, P. J., Salameh, P. K., Harth, C. M., Weiss, R. F., Greally, B. R., O'Doherty, S., Simmonds, P. G., Vollmer, M. K., Reimann, S., Kim, J., Kim, K.-R., Wang, H. J., Olivier, J. G. J., Dlugokencky, E. J., Dutton, G. S., Hall, B. D. and Elkins, J. W.: History of atmospheric SF6 from 1973 to 2008, Atmos. Chem. Phys., 10(21), 10305–10320, doi:10.5194/acp-10-10305-2010, 2010.

Rigby, M., Prinn, R. G., O'Doherty, S., Montzka, S. A., McCulloch, A., Harth, C. M., Mühle, J., Salameh, P. K., Weiss, R. F., Young, D., Simmonds, P. G., Hall, B. D., Dutton, G. S., Nance, D., Mondeel, D. J., Elkins, J. W., Krummel, P. B., Steele, L. P. and Fraser, P. J.: Re-evaluation of the lifetimes of the major CFCs and CH3CCl3 using atmospheric trends, Atmos. Chem. Phys., 13(5), 2691–2702, doi:10.5194/acp-13-2691-2013, 2013.

Simmonds, P. G., Rigby, M., Manning, A. J., Park, S., Stanley, K. M., McCulloch, A., Henne, S., Graziosi, F., Maione, M., Arduini, J., Reimann, S., Vollmer, M. K., Mühle, J., O'Doherty, S., Young, D., Krummel, P. B., Fraser, P. J., Weiss, R. F., Salameh, P. K., Harth, C. M., Park, M.-K., Park, H., Arnold, T., Rennick, C., Steele, L. P., Mitrevski, B., Wang, R. H. J. and Prinn, R. G.: The increasing atmospheric burden of the greenhouse gas sulfur hexafluoride (SF6), Atmos. Chem. Phys., 20(12), 7271–7290, doi:10.5194/acp-20-7271-2020, 2020.

Volk, C. M., Elkins, J. W., Fahey, D. W., Dutton, G. S., Gilligan, J. M., Loewenstein, M., Podolske, J. R., Chan, K. R. and Gunson, M. R.: Evaluation of source gas lifetimes from stratospheric observations, J. Geophys. Res. Atmos., 102(21), 25543–25564, doi:10.1029/97jd02215, 1997.

Wagenhäuser, T.: AtmosphericAngels/f_exTR: v.1.0.0, , doi:10.5281/zenodo.7267114, 2022a.

Wagenhäuser, T.: AtmosphericAngels/sf6-timeshifts-from-rigby2010: v1.0.0, , doi:10.5281/zenodo.7267089, 2022b.

Wagenhäuser, T. and Engel, A.: AtmosphericAngels/exTR-TR-method: v.1.0.0, , doi:10.5281/zenodo.7267203, 2022.

Wagenhäuser, T., Jesswein, M., Keber, T., Schuck, T., Engel, A. and Grooß, J.-U.: SF6 and CFC-12 measurements and mean age along HALO flight tracks during PGS, WISE and SouthTRAC, , doi:10.5281/zenodo.7275822, 2022.

Waugh, D. W. and Hall, T. M.: Age of stratospheric air: Theory, observations, and models, Rev. Geophys., 40(4), 1-1-1–26,

https://doi.org/10.5194/egusphere-2022-1197
Preprint. Discussion started: 11 November 2022

doi:10.1029/2000RG000101, 2002.